



TUNABLE AND RECONFIGURABLE OPTICAL METAMATERIALS

EDITED BY: Yuancheng Fan, Qian Zhao, Fuli Zhang and Nianhai Shen
PUBLISHED IN: Frontiers in Physics



frontiers

Frontiers eBook Copyright Statement

The copyright in the text of individual articles in this eBook is the property of their respective authors or their respective institutions or funders. The copyright in graphics and images within each article may be subject to copyright of other parties. In both cases this is subject to a license granted to Frontiers.

The compilation of articles constituting this eBook is the property of Frontiers.

Each article within this eBook, and the eBook itself, are published under the most recent version of the Creative Commons CC-BY licence.

The version current at the date of publication of this eBook is CC-BY 4.0. If the CC-BY licence is updated, the licence granted by Frontiers is automatically updated to the new version.

When exercising any right under the CC-BY licence, Frontiers must be attributed as the original publisher of the article or eBook, as applicable.

Authors have the responsibility of ensuring that any graphics or other materials which are the property of others may be included in the CC-BY licence, but this should be checked before relying on the CC-BY licence to reproduce those materials. Any copyright notices relating to those materials must be complied with.

Copyright and source acknowledgement notices may not be removed and must be displayed in any copy, derivative work or partial copy which includes the elements in question.

All copyright, and all rights therein, are protected by national and international copyright laws. The above represents a summary only. For further information please read Frontiers' Conditions for Website Use and Copyright Statement, and the applicable CC-BY licence.

ISSN 1664-8714

ISBN 978-2-88963-508-5

DOI 10.3389/978-2-88963-508-5

About Frontiers

Frontiers is more than just an open-access publisher of scholarly articles: it is a pioneering approach to the world of academia, radically improving the way scholarly research is managed. The grand vision of Frontiers is a world where all people have an equal opportunity to seek, share and generate knowledge. Frontiers provides immediate and permanent online open access to all its publications, but this alone is not enough to realize our grand goals.

Frontiers Journal Series

The Frontiers Journal Series is a multi-tier and interdisciplinary set of open-access, online journals, promising a paradigm shift from the current review, selection and dissemination processes in academic publishing. All Frontiers journals are driven by researchers for researchers; therefore, they constitute a service to the scholarly community. At the same time, the Frontiers Journal Series operates on a revolutionary invention, the tiered publishing system, initially addressing specific communities of scholars, and gradually climbing up to broader public understanding, thus serving the interests of the lay society, too.

Dedication to Quality

Each Frontiers article is a landmark of the highest quality, thanks to genuinely collaborative interactions between authors and review editors, who include some of the world's best academicians. Research must be certified by peers before entering a stream of knowledge that may eventually reach the public - and shape society; therefore, Frontiers only applies the most rigorous and unbiased reviews.

Frontiers revolutionizes research publishing by freely delivering the most outstanding research, evaluated with no bias from both the academic and social point of view. By applying the most advanced information technologies, Frontiers is catapulting scholarly publishing into a new generation.

What are Frontiers Research Topics?

Frontiers Research Topics are very popular trademarks of the Frontiers Journals Series: they are collections of at least ten articles, all centered on a particular subject. With their unique mix of varied contributions from Original Research to Review Articles, Frontiers Research Topics unify the most influential researchers, the latest key findings and historical advances in a hot research area! Find out more on how to host your own Frontiers Research Topic or contribute to one as an author by contacting the Frontiers Editorial Office: frontiersin.org/about/contact

TUNABLE AND RECONFIGURABLE OPTICAL METAMATERIALS

Topic Editors:

Yuancheng Fan, Northwestern Polytechnical University, China

Qian Zhao, Tsinghua University, China

Fuli Zhang, Northwestern Polytechnical University, China

Nianhai Shen, Iowa State University, United States

Citation: Fan, Y., Zhao, Q., Zhang, F., Shen, N., eds. (2021). Tunable and Reconfigurable Optical Metamaterials. Lausanne: Frontiers Media SA.
doi: 10.3389/978-2-88963-508-5

Table of Contents

- 04 Editorial: Tunable and Reconfigurable Optical Metamaterials**
Yuancheng Fan, Qian Zhao, Fuli Zhang and Nian-Hai Shen
- 06 Tunable Unidirectivity of Metal-Dielectric-Metal Plasmonic Nanoantennas With PT-Symmetric Potentials**
Chaowei Xu, Xiaoming Zhang, Kaiyang Cheng, Xiaobing Shang, Quan Li, Zeyong Wei, Chao Wu and Hongqiang Li
- 15 Control Electromagnetic Waves Based on Multi-Layered Transparent Metasurface**
Zhichao Sun, Mengyao Yan, Tungamirai Eric Mupona and Bijun Xu
- 22 Reflective Focusing Based on Few-Layer Gradient Metasurface Element Array**
Mengyao Yan, Zhichao Sun, Bairui Wu, Pan Cheng and Bijun Xu
- 27 Switchable Metasurface With Broadband and Highly Efficient Electromagnetic Functionality**
Zeyong Wei, Xiaoqin Liu and Yang Cao
- 33 Control of THz Surface Plasmons by Geometric Phases**
Shulin Hu, Peng Wang, Cai Zhou, Min Hu, Yuli Xiong, Huanhuan Xu, Xiaoyu Li, Mingyao Xu and Shengxiang Wang
- 40 Magnetically Tunable Graphene-Based Terahertz Metasurface**
Yafeng Lu, Chen Wang, Shiqiang Zhao and Yongzheng Wen
- 47 Dynamic Control of Ultrathin Electromagnetic Absorber Using Active High Impedance Metasurfaces**
Zeyong Wei, Hongkun Li, Weijie Xu and Yang Cao
- 52 Infrared and Terahertz Compatible Absorber Based on Multilayer Film**
Mingyang Yang, Ming Zhou, Jianwen Yu, Yibo Zhang, Benyan Xu, Wenjun Cheng and Xuyin Li
- 58 A Review of Tunable Electromagnetic Metamaterials With Anisotropic Liquid Crystals**
Jing Xu, Ruisheng Yang, Yuancheng Fan, Quanhong Fu and Fuli Zhang
- 72 Multifunctional Metasurface Lens With Tunable Focus Based on Phase Transition Material**
Yongkang Song, Weici Liu, Xiaolei Wang, Faqiang Wang, Zhongchao Wei, Hongyun Meng, Ning Lin and Hongqiang Zhang



Editorial: Tunable and Reconfigurable Optical Metamaterials

Yuancheng Fan^{1*}, Qian Zhao^{2*}, Fuli Zhang^{1*} and Nian-Hai Shen^{3*}

¹Key Laboratory of Light-Field Manipulation and Information Acquisition, Ministry of Industry and Information Technology and School of Physical Science and Technology, Northwestern Polytechnical University, Xi'an, China, ²Department of Mechanical Engineering, State Key Laboratory of Tribology, Tsinghua University, Beijing, China, ³Ames Laboratory and Department of Physics and Astronomy, Iowa State University, Ames, IA, United States

Keywords: metasurfaces, metamaterials, liquid crystals, tunable metamaterial, reconfigurable metamaterial

Editorial on the Research Topic

Tunable and Reconfigurable Optical Metamaterials

Metamaterials and 2D metasurfaces [1–8] show promising and novel methods for the manipulation of optical waves in the terahertz, infrared, and visible regimes. Their performance has been demonstrated in high-resolution imaging, nonlinear optics, radiation control, holography, and optical communications. However, their practical applications are limited by the narrow operation wavelength range resulting from the resonant nature of the constitutive microstructures.

Materials with changeable properties or reconfigurable structures are being incorporated to achieve tunable optical properties, i.e. to extend the operation bandwidth or parameter space of metamaterials [9–14]. For example, graphene and related 2D materials, semiconductors, phase changing materials like VO₂ and Ge₂Sb₂Te₅, liquid crystals, and MEMS-structured metamaterials are emerging for advanced optics and photonics spanning from terahertz to visible frequencies. These developments are important for both fundamental optical physics and possible applications in nonlinear nanophotonics and super-resolution imaging.

This research topic on **Tunable Metamaterial/Metasurface** includes some remarkable examples. From the theoretical side, Xu et al. reported a study on the tunable optical scattering properties of a kind of plasmonic nanoantenna which is composed of metal-dielectric-metal metamaterial embedded with PT-symmetric layers designed for unidirectional scattering functionality. Yang et al. exploited the radiation characteristics of an ultrathin Pt layer and impedance matching to design a wavelength-selective absorber based on planarized platinum/silicon (Pt/Si) multilayer film for infrared stealth. The absorber effectively suppresses thermal radiation in two atmospheric windows and enhances thermal radiation in the nonatmospheric window. Lu et al. proposed a magneto-controlled method to manipulate the transmittance properties of a graphene-based THz metasurface comprised of graphene cut-wire arrays. It is found that the introduced vertical electrostatic field deflects the carriers in graphene and changes the transmittance characteristics of the metasurface. Hu et al. demonstrated the anomalous launching and vortices generation of surface plasmons in a THz near-field metasurface platform by tuning the orientation as well as the geometric phase of the surface unit structure. By introducing nanofins made by phase change VO₂ material into the metasurface, Song et al. proposed a temperature-controllable multifunctional metasurface lens based on phase transition material. The metasurface based lens can be switched among dual focus, single focus, and no focus at any position. For the similar focusing functionality, Yan et al. employed phase discontinuity of the three-layer square element based reflective metasurface for a high focusing efficiency of 82%. Sun et al. further demonstrated a metasurface with three-layer aperture structures to achieve a beam deflection to the desired angle of high efficiency.

From the experimental side, various mechanisms for realizing tunable metasurface can be employed to create intelligent wave control devices. Wei et al. and Wei et al. proposed the

OPEN ACCESS

Edited and reviewed by:

Lorenzo Pavesi,
University of Trento, Trento, Italy

*Correspondence:

Yuancheng Fan
phyfan@nwpu.edu.cn
Qian Zhao
zhaoqian@tsinghua.edu.cn
Fuli Zhang
fuli.zhang@nwpu.edu.cn
Nian-Hai Shen
nhshen@ameslab.gov

Specialty section:

This article was submitted to
Optics and Photonics,
a section of the journal
Frontiers in Physics

Received: 24 May 2021

Accepted: 28 May 2021

Published: 09 July 2021

Citation:

Fan Y, Zhao Q, Zhang F and Shen N-H
(2021) Editorial: Tunable and
Reconfigurable Optical Metamaterials.
Front. Phys. 9:713966.
doi: 10.3389/fphy.2021.713966

switch transparency, reflection, and absorption of metasurfaces by loading PIN diodes in the structure. They experimentally demonstrated high power transmission modulation in the frequency range 8–12 GHz and an active metasurface with a continuous changing absorption peak between 8.5 and 9.1 GHz. Xu et al. presented a review on the experimental progress of tunable metamaterials based on nematic liquid crystals. They showed that liquid crystal-based metamaterials are promising for the remarkable improvement of the bandwidth and may facilitate related applications at terahertz or even optical regimes.

This Research Topic provides an interesting overview of the different metamaterials and metasurfaces that incorporate tunable or reconfigurable mechanisms for breaking the limitation of

narrow-operation wavelengths. These new results demonstrate recent progress in tunable metamaterials and their potential usefulness in various aspects, both experimentally and theoretically. We expect that more and more metamaterials/metasurfaces will be demonstrated for fundamental wave control phenomena in physics and that novel functional meta-devices with smart properties will soon emerge.

AUTHOR CONTRIBUTIONS

All authors listed have made a substantial, direct, and intellectual contribution to the work and approved it for publication.

REFERENCES

- Smith DR, Pendry JB, and Wiltshire MCK. Metamaterials and Negative Refractive Index. *Science* (2004) 305:788–92. doi:10.1126/science.1096796
- Shalaev VM. Optical Negative-index Metamaterials. *Nat Photon* (2007) 1: 41–8. doi:10.1038/nphoton.2006.49
- Soukoulis CM, and Wegener M. Past Achievements and Future Challenges in the Development of Three-Dimensional Photonic Metamaterials. *Nat Photon* (2011) 5:523–30. doi:10.1038/nphoton.2011.154
- Yu N, Genevet P, Kats MA, Aieta F, Tetienne J-P, Capasso F, et al. Light Propagation with Phase Discontinuities: Generalized Laws of Reflection and Refraction. *Science* (2011) 334:333–7. doi:10.1126/science.1210713
- Zheludev NI, and Kivshar YS. From Metamaterials to Metadevices. *Nat Mater* (2012) 11:917–24. doi:10.1038/nmat3431
- Chen S, Liu W, Li Z, Cheng H, and Tian J. Metasurface-Empowered Optical Multiplexing and Multifunction. *Adv Mater* (2020) 32:1805912. doi:10.1002/adma.201805912
- Chen K, Ding G, Hu G, Jin Z, Zhao J, Feng Y, et al. Directional Janus Metasurface. *Adv Mater* (2020) 32:1906352. doi:10.1002/adma.201906352
- Zhang F, Pu M, Li X, Gao P, Ma X, Luo J, et al. All-Dielectric Metasurfaces for Simultaneous Giant Circular Asymmetric Transmission and Wavefront Shaping Based on Asymmetric Photonic Spin-Orbit Interactions. *Adv Funct Mater* (2017) 27:1704295. doi:10.1002/adfm.201704295
- Chen H-T, Yang H, Singh R, O'Hara JF, Azad AK, Trugman SA, et al. Tuning the Resonance in High-Temperature Superconducting Terahertz Metamaterials. *Phys Rev Lett* (2010) 105:247402. doi:10.1103/physrevlett.105.247402
- Tassin P, Koschny T, and Soukoulis CM. Graphene for Terahertz Applications. *Science* (2013) 341:620–1. doi:10.1126/science.1242253
- Fan Y, Shen N-H, Koschny T, and Soukoulis CM. Tunable Terahertz Meta-Surface with Graphene Cut-Wires. *ACS Photon* (2015) 2:151–6. doi:10.1021/ph500366z
- Low T, and Avouris P. Graphene Plasmonics for Terahertz to Mid-infrared Applications. *ACS Nano* (2014) 8:1086–101. doi:10.1021/nn406627u
- Ma M, Li Z, Liu W, Tang C, Li Z, Cheng H, et al. Optical Information Multiplexing with Nonlinear Coding Metasurfaces. *Laser Photon Rev* (2019) 13:1900045. doi:10.1002/lpor.201900045
- Liu S, Cui TJ, Xu Q, Bao D, Du L, Wan X, et al. Anisotropic Coding Metamaterials and Their Powerful Manipulation of Differently Polarized Terahertz Waves. *Light Sci Appl* (2016) 5:e16076. doi:10.1038/lsa.2016.76

Conflict of Interest: The authors declare that the research was conducted in the absence of any commercial or financial relationships that could be construed as a potential conflict of interest.

Copyright © 2021 Fan, Zhao, Zhang and Shen. This is an open-access article distributed under the terms of the Creative Commons Attribution License (CC BY). The use, distribution or reproduction in other forums is permitted, provided the original author(s) and the copyright owner(s) are credited and that the original publication in this journal is cited, in accordance with accepted academic practice. No use, distribution or reproduction is permitted which does not comply with these terms.



Tunable Unidirectivity of Metal-Dielectric-Metal Plasmonic Nanoantennas With PT-Symmetric Potentials

Chaowei Xu^{1†}, Xiaoming Zhang^{2*†}, Kaiyang Cheng^{1,3}, Xiaobing Shang^{3,4}, Quan Li^{1,3}, Zeyong Wei^{1,3}, Chao Wu^{1,3} and Hongqiang Li^{1,3*}

¹ School of Physical Science and Engineering, Tongji University, Shanghai, China, ² College of Physics Science and Engineering Technology, Yichun University, Yichun, China, ³ Institute of Dongguan-Tongji University, Dongguan, China, ⁴ College of Electronic and Information, Tongji University, Shanghai, China

OPEN ACCESS

Edited by:

Yuancheng Fan,
Northwestern Polytechnical
University, China

Reviewed by:

Zhengyong Song,
Xiamen University, China
Yihang Chen,
South China Normal University, China
Tianyue Zhang,
Jinan University, China

*Correspondence:

Xiaoming Zhang
zhangxm8555@163.com
Hongqiang Li
hqllee@tongji.edu.cn

[†]These authors have contributed
equally to this work

Specialty section:

This article was submitted to
Optics and Photonics,
a section of the journal
Frontiers in Physics

Received: 16 July 2019

Accepted: 04 October 2019

Published: 18 October 2019

Citation:

Xu C, Zhang X, Cheng K, Shang X,
Li Q, Wei Z, Wu C and Li H (2019)
Tunable Unidirectivity of
Metal-Dielectric-Metal Plasmonic
Nanoantennas With PT-Symmetric
Potentials. *Front. Phys.* 7:161.
doi: 10.3389/fphy.2019.00161

Parity-time (*PT*) symmetric photonic systems have attracted much attention due to their intriguing properties and asymmetric behaviors. In this paper, we propose a plasmonic nanoantenna with *PT*-symmetric potential for unidirectional scattering functionality. The studied plasmonic nanoantenna is comprised of three metallic layers separated by two dielectric layers. Such kind of system, with the same coefficient κ of loss and gain in each of the two dielectric layers, holds the characteristic of *PT* symmetry. We show that the unidirectional scattering is obtained for the passive structure (i.e., $\kappa = 0$), and the switching between forward and backward directionality can be achieved with a single structure by changing the excitation wavelength, when the induced electric dipole (ED) and magnetic dipole (MD) modes satisfy the first or second Kerker conditions, respectively. In addition, we find that the forward-to-backward ratio spectra can be strongly affected by the non-Hermiticity parameter κ . In particular, it is possible to reverse the radiation direction at the same wavelength in a wide spectra band by adjusting κ . Moreover, putting the nanoantennas in an array of transverse configuration can efficiently narrow the main lobe angular beam width to be $<6^\circ$. These results contribute to the basic understanding of the optical properties of active-passive finite nanostructures with potential applications, and provide new ideas for the design of novel nanostructures displaying asymmetric and tunable responses.

Keywords: optical nanoantenna, unidirectional scattering, metallic and dielectric hybrid, parity-time symmetric, Kerker condition, tunable

INTRODUCTION

Surface plasmon polaritons (SPPs) refer to collective oscillations of conductive electrons at metal and dielectric interface [1]. With metallic nanostructures at the interface, these excitations couple strongly with light, giving rise to large interaction cross-sections, and enhanced near-fields [2, 3]. When the optical field couples with the SPPs in plasmonic nanostructures, some fascinating features, and applications arise, such as photo-thermal cancer therapy [4], ultra-sensitive bio-sensing [5], and improved solar energy harvesting [6], etc. However, it is well known that the intrinsic absorption of plasmonic nanostructures is usually high, especially at optical frequency,

resulting in low performance efficiency [7]. Intrinsic absorption of the metallic nanostructures [8–11] can be substantially reduced with the assistance of active materials such as dye molecules, rare earth ions, or semiconductor crystals [3]. This is because the active materials can give rise to lasing or field amplification under external pumping, and transfer energy to compensate the losses of the SPPs [12–15]. Consequently, active materials enable the development of novel light-emitting devices [16, 17], such as spasers [18–20] or, more generally, plasmonic nanolasers [21–27]. It is also important to note that tuning the level of gain shall pave a path to dynamically control the response of these systems [3, 28, 29].

Recently, a new wave of interest in active materials appears in the realm of *PT*-symmetric systems [3, 30]. A system with *PT*-symmetry is comprised of active and absorptive elements which are in appropriate spatial distribution, such that the system presents a balanced gain and loss. *PT*-symmetry condition is directly translated into a requirement for the dielectric function of the system, $\varepsilon(r) = \varepsilon^*(-r)$, which can be achieved using active elements [3, 31, 32]. In other words, to achieve a *PT*-symmetric optical potential, the real part of the permittivity shall be an even function of position while its imaginary part must be an odd one. The interest in *PT*-symmetry of photonic systems relies on the exotic properties including, to cite some [3], asymmetric propagation [33, 34], reflection [35], scattering [36], unidirectional invisibility [37, 38], switching [39, 40], and extraordinary non-linear behaviors [41, 42]. These intriguing phenomena have been already observed in dielectric waveguides [43] and cavities [44] or photonic lattices [45, 46], among other realizations [3].

In this regard, plasmonic nanostructures with *PT*-symmetry have been attracting increased attention. A pioneer study has shown that the strong interaction of surface plasmons with light can be exploited to enhance the extraordinary properties arising from the *PT*-symmetry [3, 47]. Successive works demonstrate asymmetric behaviors in waveguides [48] and metamaterials [49, 50], transition from absorption to amplification in cavities [51] and waveguides [52], unidirectional cloaking [53], switching [54], multiplexing [55], anisotropic emission in hybrid nanoparticles [56], and giant near-field radiative heat transfer [3, 57].

In this paper, we investigate asymmetric optical response of a plasmonic nanoantenna that operates near the *PT*-symmetry condition. The nanoantenna is stacked with three metallic blocks and two dielectric blocks. Each of the two dielectric blocks, sandwiched by metallic ones, is either absorptive or active, respectively, with the same value of κ but in opposite sign. With such a *PT*-symmetric configuration, the antenna supports a highly tunable magnetic dipole (MD) that spectrally overlaps an electric dipole (ED) mode. And the tunability is primarily dependent on the variation of κ . It is also interesting to note that the interference between the MD and ED modes gives rise to superior unidirectional scattering. The side lobe level, of forward and backward radiation, can be suppressed in the cases provided that the Kerker conditions are well-satisfied. Furthermore, we show that the scattering direction of the nanoantenna strongly

depends on the non-Hermiticity parameter κ . In particular, it is feasible to switch the scattering direction of the antenna at the same wavelength in a wide spectra band by adjusting κ . We also find that the beam-width of the scattered light can be further narrowed when the antenna multilayers are arranged in a chain.

MATERIALS AND METHODS

For The scattered far-field for homogeneous and substrate environments can be written as [58],

$$\mathbf{E}_{\text{SC}}^{0,\text{FF}}(\mathbf{r}) \simeq \omega^2 \mu_0 \frac{e^{ik_d(r-\mathbf{n}\cdot\mathbf{r}_0)}}{4\pi r} \left[\mathbf{n} \times (\mathbf{p} \times \mathbf{n}) - \frac{1}{v_d} (\mathbf{n} \times \mathbf{m}) + \frac{ik_d}{6} [\mathbf{n} \times (\mathbf{n} \times \mathbf{Q}^e \mathbf{n})] + \frac{ik_d}{2v_d} (\mathbf{n} \times \mathbf{Q}^m \mathbf{n}) + \mathbf{n} \times \left(\frac{ik_d}{v_d} \mathbf{T} \times \mathbf{n} \right) \right] \quad (1)$$

where ω is the angular frequency, \mathbf{r} is the spatial coordinate vector, $\mu_0 = 4\pi \cdot 10^{-7}$ H/m is the vacuum permeability, $v_d = c(\varepsilon_d)^{-1/2}$, c is the speed of light in vacuum, ε_d is the relative permittivity of dielectric surrounding, $r = |\mathbf{r}|$ and $\mathbf{n} = \mathbf{r}/r$ is the unit vector in the direction of observation, \mathbf{p} (\mathbf{m}) is the electric (magnetic) dipole moment, \mathbf{Q}^e (\mathbf{Q}^m) is the electric (magnetic) quadrupole tensor, and \mathbf{T} is the tensor of the toroidal dipole moment [59].

The multipole decompositions are accomplished in both the Cartesian basis (source-representation) and the spherical basis (field-representation). The irreducible Cartesian multipole moments are evaluated by [58].

$$\mathbf{p} = -\frac{1}{i\omega} \left\{ \int d^3r J_\alpha^\omega j_0(kr) + \frac{k^2}{2} \int d^3r [3(\mathbf{r} \cdot \mathbf{J}_\omega) r_\alpha - r^2 J_\alpha^\omega] \frac{j_2(kr)}{(kr)^2} \right\} \quad (2)$$

$$\mathbf{m} = \frac{3}{2} \int d^3r [\mathbf{r} \times \mathbf{J}_\omega]_\alpha \frac{j_1(kr)}{kr} \quad (3)$$

$$\mathbf{Q}^e = -\frac{3}{i\omega} \left\{ \int d^3r [3(r_\alpha J_\beta^\omega + J_\alpha^\omega r_\beta) - 2\delta_{\alpha\beta}(\mathbf{r} \cdot \mathbf{J}_\omega)] \frac{j_1(kr)}{kr} + 2k^2 \int d^3r [5r_\alpha r_\beta (\mathbf{r} \cdot \mathbf{J}_\omega) - (r_\alpha J_\beta + J_\alpha r_\beta) - r^2 \delta_{\alpha\beta}(\mathbf{r} \cdot \mathbf{J}_\omega)] \frac{j_3(kr)}{(kr)^3} \right\} \quad (4)$$

$$\mathbf{Q}^m = 15 \int d^3r \{ r_\alpha [\mathbf{r} \times \mathbf{J}_\omega]_\beta + r_\beta [\mathbf{r} \times \mathbf{J}_\omega]_\alpha \} \frac{j_2(kr)}{(kr)^2} \quad (5)$$

where $\alpha, \beta = x, y, z$, the electric current density is obtained by using $\mathbf{J}_\omega(\mathbf{r}) = -i\omega\varepsilon_0(\varepsilon_r - \varepsilon_d) \mathbf{E}_\omega(\mathbf{r})$, where $\varepsilon_0 = 8.845 \cdot 10^{-12}$ F/m is the permittivity of free space, ε_r is the relative permittivity of particle, $\mathbf{E}_\omega(\mathbf{r})$ is electric field distribution. Multipole contributions show that the resonance peaks correspond to the overlap of several different multipole decomposition of the scattered field [59].

The scattering cross sections C_{sca} are defined from far-field scattered power (I) by normalizing to the energy flux of the incident wave (I_{inc}). The total scattering power can be obtained by summing the energy fluxes of multipoles

which are integrations of the Poynting vector over the total solid angle,

$$I = \frac{1}{8\pi\epsilon_0} \left[\frac{2\omega^4}{3c^3} |\mathbf{P}|^2 + \frac{2\omega^4}{3c^3} |\mathbf{M}|^2 + \frac{\omega^6}{20c^5} |\mathbf{Q}^e|^2 + \frac{\omega^6}{20c^5} |\mathbf{Q}^m|^2 \right] \quad (6)$$

$$C_{\text{sca}} = \frac{I}{I_{\text{inc}}} \quad (7)$$

Here, ω is the angular frequency, c is the speed of light in a vacuum, the more high-order multipoles are not shown [59].

Figure 1A shows schematic of the multi-layered metal-dielectric-metal (MDM) nanoantenna. The nanoantenna is comprised of three identical gold strips, and two dielectric strips sandwiched by gold strips. Each strip has the same lengths $l = 100$ nm, different thicknesses (i.e., a thickness of gold strip $d = 20$ nm and a thickness of dielectric strip $t = 15$ nm). The refractive index of the passive and active dielectric strip is $n + i\kappa$ and $n - i\kappa$, respectively. Here the real parts of the refractive index are fixed as $n = 1.44$ while the non-Hermiticity parameter κ in imaginary parts is varied for different simulations. Note that regardless of the value of κ , loss and gain are always balanced in the system. The permittivity of gold is taken from Johnson and Christy [60]. For simplicity, the whole structure is assumed to be freestanding in air ($\epsilon_0 = 1$) [61].

RESULTS AND DISCUSSION

Figure 1B shows the extinction cross-section of the antenna, as a function of κ and λ . The incident plane wave, polarized in the y axis, is propagating along the x axis (see **Figure 1A**). All numerical calculations are performed with the finite element method (FEM) by COMSOL Multiphysics [62]. For a passive structure (i.e., $\kappa = 0$), the extinction cross-section shows two peaks corresponding to the excitations of plasmon ED and MD at shorter and longer wavelength, respectively [61]. With the increase of κ , the gain starts to compensate the loss of the system. One interesting feature is that the ED peak remains at the same wavelength of about 623 nm. Moreover, at a certain critical value ($\kappa = 0.25$ for this system), a region with negative extinction cross-section appears (see green area in **Figure 1B**). Beyond this critical point, the MD peak disappears and the extinction cross-section at the longer wavelength vanishes. The above behaviors are explored and demonstrated in details in **Figure 1C**, where the extinction (blue curves), scattering (red curves), and absorption (black curves) cross sections of the structure are plotted for three different values of κ . As anticipated, when $\kappa = 0$ (top panel), we observe two resonances that correspond to the ED and MD modes, respectively. Close to the critical point, $\kappa = 0.25$ (middle panel), the absorption cross-section (ACS) and extinction cross-section (ECS) becomes negative and predominant at the longer wavelength. With the amount of loss and gain increasing in the system, we observe the splitting of the MD. It suggests that one of the eigenmodes that is dark and not excited in the case of the passive system becomes bright when bringing loss and gain in the system. As κ is increased to 0.4 (bottom panel), the gain partially mitigates absorption losses, thus yielding a zero extinction at

MD resonance. From the evolution of the MD and ED spectra based upon different κ in **Figure 2**, we can see that the MD mode shows strong dependence on κ , whereas the ED mode is almost unchanged. The sharp changes, occurring in the optical response of the antenna as κ approaches to the critical point, are a typical signature of a PT-symmetric system [42]. Therefore, associated with that behavior, we expect the system to exhibit an anisotropic response [3].

To clarify the contributions of different modes, multipole decomposition including the electric dipole moment \mathbf{P} , magnetic dipole moment \mathbf{M} , electric quadrupole (EQ) moment \mathbf{Q}^e , and magnetic quadrupole (MQ) moment \mathbf{Q}^m can be obtained according to Khandekar et al. [57]. The radiated power of all the multipole moments sums over their contributions as:

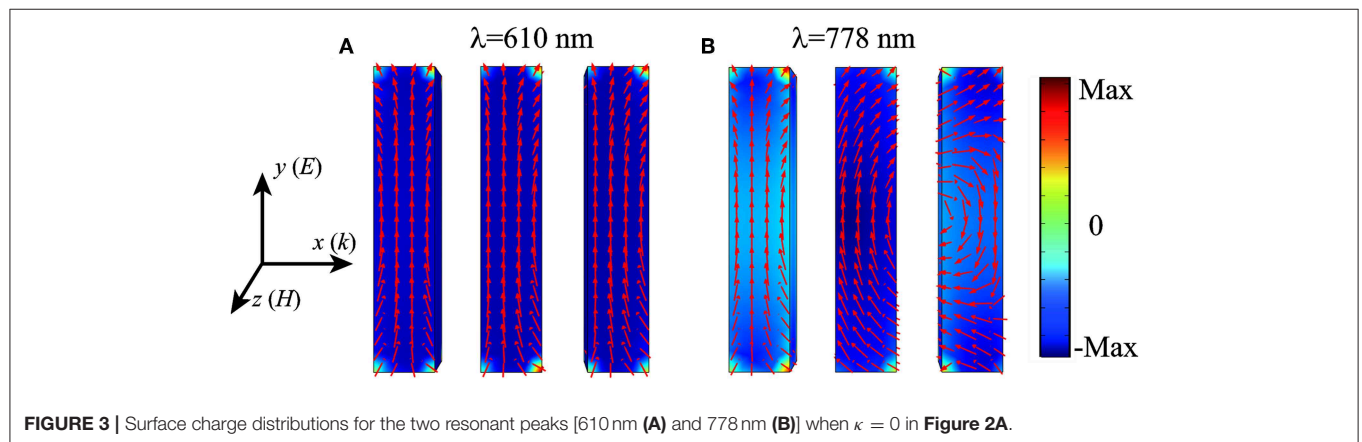
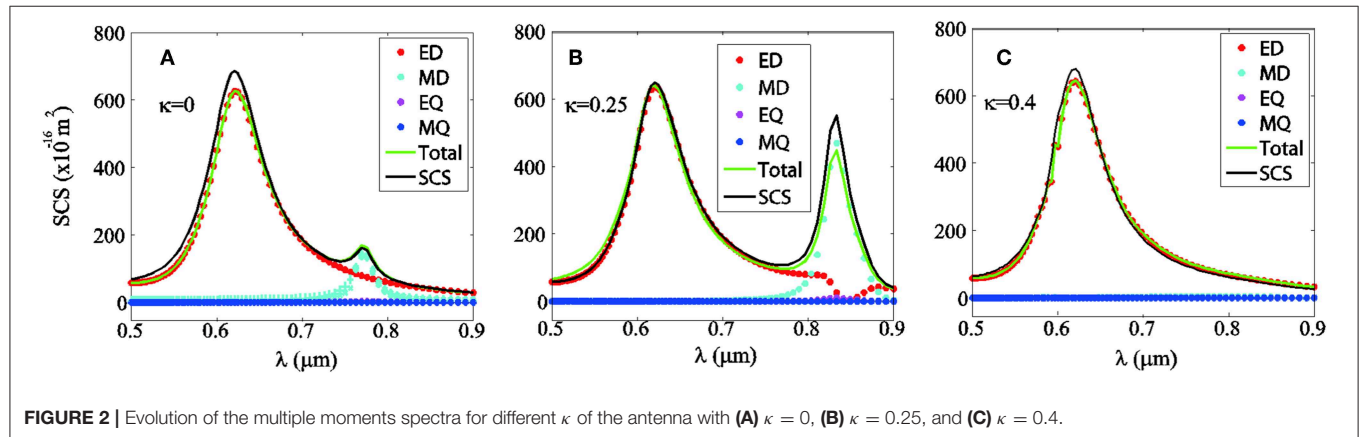
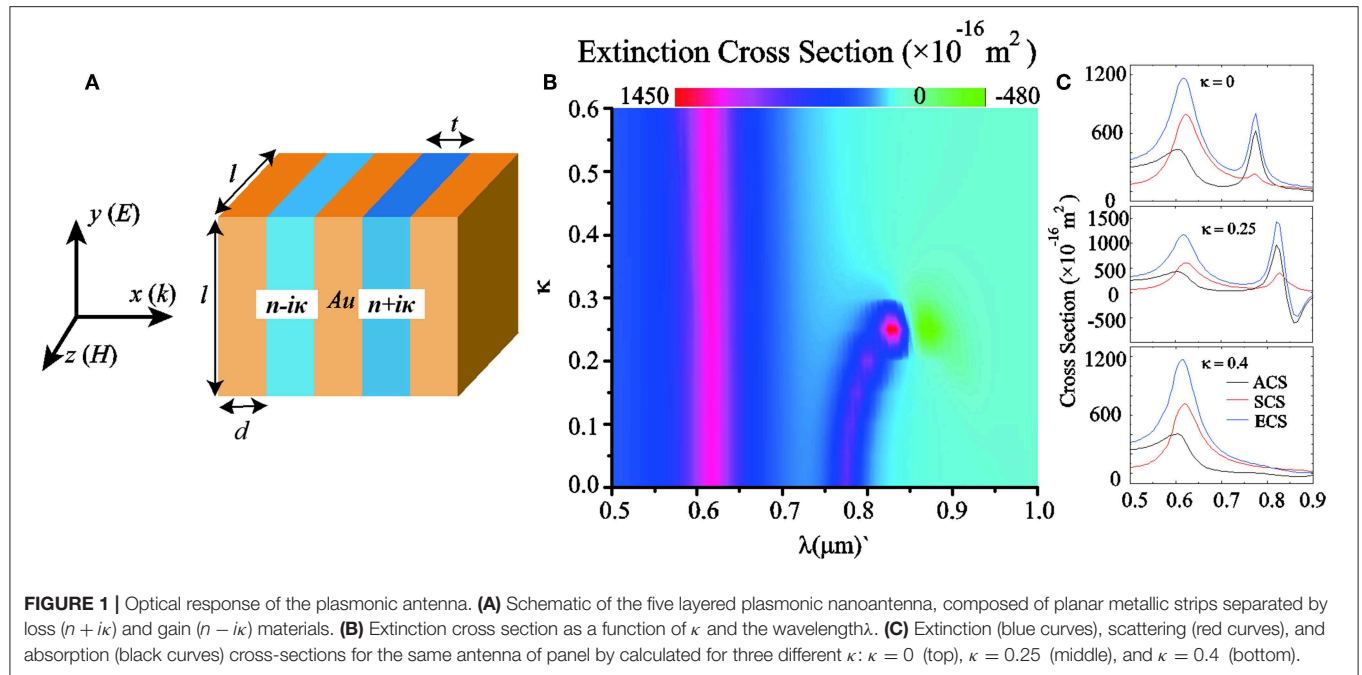
$$I = \frac{1}{8\pi\epsilon_0} \left[\frac{2\omega^4}{3c^3} |\mathbf{P}|^2 + \frac{2\omega^4}{3c^3} |\mathbf{M}|^2 + \frac{\omega^6}{20c^5} |\mathbf{Q}^e|^2 + \frac{\omega^6}{20c^5} |\mathbf{Q}^m|^2 \right] \quad (8)$$

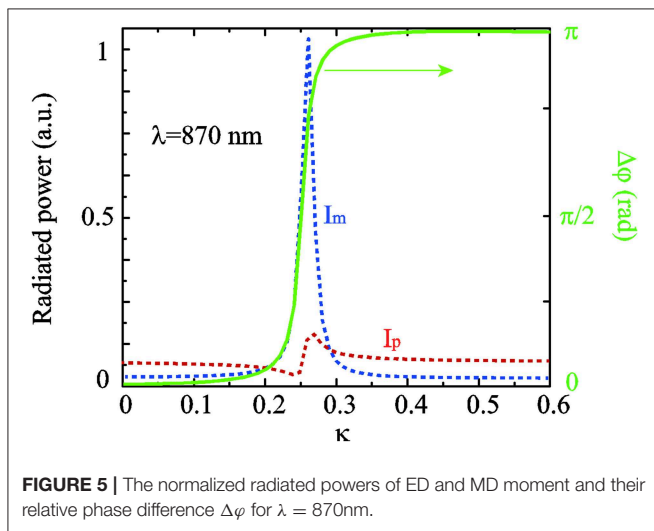
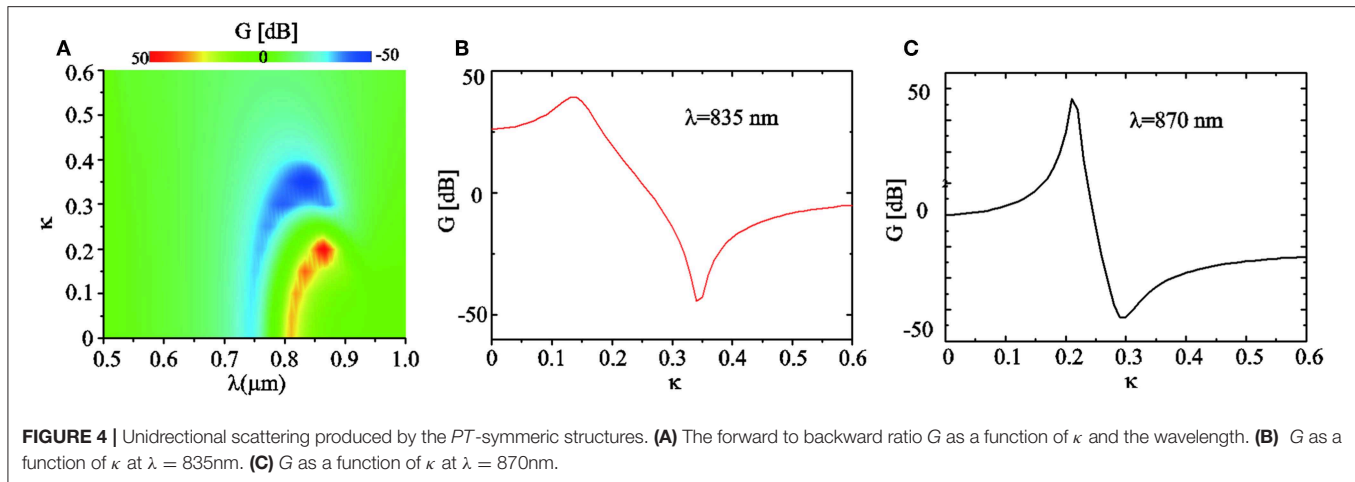
In **Figure 2**, we show the multiple scattering spectra for $\kappa = 0$, $\kappa = 0.25$, and $\kappa = 0.4$. It is seen that the contributions from the induced ED and MD are significantly larger than those of EQ and MQ. Therefore, it is reasonable to neglect the high order multipole moments (EQ and MQ) that have negligible effects on the SCS for the three cases [61]. Clearly, it is seen that when $\kappa = 0.4$ the radiation from MD vanishes. Moreover, the green solid line in **Figure 2** is the summation of the SCSs of the ED, MD, EQ, and MQ, which shows good agreement with the total SCS (black solid lines) obtained from the FEM simulation for the three cases, further confirming negligible contributions from other higher order modes [63].

To gain clearly understanding of the resonant dipole modes, we plot the surface charge distributions for two wavelength peak position of the SCS spectra when $\kappa = 0$ in **Figure 3**. Our previous work has shown that the first peak (i.e., $\lambda = 610$ nm) in this system corresponds to an electric dipole resonance in which the induced currents on the three plasmonic strips oscillate in phase [61], and the corresponding surface charge distribution is plotted in **Figure 3A**. The ED is induced by the metallic strips and it remains almost unchanged when varying κ , this can be confirmed in **Figure 2** [58]. In order to better understand how the MD mode can be excited, the charge distribution of the other mode at $\lambda = 778$ nm is shown in **Figure 3B**, we can see that the forming strong circulating displacement currents in the both left two and right two metallic strips induced the strong cavity magnetic dipole resonance mode. This kind of cavity mode is strongly affected by the material of dielectric layers (see **Figure 2**) [61]. Furthermore, as shown in **Figures 2A,B**, we can see that the ED and MD modes spectrally overlap in the spectrum and may have different radiation interferences that can shape the scattering pattern. The differential directionality (measured in decibels) of an antenna reads as follows [61, 63]:

$$D(\theta, \varphi) = 10 \times \log_{10} [4\pi S(\theta, \varphi) / \int_{\varphi} \int_{\theta} S(\theta, \varphi) \sin(\theta) d\theta d\varphi], \quad 0 \leq \theta \leq \pi, 0 \leq \varphi \leq 2\pi \quad (9)$$

Where θ and φ are spherical angles, and $S(\theta, \varphi)$ is the radiated power in the given direction θ and φ . Here, we are primarily





interested in the forward-backward (FB) ratio $G = D_F - D_B = 10 \times \log_{10}(S_F/S_B)$, where S_F and S_B are the far-field radiated powers in the forward and backward directions, respectively. The forward-backward ratio G allows a rough assessment of the directionality of the antennas [61]. The FB ratio G is plotted in **Figure 4** as a function of wavelength λ and non-Hermiticity parameter κ . For a passive structure (i.e., $\kappa = 0$), we can see that G reaches about -30 dB at $\lambda = 747$ nm and nearly 34 dB at $\lambda = 813$ nm. Notice that positive(negative) G means that forward(backward) scattering dominates [61]. As κ increases, the gain starts to compensate the loss of the system, while both the peak and dip of G are red-shifted and become broader. Interestingly, in the wavelength range from 807 to 885 nm, we can change the sign of G at the same wavelength by tuning κ . Here we give two cases for $\lambda = 835$ nm and $\lambda = 870$ nm in **Figures 4B,C**, respectively. It is seen that for $\lambda = 835$ nm, G reaches the peak (dip) of $+41$ dB (-47 dB) when $\kappa = 0.14$ ($\kappa = 0.34$). Similarly, it is seen that for $\lambda = 870$ nm, G reaches the peak (dip) of $+49$ dB (-51 dB) when $\kappa = 0.21$ ($\kappa = 0.3$).

The scattered electric farfield resulting from the combination of such \mathbf{p} and \mathbf{m} are as follows:

$$\mathbf{E}(\mathbf{r}) = \frac{k^2 e^{ik \cdot \mathbf{r}}}{4\pi \epsilon_0 r} [\mathbf{n} \times (\mathbf{p} \times \mathbf{n}) + (\mathbf{m} \times \mathbf{n}) + \dots] \quad (10)$$

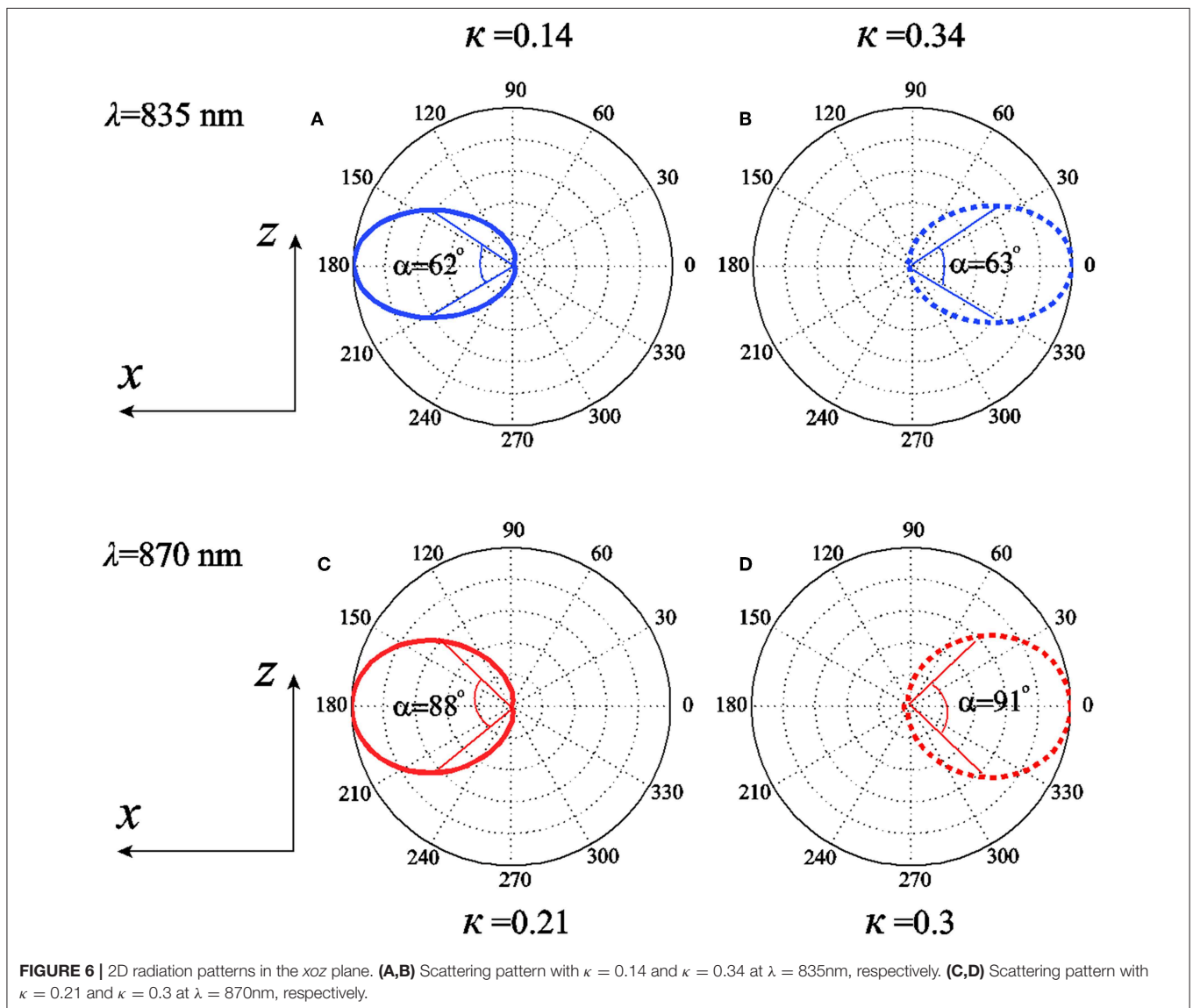
Where $\mathbf{p}(\mathbf{m})$ is the dipole moment of the ED (MD), \mathbf{k} is the wave vector, $\mathbf{n} = \mathbf{k}/|\mathbf{k}|$ is the unit vector in the emission direction, and \mathbf{r} is the coordinate vector. According to Equation (10), zero forward or backward scattering requires (1) the two dipoles (ED and MD) are orthogonal to each other, (2) their radiated powers are nearly identical, and (3) the phase difference $\Delta\varphi = \varphi_p - \varphi_m = 0$ (forward scattering) or $\Delta\varphi = \pm\pi$ (backward scattering), where φ_p and φ_m are the relative phase of the induced \mathbf{p} and \mathbf{m} in the nanoantenna. In our case, when $\Delta\varphi = \varphi_p - \varphi_m = 0$ is fulfilled (i.e., the first Kerker condition) [64], most radiated power is directed to the left half space ($+x$ direction). Likewise, when $\Delta\varphi = \varphi_p - \varphi_m = \pm\pi$ (i.e., the second Kerker condition) is nearly fulfilled, scattering to the right half space ($-x$ direction) dominates [61]. In our system, it is reasonable to assume the ED and MD to be oriented along the corresponding vectors of the incident field. It means that the induced electric and magnetic dipole moments of the antenna in **Figure 1A** should be $\mathbf{p} = (0, p_y, 0)$ and $\mathbf{m} = (0, 0, m_z)$, respectively. To demonstrate the first and second Kerker conditions can be switched at the same wavelength by adjusting κ , we take the case shown in **Figure 4C** (i.e., $\lambda = 870$ nm) as the example. **Figure 5** shows the normalized radiated powers (left axis) and the phase difference (right axis) of the induced dipole moments p_y and m_z as a function of the non-Hermiticity parameter κ . It is seen that at $\kappa = 0.21$ the radiated powers of p_y and m_z have comparable amplitudes (see the dashed curve in **Figure 5**) and relatively small phase difference $\Delta\varphi = 0.09\pi$ (see the green solid curve in **Figure 5**), thus the first Kerker condition is approximately reached. In a similar way, the second Kerker condition is nearly met at $\kappa = 0.3$ with $\Delta\varphi = 0.94\pi$. We note that the first (second) Kerker condition can be achieved at

all the peaks (dips) of G which corresponding to the red (blue) area in **Figure 4A** (results not shown here).

In **Figures 6A,B**, we plot the 2D far-field scattering patterns in xoz plane at $\lambda = 835$ nm for $\kappa = 0.14$ and $\kappa = 0.34$, respectively. It shows that an almost complete cancellation of the radiation toward the left-half space ($+x$ direction) and a predominated radiation toward to the right-half space ($-x$ direction) for $\kappa = 0.14$ (see **Figure 6A**). In sharp contrast, for $\kappa = 0.34$, the radiated power scatters almost completely toward the $-x$ direction (see **Figure 6B**) [61]. Similar features can be seen for $\kappa = 0.21$ and $\kappa = 0.3$ when $\lambda = 870$ nm as shown in **Figures 6C,D**. To better characterize the directivity of the scattering, we also label the main lobe angular beam-width α which corresponds to the angle for the full width at half-maximum of the differential scattering intensity [63], as shown in **Figure 6**. It is seen that for $\lambda = 835$ nm α is 62° when $\kappa = 0.14$ and 63° when $\kappa = 0.34$. For

$\lambda = 870$ nm shown in **Figures 6C,D**, α is 88° when $\kappa = 0.21$ and 91° when $\kappa = 0.3$. **Figure 6** further shows that the scattering direction of the antenna at a fixed wavelength can be reversed by adjusting κ .

In order to explore more scattering properties of the PT-symmetric systems, we investigated a series of five-layer plasmonic nanoantennas. First, a five-layer plasmonic nanoantenna, composed of planar metallic strips separated by two materials with different amount of gains, $n - i\kappa_1$ and $n - i\kappa_2$, is simulated as shown in **Supplementary Figure 1**. There is no positive and negative change of unidirectionality in this system. The unidirectionality keeps positive at all values of κ_1 and κ_2 . Secondly, a five-layer plasmonic nanoantenna, composed of planar metallic strips separated by two materials with different amount of losses, $n + i\kappa_1$ and $n + i\kappa_2$, is simulated as shown in **Supplementary Figure 2**. Similarly, there is no positive and



negative change of unidirectivity and the unidirectivity keeps positive at all values of κ_1 and κ_2 . Finally, the previous constructed PT-symmetric structure is also calculated with different loss ($n+i\kappa_1$) and gain ($n-i\kappa_2$) materials, as shown in **Supplementary Figure 3**. In the results, it is shown that the unidirectivity could switch between positive and negative with the change of κ_1 and κ_2 . When $\kappa_1 = \kappa_2 = \kappa$, the results are coincident with the previous results in **Figure 4**. In order to investigate the presence of critical point, we describe state coalescence and power flow along the waveguide, as shown in **Supplementary Figure 4**.

We also studied the opposite incidence ($-x$ direction, from right to left) in the PT-symmetric system, as shown in **Supplementary Figure 5**. The forward-backward ratio G results are smaller than the positive incidence results in **Figure 4**. The transmission and reflection properties of the PT-symmetric structure are simulated in plane wave incidence at $\lambda = 835$ nm and $\lambda = 870$ nm (see **Supplementary Figure 6**). The peaks(dips) of transmissivity/reflectivity ratio basically correspond to the peaks(dips) of G in **Figure 4C**. It is demonstrated that the positive and negative unidirectivities are related to transmission and reflection enhancements.

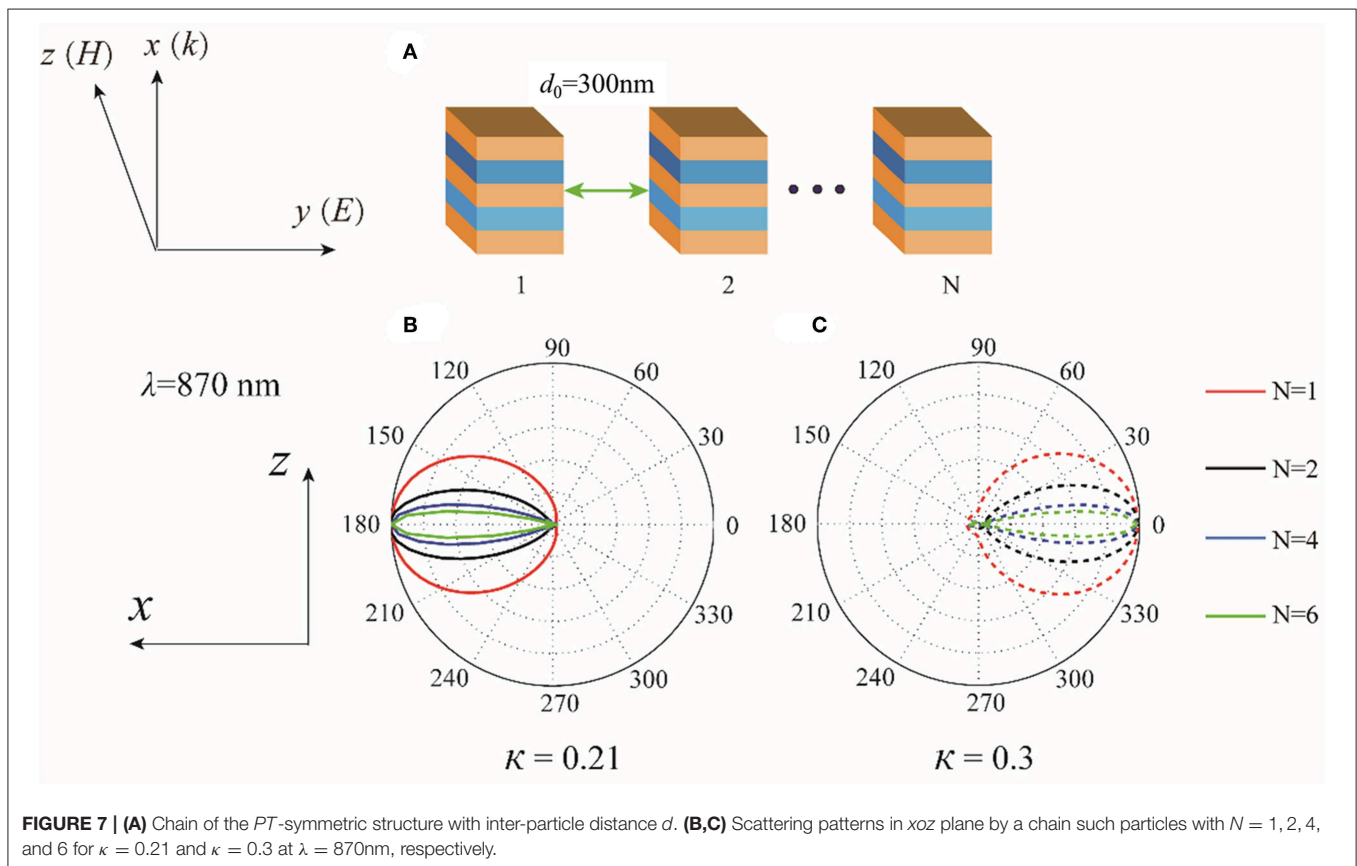
In **Figures 7B,C**, we show the scattering patterns in xoz plane by putting the antennas in a chain along y axis. The operating wavelength is $\lambda = 870$ nm and the inter-particle distance is fixed at $d_0 = 300$ nm. Significant reduction in α is obtained with

increasing number of antennas N due to the constructive far-field interferences, which is quite similar to previously reported study in high-index dielectric particle chain of longitudinal configuration [63]. The operating wavelength of $\lambda = 870$ nm can offer the best directionality with the narrowest α of 5.6° for $\kappa = 0.21$ and 5.8° for $\kappa = 0.3$ when $N = 6$ [63]. As a result, arranging the antennas into an array can achieve needle-like radiation [65].

Considering low values of non-Hermiticity parameter, we also redesigned a five-layer plasmonic nanoantenna with the geometric parameters ($l_1 = 30$ nm, $d_1 = 8$ nm, $t_1 = 6$ nm), as shown in **Supplementary Figure 7**. For an available gain material with the $\kappa \leq 0.2$, the tunable unidirectivity could also be realized in designed structure. In addition, the structure parameters could be further optimized to obtain excellent performance, and we will research more about it in the following work.

CONCLUSIONS

In conclusion, we have studied the scattering properties of a multi-layered MDM plasmonic nanoantenna with balanced gain and loss in the dielectric layers. We showed that the non-Hermiticity parameter has strong influences on the total cross sections and the scattering directionality of the antenna. In particular, the antenna exhibits unidirectional scattering which can be tuned by changing the non-Hermiticity parameter κ .



These interesting scattering features of the antenna can be understood by the phase shifts between the electric and magnetic dipole moments induced in the asymmetric material composition. Our results are useful in designing unidirectional plasmonic nanoantennas with active materials.

DATA AVAILABILITY STATEMENT

All datasets generated for this study are included in the manuscript/**Supplementary Files**.

AUTHOR CONTRIBUTIONS

HL and XZ conceived the idea and supervised the whole study. XZ, CX, and KC conducted the numerical calculations and drafted the first manuscript. XZ, CX, XS,

QL, KC, CW, ZW, and HL derived the theory and carried out the analysis. All authors contributed to the review of manuscript.

ACKNOWLEDGMENTS

This work was supported by National Natural Science Foundation of China (NSFC) (11174221, 11204218, 11404213, 11674248, 61205041, 11174057); supported by the Fundamental Research Funds for the Central Universities.

SUPPLEMENTARY MATERIAL

The Supplementary Material for this article can be found online at: <https://www.frontiersin.org/articles/10.3389/fphy.2019.00161/full#supplementary-material>

REFERENCES

- Zhang X, Xiao J, Zhang Q, Li L, Yao Y. Plasmonic TM-like cavity modes and the hybridization in multilayer metal-dielectric nanoantenna. *Opt Exp.* (2015) **23**:16122–32. doi: 10.1364/OE.23.016122
- Halas NJ, Lal S, Chang W, Link S, Nordlander P. Plasmons in strongly coupled metallic nanostructures. *Chem Rev.* (2011) **111**:3913–61. doi: 10.1021/cr200061k
- Manjavacas A. Anisotropic optical response of nanostructures with balanced gain and loss. *ACS Photon.* (2016) **3**:1301–7. doi: 10.1021/acsp Photonics.6b00274
- O'Neal DP, Hirsch LR, Halas NJ, Payne JD, West JL. Photo-thermal tumor ablation in mice using near infrared absorbing nanoparticles. *Cancer Lett.* (2004) **209**:171–6. doi: 10.1016/j.canlet.2004.02.004
- Alvarez-Puebla R, Liz-Marzán LM, Abajo FJGD. Light concentration at the nanometer scale. *J Phys Chem Lett.* (2010) **1**:2428–2434. doi: 10.1021/jz100820m
- Atwater HA, Polman A. Plasmonics for improved photovoltaic devices. *Nat Mater.* (2010) **9**:205–13. doi: 10.1038/nmat2629
- Khurgin JB. How to deal with the loss in plasmonics and metamaterials. *Nat Nanotechnol.* (2015) **10**:2–6. doi: 10.1038/nnano.2014.310
- Nezhad M, Tetz K, Fainman Y. Gain assisted propagation of surface plasmon polaritons on planar metallic waveguides. *Opt Exp.* (2004) **12**:4072–9. doi: 10.1364/OPEX.12.004072
- Gather MC, Meerholz K, Danz N, Leosson K. Net optical gain in a plasmonic waveguide embedded in a fluorescent polymer. *Nat Photonics.* (2010) **7**:457–61. doi: 10.1038/nphoton.2010.121
- Hess O, Pendry JB, Maier SA, Oulton RF, Hamm JM, Tsakmakidis KL. Active nanoplasmonic metamaterials. *Nat Mater.* (2012) **11**:573–84. doi: 10.1038/nmat3356
- Zhang X, Xiao J, Zhang Q. Interaction between single nano-emitter and plasmonic disk-ring nanostructure with multiple Fano resonances. *J Opt Soc Am B.* (2014) **31**:2193–200. doi: 10.1364/JOSAB.31.002193
- Noginov VA, Podolskiy VA, Zhu G, Mayy M, Bahoura M, Adegoke JA, et al. Compensation of loss in propagating surface plasmon polariton by gain in adjacent dielectric medium. *Opt Exp.* (2008) **16**:1385–92. doi: 10.1364/OE.16.001385
- Xian J, Chen L, Niu H, Qu J, Song J. Significant field enhancements in an individual silver nanoparticle near a substrate covered with a thin gain film. *Nanoscale.* (2004) **6**:13994–4001. doi: 10.1039/C4NR03678F
- Song J, Xian J, Yu M, Wang D, Ye S, Niu H, et al. Ultrahigh enhancement factor by using a silver nanoshell with a gain core above a silver substrate for surface-enhanced Raman scattering at the single-molecule level. *IEEE Photon J.* (2015) **7**:1–8. doi: 10.1109/JPHOT.2015.2481599
- Stockman MI. Spaser action, loss compensation, and stability in plasmonic systems with gain. *Phys Rev Lett.* (2011) **106**:156802. doi: 10.1103/PhysRevLett.106.156802
- Lozano G, Louwers DJ, Rodriguez SRK, Murai S, Jansen OTA, Verschuuren MA, et al. Plasmonics for solid state lighting: enhanced excitation and directional emission of highly efficient light sources. *Light.* (2013) **2**:e66. doi: 10.1038/lsa.2013.22
- Liu K, Li N, Sadana DK, Sorger VJ. Integrated nanocavity plasmon light sources for on-chip optical interconnects. *ACS Photonics.* (2016) **3**:233–42. doi: 10.1021/acsp Photonics.5b00476
- Bergman DJ, Stockman MI. Surface plasmon amplification by stimulated emission of radiation: quantum generation of coherent surface plasmons in nanosystems. *Phys Rev Lett.* (2003) **90**:027402. doi: 10.1103/PhysRevLett.90.027402
- Stockman MI. Spasers explained. *Nat Photonics.* (2008) **2**:327–9. doi: 10.1038/nphoton.2008.85
- Zheludev NI, Prosvirnin SL, Papasimakis N, Fedotov VA. Lasing spaser. *Nat Photonics.* (2008) **2**:351–4. doi: 10.1038/nphoton.2008.82
- Noginov MA, Zhu G, Belgrave AM, Bakker R, Shalae VM, Narimanov EE, et al. Demonstration of a spaser-based nanolaser. *Nature.* (2009) **460**:1110–2. doi: 10.1038/nature08318
- Oulton RF, Sorger VJ, Zentgraf T, Ma RM, Gladden C, Dai L, et al. Plasmon lasers at deep subwavelength scale. *Nature.* (2009) **461**:629–32. doi: 10.1038/nature08364
- Sorger VJ, Zhang X. Spotlight on plasmon lasers. *Science.* (2011) **333**:709–10. doi: 10.1126/science.1204862
- Berini P, Leon ID. Surface plasmon-polariton amplifiers and lasers. *Nat Photonics.* (2012) **6**:16–24. doi: 10.1038/nphoton.2011.285
- Zhou W, Dridi M, Suh JY, Kim CH, Co DT, Wasielewski MR, et al. Lasing action in strongly coupled plasmonic nanocavity arrays. *Nat Nanotechnol.* (2013) **8**:506–11. doi: 10.1038/nnano.2013.99
- Yang A, Odom TW. Breakthroughs in photonics 2014: advances in plasmonic nanolasers. *IEEE Photonics J.* (2015) **7**:1–6. doi: 10.1109/JPHOT.2015.2413773
- Ho J, Tatebayashi J, Sergeant S, Fong CF, Iwamoto S, Arakawa Y. Low-threshold near-infrared GaAs-AlGaAs core-shell nanowire plasmon laser. *ACS Photonics.* (2015) **2**:165–71. doi: 10.1021/ph5003945
- Krasavin AV, Vo TP, Dickson W, Bolger PM, Zayats AV. All-plasmonic modulation via stimulated emission of copropagating surface plasmon polaritons on a substrate with gain. *Nano Lett.* (2011) **11**:2231–35. doi: 10.1021/nl200255t
- Zhu W, Premaratne M, Gunapala SD, Agrawal GP, Stockman MI. Quasi-static analysis of controllable optical crosssections of a layered nanoparticle with a sandwiched gain layer. *J Opt.* (2014) **16**:075003. doi: 10.1088/2040-8978/16/7/075003

30. Bender CM, Boettcher S. Real spectra in non-hermitian hamiltonians having PT symmetry. *Phys Rev Lett.* (1998) **80**:5243–6. doi: 10.1103/PhysRevLett.80.5243
31. El-Ganainy R, Makris KG, Christodoulides DN, Musslimani ZH. Theory of coupled optical PT-symmetric structures. *Opt Lett.* (2007) **32**:2632–4. doi: 10.1364/OL.32.002632
32. Klaiman S, Günther U, Moiseyev N. Visualization of branch points in PT-symmetric waveguides. *Phys Rev Lett.* (2008) **101**:080402. doi: 10.1103/PhysRevLett.101.080402
33. Longhi S. Bloch oscillations in complex crystals with PT symmetry. *Phys Rev Lett.* (2009) **103**:123601. doi: 10.1103/PhysRevLett.103.123601
34. Ruter CE, Makris KG, El-Ganainy R, Christodoulides DN, Segev M, Kip D. Observation of parity-time symmetry in optics. *Nat Phys.* (2010) **6**:192–5. doi: 10.1038/nphys1515
35. Kulishov M, Laniel JM, Bélanger N, Azaña N, Plant DV. Nonreciprocal waveguide Bragg gratings. *Opt Exp.* (2005) **13**:3068–78. doi: 10.1364/OPEX.13.003068
36. Miri MA, Eftekhar MA, Facao M, Abouraddy AF, Bakry A, Razvi MAN, et al. Scattering properties of PT-symmetric objects. *J Opt.* (2016) **18**:075104. doi: 10.1088/2040-8978/18/7/075104
37. Lin Z, Ramezani H, Eichelkraut T, Kottos T, Cao H, Christodoulides DN. Unidirectional invisibility induced by PT symmetric periodic structures. *Phys Rev Lett.* (2011) **106**:213901. doi: 10.1103/PhysRevLett.106.213901
38. Longhi S. Invisibility in PT-symmetric complex crystals. *J Phys A.* (2011) **44**:2813–21. doi: 10.1088/1751-8113/44/48/485302
39. Lupu A, Benisty H, Degiron A. Using optical PT-symmetry for switching applications. *Phot Nano Fundam Appl.* (2014) **12**:305–11. doi: 10.1016/j.photonics.2014.05.003
40. Rivolta NXA, Maes B. Diffractive switching by interference in a tailored PT-symmetric grating. *J Opt Soc Am.* (2015) **32**:1330–7. doi: 10.1364/JOSAB.32.001330
41. Miroshnichenko AE, Malomed BA, Kivshar YS. Nonlinearly PT-symmetric systems: spontaneous symmetry breaking and transmission resonances. *Phys Rev.* (2011) **84**:911–6. doi: 10.1103/PhysRevA.84.012123
42. Guo A, Salamo GJ, Duchesne D, Morandotti R, Volatier-Ravat M, Aimez V, et al. Observation of PT-symmetry breaking in complex optical potentials. *Phys Rev Lett.* (2009) **103**:093902. doi: 10.1103/PhysRevLett.103.093902
43. Jia Y, Yan Y, Kesava SV, Gomez ED, Giebink NC. Passive parity-time symmetry in organic thin film waveguides. *ACS Photonics.* (2015) **2**:319–25. doi: 10.1021/ph500459j
44. Peng B, Özdemir SK, Lei F, Monifi F, Gianfreda M, Long GL, et al. Parity-timesymmetric whispering-gallery microcavities. *Nat Phys.* (2014) **10**:394–8. doi: 10.1038/nphys2927
45. Regensburger A, Bersch C, Miri MA, Onishchukov G, Christodoulides DN, Peschel U. Parity-time synthetic photonic lattices. *Nature.* (2012) **488**:167–71. doi: 10.1038/nature11298
46. Wimmer M, Regensburger A, Miri MA, Bersch C, Christodoulides DN, Peschel U. Observation of optical solitons in PT-symmetric lattices. *Nat Commun.* (2015) **6**:394–8. doi: 10.1038/ncomms8782
47. Benisty H, Degiron A, Lupu A, Lustrac AD, Chénais S, Forget S, et al. Implementation of PT symmetric devices using plasmonics: principle and applications. *Opt Exp.* (2011) **19**:18004–19. doi: 10.1364/OE.19.018004
48. Alaeian H, Dionne JA. Non-hermitian nanophotonic and plasmonic waveguides. *Phys Rev B.* (2014) **89**:188–92. doi: 10.1103/PhysRevB.89.075136
49. Alaeian H, Dionne JA. Parity-time-symmetric plasmonic metamaterials. *Phys Rev A.* (2014) **89**:429–35. doi: 10.1103/PhysRevA.89.033829
50. Alaeian H, Dionne JA. Controlling electric, magnetic, and chiral dipolar emission with PT-symmetric potentials. *Phys Rev B.* (2015) **91**:245108. doi: 10.1103/PhysRevB.91.245108
51. Baum B, Alaeian H, Dionne JA. A parity-time symmetric coherent plasmonic absorber-amplifier. *J Appl Phys.* (2015) **117**:063106. doi: 10.1063/1.4907871
52. Mattheakis M, Oikonomou T, Molina MI, Tsironis GP. Phase transition in PT symmetric active plasmonic systems. *IEEE J Sel Top Quant Electron.* (2016) **22**:76–81. doi: 10.1109/JSTQE.2015.2490018
53. Sounas DL, Fleury R, Alù A. Unidirectional cloaking based on metasurfaces with balanced loss and gain. *Phys Rev Appl.* (2015) **4**:014005. doi: 10.1103/PhysRevApplied.4.014005
54. Lupu A, Benisty H, Degiron A. Switching using PT symmetry in plasmonic systems: positive role of the losses. *Opt Exp.* (2013) **21**:21651–68. doi: 10.1364/OE.21.021651
55. Alaeian H, Baum B, Jankovic V, Lawrence M, Dionne JA. Towards nanoscale multiplexing with parity-time symmetric plasmonic coaxial waveguides. *Phys Rev B.* (2016) **93**:205439. doi: 10.1103/PhysRevB.93.205439
56. Jin W, Khandekar C, Pick A, Polimeridis AG, Rodriguez AW. Amplified and directional spontaneous emission from arbitrary composite bodies: a self-consistent treatment of Purcell effect below threshold. *Phys Rev B.* (2016) **93**:433–46. doi: 10.1103/PhysRevB.93.125415
57. Khandekar C, Jin W, Miller OD, Pick A, Rodriguez AW. Giant frequency-selective near-field energy transfer in active-passive structures. *Phys Rev B.* (2016) **94**:115402. doi: 10.1103/PhysRevB.94.115402
58. Alaeian H, Rockstuhl C, Fernandez-Corbaton I. An electromagnetic multipole expansion beyond the long-wavelength approximation. *Opt Commun.* (2018) **407**:17–21. doi: 10.1016/j.optcom.2017.08.064
59. Xu C, Cheng K, Li Q, Shang X, Wu C, Wei Z, et al. The dual-frequency zero-backward scattering realized in a hybrid metallo-dielectric nanoantenna. *AIP Adv.* (2019) **9**:075121. doi: 10.1063/1.5099533
60. Johnson PB, Christy RW. Optical constants of the noble metals. *Phys Rev B.* (1972) **6**:4370–9. doi: 10.1103/PhysRevB.6.4370
61. Zhang X, Xiao J, Zhang Q, Qin F, Cai X, Ye F. Dual-band unidirectional emission in a multilayered metal–dielectric nanoantenna. *ACS Omega.* (2017) **2**:774–83. doi: 10.1021/acsomega.7b00121
62. Available online at: <http://www.comsol.com> (accessed July 01, 2019).
63. Zhang X, Zhang Q, Zeng S, Liu Z, Xiao J. Dual-band unidirectional forward scattering with all-dielectric hollow nanodisk in the visible. *Opt Lett.* (2018) **43**:1275–8. doi: 10.1364/OL.43.001275
64. Kerker M, Wang DS, Giles CL. Electromagnetic scattering by magnetic particles. *J Opt Soc Am B.* (1983) **73**:765–7. doi: 10.1364/JOSA.73.000765
65. Ziolkowski RW. Using Huygens multiple arrays to realize unidirectional need-like radiation. *Phys Rev X.* (2017) **7**:031017. doi: 10.1103/PhysRevX.7.031017

Conflict of Interest: The authors declare that the research was conducted in the absence of any commercial or financial relationships that could be construed as a potential conflict of interest.

Copyright © 2019 Xu, Zhang, Cheng, Shang, Li, Wei, Wu and Li. This is an open-access article distributed under the terms of the Creative Commons Attribution License (CC BY). The use, distribution or reproduction in other forums is permitted, provided the original author(s) and the copyright owner(s) are credited and that the original publication in this journal is cited, in accordance with accepted academic practice. No use, distribution or reproduction is permitted which does not comply with these terms.



Control Electromagnetic Waves Based on Multi-Layered Transparent Metasurface

Zhichao Sun, Mengyao Yan, Tungamirai Eric Mupona and Bijun Xu*

School of Sciences, Zhejiang University of Science and Technology, Hangzhou, China

OPEN ACCESS

Edited by:

Qian Zhao,
Tsinghua University, China

Reviewed by:

Jiafu Wang,
Air Force Engineering University, China

Weiren Zhu,
Shanghai Jiao Tong University, China

Zhengren Zhang,
Chongqing Jiaotong University, China

Peng Zhang,
Seagate Technology, United States

*Correspondence:

Bijun Xu
xubijun@zust.edu.cn

Specialty section:

This article was submitted to
Optics and Photonics,
a section of the journal
Frontiers in Physics

Received: 27 August 2019

Accepted: 24 October 2019

Published: 20 November 2019

Citation:

Sun Z, Yan M, Eric Mupona T and
Xu B (2019) Control Electromagnetic
Waves Based on Multi-Layered
Transparent Metasurface.
Front. Phys. 7:181.
doi: 10.3389/fphy.2019.00181

Metasurface was presented to be the two-dimensional analogs of metamaterials that regulate the beam by adjusting the phase and amplitude of the wavefront. By properly designing and arranging the metasurface elements to form an array, the singularity of the metasurface to the propagation direction of the electromagnetic wave beam can be controlled; such unique electromagnetic properties offer additional opportunities to innovate new antennas. In this paper, we present the design and numerical simulation of the multi-layered microwave metasurface. The structure is designed to control the phase change of the transmission wave by changing the size of the multi-layered transparent microwave metasurface unit. Numerical simulation results show that the specific degree deflection of the electromagnetic wave is achieved in the microwave band. The design expands the application of phase gradient metasurface in the microwave field and provides a new method for metasurface electromagnetic beam steering.

Keywords: metasurface, multi-layer, beam steering, lens, microwave, wavefront control

INTRODUCTION

In fundamental physics, free space, and integrated photonics applications, it is important to regulate the deflection angle of electromagnetic waves [1]. Fermat's principle points out that the wavefront of a light beam can be modified by controlling the phase of light wave [2]. Conventional optical components rely on the design of complex dielectric constant distributions. These components also use wave plates made of natural birefringent crystals [3] and sub-wavelength gratings to achieve conversion between different deflection angles to gradually modulate the phase of the light waves for controlling of propagation path in bulk materials. However, due to the limited birefringence (Δn , typically <0.3) limitation [4], large device thicknesses are required to accumulate phase differences. In contrast, metamaterials exhibit peculiar optical properties in controlling electromagnetic waves [5, 6], providing an unprecedented method for precise control of electromagnetic waves with controllable amplitude [7], phase [8], and polarization [9] at sub-wavelength scales [10].

The mechanism of metasurface [11]-regulated electromagnetic waves is to introduce a catastrophic phase at the interface, so that the scattered electromagnetic waves have different phase differences at different positions and finally cause changes in the surface of constant phase, thereby changing the propagation direction of the electromagnetic waves [12]. A plurality of sub-wavelength unit structures are organized to form an array structure, and beam steering is realized by setting a transmission phase or a reflection phase of each unit. Therefore, the metasurface is required to adjust the phase of transmission or reflection by combining phase gradient and coding sequence [13] or specific unit [14]. In order to increase the overall transmission efficiency of

the antenna array, and better control beam shaping and beam steering, the phase change of the reflection or transmission of the local unit structure should be $[0, 2\pi]$ range [12, 15]. Another important indicator for judging performance is reflectivity and transmittance. In recent years, bi-layer transmissive metasurfaces with high efficiency have appeared. Zhang et al. proposed and experimentally demonstrated a light sword metasurface lens with multiple functionalities [16]; Wang et al. proposed a circular-polarized vortex beam reflector antenna [17]; Akram with his team controlled beam using photon spin Hall effect [18, 19]. Most metasurface structures utilize resonance to get efficient phase tuning, and to cover a 2π phase shift range, two kinds of resonance are needed. High reflectivity and transmittance mean high transmission efficiency, but the conventional single layer [16, 20] for beam steering cannot meet high transmission efficiency, and the operating frequency is mainly concentrated in microwave [15] or the terahertz band; the frequency is either too high or too low, and little research has been done on metasurface beam steering in the millimeter band.

In this paper, we present the design and simulation of multi-layered transparent microwave metasurface with six and eight elements phased patch array that can simultaneously control electromagnetic waves at a frequency of 32 GHz. The far fields and electric fields of different angles are discussed in detail. Numerical simulation of multi-layer beam control metasurface is done using electromagnetic solution based on finite integral technique (FIT)–CST Microwave Studio [21, 22]. The unit cell proposed by us has a certain working bandwidth from 30 to 34 GHz; in this paper, the beam wavefront control of the operating frequency at 32 GHz is mainly explained. An efficiency of 86% and a deflection angle of 22.99° and an efficiency of 83% and a deflection angle of 31.88° are verified by measuring the far-field radiation and electric field pattern. Due to the high transmission and flexible phase control in the range of frequency, the proposed element surface can refract the incident beam at a predetermined deflection angle under arbitrary polarization.

PRINCIPLE AND ANALYSIS

Fermat's principle is also called the shortest time theorem. It means that a beam of light always propagates from one point to another along the path with the shortest time. That is, the propagation of light waves between two points A and B is the path along the optical path $\int_A^B n ds$, where n is the refractive index of the medium. The generalized Snell's law is derived from the Fermat principle [23]. In general, Fermat's principle can be understood in the optical path as the phase change takes the extreme value, that is, when a phase change $\Phi(r_s)$ is introduced at the junction, the total phase change of the light wave in different paths is $\Phi(r_s) + \int_A^B n ds$, where r_s indicates the position on the interface, the first term represents the amount of phase abrupt change, and the second term represents the phase change corresponding to the optical path.

As shown in the **Figure 1**, the light wave irradiates the interface at the incident angle, and the x -axis represents the interface. There are two points A and B on both sides of

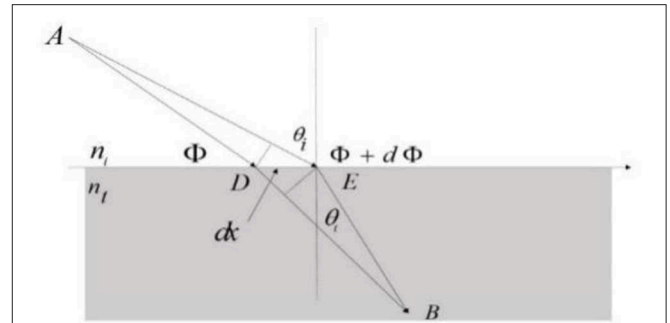


FIGURE 1 | Refraction with the phase difference.

the interface.

$$(k_0 n_i \sin \theta_i dx + \Phi + d\Phi) - (k_0 n_t \sin \theta_t dx + \Phi) = 0 \quad (1)$$

Then, the phase difference between ADB and AEB is 0 and Snell refraction law can be obtained. θ_t is the refraction angle, n_i and n_t are the dielectric constants on both sides of the interface, dx is the distance difference between two beams at the interface, and Φ and $\Phi + d\Phi$ are the phase mutation of two beams passing through the interface.

If the phase change rate $\frac{d\Phi}{dx}$ is constant, the transmission phase change is continuous. Generalized Snell's law consider the formula (1, 2).

$$n_t \sin \theta_t - n_i \sin \theta_i = \frac{1}{k_0} \cdot \frac{d\Phi}{dx} = \frac{\lambda_0}{2\pi} \cdot \frac{d\Phi}{dx} \quad (2)$$

METASURFACE DESIGN

In this paper, the basic structure with a multilayer transparent microwave element surface is presented. The designed structure unit is schematically depicted in **Figures 2A,B**, and the corresponding parameters are given. The ring aperture structure, three-layer perfect electronic conductors (PEC), and two-layer dielectric layers were selected for the unit structure design. The PEC thickness was 0.035 mm, the dielectric layer thickness was $d = 0.8$ mm, and the dielectric constant was 2.0. The unit structure is square in size and $p = 3$ mm in length and width. The PEC layer is composed of two rings, the outer ring has an outer radius of 1.5 mm, and the inner radius " a " varies uniformly from 0.4 to 1.4 mm. The outer radius of the inner ring b ($b = 0.5$ a) varies uniformly from 0.2 to 0.7 mm, and the inner radius is 0.1 mm. The element is analyzed using CST Microwave Studio by applying unit cell boundaries in both x - and y -directions. In order to tune the phase variation efficiently, only the length of the inner radius " a " is adjusted and optimized while fixing $d = 0.8$ mm and $p = 3$ mm.

As shown in **Figure 3A**, a continuous curve phase shift in the range of $[-157^\circ, 158^\circ]$ can be achieved by changing the radius of the metallic patch layers. The black line marked with triangle and the red marked with square represent the transmission

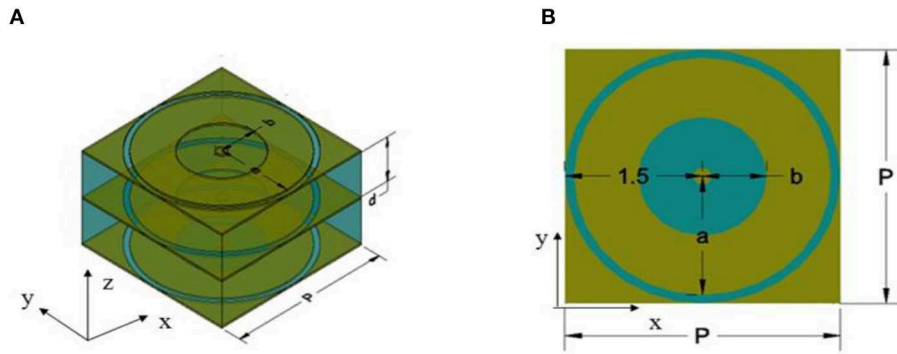


FIGURE 2 | The proposed PGMS element and its simulated setup. **(A)** Perspective view. **(B)** Top view.

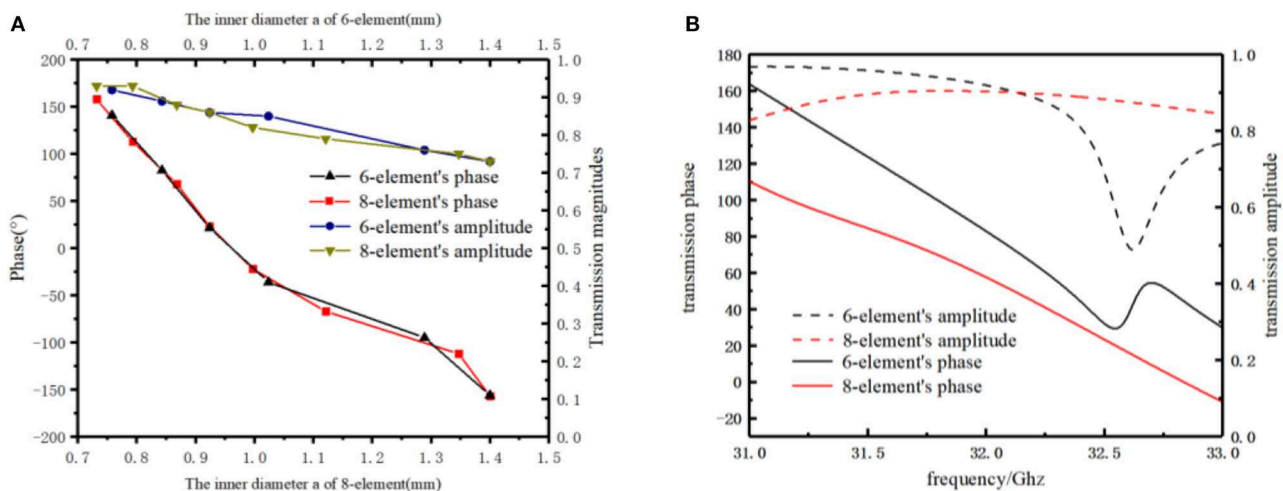


FIGURE 3 | **(A)** The transmission phase and magnitude of the 6-element and 8-element array varies with the inner diameter. **(B)** Parameters of the transmission varies with the frequency.

phase of six-element and eight-element, respectively; the blue line marked with circle and the yellow marked with triangle represent the transmission amplitude of six-element and eight-element, respectively. The maximum range of the phase shift at 32 GHz can reach 315° , which is close to a full cycle and sufficient for the intended operation of transmission while maintaining the amplitude of the transparent microwave. The transmission amplitude of six-element and eight-element both decreases and are inversely proportional to a , but they are all larger than 0.7, and the maximum is 0.91 and 0.93, respectively. It means our model can deflect the transmission beam in good condition. In this model, the operational frequency is 32 GHz and the focal length is 5 mm. In the structure, we get the desired phase shift by just changing the inner radius parameter of the metallic patch. The phase from -157° to 158° can be realized with the phase change of the transmission coefficient along with the inner diameter, which is beneficial to realize the composition of the transmission phase gradient changing on the deflection surface. **Figure 3B** shows the transmission amplitude and the transmission phase. It can be seen that the transmission amplitude is 0.91 and

between 31 and 32.6 GHz, the transmission phase is inversely proportional to the frequency. Due to the symmetry of the closed ring structure, when electromagnetic wave is incident into metasurface ring structure, electromagnetic resonance will be generated at a certain frequency. As shown in **Figure 3B**, the dotted black line and red line indicate the transmission amplitude of the six-element and eight-element array, respectively; the black line and red line represent the transmission phase of the six-element and eight-element array, respectively. When the array is six-element, at 32.6 GHz, the electromagnetic wave frequency approaches the plasma frequency of the metasurface, resulting in an absorption peak of 0.48 based on the Drude model. At the same time, from 32.5 to 32.7 GHz, the phase changed fastest at 32.6 GHz. When the array is eight-element, it can be approximated as a straight line with the transmission amplitude of 0.93 from 31 to 33 GHz. This component can be used for a hyperbolic lens antenna with good performance, which has been verified by previous work.

By choosing the appropriate value of a_n , the transmission intensity and phase difference spectrum provide enough

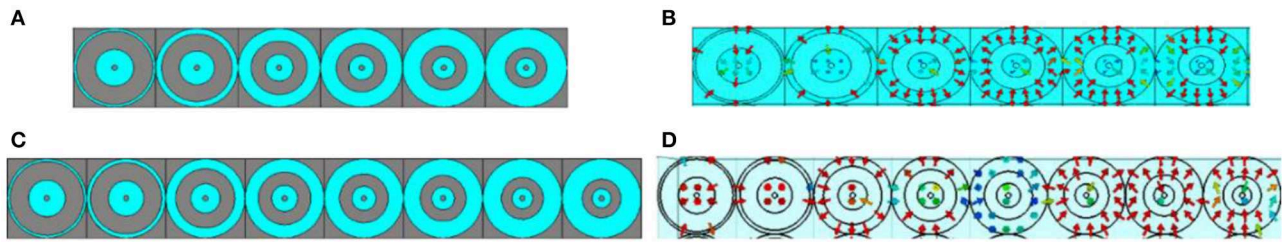


FIGURE 4 | (A) The $\pi/3$ phase increment at two adjacent units along the x -axis. **(B)** The current distribution of the six-element. **(C)** The $\pi/4$ phase increment at two adjacent unit along the x -axis. **(D)** The current distribution of the six-element and eight-element.

information for the design of the transmitter. As **Figure 4** shows, we select six elements (see **Figure 4A**) and eight elements (see **Figure 4C**), respectively, along the x -axis. The rules are to ensure the $\pi/3$ and $\pi/4$ phase increment at two adjacent units along the x -axis. **Figures 4B,D** represent the current distribution of the six-element and eight-element, respectively. As the radius of the ring increases, so does the current density on each element's surface. It shows that the deflection phase of transmission beam and the intensity of resonance also increases, following the generalized Snell's law for refraction [11, 14].

According to the generalized Snell's law, when the incident beam is vertical, the relationship between the deflection angle of the transmitted wave and the transmission phase gradient of the interface conforms to Equation (3), and $n_i = n_t = 1$. Deflection beam steering of transmitted waves can be achieved by designing gradient changes in the transmission phase of a multilayer transparent microwave metasurface [20, 21].

$$\theta_t = \arcsin\left(\frac{\lambda}{2\pi} \cdot \frac{d\phi}{dx}\right) \quad (3)$$

where ϕ is the phase discontinuities at a local point brought by the metasurface and λ is wavelength. Assume that the phase difference between adjacent elements is $\pi/4$, for the calculation consider Equation (3).

$$\theta_t = \arcsin\left(\frac{\lambda}{2\pi} \cdot \frac{d\phi}{dx}\right) = \arcsin\left(\frac{9.375}{2\pi} \cdot \frac{\pi}{4 \cdot 3}\right) \quad (4)$$

At this point, the deflection array can achieve 22.99° angular deflection. If $\pi/3$ is chosen as the difference of phase between adjacent elements, $\theta_t = 31.388^\circ$. Theoretically, the deflection array can achieve a beam deflection of 22.99° and 31.88° . **Tables 1, 2** show the inner radii a_n of the proposed model, where a_{n1} is the radii of the six elements while a_{n2} is the radii of the eight elements, N_1 and N_2 are serial numbers.

RESULTS AND DISCUSSION

The theoretical predictions are validated by simulation software CST. The boundary condition is unit cell, and the incident wave direction is positive along the z -axis. Based on the above theoretical analysis [22, 23], six transmission phases are

TABLE 1 | Deflection 22.92° array unit selection.

N_1	a_{n1} (mm)	Transmission phase ($^\circ$)	Theoretical transmission phase ($^\circ$)
1	1.4	-156.0	-157
2	1.289	-95.0	-97
3	1.024	-36.1	-37
4	0.924	21.5	23
5	0.843	82.5	83
6	0.758	141.8	143

TABLE 2 | Deflection 31.88° array unit selection.

N_2	a_{n1} (mm)	Transmission phase ($^\circ$)	Theoretical transmission phase ($^\circ$)
1	1.4	-156.0	-157
2	1.347	-110.0	-112
3	1.121	-66.2	-67
4	0.997	-21.5	-22
5	0.924	22	23
6	0.868	68.3	68
7	0.794	112	113
8	0.732	156	158

selected along the x -axis to increase $\pi/4$ in turn. Designing the metasurface according to the data in **Table 1**, the phase difference of the first unit is also $\pi/4$. The structure can deflect the transmitted beam by 22.99° . The simulation software CST is used for full-wave simulation and the periodic structure simulation [24–28] is used for calculation, the distribution of electric field is shown in **Figures 5A,B** shows the far-field 3D distribution map at 32 GHz; we can see that the vertical incident electromagnetic wave deflects by 22.99° , which is consistent with the theoretical results. When the center frequency is 30 and 34 GHz, the simulation results are shown in **Figures 5E,F,I,J**, and the deflection angles are all close to the theoretical calculation. The data are shown in **Table 3**. Then, we replace the lossless dielectric materials [29] with the typically lossy polyimide with the lossy tangent angle [30–33], 0.0571. As shown as **Figures 5C,D,G,H,K,L**, the beam deflection can also be realized with lossy materials and the deflection angle is smaller than that

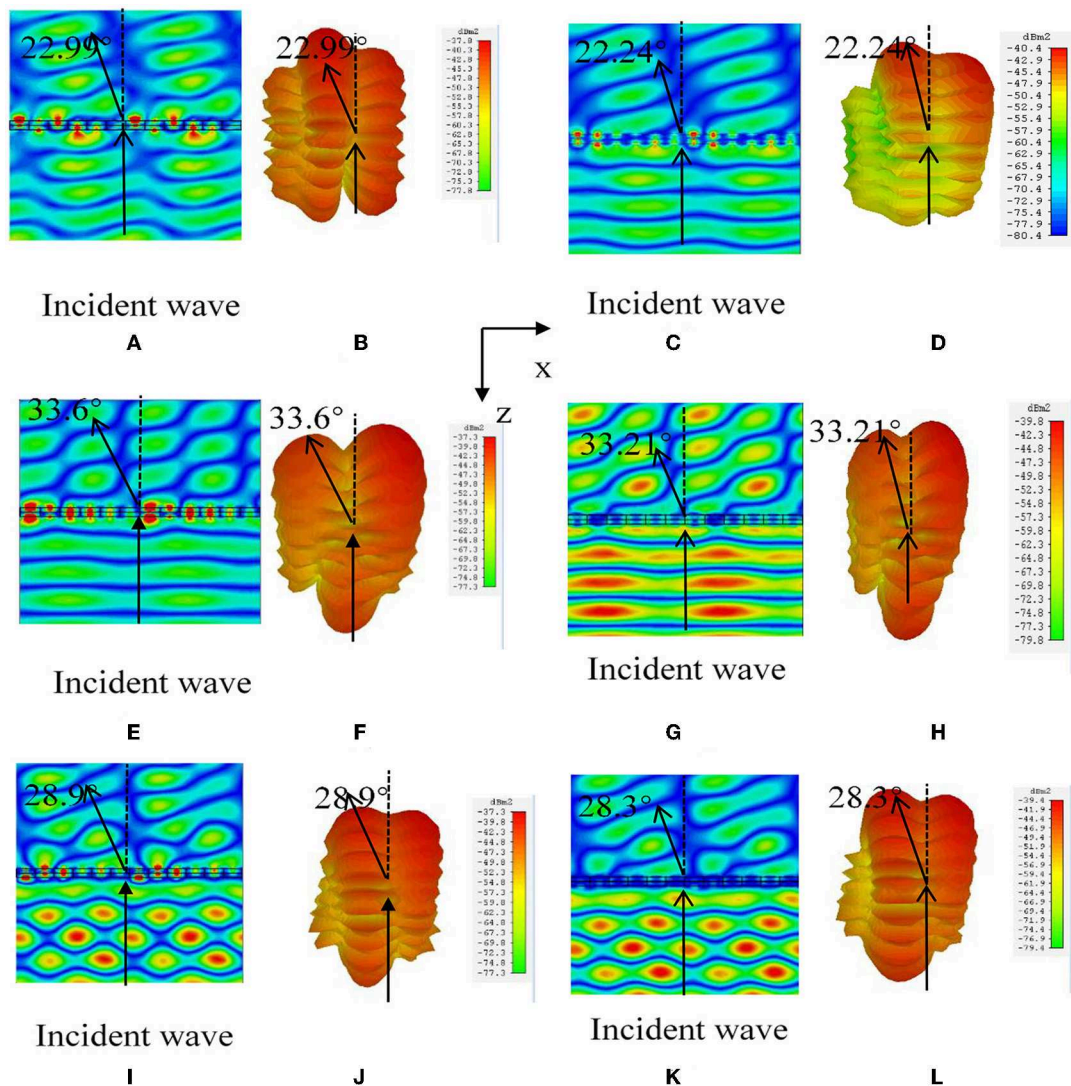


FIGURE 5 | Electric field and far-field 3D distribution of hypersurface array at 32 GHz (A–D), 30 GHz (E–H), and 34 GHz (I–L) of six-element, respectively, where (A,B,E,F,I,J) indicate the results of lossless material, and (C,D,G,H,K,L) indicate the results of lossy material.

TABLE 3 | The deflection angles of six elements with a lossless and lossy at different frequencies.

f (GHz)	Lossless material		Lossy material
	Theoretical ($^{\circ}$)	Actual ($^{\circ}$)	Actual ($^{\circ}$)
30	33.75	33.6	22.24
32	22.99	22.99	21.88
34	29.355	28.9	28.3

of the pure lossless materials in a reasonable error range. Besides, according to the value of $S_{21} = 0.91$, the transmission efficiency is calculated to be 86%.

According to **Table 2**, eight transmission phases with an adjacent phase difference are selected along the x -axis to form the

metasurface. According to Equation (3), the theoretical deflection angle is 31.88° . **Figures 6A,B,E,F,I,J** show the simulation results with pure lossless materials and **Figures 6C,D,G,H,K,L** indicate the results with lossy polyimide at 32, 30, and 34 GHz, respectively. **Figure 6A** shows the electric field E_x -distribution and (b) shows the far-field distribution map at 32 GHz. Due to the coupling effect between the adjacent elements of the array, the radiation of a single element will change the effective excitation of the adjacent elements. Meanwhile, because of the limited number of elements in the array, the coupling effect between the elements of the array is obvious, resulting in strong sidelobes. It can be seen that the beam deflection is 31.88° when the vertical incident electromagnetic wave passes through the metasurface, which is consistent with the theoretical calculation results. The $S_{21} = 0.93$, which means the transmission efficiency is approximately 83%. **Figures 6C–F** show the electric field

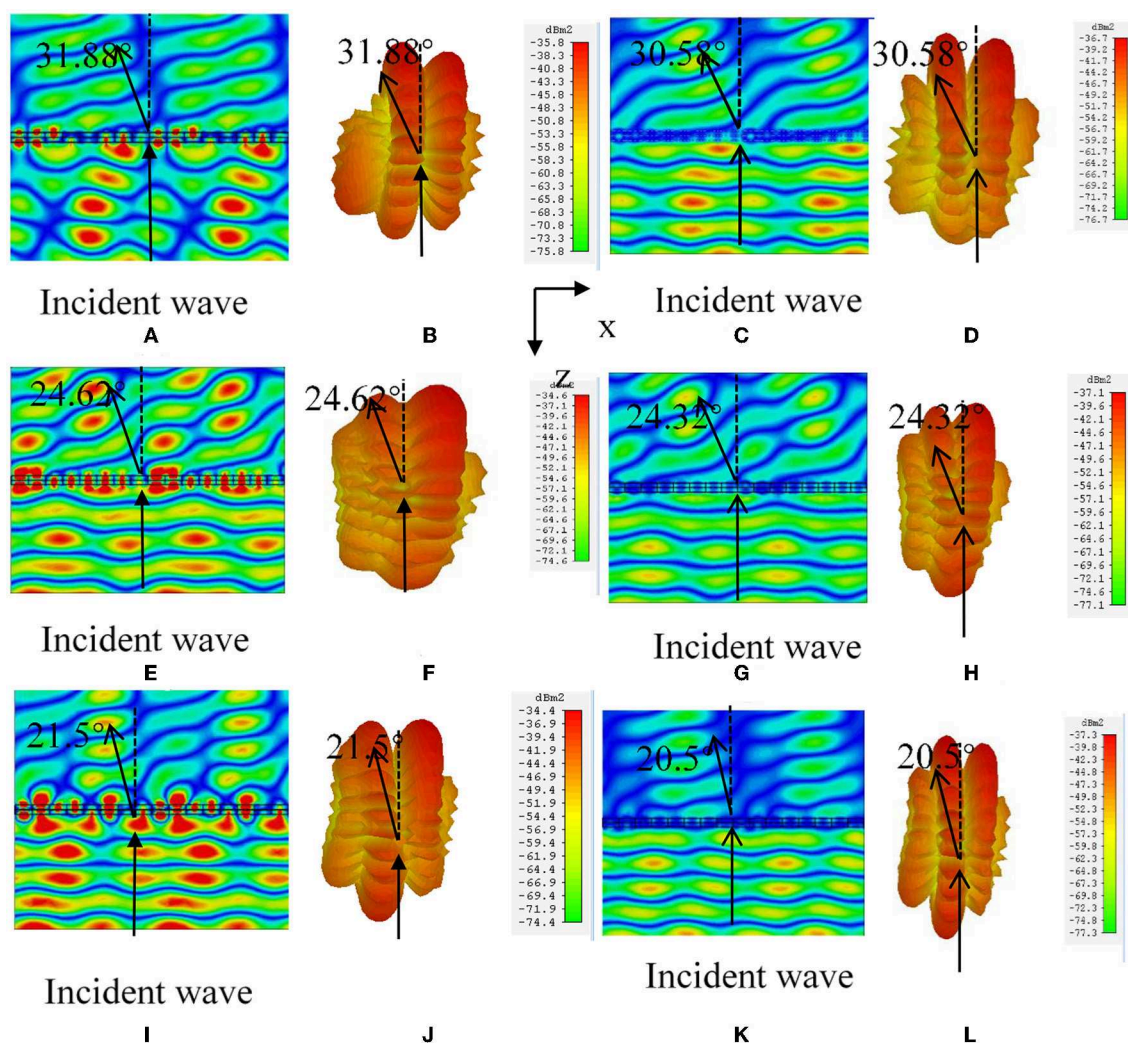


FIGURE 6 | Electric field and far-field 3D distribution of hypersurface array at 32 GHz (A–D), 30 GHz (E–H), and 34 GHz (I–L) of eight-element, respectively, where (A,B,E,F,I,J) indicate the results of lossless material, and (C,D,G,H,K,L) indicate the results of lossy material.

Ex-distribution and the far-field distribution map at 30 and 34 GHz.

Tables 3, 4 show the theoretical deflection angles and the simulation results at different frequencies and compare lossless material with lossy material. It can be seen from the data that the error is the smallest when working at 32 GHz in the frequency range from 30 to 34 GHz. Lossy material and lossless material effect is consistent.

CONCLUSION

It is proved by simulation results that the multilayer transparent microwave metasurface designed in this paper has a good beam control effect. In order to reduce the influence of evanescent wave coupling, we choose a three-layer aperture structure with high stability and transmission type to design a multi-layer

TABLE 4 | The deflection angles of eight elements with a lossless and lossy at different frequencies.

f (GHz)	Lossless material		Lossy material
	Theoretical (°)	Actual (°)	Actual (°)
30	24.62	24.6	24.32
32	31.88	31.88	30.85
34	21.572	21.5	20.5

metasurface, which can flexibly control discontinuous phases in $[-\pi, \pi]$. The phase difference between adjacent elements can be changed by making the beam reach a specific deflection angle; in this paper, we chose $\pi/4$ and $\pi/3$ as phase difference of adjacent elements, respectively. In the calculation, the periodic structure simulation is used. The results show that the transmittance

is higher than 80% with the change of inner diameter, which realizes the efficient transmission of a transmission wave. At the same time, the model with lossy materials can also achieve the purpose of beam deflection and are more widely used in practical production. The purpose of controlling the beam deflection to the desired angle can be achieved according to changing the phase difference. Since the structure has a good beam steering effect, it can be applied to an antenna array arrangement that produces a focusing effect. In addition, due to the common media materials used, in actual manufacturing, the whole structure can be realized with printed circuit boards. The structure is simpler and easier to manufacture.

REFERENCES

- Leib KG. *Radiation Beam Deflection System*. Google Patents (1981).
- Born M, Wolf E. Electromagnetic theory of propagation, interference and diffraction of light. In: *Principles of Optics*. New York, NY: Pergamon Press (1980). p. 370–458.
- Flossmann F, Schwarz, UT, Maier M, Dennis MR. Polarization singularities from unfolding an optical vortex through a birefringent crystal. *Phys Rev Lett*. (2005) 95:253901. doi: 10.1103/PhysRevLett.95.253901
- Enkrich C, Wegener M, Linden S, Burger S, Zschiedrich L, Schmidt F, et al. Magnetic metamaterials at telecommunication and visible frequencies. *Phys Rev Lett*. (2005) 95:203901. doi: 10.1103/PhysRevLett.95.203901
- Engheta N, Ziolkowski RW, editors. *Metamaterials: Physics and Engineering Explorations*. John Wiley & Sons (2006). doi: 10.1002/0471784192
- Wenshan C, Shalaev V. *Optical Metamaterials: Fundamentals and Applications*. New York, NY: Springer (2009).
- Pfeiffer C, Grbic A. Controlling vector Bessel beams with metasurfaces. *Phys Rev Appl*. (2014) 2:044011. doi: 10.1103/PhysRevApplied.2.044012
- Lin D, Fan P, Hasman E, Brongersma ML. Dielectric gradient metasurface optical elements. *Science*. (2014) 345:298–302. doi: 10.1126/science.1253213
- Pfeiffer C, Grbic A. BIANISOTROPIC metasurfaces for optimal polarization control: analysis and synthesis. *Phys Rev Appl*. (2014) 2:044011. doi: 10.1103/PhysRevApplied.2.044011
- Asadchy VS, Faniayeu IA, Radi Y, Khakhomov S, Semchenko I, Tretyakov S. Broadband reflectionless metasheets: frequency-selective transmission and perfect absorption. *Phys Rev X*. (2015) 5:031005. doi: 10.1103/PhysRevX.5.031005
- Liu WE, Chen ZN, Qing X, Shi J, Lin FH. Miniaturized wideband metasurface antennas. *IEEE Trans Antennas Propag*. (2017) 65:7345–9. doi: 10.1109/TAP.2017.2761550
- Fattal D, Li J, Peng Z, Fiorentino M, Beausoleil RG. Flat dielectric grating reflectors with focusing abilities. *Nat Photonics*. (2010) 4:466–70. doi: 10.1038/nphoton.2010.116
- Akram MR, Mehmood MQ, Tauqeer T, Rana AS, Rukhlenko ID, Zhu W. Highly efficient generation of Bessel beams with polarization insensitive metasurfaces. *Opt Express*. (2019) 27:9467–80. doi: 10.1364/OE.27.009467
- Yeh C. Reflection and transmission of electromagnetic waves by a moving dielectric medium. *J Appl Phys*. (1965) 36:3513–7. doi: 10.1063/1.1703029
- Yin JY, Ren J, Zhang Q, Zhang HC, Liu YQ, Li YB, et al. Frequency-controlled broad-angle beam scanning of patch array fed by spoof surface plasmon polaritons. *IEEE Trans Antennas Propag*. (2016) 64:5181–9. doi: 10.1109/TAP.2016.2623663
- Zhang Z, Wen D, Zhang C, Chen M, Wang W, Chen S, et al. Multifunctional light sword metasurface lens. *ACS Photonics*. (2018) 5:1794–9. doi: 10.1021/acsp Photonics.7b01536
- Wang H, Li YF, Chen HY, Han YJ, Fan Y, Sui S, et al. Vortex beam generated by circular-polarized metasurface reflector antenna. *Appl Phys Exp*. (2019) 12:255306. doi: 10.1088/1361-6463/ab1742
- Wang H, Li YF, Chen HY, Han YJ, Fan Y, Yang ZT, et al. Multi-beam metasurface antenna by combing phase gradients and coding sequences. *IEEE Access*. (2019) 7:62087–94. doi: 10.1109/ACCESS.2019.2915960
- Akram MR, Mehmood MQ, Bai X, Jin R, Premaratne M, Zhu W. High efficiency ultrathin transmissive metasurfaces. *Adv Opt Mater*. (2019) 7:1801628. doi: 10.1002/adom.201801628
- Liu W, Chen ZN, Qing X. Metamaterial-based low-profile broadband mushroom antenna. *IEEE Trans Antennas Propag*. (2013) 62:1165–72. doi: 10.1109/TAP.2013.2293788
- CST Microwave Studio. Available online at: www.cst.com (2013).
- CST Microwave Studio User Manual. Available online at: www.cst.com/products/cstms (2016).
- Yu N, Genevet P, Kats MA, Aieta F, Tetienne JP, Capasso F, et al. Light propagation with phase discontinuities: generalized laws of reflection and refraction. *Science*. (2011) 334:333–7. doi: 10.1126/science.1210713
- Xu BJ, Wei Z, Wu C, Fan Y, Wang Z, Li H. Near-diffraction-limited focusing with gradient high-impedance metasurface. *Opt Mater Express*. (2017) 7:1141–6. doi: 10.1364/OME.7.001141
- Richdale K, Bullimore MA, Zadnik K. Lens thickness with age and accommodation by optical coherence tomography. *Ophthalmic Physiol Opt*. (2008) 28:441–7. doi: 10.1111/j.1475-1313.2008.00594.x
- Yin X, Zhu H, Guo H, Deng M, Xu T, Gong Z, et al. Hyperbolic metamaterial devices for wavefront manipulation. *Laser Photonics Rev*. (2019) 13:1800081. doi: 10.1002/lpor.201800081
- Shaltout AM, Shalaev VM, Brongersma ML. Spatiotemporal light control with active metasurfaces. *Science*. (2019) 364:eaat3100. doi: 10.1126/science.aat3100
- Akram MR, Bai X, Jin R, Vandenbosch GAE, Premaratne M, Zhu W. Photon spin Hall effect based ultra-thin transmissive metasurface for efficient generation of OAM waves. *IEEE Trans Antennas Propag*. (2019) 67:4650–8. doi: 10.1109/TAP.2019.2905777
- Yin JY, Ren J, Zhang L, Li H, Cui TJ. Microwave vortex-beam emitter based on spoof surface plasmon polaritons. *Laser Photonics Rev*. (2018) 12:1600316. doi: 10.1002/lpor.201600316
- Li YB, Wan X, Cai BG, Cheng Q, Cui T. Frequency-controls of electromagnetic multi-beam scanning by metasurfaces. *Sci Rep*. (2014) 4:6921. doi: 10.1038/srep06921
- Aoni RA, Rahmani M, Xu L, Kamali KZ, Komar A, Yan J, et al. High-efficiency visible light manipulation using dielectric metasurfaces. *Sci Rep*. (2019) 9:6510. doi: 10.1038/s41598-019-42444-y
- Wei Z, Cao Y, Su X, Gong Z, Long Y, Li H, et al. Highly efficient beam steering with a transparent metasurface. *Opt Express*. (2013) 21:10739–45. doi: 10.1364/OE.21.010739
- Povinelli ML, Lončar M, Ibanescu M, Smythe EJ, Johnson SG, Capasso F, et al. Evanescent-wave bonding between optical waveguides. *Opt Lett*. (2005) 30:3042–4. doi: 10.1364/OL.30.003042

DATA AVAILABILITY STATEMENT

All datasets generated for this study are included in the article/supplementary material.

AUTHOR CONTRIBUTIONS

BX developed the concept and supervised the whole project. ZS carried out the simulations. ZS and MY analyzed the simulation data. BX and ZS contributed to writing and finalizing the paper. TE contributed to paper revision and language editing.

Conflict of Interest: The authors declare that the research was conducted in the absence of any commercial or financial relationships that could be construed as a potential conflict of interest.

Copyright © 2019 Sun, Yan, Eric Mupona and Xu. This is an open-access article distributed under the terms of the Creative Commons Attribution License (CC BY). The use, distribution or reproduction in other forums is permitted, provided the original author(s) and the copyright owner(s) are credited and that the original publication in this journal is cited, in accordance with accepted academic practice. No use, distribution or reproduction is permitted which does not comply with these terms.



Reflective Focusing Based on Few-Layer Gradient Metasurface Element Array

Mengyao Yan, Zhichao Sun, Bairui Wu, Pan Cheng and Bijun Xu*

School of Science, Zhejiang University of Science and Technology, Hangzhou, China

This study proposes a three-layer focusing gradient metasurface for wavefront processing. The structure works in the frequency range of 15–25 GHz and has a central frequency of 19.6 GHz. The metasurface unit is organized in a square and has high-impedance elements that reflect the full range of phase shifts. When the microwave beam is incident on this metasurface, the high-impedance elements modulate the beam according to the gradient arrangement, to realize the focusing effect of the lens, and the efficiency reaches 82%. The simulation results are consistent with the theoretical results.

Keywords: metasurface, reflective, focus, wavefront, simulation

OPEN ACCESS

Edited by:

Yuancheng Fan,
Northwestern Polytechnical
University, China

Reviewed by:

Xiangping Li,
Jinan University, China
Zhengren Zhang,
Chongqing Jiaotong University, China
Rui-Pin Chen,
Zhejiang Sci-Tech University, China

*Correspondence:

Bijun Xu
xubijun@zust.edu.cn

Specialty section:

This article was submitted to
Optics and Photonics,
a section of the journal
Frontiers in Physics

Received: 28 December 2019

Accepted: 20 February 2020

Published: 20 March 2020

Citation:

Yan M, Sun Z, Wu B, Cheng P and
Xu B (2020) Reflective Focusing
Based on Few-Layer Gradient
Metasurface Element Array.
Front. Phys. 8:46.
doi: 10.3389/fphy.2020.00046

INTRODUCTION

The acquisition of new materials with new optical properties has become an important research field [1]. People acquire new materials by chemical synthesis [2], and they manipulate the optical properties by artificially designing dielectric constants and magnetic permeability [3, 4]. The degree of freedom and maneuverability of the artificial optical structure is higher than that of chemical synthesis methods [5]. From 2000 to 2010, the use of metamaterials to design new optical devices and achieve unique optical functions has received significant attention. Examples of these include negative refraction, metalenses, optical stealth cloaks, and artificial chirality [6, 7].

Fermat's principle [8] points out that the wavefront of a light beam can be modified by controlling the phase of the light wave [9, 10]. A metasurface exhibits peculiar optical properties in controlling electromagnetic waves [11, 12]; it is also widely used in the terahertz band [13]. Traditional metal-based metasurfaces can effectively reduce losses during electromagnetic wave propagation [14, 15], but the interaction intensity decreases as the distance between the metasurface and the electromagnetic beam increases [16, 17]. The metal—medium—metal structure [18] provides an effective way to achieve efficient control of light wave amplitude, phase, and polarization [19]. In this study, we propose and validate a new type of focusing lens based on a three-layer square gradient metasurface reflector array, which can approximate and the reflection phase in the range of 2π by controlling the metasurface unit.

MODEL DESIGN

As shown in **Figure 1A**, an element of the metasurface array has three layers, and the metal layers use a perfect electrical conductor (PEC). Metals behave like PEC in the microwave band and a reflectarray built using elements of variable dimensions can reflect the incident waves with high efficiency. As shown in **Figure 1B**, the top metallic patch layer is a square that is hollowed from the inside to the outside. **Figure 1C** shows the element parameters. The thickness of each metal layer and the dielectric are $t = 0.035$ mm and $h = 1.60$ mm, respectively, and the dielectric constant

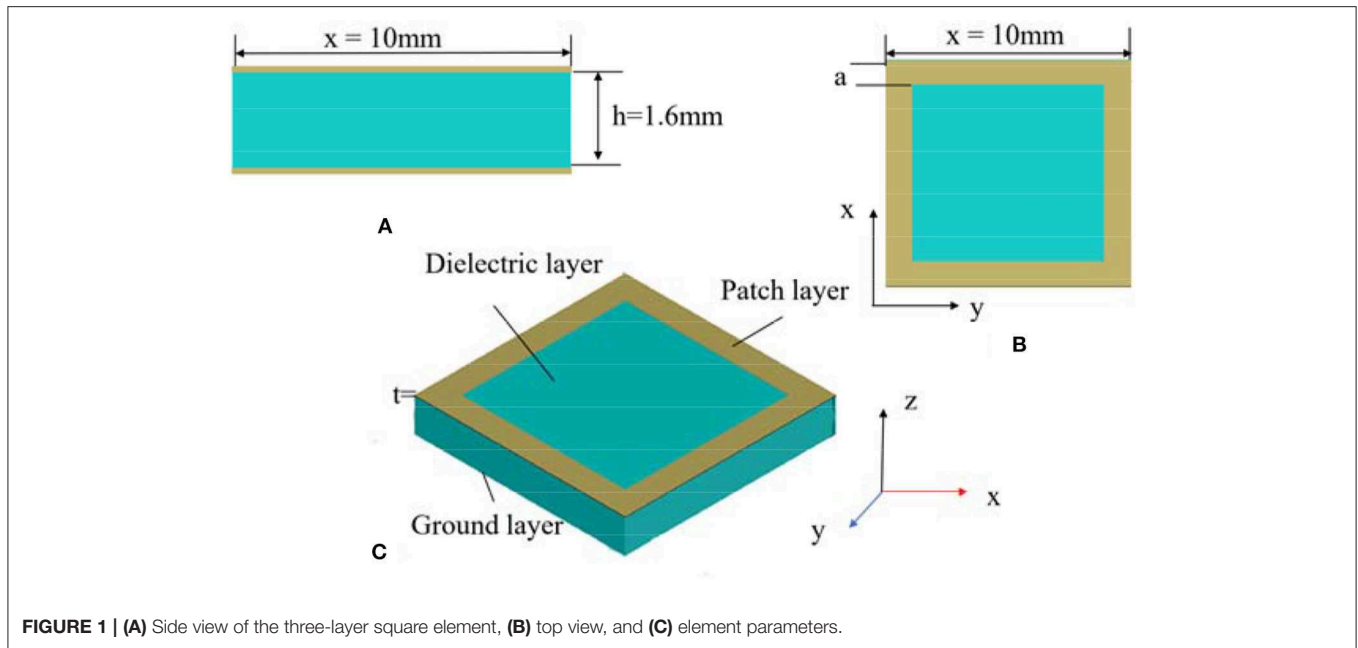


FIGURE 1 | (A) Side view of the three-layer square element, (B) top view, and (C) element parameters.

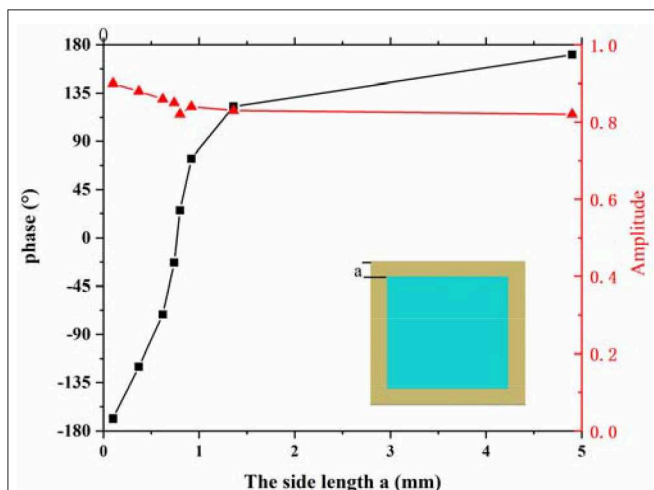


FIGURE 2 | The amplitudes (red triangle dots) and reflection phase shift (black square dots) of a metasurface with different side lengths at 19.6 GHz frequency.

is 2.60. The lattice constant is $x = 10$ mm. The width of the metallic patch is the only adjustable parameter, and it has a significant influence on the reflection phase. By changing the value of the parameter, it is possible to control the incident beam and make it converge at one point.

Compared with other focusing structures [20, 21], the thickness of the proposed design only is 1.67 mm, which is much smaller than the operational wavelength. It is easy to manufacture. The phase (ϕ) distribution of the focusing gradient metasurfaces usually follows Equation (1) [22].

$$f(x, y) = \frac{2\pi}{\lambda_0} (\sqrt{x^2 + y^2 + f^2} - f) + f_0 \quad (1)$$

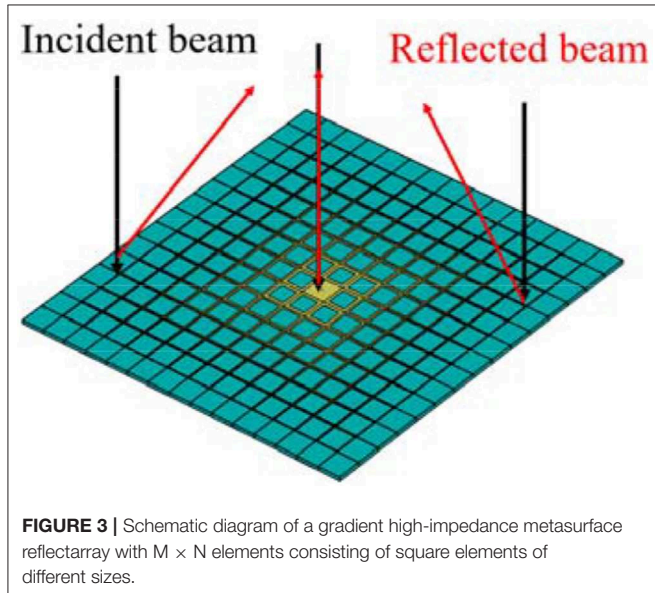
Where f is the focal length, and λ_0 is the free-space wavelength [23, 24].

A continuous curve of phase shift in the range of -168.5° to 170.8° , as shown in **Figure 2**, can be achieved by changing the width of the metallic patch layer. The maximum range of the phase shift can reach 339° , which is close to a full cycle and sufficient for the intended operation of a reflectarray while maintaining the amplitude of the reflected wave above 0.82. The focal length is 150 mm. As shown in **Figure 3**, the three-layer metasurface array consisted of 13×13 square elements. The desired phase shift is obtained by just changing the inner radius parameter of the metallic patch. The radii of the patches in the eight parts are 0.1, 0.37, 0.62, 0.74, 0.80, 0.92, 1.36, and 4.9 mm, respectively. The element can be used for a metasurface lens with good performance. The reflection phases of the eight concentric parts fulfill Equation (1).

RESULTS AND DISCUSSION

The CST Microwave Studio software was used to solve the reflection spectra of the metasurface structure. The plane wave propagated in the negative z direction and linearly polarized along the direction of incidence of the beam. The simulation results are shown in **Figure 4**. **Figure 4A** shows the reflected electric-field intensity distribution in the x - y plane, where the focal length f is ~ 146 mm. **Figure 4B** shows the reflection intensity distribution in the x - y plane at $z = 146$ mm, $z = 150$ mm, and $z = 170$ mm, respectively. One can see that the energy is the strongest, the light spot is the smallest, and the focusing effect is the best at $z = 146$ mm. **Figure 4C** shows

the 3D radiation pattern at 19.6 GHz, and **Figure 4D** shows the electric-field energy density distribution in the x - z plane. Focus conversion efficiency was $\sim 82\%$. The calculation method is the ratio of focus energy of the focal spot to the total

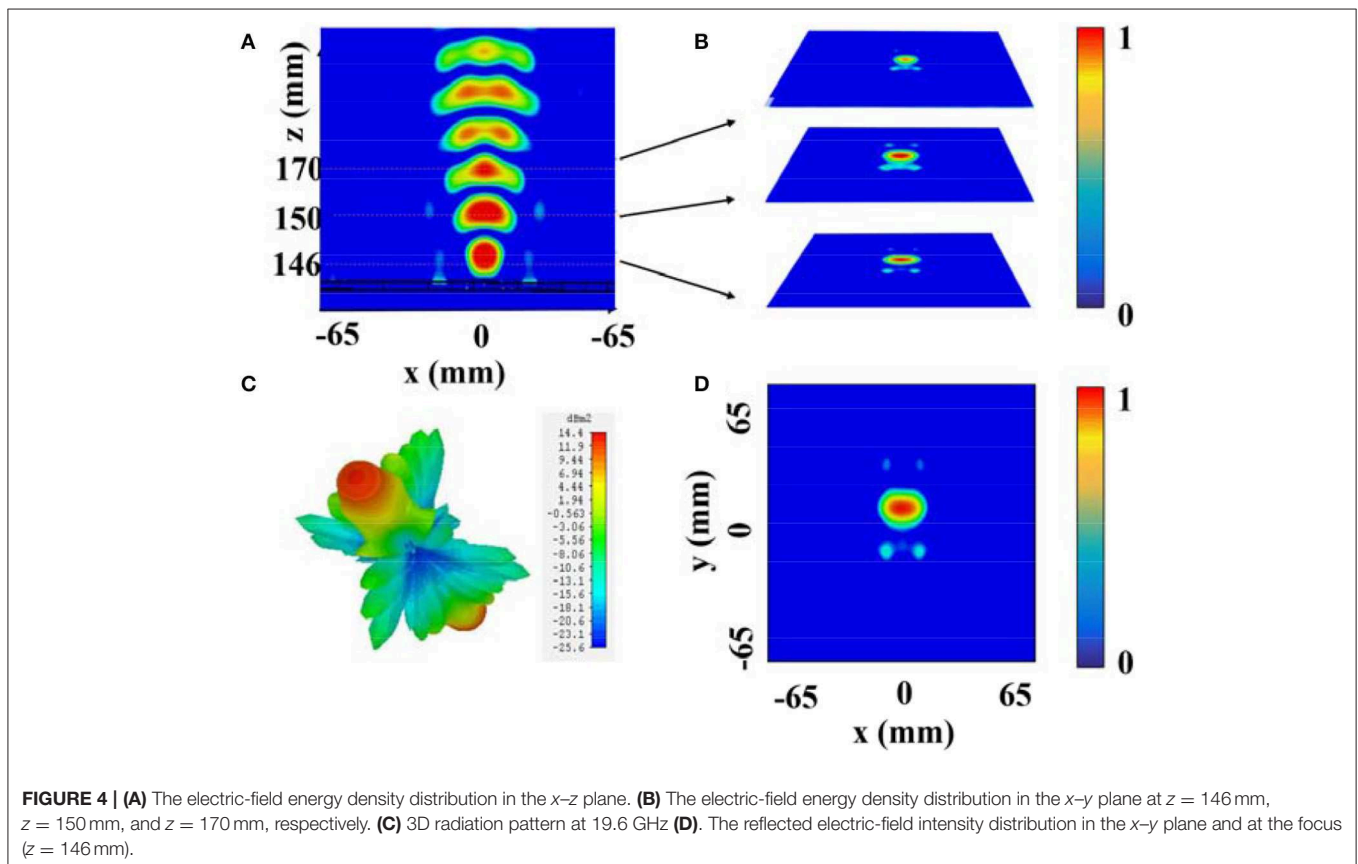


energy of the incident wave. Owing to the good focusing performance, the proposed array can achieve a pencil-shaped radiation pattern.

It is reasonable to infer that the high-efficiency focusing has a broadband characteristic. As shown in **Figure 5**, the results of near-field distribution at 18, 19, and 20 GHz show a high focusing efficiency over a wide frequency range. **Figures 5B,E,H** and **Figures 5C,F,I** show that the focal length increases and the far-field radiation decreases with the decrease of working frequency. Specifically, the focal length is 150 mm at 18 GHz, the far-field value is 13.7 dB, the focal length is 110 mm at 19 GHz, the far-field value is 14.5 dB, the focal length is 90 mm at 20 GHz, and the far-field value is 14.7 dB. The simulation results verify the hypothesis and show a wide broadband of operation, and the demonstrated high efficiency and broadband wavefront steering can be applied in imaging and high-directional antennas.

CONCLUSION

A three-layer square reflective array was simulated based on a focused gradient metasurface. In the microwave frequency band, the reflection phase of a single element to electromagnetic waves varies only with the width of the metallic patch layer. The phase discontinuity on the metasurface depends only on the precise control of the three-layer square elements



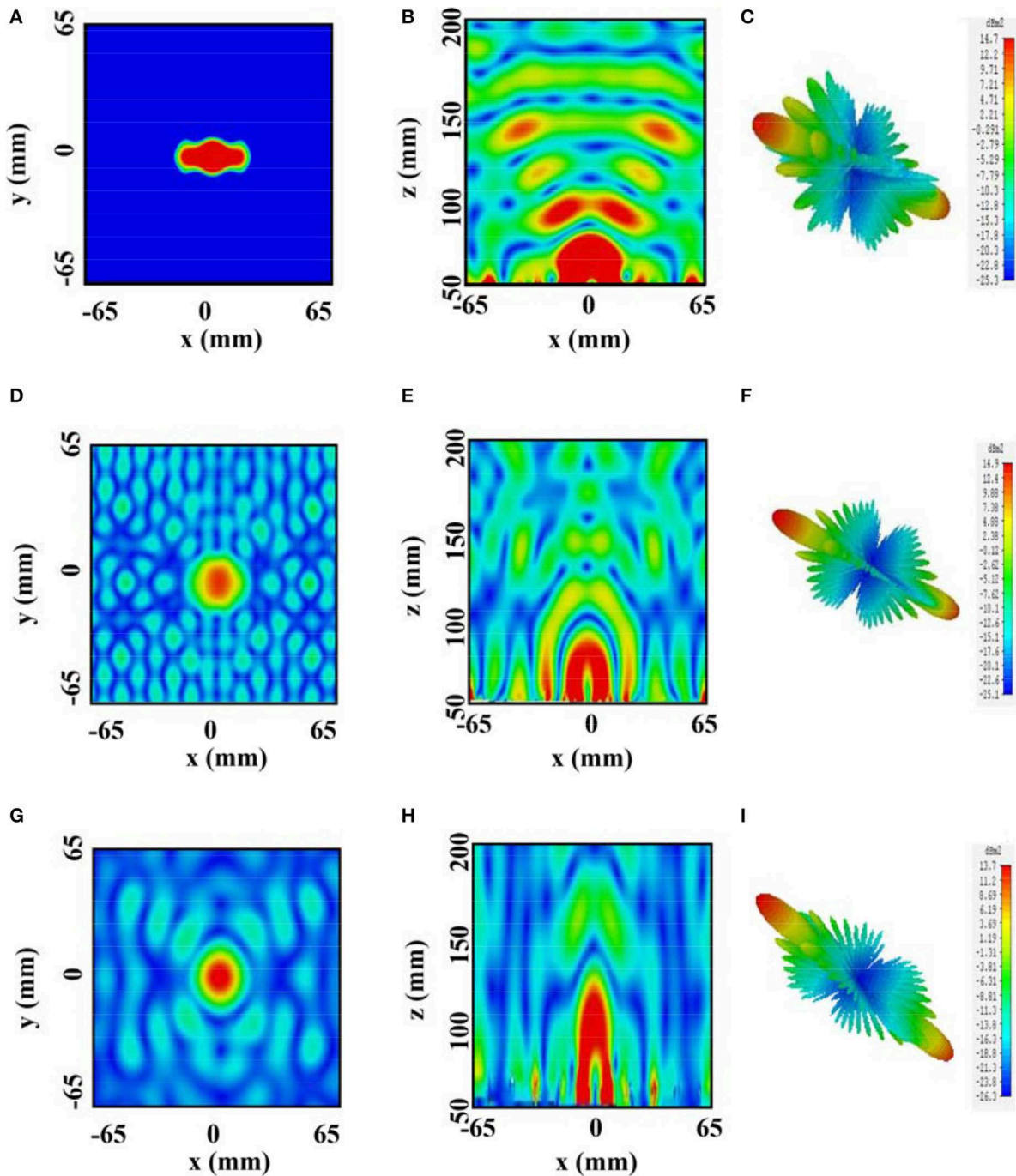


FIGURE 5 | The field intensity, distribution in the y-z plane, x-y plane, and 3D radiation pattern at 20 GHz (A-C), 19 GHz (D-F), and 18 GHz (G-I), respectively.

in a subwavelength dimension, in which the size of the square metasurface has a linear relationship with the phase discontinuity. The proposed gradient metasurface can be used for the realization of approximately full range reflection phase shift modulation, and the simulation results show that the three-layer gradient metasurface reflection array has a good

focusing efficiency of 82%. In addition, because of the simple structure of the components, the three layers can be made of common materials, which makes the device convenient to design and manufacture. It provides a new method for the design of passive-reflection focusing arrays, which improves the guiding efficiency of electromagnetic beams.

AUTHOR CONTRIBUTIONS

BX developed the concept and supervised the whole project. MY carried out the simulations and analyzed the simulation data. BX and ZS contributed to writing and finalizing the paper. BW and PC contributed to paper revision and language editing.

ACKNOWLEDGMENTS

The simulation software and writing assistance were provided by BX. The laboratory support was provided by School of Sciences, Zhejiang University of Science and Technology.

REFERENCES

- Pfeiffer C, Grbic A. Controlling vector Bessel beams with metasurfaces. *Phys Rev A*. (2014) 2:044012. doi: 10.1103/PhysRevApplied.2.044012
- Lin D, Fan P, Hasman E, Brongersma ML. Dielectric gradient metasurface optical elements. *Science*. (2014) 345:298–302. doi: 10.1126/science.1253213
- Ni X, Kildishev AV, Shalae VM. Metasurface holograms for visible light. *Nat Commun*. (2013) 4:2807. doi: 10.1038/ncomms3807
- Tamilchelvan R, Senthikumar VJ. Design and optimization of wideband microwave amplifier using nonlinear technique. *Wirel Pers Commun*. (2018) 99:1589–604. doi: 10.1007/s11277-018-5293-5
- Asadchy VS, Díaz-Rubio A, Tretyakov SA. Bianisotropic metasurfaces: physics and applications. *Nanophotonics*. (2018) 7:1069–94. doi: 10.1515/nanoph-2017-0132
- Zheludev NI. The road ahead for metamaterials. *Science*. (2010) 328:582–3. doi: 10.1126/science.1186756
- Liu L, Ding Y, Yvind K, Hvam JM. Silicon-on-insulator polarization splitting and rotating device for polarization diversity circuits. *Opt Express*. (2011) 19:12646–51. doi: 10.1364/OE.19.012646
- Ding F, Yang Y, Deshpande RA, Bozhevolnyi SI. A review of gap-surface plasmon metasurfaces: fundamentals and applications. *Nanophotonics*. (2018) 7:1129–56. doi: 10.1515/nanoph-2017-0125
- Chou HC, Tung NL, Kehn MNM. The double-focus generalized luneburg lens design and synthesis using metasurfaces. *IEEE Trans Antennas Propag*. (2018) 66:4936–41. doi: 10.1109/TAP.2018.2845550
- Yun H, Chrostowski L, Jaeger NAF. Ultra-broadband 2×2 adiabatic 3 dB coupler using subwavelength-grating-assisted silicon-on-insulator strip waveguides. *Opt Lett*. (2018) 43:1935–8. doi: 10.1364/OL.43.001935
- Cai W, Shalae VM. *Optical Metamaterials*. New York, NY: Springer (2010). doi: 10.1007/978-1-4419-1151-3
- Fu Y, Shen C, Cao Y, Gao L, Chen H, Chan CT. Reversal of transmission and reflection based on acoustic metagratings with integer parity design. *Nat Commun*. (2019) 10:2326. doi: 10.1038/s41467-019-10377-9
- Barwicz T, Watts MR, Popović MA, Rakich PT, Succi L, Kärtner FX, et al. Polarization-transparent microphotonic devices in the strong confinement limit. *Nature photonics*. (2007) 1:57–60. doi: 10.1038/nphoton.2006.41
- Wang Y, Ma M, Yun H, Lu Z, Wang X, Jaeger NA, et al. Ultra-compact sub-wavelength grating polarization splitter-rotator for silicon-on-insulator platform. *IEEE Photonics J*. (2016) 8:1–9. doi: 10.1109/JPHOT.2016.2630849
- Ding Y, Ou H, Peucheret C. Wideband polarization splitter and rotator with large fabrication tolerance and simple fabrication process. *Opt Lett*. (2013) 38:1227–9. doi: 10.1364/OL.38.001227
- Zhang Z, Yang Q, Gong M, Chen M, Long Z. Metasurface lens with angular modulation for extended depth of focus imaging. *Opt Lett*. (2020) 45:611–4. doi: 10.1364/OL.382812
- Zhang Z, Yang Q, Gong M, Long Z. Toroidal dipolar bound state in the continuum and antiferromagnetic in asymmetric metasurface. *J Phys D Appl Phys*. (2019) 53:075106. doi: 10.1088/1361-6463/ab5983
- Shi Z, Khorasaninejad M, Huang YW, Roques Carmes C, Zhu AY, Chen WT, et al. Single-layer metasurface with controllable multiwavelength functions. *Nano Lett*. (2018) 18:2420–7. doi: 10.1021/acs.nanolett.7b05458
- Xu B, Wei Z, Wu C, Fan Y, Wang Z, Li H. Near-diffraction-limited focusing with gradient high-impedance metasurface. *Opt Mater Express*. (2017) 7:1141–6. doi: 10.1364/OME.7.001141
- Dong X, Sun H, Gu CQ, Li Z, Chen X, Xu B. Generation of ultra-wideband multi-mode vortex waves based on monolayer reflective metasurface. *Prog Electromagn Res*. (2019) 80:111–20. doi: 10.2528/PIERM19010504
- Wang H, Li Y, Han Y, Fan Y, Sui S, Chen H, et al. Vortex beam generated by circular-polarized metasurface reflector antenna. *J Phys D Appl Phys*. (2019) 52:255306. doi: 10.1088/1361-6463/ab1742
- Chrostowski L, Hochberg M. *Silicon Photonics Design: From Devices to Systems*. Oxford: Cambridge University Press (2015). doi: 10.1017/CBO9781316084168
- Fan Q, Huo P, Wang D, Liang Y, Yan F, Xu T. Visible light focusing flat lenses based on hybrid dielectric-metal metasurface reflector-arrays. *Sci Rep*. (2017) 7:45044. doi: 10.1038/srep45044
- Sun Z, Mengyao Y, Mupona TE, Bijun X. Control electromagnetic waves based on multi-layered transparent metasurface. *Front Phys*. (2019) 7:181. doi: 10.3389/fphy.2019.00181

Conflict of Interest: The authors declare that the research was conducted in the absence of any commercial or financial relationships that could be construed as a potential conflict of interest.

Copyright © 2020 Yan, Sun, Wu, Cheng and Xu. This is an open-access article distributed under the terms of the Creative Commons Attribution License (CC BY). The use, distribution or reproduction in other forums is permitted, provided the original author(s) and the copyright owner(s) are credited and that the original publication in this journal is cited, in accordance with accepted academic practice. No use, distribution or reproduction is permitted which does not comply with these terms.



Switchable Metasurface With Broadband and Highly Efficient Electromagnetic Functionality

Zeyong Wei^{1,2*}, Xiaoqin Liu^{1,2} and Yang Cao^{3*}

¹ School of Physics Science and Engineering, Tongji University, Shanghai, China, ² Key Laboratory of Advanced Micro-structure Materials (MOE), Shanghai, China, ³ Shanghai Mi Xuan Electronic Technology Co., Ltd., Shanghai, China

OPEN ACCESS

Edited by:

Yuancheng Fan,
Northwestern Polytechnical
University, China

Reviewed by:

Zhengyong Song,
Xiamen University, China
Yongqiang Pang,
Xi'an Jiaotong University, China
Xu Bijun,
Zhejiang University of Science and
Technology, China

*Correspondence:

Zeyong Wei
weizeyong@tongji.edu.cn
Yang Cao
caoyang85@163.com

Specialty section:

This article was submitted to
Optics and Photonics,
a section of the journal
Frontiers in Physics

Received: 05 February 2020

Accepted: 12 March 2020

Published: 03 April 2020

Citation:

Wei Z, Liu X and Cao Y (2020)
Switchable Metasurface With
Broadband and Highly Efficient
Electromagnetic Functionality.
Front. Phys. 8:90.
doi: 10.3389/fphy.2020.00090

Electromagnetic metasurface is a kind of artificial electromagnetic structure, which can control the transmission, reflection, polarization and beam of electromagnetic wave within sub-wavelength thickness. Efficiency, bandwidth and dynamic control are very important in the application of metasurface. The bandwidth of electromagnetic transparency can be broadened by interlayer coupling of local resonance modes of the stacked layers. In this paper, we propose that the electromagnetic wave could be switched on or off in a broadband frequency range by metasurface which consists of three layers of metal microstructures with PIN diodes. When the diodes are biased with forward voltage, the switching diodes are in the on state, and the slab reflects electromagnetic wave completely, just like a perfect metal. When the diodes are biased with backward voltage, the switching diodes are equivalent to a capacitor, and all the electromagnetic wave energy passes through the sample. The simulation results show that the transmissivity is <1% when the sample is loaded with forward voltage in the frequency range of 8–12 GHz, while the transmittance is more than 96% when the sample is loaded with reverse bias. We have fabricated the corresponding samples and measured the reflection and transmission in the waveguide. The measurements verify the properties of broadband highly efficient electromagnetic transparency and perfect reflection.

Keywords: metasurface, switchable, broadband, high efficiency, PIN diode

INTRODUCTION

Manipulating the amplitude and phase of the electromagnetic waves in a desired manner has broad applicability in areas such as imaging, sensing, and communication [1]. In practical applications, full control of transmitted wave with high efficiency covering a wide frequency range is of great importance [2, 3]. In recent years, metasurfaces with subwavelength thickness of artificial structures have attracted great interest and yielded ground-breaking electromagnetic and photonic phenomena [4–13]. Among them, active devices have attracted much attention for their key role in communication and imaging systems in recently years [14–24]. Phase change materials (GST and VO₂), graphene and PIN diodes are proposed to realize tunable metamaterials [25–28]. However, due to the resonant feature of artificial structures, it is very difficult to manipulate the electromagnetic wave in a broadband frequency range, and metasurfaces only exhibit fascinating

physical properties at specific frequencies [29–33]. Such a narrowband feature dramatically restricts the application of the metastructures in versatile areas.

The resonant tunneling of surface plasmon polaritons (SPPs) can effectively enhance the transmissivity of metal slab perforated with an array of subwavelength-sized holes, which has been widely studied as a phenomenon of extraordinary optical transmission (EOT) [34–38]. It is reported that, in the EOT of metallic films, perfect transparency only occurs at a single or a set of discrete frequencies, and is sensitive to the incident angle of the electromagnetic wave. Then it is further revealed that, local resonance modes of specific hole arrays also lead to EOT phenomena which are robust to the incident angle [39, 40]. And the bandwidth of EOT passband was broadened by the evanescent coupling of the local resonance modes of the cascaded multi-layer system that is perforated with an array of coaxial annular apertures [41–46].

In this paper, a cascaded design is proposed to realize electrically switchable metasurface with high efficiency over a continuous frequency range from 8 to 12GHz. The electromagnetic metasurface exhibits tunable transmission and reflection properties which can be freely controlled by changing the state of the loaded PIN diodes. The simulation of finite-difference-time-domain (FDTD) method indicates that the incident wave perfectly transmits through the multilayer when the PIN diodes are switched off, and the transmission efficiency is above 96% within the whole frequency range. When the PIN diodes are loaded with forward bias voltage, the transmission is suppressed below 1%, while the reflectivity reaches 88%. It can be observed from the field distributions that the electromagnetic transparency comes from the near-field coupling of the magnetic resonance modes [23, 47–51]. We fabricated the corresponding samples in the microwave frequency regime, and measured the transmissivity and reflectivity for different states in the waveguide. The experimental results are in good agreement with the simulations. This research is expected to have a good application prospect in imaging, communication and other fields.

MODEL DESCRIPTION

As schematically shown in **Figure 1A**, the broadband metasurface for electromagnetic manipulation is composed of three layers of metallic structure (colored in yellow) separated by two layers of dielectric medium (colored in blue). The thickness of dielectric layers and metallic layers is $h = 1.575 \text{ mm}$ and $t = 0.035 \text{ mm}$, respectively. **Figure 1B** presents the top view of the metallic structure in upper surface, which is the same as that in bottom surface. They are periodically arranged gratings with a period of $p = g + b = 2.1 \text{ mm}$, and a gap width of $g = 1.5 \text{ mm}$. Lumped PIN diodes are loaded on the gratings to switch the state of the metasurface by changing the DC bias. The structure in the middle layer is metallic mesh with periods of $p_x = 7.62 \text{ mm}$ in x direction and $p_y = 4.98 \text{ mm}$ in y direction, as shown in **Figure 1C**, and the width of metallic wire is $w_m = 0.7 \text{ mm}$.

SIMULATIONS AND MEASUREMENTS OF HIGHLY EFFICIENT SWITCHABLE METASURFACE

The state switch of the metasurface is achieved by changing the voltage loaded on the PIN diodes. The diodes are conductive when loaded with forward bias voltage (On-State) that the gratings behave as metallic mesh. Therefore the metasurface is equivalent to three-layered meshes with cutoff frequency much higher than the operational frequency, so that the electromagnetic incidence is strongly reflected. In contrast, the diodes work as capacitors while they are not biased or loaded with reverse bias voltage (Off-State). In this instance, the gratings together with the metallic mesh in the middle layer form a kind of magnetic resonant structure. Although the working frequency is below the cutoff frequency of the mesh in the middle layer that the incident wave cannot directly pass through the structure, near-field coupling between the magnetic modes leads to electromagnetic wave tunneling, similar to the electronic tunneling effect. Therefore, we

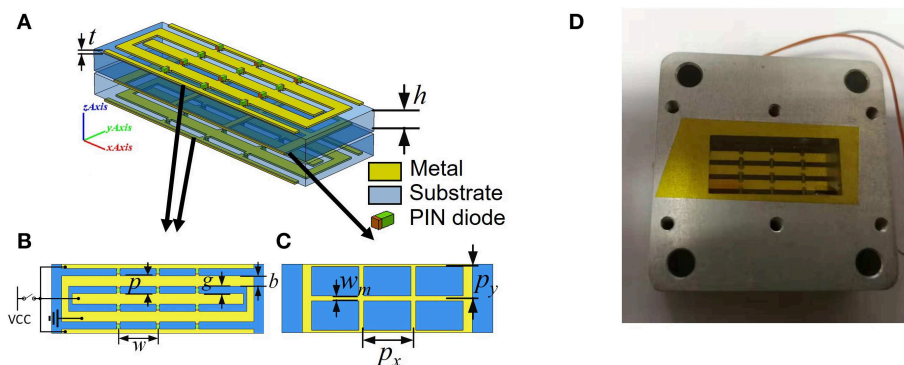
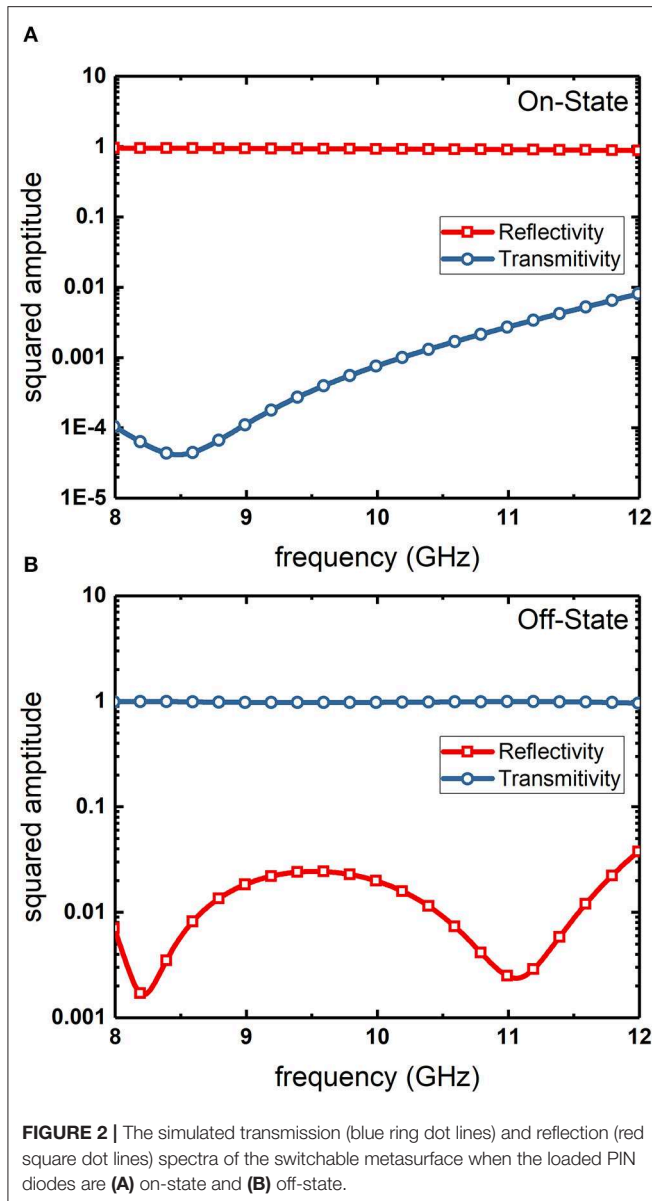
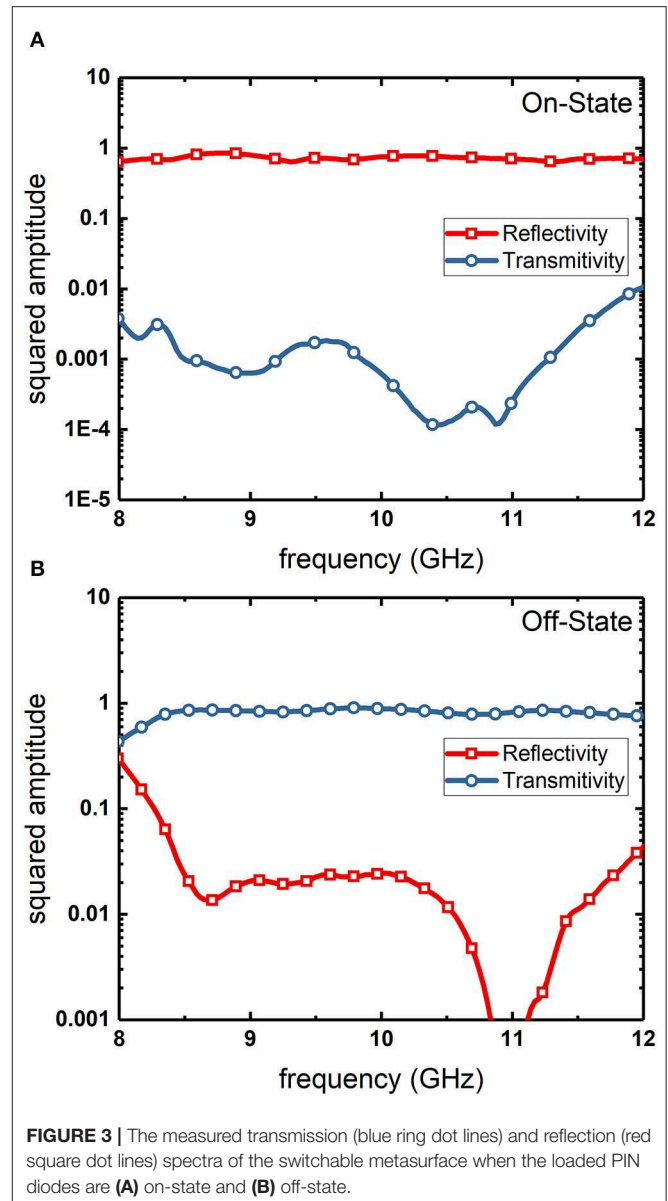


FIGURE 1 | (A) Schematic of the switchable metasurface with three metallic layers and two dielectric layers. Top views of **(B)** the upper layer and the bottom layer, **(C)** the middle layer. **(D)** The photo of our sample with the waveguide.



achieved transmittance manipulation through the control of bias voltage.

FDTD method is employed to calculate the transmission of the metasurface for both states. In the simulation, perfect electric conductor (PEC) boundaries are set at the x and y directions, and absorbing boundary is set at negative z direction. Waveguide port excitation is imposed at positive z direction with the incident wave propagating along z-direction. **Figure 2** shows the calculated transmissivity and reflectivity of the metasurface for the two states. When the diode is loaded with forward bias, it is replaced by a resistor with a resistance of 4.2Ω in the simulation model. As shown in **Figure 2A** that, for on-state, the transmissivity is $<1\%$ and the reflectivity is more than 88%, implying that the electromagnetic wave is almost completely reflected back in a broad frequency band from 8 to 12 GHz. Due to the thermal effect of resistance, there is about 10% absorption



loss in the on-state. **Figure 2B** presents the spectrum for off-state when no bias voltage is applied. The diode is replaced by a capacitor with a capacitance of 0.02 pF in simulation. It is observed that the metasurface is perfectly transparent with transmissivity $>96\%$ and reflectivity $<4\%$ within the band.

In order to verify the proposed switchable metasurface for wide-band electromagnetic manipulation, we fabricate the microwave samples by printed circuit board (PCB) technology, as shown in **Figure 1D**. Taconic TLX-6 is used with a dielectric constant of 2.65, and the geometric parameters of the sample is kept the same as those of simulation model. Then 24 PIN diodes are loaded on the gratings in upper and bottom surfaces. We adopt Aluminum Gallium Arsenide (AlGaAs) flip-chip PIN diodes (MA4AGP907) because of their small geometry and junction capacitance. When applied with forward bias

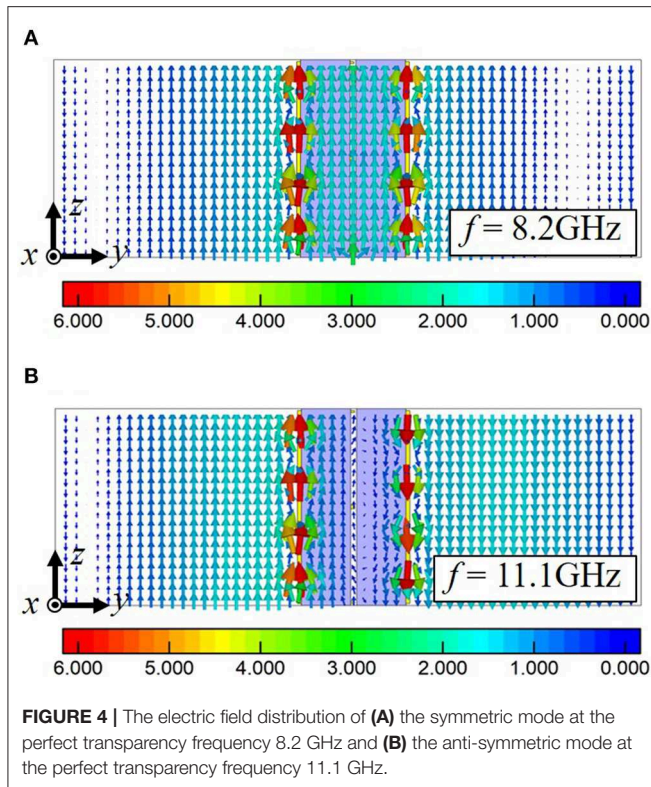


FIGURE 4 | The electric field distribution of (A) the symmetric mode at the perfect transparency frequency 8.2 GHz and (B) the anti-symmetric mode at the perfect transparency frequency 11.1 GHz.

voltage, the diode is equivalent to a resistor with a resistance of 4.2Ω at 10 GHz, otherwise it behaves as a capacitor with a capacitance of 0.02 pF. The electrodes are leaded from gratings to impose the bias voltage (shown in **Figure 1B**). The metasurface is placed in standard waveguide with a length of 22.86 mm and a width of 10.16 mm. Then the waveguide is connected to the vector network analyzer (PNA52224) with a coaxial-to-waveguide converter. By measuring the S parameters, we extract the transmissivity and reflectivity of the sample. **Figure 3** shows the experimental results for the two states which are in good agreement with the simulation results, confirming the wide-band control of electromagnetic transparency from the metasurface.

The bandwidth and efficiency are key points to the electromagnetic wave control. It has been proved that the working bandwidth can be broadened by near-field coupling of resonance modes between adjacent layers [41]. Due to the mutual coupling [44, 52, 53] of magnetic resonance modes, the transmission peak of the metasurface extends to a transmission band as shown in **Figures 2B, 3B**. The simulated power transmission is above 96% in the frequency range of 8–12 GHz, and the reflectivity reaches minimum at two resonant frequencies at $f = 8.2$ and $f = 11.1 \text{ GHz}$, while the simulation transmission is above 80% in the frequency range of 8.4–12 GHz, and the reflectivity reaches minimum at two resonant frequencies at $f = 8.6$ and $f = 11.0 \text{ GHz}$. The calculated field distributions provide further insight into the cause of wide-band transparency. **Figure 4** shows the spatial distributions of the electric field in the yz plane at the two resonant frequencies. Arrows in the field distributions represent the direction of the electric field vector, with their size and color indicating the scale of the field.

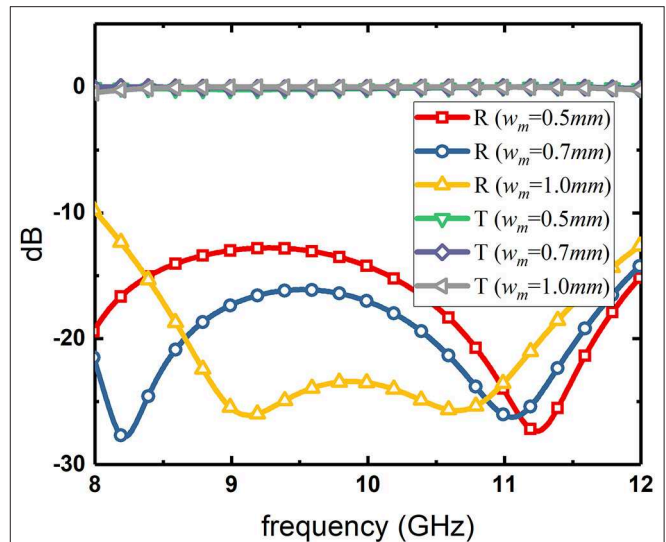


FIGURE 5 | The simulated transmission and reflection spectra of the switchable metasurface when the loaded PIN diodes are off-state. The bandwidth of the transparency can be tuned by the coupling coefficient of the magnetic modes.

It can be read from the color bar that the near-field electric field is magnified six times at these two frequencies of perfect transparency, while the magnitude of plane wave incidence is set as unit. It also can be seen from the field distributions that the y component of electric field is symmetric about the $y = 0$ plane at 8.2 GHz and is antisymmetric at 11.1 GHz. Considering the symmetry of these two modes, we can draw the conclusion that the perfect transparency peaks result from the inter-layer coupling of the magnetic resonance modes.

As the bandwidth of transparent state can be broadened by the near-field coupling of the resonance modes in the metasurface, the coupling coefficient can be adjusted by metallic mesh in the middle layer. Inspired by tight binding theory, the weaker the coupling is, the smaller is the energy difference between symmetric and antisymmetric states, vice versa, the stronger the coupling is, the larger is the energy difference. Therefore, it provides a way to control the bandwidth of electromagnetic transparency by adjusting the mesh size in the middle layer. For demonstration, the transmission spectra of $w_m = 0.5, 0.7, 1.0 \text{ mm}$ are calculated and shown in **Figure 5**. As the value of w_m increases, the transparency bandwidth becomes narrower, which agrees well with the theoretical prediction.

CONCLUSION

In this paper, we have proposed a general scheme to design broadband active metasurface, which switches the transparency and reflection electromagnetic properties by controlling the loaded PIN diodes in the upper surface and bottom surface. The origin of the broadband property is studied in detail, and electric field distributions are presented for the explanation of perfect transparency occurring in the structure. The broadband nature of dynamic manipulation of the transmission and reflection

states in the proposed structure is verified both numerically and experimentally. The simulated insertion loss of the metasurface on the transparency state is <0.5 dB within the frequency range 8–12 GHz, which is benefit from evanescent coupling and hybridization of the magnetic resonate modes. The simulated transmission of the metasurface on the reflection state is <-15 dB. The proposed structure is suitable for microwave communication, sensing systems.

DATA AVAILABILITY STATEMENT

The raw data supporting the conclusions of this article will be made available by the authors, without undue reservation, to any qualified researcher.

REFERENCES

- Born M, Wolf E. *Principles of Optics: Electromagnetic Theory of Propagation, Interference and Diffraction of Light*. Oxford, Angletterre: Pergamon Press (1980).
- Engheta N, Ziolkowski RW. *Metamaterials: Physics and Engineering Explorations*. New York, NY: Wiley-IEEE Press (2006).
- Cai W, Shalaev V. *Optical Metamaterials: Fundamentals and Applications*. New York NY: Springer (2009).
- Yu NF, Genevet P, Kats MA, Aieta F, Tetienne JP, Capasso F, et al. Light propagation with phase discontinuities: generalized laws of reflection and refraction. *Science*. (2011) 334:333–7. doi: 10.1126/science.1210713
- Aieta F, Genevet P, Yu NF, Kats MA, Gaburro Z, Capasso F. Out-of-plane reflection and refraction of light by anisotropic optical antenna metasurfaces with phase discontinuities. *Nano Lett*. (2012) 12:1702–6. doi: 10.1021/nl300204s
- Yu NF, Capasso F. Flat optics with designer metasurfaces. *Nat Mater*. (2014) 13:139–50. doi: 10.1038/nmat3839
- Chen HT, Taylor AJ, Yu NF. A review of metasurfaces: physics and applications. *Rep Progr Phys*. (2016) 79:076401. doi: 10.1088/0034-4885/79/7/076401
- Glybovski SB, Tretyakov SA, Belov PA, Kivshar YS, Simovski CR. Metasurfaces: from microwaves to visible. *Phys Rep*. (2016) 634:1–72. doi: 10.1016/j.physrep.2016.04.004
- Zhang L, Mei ST, Huang K, Qiu CW. Advances in full control of electromagnetic waves with metasurfaces. *Adv Opt Mater*. (2016) 4:818–33. doi: 10.1002/adom.201500690
- Genevet P, Capasso F, Aieta F, Khorasaninejad M, Devlin R. Recent advances in planar optics: from plasmonic to dielectric metasurfaces. *Optica*. (2017) 4:139–52. doi: 10.1364/OPTICA.4.000139
- Chen SQ, Li Z, Zhang YB, Cheng H, Tian JG. Phase manipulation of electromagnetic waves with metasurfaces and its applications in nanophotonics. *Adv Opt Mater*. (2018) 6:1800104. doi: 10.1002/adom.201800104
- Luo XG. Subwavelength artificial structures: opening a new era for engineering optics. *Adv Mater*. (2019) 31:1804680. doi: 10.1002/adma.201804680
- Sun SL, He Q, Hao JM, Xiao SY, Zhou L. Electromagnetic metasurfaces: physics and applications. *Adv Opt Photon*. (2019) 11:380–479. doi: 10.1364/AOP.11.000380
- Chen HT, Padilla WJ, Zide JMO, Gossard AC, Taylor AJ, Averitt RD. Active terahertz metamaterial devices. *Nature*. (2006) 444:597–600. doi: 10.1038/nature05343
- Chowdhury DR, Azad AK, Zhang WL, Singh R. Near field coupling in passive and active terahertz metamaterial devices. *IEEE Trans Terahertz Sci Technol*. (2014) 4:400–. doi: 10.1109/TTHZ.2014.2312771

AUTHOR CONTRIBUTIONS

ZW conceived the idea and supervised the whole study. XL conducted the numerical calculations and performed the experiments. YC derived the theory, carried out the analysis, and drafted the manuscript. All authors contributed to the review of manuscript.

FUNDING

This work was supported by the National Natural Science Foundation of China (Grant Nos. 11674248, 11874285, and 11204218); supported by the Fundamental Research Funds for the Central Universities.

- Ma X, Pan W, Huang C, Pu M, Wang Y, Zhao B, et al. An active metamaterial for polarization manipulating. *Adv Opt Mater*. (2014) 2:945–9. doi: 10.1002/adom.201400212
- Qiao S, Zhang YX, Liang SX, Sun LL, Sun H, Xu GQ, et al. Multi-band terahertz active device with complementary metamaterial. *J Appl Phys*. (2015) 118:123106. doi: 10.1063/1.4931583
- Wang DC, Zhang LC, Gu YH, Mehmood MQ, Gong YD, Srivastava A, et al. Switchable ultrathin quarter-wave plate in terahertz using active phase-change metasurface. *Sci Rep*. (2015) 5:15020. doi: 10.1038/srep15020
- Xu HX, Sun SL, Tang SW, Ma SJ, He Q, Wang GM, et al. Dynamical control on helicity of electromagnetic waves by tunable metasurfaces. *Sci Rep*. (2016) 6:27503. doi: 10.1038/srep27503
- Liu F, Tsilipakos O, Ptilakis A, Tasolamprou AC, Mirmoosa MS, Kantartzis NV, et al. Intelligent metasurfaces with continuously tunable local surface impedance for multiple reconfigurable functions. *Phys Rev Appl*. (2019) 11:044024. doi: 10.1103/PhysRevApplied.11.044024
- Li Y, Lin J, Guo HJ, Sun WJ, Xiao SY, Zhou L. A tunable metasurface with switchable functionalities: from perfect transparency to perfect absorption. *Adv Opt Mater*. (2020) 8:1901548. doi: 10.1002/adom.201901548
- Wu ZL, Chen XD, Wang MS, Dong JW, Zheng YB. High-performance ultrathin active chiral metamaterials. *ACS Nano*. (2018) 12:5030–41. doi: 10.1021/acsnano.8b02566
- Fan YC, Shen NH, Zhang FL, Zhao Q, Wei ZY, Zhang P, et al. Photoexcited graphene metasurfaces: significantly enhanced and tunable magnetic resonances. *ACS Photon*. (2018) 5:1612–8. doi: 10.1021/acsp Photonics.8b00057
- Fan YC, Shen NH, Zhang FL, Wei ZY, Li HQ, Zhao Q, et al. Electrically tunable goos-hanchen effect with graphene in the terahertz regime. *Adv Opt Mater*. (2016) 4:1824–8. doi: 10.1002/adom.201600303
- Chu QQ, Song ZY, Liu QH. Omnidirectional tunable terahertz analog of electromagnetically induced transparency realized by isotropic vanadium dioxide metasurfaces. *Appl Phys Expr*. (2018) 11:082203. doi: 10.7567/APEX.11.082203
- Wang WH, Song ZY. Multipole plasmons in graphene nanoellipses. *Phys B Condens Matter*. (2018) 530:142–6. doi: 10.1016/j.physb.2017.11.038
- Song ZY, Chen AP, Zhang JH, Wang JY. Integrated metamaterial with functionalities of absorption and electromagnetically induced transparency. *Opt Exp*. (2019) 27:25196–204. doi: 10.1364/OE.27.025196
- Wei ML, Song ZY, Deng YD, Liu YN, Chen Q. Large-angle mid-infrared absorption switch enabled by polarization-independent GST metasurfaces. *Mater Lett*. (2019) 236:350–3. doi: 10.1016/j.matlet.2018.10.136
- Liu LX, Zhang XQ, Kenney M, Su XQ, Xu NN, Ouyang CM, et al. Broadband metasurfaces with simultaneous control of phase and amplitude. *Adv Mater*. (2014) 26:5031–6. doi: 10.1002/adma.201401484
- Ding F, Wang ZX, He SL, Shalaev VM, Kildishev AV. Broadband high-efficiency half-wave plate: a supercell-based plasmonic metasurface approach. *ACS Nano*. (2015) 9:4111–9. doi: 10.1021/acsnano.5b00218

31. Wang SM, Wu PC, Su VC, Lai YC, Chu CH, Chen JW, et al. Broadband achromatic optical metasurface devices. *Nat Commun.* (2017) 8:187. doi: 10.1038/s41467-017-00166-7
32. Fan RH, Xiong B, Peng RW, Wang M. Constructing metastructures with broadband electromagnetic functionality. *Adv Mater.* (2019) 1904646. doi: 10.1002/adma.201904646
33. Fan YC, Tu LQ, Zhang FL, Fu QH, Zhang ZR, Wei ZY, et al. Broadband terahertz absorption in graphene-embedded photonic crystals. *Plasmonics.* (2018) 13:1153–8. doi: 10.1007/s11468-017-0615-0
34. Ebbesen TW, Lezec HJ, Ghaemi HF, Thio T, Wolff PA. Extraordinary optical transmission through sub-wavelength hole arrays. *Nature.* (1998) 391:667–9. doi: 10.1038/35570
35. Barnes WL, Dereux A, Ebbesen TW. Surface plasmon subwavelength optics. *Nature.* (2003) 424:824–30. doi: 10.1038/nature01937
36. de Abajo FJG. Colloquium: light scattering by particle and hole arrays. *Rev Mod Phys.* (2007) 79:1267–90. doi: 10.1103/RevModPhys.79.1267
37. Garcia-Vidal FJ, Martin-Moreno L, Ebbesen TW, Kuipers L. Light passing through subwavelength apertures. *Rev Mod Phys.* (2010) 82:729–87. doi: 10.1103/RevModPhys.82.729
38. Carretero-Palacios S, Garcia-Vidal FJ, Martin-Moreno L, Rodrigo SG. Effect of film thickness and dielectric environment on optical transmission through subwavelength holes. *Phys Rev B.* (2012) 85:035417. doi: 10.1103/PhysRevB.85.035417
39. Ruan ZC, Qiu M. Enhanced transmission through periodic arrays of subwavelength holes: The role of localized waveguide resonances. *Phys Rev Lett.* (2006) 96:233901. doi: 10.1103/PhysRevLett.96.233901
40. Wei ZY, Fu JX, Cao Y, Wu C, Li HQ. The impact of local resonance on the enhanced transmission and dispersion of surface resonances. *Photon Nanostruct Fund Appl.* (2010) 8:94–101. doi: 10.1016/j.photonics.2009.10.001
41. Wei ZY, Cao Y, Fan YC, Yu X, Li HQ. Broadband transparency achieved with the stacked metallic multi-layers perforated with coaxial annular apertures. *Opt Exp.* (2011) 19:21425–31. doi: 10.1364/OE.19.021425
42. Wei ZY, Cao Y, Fan YC, Yu X, Li HQ. Broadband polarization transformation via enhanced asymmetric transmission through arrays of twisted complementary split-ring resonators. *Appl Phys Lett.* (2011) 99:221907. doi: 10.1063/1.3664774
43. Wei ZY, Cao Y, Su XP, Gong ZJ, Long Y, Li HQ. Highly efficient beam steering with a transparent metasurface. *Opt Exp.* (2013) 21:10739–45. doi: 10.1364/OE.21.010739
44. Cheng KY, Wei ZY, Fan YC, Zhang XM, Wu C, Li HQ. Realizing broadband transparency via manipulating the hybrid coupling modes in metasurfaces for high-efficiency metalens. *Adv Opt Mater.* (2019) 7:1900016. doi: 10.1002/adom.201900016
45. Cong LQ, Xu NN, Gu JQ, Singh R, Han JG, Zhang WL. Highly flexible broadband terahertz metamaterial quarter-wave plate. *Laser Photon Rev.* (2014) 8:626–32. doi: 10.1002/lpor.201300205
46. Fan RH, Zhou Y, Ren XP, Peng RW, Jiang SC, Xu DH, et al. Freely tunable broadband polarization rotator for terahertz waves. *Adv Mater.* (2015) 27:1201–6. doi: 10.1002/adma.201404981
47. Sievenpiper D, Zhang L, Broas R, Alexopolous N, Yablonovitch E. High-impedance electromagnetic surfaces with a forbidden frequency band. *IEEE Trans Microwave Theory Techn.* (1999) 47:2059–74. doi: 10.1109/22.798001
48. Zhou L, Wen W, Chan C, Sheng P. Multiband subwavelength magnetic reflectors based on fractals. *Appl Phys Lett.* (2003) 83:3257–9. doi: 10.1063/1.1622122
49. Zhou L, Li HQ, Qin YQ, Wei ZY, Chan CT. Directive emissions from subwavelength metamaterial-based cavities. *Appl Phys Lett.* (2005) 86:101101. doi: 10.1063/1.1881797
50. Wei ZY, Li HQ, Cao Y, Wu C, Ren JZ, Hang ZH, et al. Spatially coherent surface resonance states derived from magnetic resonances. *New J Phys.* (2010) 12:093020. doi: 10.1088/1367-2630/12/9/093020
51. Wei ZY, Li HQ, Wu C, Cao Y, Ren JZ, Hang ZH, et al. Anomalous reflection from hybrid metamaterial slab. *Opt Exp.* (2010) 18:12119–26. doi: 10.1364/OE.18.012119
52. Tassin P, Zhang L, Zhao RK, Jain A, Koschny T, Soukoulis CM. Electromagnetically induced transparency and absorption in metamaterials: the radiating two-oscillator model and its experimental confirmation. *Phys Rev Lett.* (2012) 109:187401. doi: 10.1103/PhysRevLett.109.187401
53. Kelly C, Khorashad LK, Gadegaard N, Barron LD, Govorov AO, Karimullah AS, et al. Controlling metamaterial transparency with superchiral fields. *ACS Photon.* (2018) 5:535–43. doi: 10.1021/acsp Photonics.7b01071

Conflict of Interest: YC was employed by the company Shanghai Mi Xuan Electronic Technology Co., Ltd.

The remaining authors declare that the research was conducted in the absence of any commercial or financial relationships that could be construed as a potential conflict of interest.

Copyright © 2020 Wei, Liu and Cao. This is an open-access article distributed under the terms of the Creative Commons Attribution License (CC BY). The use, distribution or reproduction in other forums is permitted, provided the original author(s) and the copyright owner(s) are credited and that the original publication in this journal is cited, in accordance with accepted academic practice. No use, distribution or reproduction is permitted which does not comply with these terms.



Control of THz Surface Plasmons by Geometric Phases

Shulin Hu^{1,2}, Peng Wang^{1,2}, Cai Zhou^{1,2}, Min Hu^{1,2,3}, Yuli Xiong^{1,2,3}, Huanhuan Xu^{1,2,3}, Xiaoyu Li^{1,2,3}, Mingyao Xu^{1,2,3*} and Shengxiang Wang^{1,2,3*}

¹Hubei Engineering and Technology Research Center for Functional Fiber Fabrication and Testing, Wuhan Textile University, Wuhan, China, ²School of Electronic and Electrical Engineering, Wuhan Textile University, Wuhan, China, ³Hubei Province Engineering Research Center for Intelligent Micro-nano Medical Equipment and Key Technologies, Wuhan Textile University, Wuhan, China

OPEN ACCESS

Edited by:

Yuancheng Fan,
Northwestern Polytechnical
University, China

Reviewed by:

Xueqian Zhang,
Tianjin University, China
Oleg Rybin,
V. N. Karazin Kharkiv National
University, Ukraine

*Correspondence:

Mingyao Xu
1988018@wtu.edu.cn
Shengxiang Wang
shxwang@wtu.edu.cn

Specialty section:

This article was submitted to
Optics and Photonics,
a section of the journal
Frontiers in Physics

Received: 30 September 2020

Accepted: 03 December 2020

Published: 19 January 2021

Citation:

Hu S, Wang P, Zhou C, Hu M, Xiong Y,
Xu H, Li X, Xu M and Wang S (2021)
Control of THz Surface Plasmons by
Geometric Phases.
Front. Phys. 8:612163.
doi: 10.3389/fphy.2020.612163

Surface plasmons (SPs) are expected to have a wide range of applications in many fields, so they have recently attracted much attention. However, most of the previous studies achieved the manipulation of SPs through designing the structure of the individual meta-atom. When developing the next generation of integrated photonic devices and components, it is essential to seek out new methods of software control, which enable more diverse modulation and higher efficiency. Here, the tunable emission of SPs with metasurfaces is systematically studied. SPs are a source of on-chip plasmonic vortices (PVs). To verify the controllability of the directional excitation of SPs, we designed beam deflectors with different angles of surface waves (SWs). Furthermore, PVs with different topological charges were generated by arranging spatially varied microslits. The proposed control strategy provides a common platform for various promising applications, such as on-chip generation of the propagation control of SPs and PVs.

Keywords: surface plasmons, metasurfaces, geometric phases, plasmonic vortices, beam deflectors

INTRODUCTION

Surface plasmons (SPs) are bound electromagnetic waves that propagate along the metal-dielectric interface and decay exponentially in the direction perpendicular to the interface [1]. They promise unique applications ranging from sub-wavelength lasing, biological sensing, near-field imaging, holography, and sensing, to plasmonic circuitry [2–12]. It is worth noting that an on-chip plasmonic device, which is much smaller than similar products in free space, has attracted widespread attention [13, 14]. Although it is challenging to control the wavefront of SPs, this is necessary in order to enable various functional SP devices [15]. Investigations into SPs initially focused on far-infrared and visible frequencies, and were then extended to terahertz and microwave regimes. In the early years, prisms, periodic ripples, and topological defects were the most common methods of emitting SWs. However, prism coupling requires a large volume, which is impractical for integration into a compact micro-SW device. There is a growing demand for simplifying the design and manufacture of integrated plasma devices, and thus for plasma technology research, and so exploring new methods for manipulating SPs during launch has become an intriguing research topic.

A metasurface [16, 17] is a two-dimensional (2D) metamaterial [18–20], which has excellent maneuver ability when forming the wavefront of the outgoing electromagnetic wave. The key feature of the metasurface platform is the ability to construct a local abrupt phase [21–24], amplitude [25, 26], and polarization [27–31]. Metasurfaces are also applicable to the field of SPs, and SP couplers [32–35], SP wavefront control, and SP holography [36–38] have been implemented. In addition, the terahertz (THz) range of the electromagnetic spectrum contains absorption lines of various rotating

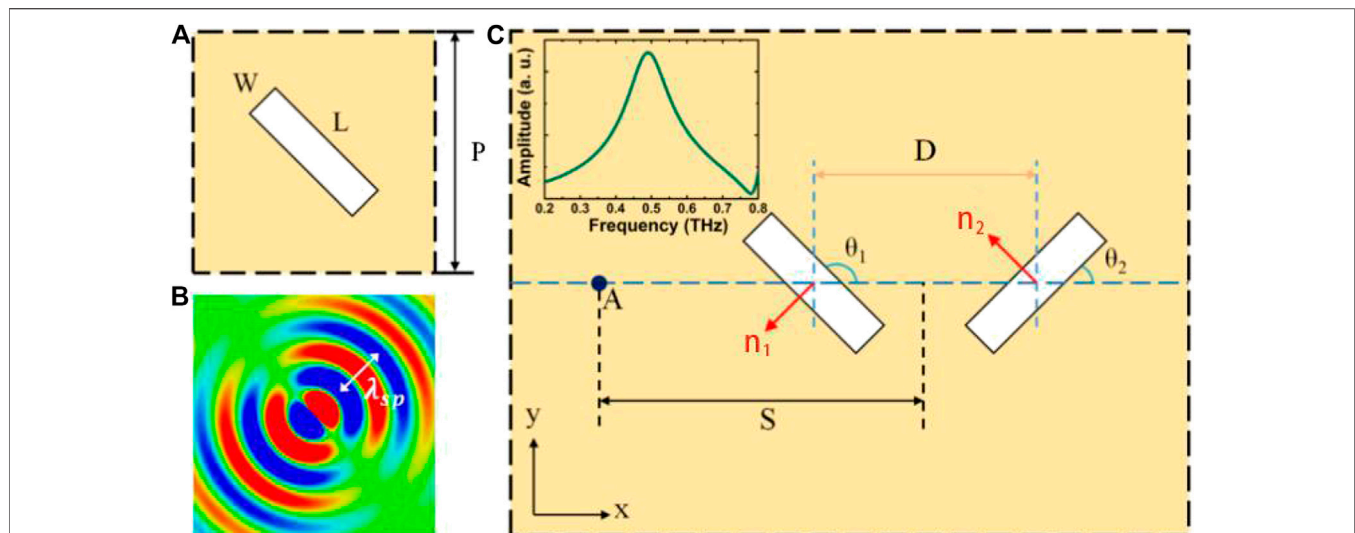


FIGURE 1 | (A) The unit cell schematic of the proposed metasurface. The geometric parameters of the microslit were $L = 200 \mu\text{m}$, $W = 50 \mu\text{m}$, and $p = 300 \mu\text{m}$. **(B)** The simulated SP radiation pattern was excited by a narrow sub-wavelength microslit on the aluminum film under the incidence of a normal plane wave. **(C)** A schematic diagram of a pair of microslit resonators. They were used to derive the SP emission field at point A at a distance S from the center of the pair of microslits. D is the distance between the centers of the microslits.

and vibrating molecules, so it has attracted attention as a fingerprint region for many spectroscopy and sensing applications. Metasurfaces designed with appropriate sub-wavelength sub-atoms and arranged in a prescribed spatial distribution have become an ideal tool for the fine control of SPs. In particular, the sub-wavelength metal slot resonator is one of the most commonly used unit elements when designing metasurfaces for SP manipulation. Metasurfaces composed of metal slits have excellent flexibility, and the wavefront of the coupled SP can be controlled arbitrarily, using iterative algorithms [39], holographic principles [40], Pancharatnam-Berry phase (PB phase) concepts [33], or coupled mode theory [41]. They can pave the way for future research if the SPs can be controlled in the THz regime.

In the 1990s, it was found that phase vortex beams by Allen et al. [42], which have a phase term that can be described by $\exp(-il\theta)$, have an orbital angular momentum of light (OAM) of $l\hbar$ per photon, where l is the topological charge, θ is the azimuthal angle, and \hbar is Planck's constant h divided by 2π . OAM is the angular momentum component of the beam, which depends on the spatial distribution of the light field. Unlike the spin angular momentum (SAM) associated with the spin of a photon, OAM is infinite, so more degrees of freedom can be used. Similar to optical vortices, SPs with orbital angular momentum are defined as SVs. The SPs propagate along the interface.

In this article, we used the commercial electromagnetic software CST to demonstrate the manipulation of SPs, emitted by metasurfaces composed of metallic microslits. Phase control is achieved by interference between a pair of slits on the metal surface. The spatial spacing and direction of the paired microslits can be adjusted to give almost any phase distribution, thereby

allowing abnormal SP emission. The proposed metasurface can match the momentum difference between free-space light and SPs, can be used as an effective SP element coupler, and can also support the propagation of coupled SPs, showing higher efficiency in a large excitation range. This is because evanescent waves such as ordinary SPP will quickly dampen or decay, but metamaterials are a good medium that can greatly improve its efficiency. More importantly, the phase of the coupled SP can be continuously controlled by carefully changing the rotation angle of the microslits, which can provide great flexibility in the manipulation of SP emissions. Furthermore, for verifying the demonstration, we proposed a PV generator which consists of spatially varying microslits arranged in a ring carved in aluminum film. In this way, the PV generator can generate any combination of spin-dependent OAMs for the SP on the metal/dielectric interface. The proposed methodology illustrates the powerful function of combining the Pancharatnam-Berry phase with the complex SP startup, and it may provide a novel method for designing various SP devices.

EXPERIMENT, RESULTS, AND DISCUSSION

As shown in **Figure 1A**, the sub-wavelength metallic microslit structure was highly effective due to its ability to confine electric fields. This function is very different from the well-known bar structure, which can be explained by Babinet's principle. The unit cell had a length of $L = 200 \mu\text{m}$, a width of $W = 50 \mu\text{m}$, and a unit cell length of $p = 300 \mu\text{m}$. The metallic microslit was made on a 200 nm thick aluminum film on a modified polyimide (MPI) substrate. **Figure 1B** shows the SP radiation pattern (E_z

component) of the microslit design, which acts as an in-plane magnetic dipole with a resonance wavelength of λ_{sp} . In order to prove the correctness of the design strategy, the CST Microwave Studio basic finite integration technique was used to simulate the field distribution of SPs. The SP propagating along the metal surface is usually referred to as surface plasmon polarons under visible light and infrared. However, at the THz frequency, an SP is called a Zenneck terahertz surface wave (ZTSW). Its field strength is not tightly bound to the metal surface, and the resonance wavelength of λ_{ZTSW} is almost equal to the vacuum wavelength of λ_0 [43, 44]. This can be attributed to the fact that at terahertz frequencies metals behave as perfect electrical conductors and do not allow waves to penetrate. In the simulations, the slit pairs were carved on a 200 nm thick aluminum layer ($\sigma = 3.72e7$ S/m) which was deposited on a 50 μ m thick MPI substrate with a relative permittivity of $\epsilon' = 3.1$ and a loss tangent of $\delta = 0.006$ at 1.0 THz.

The coupling of the microslit pair, as shown in **Figure 1C**, is excited by the plane wave and the electric field $\vec{E}_{in} = (E_x, E_y)$ at normal incidence, so the field at point A ($S \geq D/2$) is the superposition of the SP field in the two microslits [45]:

$$\vec{E}_A = I \text{sign}(S) \left[\left(\vec{E}_1 \cdot \hat{e}_x \right) e^{ik_{sp}|S+\frac{D}{2}|} + \left(\vec{E}_2 \cdot \hat{e}_x \right) e^{ik_{sp}|S-\frac{D}{2}|} \right] \hat{a} \quad (1)$$

where I represents the field amplitude of SP; $\vec{E}_1 = (\vec{E}_{in}, \hat{n}_1)\hat{n}_1$ and $\vec{E}_2 = (\vec{E}_{in}, \hat{n}_2)\hat{n}_2$ are incident polarization components along \hat{n}_1 and \hat{n}_2 , where $\hat{n}_1 = (\cos\theta_1, \sin\theta_1)$ and $\hat{n}_2 = (\cos\theta_2, \sin\theta_2)$ are unit vectors perpendicular to the two microslits respectively; θ_1 and θ_2 represent the angles of \vec{E}_1 and \vec{E}_2 with respect to the x -axis, respectively, while $\theta_2 - \theta_1 = 90^\circ$; \hat{e}_x is the unit vector in the positive x direction; $k_{sp} = 2\pi/\lambda_{sp}$ is the SP wave number; \hat{a} is the unit vector given by $-[-ik_z, 0, k_{sp}\text{sign}(S)]/\sqrt{|k_z|^2 + |k_{sp}|^2}$, where $k_z = \sqrt{k_0^2 - k_{sp}^2}$ is the vacuum wave number and k_0 is the vacuum wave number. If the incident wave is circularly polarized by $(E_x, E_y) = \sqrt{2}/2(1, \sigma i)$, where $\sigma \in \{+, -\}$ represents left-hand circular polarization (LCP) and right-hand circular polarization (RCP), respectively, and if it represents $k_{sp}D = \pi$, then **Eq. (1)** can be simplified to

$$\vec{E}_A = i\sqrt{2}/2I \text{sign}(S) e^{ik_{sp}S} e^{i2\sigma\theta_1} \hat{a} \quad (2)$$

It can be easily obtained from **Eq. (2)** that the amplitude of the SP field at A is fixed, while the phase is freely controllable with a sign determined by the circular-polarization handedness and shift by the orientation angle. This shows that circular polarization can be used to switch the sign of the phase, thereby controlling the shape of the SP wavefront while maintaining the SP amplitude constant. In addition, a nearly arbitrary phase profile could be achieved even using a single straight column of microslit resonators because the phase shift enables the cover of whole 2π range. Simultaneously, as shown in the inset of **Figure 1C**, the simulated amplitude of E_z reaches the maximum value under the designed geometry.

From the generalized Snell law, the SP coupling can be realized through constructing the phase of the microslits to satisfy $\frac{d\varphi}{dx} = k_{sp}$. In this way, each row of microslits satisfying the

coupling phase condition $\frac{d\varphi}{dx} = k_{sp}$ can be regarded as the source of the secondary output SP. However, although the output SPs are in phase with each other and together produce a normal wavefront, they can be transmitted in only the x direction. In this case, the introduction of the phase gradient along the y direction $\frac{d\varphi}{dy}$ is a non-negligible factor in achieving the arbitrary modulation of launching SPs. The Pancharatnam-Berry phase enables the accurate control of the phase of the electromagnetic wave due to the double relationship between the angle of geometric rotation and the angle of the output SPs. As shown in **Figure 2A**, the phase of the proposed microslit structure can cover the entire 2π range by rotating the angle between the microslits. At the same time, the amplitude of the wave is close to 50%. Based on this, the spatial distribution of the phase discontinuity at the interface between the two media can be freely constructed, where the abnormal refraction angle can be expressed as $\theta_t = \arcsin\left(\frac{1}{k_0} \frac{d\varphi}{dy}\right)$.

To demonstrate the proposed scheme, we numerically demonstrated three types of metasurface with different phase gradients in the y direction. **Figures 2B,E** show different SP launches when the incident THz waves are LCP and RCP, respectively. The angle shift between two adjacent microslits is 22.5° in the y direction, which means that the metasurface can complete the shape of the wavefront within 8 unit cells. The anomalous angle of SP launch can be calculated easily as $\theta_t = 7.2^\circ$. Increasing the phase shift between adjacent microslits will increase the anomalous angle of SP launch and so achieve 2π modulation at a shorter distance. The angle shift between the two adjacent microslits was increased to 45° and 90° , and the anomalous angles of SP launch became $\theta_t = 14.6^\circ$ and $\theta_t = 30.3^\circ$, respectively. The simulated corresponding real part of the E_z -field distributions is shown in **Figures 2C,D,F,G**. It can be seen that the sign of the anomalous refracted angle was reversed due to the different chirality of incidence. In simple terms, manipulation of the SP launch was realized by precisely designing the phase shift between the adjacent microslits in the y direction.

The reason SP launching can be accurately and continuously manipulated is the proper relationship between adjacent microslit structures. And the distance D between the adjacent microslits played a vital role in achieving the launch of high efficiency SPs. The calculated field distributions at distance D of 200–400 μ m, with a step of 50 μ m, while keeping $\theta_2 - \theta_1 = 90^\circ$ under LCP incidence at 0.496 THz, is shown in **Figure 3**. The mismatch spacing significantly affected the coupling between the microslits, which prevented the wavefront of SPs from being modulated effectively. It can be seen that the field distribution changed dramatically with varying D , which shows that the SP launch was sensitive to the spacing of the microslits. The rugged wavefronts at $D \neq 302 \mu$ m indicate that an additional SP launching order occurs. There is no doubt that similar results will also be found under RCP incidence. It is worth noting that, as D gets larger, the overall area of simulation needs to grow, in order to ensure that the number of structures is consistent.

To verify the controllability of launching SPs, a configuration was set up for generating a phase distribution by changing the

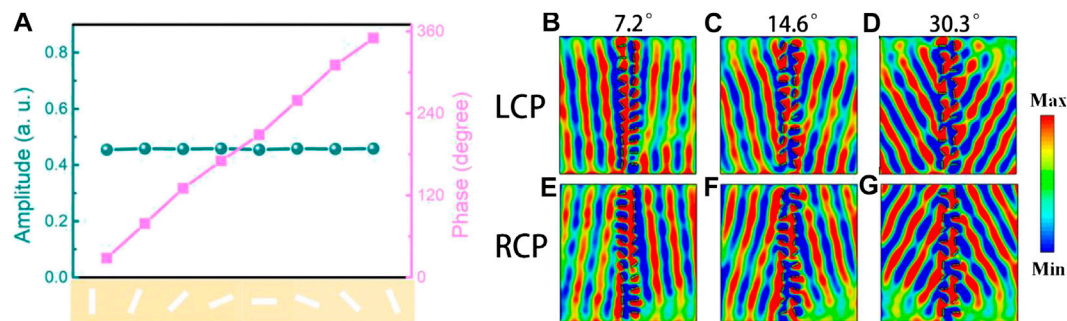


FIGURE 2 | Simulated E_z -field distributions of the ZTSW from a linear-phase-profile structure under normal incidences of LCP with a (B) 7.2°, (C) 14.6°, and (D) 30.3° deflected angle. The corresponding E_z -field distributions of the ZTSW under normal incidences of RCP with a (E) 7.2°, (F) 14.6°, and (G) 30.3° deflected angle while the geometry and rotation of the microslits were fixed. (G) Simulated amplitude and phase shift of microslits shown at 0.49 THz.

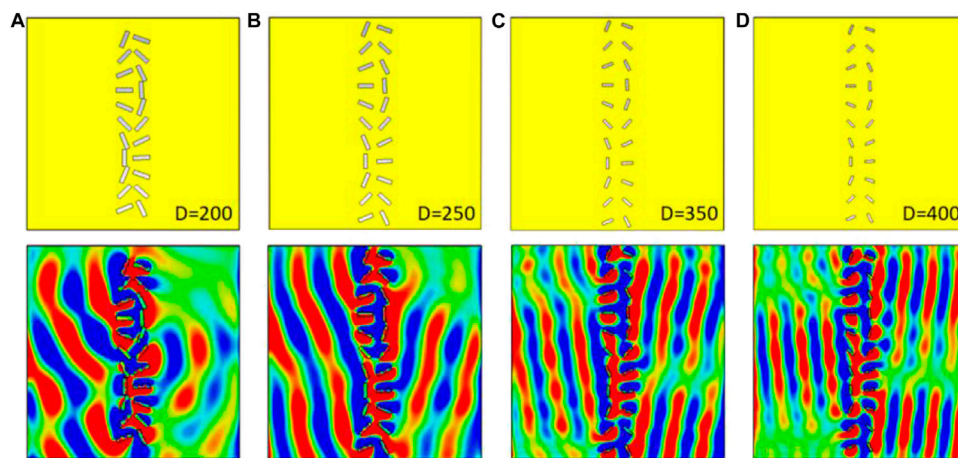


FIGURE 3 | Calculated E_z -field distributions of ZTSW under normal incidence of LCP at 0.496 THz with a distance D of (A) 200 μm , (B) 250 μm , (C) 350 μm , and (D) 400 μm . The top panel is a schematic of the structures.

orientation angle of each microslit (Figure 4). First, the microslits were distributed uniformly around a circle. Their orientation angles θ_1 were changed by $n\pi$ ($n = 0, \pm 1, \pm 2 \dots$) clockwise around the circumference. The orientation of θ_2 can be easily obtained due to the fixed difference between the θ_1 and θ_2 . More importantly, the SP launched by each microslit had a different initial rotation, which was dependent on its orientation angle θ_i . We observed the distributions of the E_z -fields. The overall phase shift of SPs propagating toward the center across a whole turn equals to $2(n-1)\sigma\pi$, which can be acknowledged by observing the relationship between the number of the topological charges carried by structures and the arrangement of the microslits. It can be understood as the contribution of two parts: one is the phase shift caused by the change in the orientation angle, which can be represented by $2n\sigma\pi$. The other is the phase shift associated with the reverse mode, given by $-2\sigma\pi$. Obviously, the latter is caused by a fixed change in the azimuth of the antenna position, which is completely

independent of l . In this way, the topological charges of the PVs can be expressed as $l = \sigma(n-1)$, which can be flexibly modulated by varying n .

Figures 4A,B show the phase distribution of the E_z -field for LCP and RCP, respectively. The phase distribution in the center of the structure clearly shows that the topological charge is 0 because there is no spiral phase. The structure also shows no difference between the responses to LCP and RCP incidence. However, Figures 4C,D show a clear difference in response to LCP and RCP. Figures 4C,D illustrate the corresponding simulated SP field distributions, where the phase evolution along the intensity distribution of the “doughnut” is equal to 2π , corresponding to a topological charge of 1 plasmon vortex. The direction of the phase change is closely related to the polarization of the incident wave. It is important to note that the direction of the SV phase change was reversed when the sign of the incidence changed. Figures 4E–J show the distributions of the E_z -field with different topological charges carried by PVs. It can be seen that the

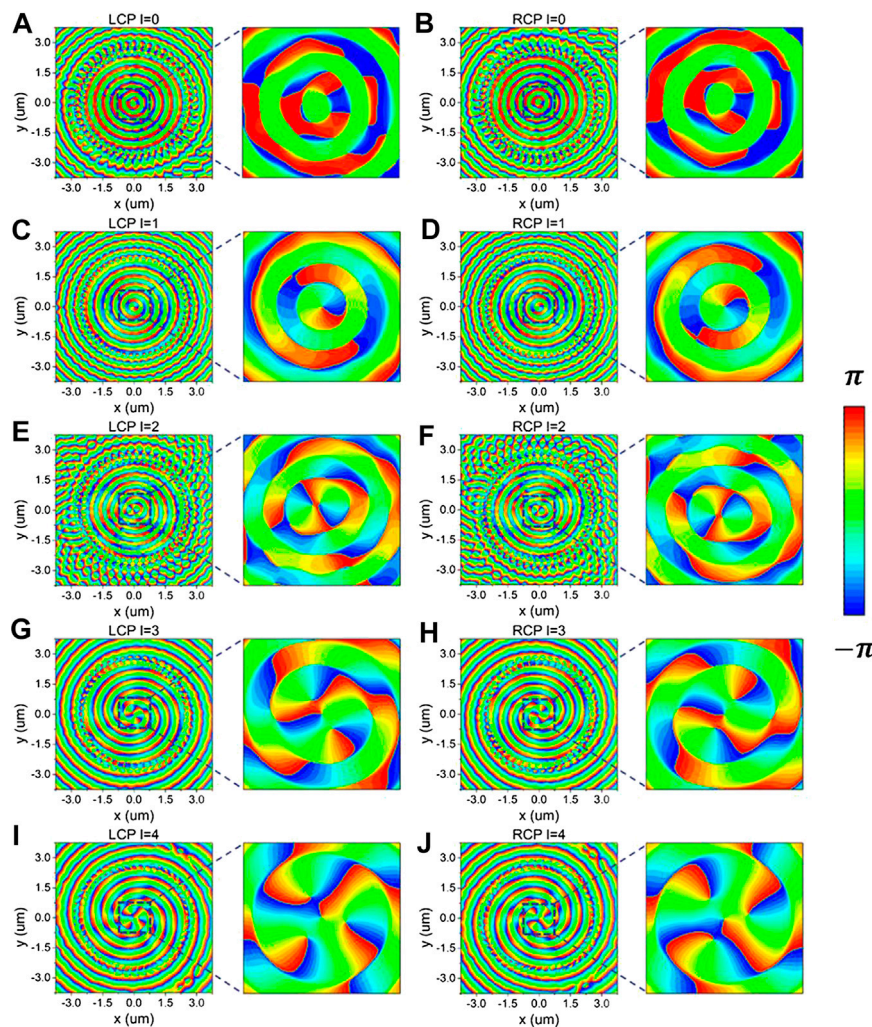


FIGURE 4 | When the incident is LCP, the E_z -field phase distribution on the PV generator is calculated and the topological charges are 0 (A), 1 (C), 2 (E), 3 (G), and 4 (I), respectively. And the E_z -field phase distribution of the PV generator are shown in (B), (D), (F), (H), and (J) when the incident is RCP.

direction of the phase change was unchanged with the increase of the topological charges under the same polarized incidence. Although the vertices of phase were not connected when the topological charge n was greater than 2, it can be seen clearly that the phase had occurred during the change of $2n\pi$. Therefore, the proposed structures were able to effect multi-channel information communication by varying the parameter n .

CONCLUSION

In conclusion, anomalous launching and PV generators of SPs are theoretically demonstrated in a THz near-field metasurface platform by geometric phase. It should be noted that the

diameter of the sub-wavelength metal microslit was less than $\lambda/2 \sim \lambda/3$. Through the simple arrangement of the microslits, arbitrary phase distribution could be realized under any excitation mode. In addition, compared with conventional SP launching manipulation with phase discontinuities, the structure we proposed enabled continuous phase change. A PV with a topological charge of $1 \setminus 2 \setminus 3 \setminus 4$ was discussed, and the design scheme could be applied to PV with any charge only by introducing the geometric phase. These findings illustrate the importance of phase control in the SP launch process, which suggests promising THz imaging and sensing applications. Combining the SPs activated by the metasurface can open a gateway to electrically reconfigurable applications, including capturing particles and communicating on-chip information.

EXPERIMENTAL SECTION

Simulations were carried out by using the commercially available software package CST Microwave Studio. An open boundary condition was applied to the x and z directions to prevent reflections from the boundaries. For the deflector structure, a periodic boundary condition was used on the y direction with a $3,500\text{ um} \times 3,500\text{ um}$ simulation area, but as the distance D changed, the simulation range changed accordingly; while for the OAM generator structure, an open boundary condition was applied to the y direction with a $6,500\text{ um} \times 6,500\text{ um}$ simulation area. A normally incident circularly-polarized plane wave at 0.49 THz excited ZTSW on the substrate side and field distribution was observed from the air side.

REFERENCES

- Barnes WL, Dereux A, Ebbesen TW. Surface plasmon subwavelength optics. *Nature*. (2003) 424:824–30. doi:10.1038/nature01937
- Nie S, Emory SR. Probing single molecules and single nanoparticles by surface-enhanced Raman scattering. *Science*. (1997) 275:1102–6. doi:10.1126/science.275.5303.1102
- Oulton RF, Sorger VJ, Zentgraf T, Ma RM, Gladden C, Dai L, et al. Plasmon lasers at deep subwavelength scale. *Nature*. (2009) 461:629–32. doi:10.1038/nature08364
- Berini P, Leon ID. Nat. Surface plasmon-polariton amplifiers and lasers. *Nat Photon*. (2011) 6:16–24. doi:10.1038/nphoton.2011.285
- Ebbesen TW, Genet C, Bozhevolnyi SI. Surface-plasmon circuitry. *Phys Today*. (2008) 61:44. doi:10.1063/1.2930735
- Sorger VJ, Oulton RF, Ma R, Zhang X. Toward integrated plasmonic circuits. *MRS Bull*. (2012) 37:728. doi:10.1557/mrs.2012.170
- Liu J, Gao Y, Ran L, Guo K, Lu Z, Liu S. Focusing surface plasmon and constructing central symmetry of focal field with linearly polarized light. *Appl Phys Lett*. (2015) 106:013116. doi:10.1063/1.4905307
- Xu Y, Zhang X, Tian Z, Gu J, Ouyang C, Li Y, et al. Mapping the near-field propagation of surface plasmons on terahertz metasurfaces. *Appl Phys Lett*. (2015) 107:021105. doi:10.1063/1.4926967
- Xu Q, Zhang X, Xu Y, Ouyang C, Tian Z, Gu J, et al. Polarization-controlled surface plasmon holography. *Laser Photon Rev*. (2016) 11:1600212. doi:10.1002/lpor.201600212
- Xu Q, Zhang X, Xu Y, Li Q, Li Y, Ouyang C, et al. Plasmonic metalens based on coupled resonators for focusing of surface plasmons. *Sci Rep*. (2016) 6:37861. doi:10.1038/srep37861
- Yashunsky V, Lirtsman V, Zilbershtein A, Bein A, Schwartz B, Aroeti B, et al. Surface plasmon-based infrared spectroscopy for cell biosensing. *J Biomed Opt*. (2012) 17:081409. doi:10.1117/1.JBO.17.8.081409
- Tan Q, Guo Q, Liu H, Huang X, Zhang S. Controlling the plasmonic orbital angular momentum by combining the geometric and dynamic phases. *Nanoscale*. (2017) 9:4944–4949. doi:10.1039/c7nr00124j
- Gao Y, Gan Q, Xin Z, Cheng X, Bartoli FJ. Plasmonic mach-zehnder interferometer for ultrasensitive on-chip biosensing. *ACS Nano*. (2011) 5:9836–44. doi:10.1021/nn2034204
- Liu Y, Palomba S, Park Y, Zentgraf T, Yin X, Zhang X. Compact magnetic antennas for directional excitation of surface plasmons. *Nano Lett*. (2012) 12:4853–8. doi:10.1021/nl302339z
- Epstein I, Tsur Y, Arie A. Surface-plasmon wavefront and spectral shaping by near-field holography. *Laser Photon Rev*. (2016) 10:360. doi:10.1002/lpor.201500242
- Yu N, Capasso F. Flat optics with designer metasurfaces. *Nat Mater*. (2014) 13:139. doi:10.1038/nmat3839
- Chen HT, Taylor AJ, Yu N. A review of metasurfaces: physics and applications. *Rep Prog Phys*. (2016) 79:076401. doi:10.1088/0034-4885/79/7/076401

DATA AVAILABILITY STATEMENT

The original contributions presented in the study are included in the article/Supplementary Material, further inquiries can be directed to the corresponding authors.

AUTHOR CONTRIBUTIONS

SW proposed the idea; PW, SH, CZ, and MH conducted pattern designs and numerical simulations; PW, SH, and YX fabricated the sample; PW performed the measurements; and SH and PW prepared the manuscript. XL and MX and MH supervised the overall projects. SW, PW, and SH analysed the data and discussed the results.

- Smith DR, Pendry JB, Wiltshire MC. Metamaterials and negative refractive index. *Science*. (2004) 305:788–92. doi:10.1126/science.1096796
- Shalaev VM. Optical negative-index metamaterials. *Nat Photon*. (2007) 1:41. doi:10.1364/META.2006.TuC3
- Soukoulis CM, Wegener M. Past achievements and future challenges in the development of three-dimensional photonic metamaterials. *Nat Photon*. (2011) 5:523. doi:10.1038/nphoton.2011.154
- Yu N, Genevet P, Kats MA, Aieta F, Tetienne JP, Capasso F, et al. Light propagation with phase discontinuities: generalized laws of reflection and refraction. *Science*. (2011) 334:333–7. doi:10.1126/science.1210713
- Ni X, Emani NK, Kildishev AV, Boltasseva A, Shalaev VM. Broadband light bending with plasmonic nanoantennas. *Science*. (2012) 335:427. doi:10.1126/science.1214686
- Zhang X, Tian Z, Yue W, Gu J, Zhang S, Han J, et al. Broadband terahertz wave deflection based on C-shape complex metamaterials with phase discontinuities. *Adv Mater Weinheim*. (2013) 25:4567–72. doi:10.1002/adma.201204850
- Zhang X, Zhu Y, Mao C, Xu W, Ding H, Xie J, et al. Manipulating terahertz plasmonic vortex based on geometric and dynamic phase. *Advanced Optical Materials*. (2018) 1801328. doi:10.1002/adom.201801328
- Liu L, Zhang X, Kenney M, Su X, Xu N, Ouyang C, et al. Broadband metasurfaces with simultaneous control of phase and amplitude. *Adv Mater Weinheim*. (2014) 26:5031–6. doi:10.1002/adma.201401484
- Kim M, Wong AMH, Eleftheriades GV. Optical Huygens' metasurfaces with independent control of the magnitude and phase of the local reflection coefficients. *Phys. Rev. X*. (2014) 4:041042. doi:10.1103/PhysRevX.4.041042
- Yu N, Aieta F, Genevet P, Kats MA, Gaburro Z, Capasso F. A broadband, background-free quarter-wave plate based on plasmonic metasurfaces. *Nano Lett*. (2012) 12:6328–33. doi:10.1021/nl303445u
- Cong L, Xu N, Han J, Zhang W, Singh R. A tunable dispersion-free terahertz metadvice with Pancharatnam-Berry-phase-enabled modulation and polarization control. *Adv Mater Weinheim*. (2015) 27:6630–6. doi:10.1002/adma.201502716
- Cong L, XuZhang W, Singh R. Polarization control in terahertz metasurfaces with the lowest order rotational symmetry. *Adv. Opt. Mater*. (2015) 3:1176. doi:10.1002/adom.201500100
- Cong L, Srivastava YK, Singh R. Inter and intra-metamolecular interaction enabled broadband high-efficiency polarization control in metasurfaces. *Appl Phys Lett*. (2016) 108:011110. doi:10.1063/1.4939564
- Wu PC, Tsai WY, Chen WT, Huang YW, Chen TY, Chen JW, et al. Versatile polarization generation with an aluminum plasmonic metasurface. *Nano Lett*. (2017) 17:445–452. doi:10.1021/acs.nanolett.6b04446
- Sun S, He Q, Xiao S, Xu Q, Li X, Zhou L. Gradient-index meta-surfaces as a bridge linking propagating waves and surface waves. *Nat Mater*. (2012) 11:426–31. doi:10.1038/nmat3292
- Lin J, Mueller JP, Wang Q, Yuan G, Antoniou N, Yuan XC, et al. Polarization-controlled tunable directional coupling of surface plasmon polaritons. *Science*. (2013) 340:331–4. doi:10.1126/science.1233746
- Huang L, Chen X, Bai B, Tan Q, Jin G, Zentgraf T, et al. Helicity dependent directional surface plasmon polariton excitation using a metasurface with

- interfacial phase discontinuity. *Light Sci. Appl.* (2013) 2:e70. doi:10.1038/lsa.2013.26
35. Pors A, Nielsen MG, Bernardin T, Weeber J-C, Bozhevolnyi SI. Efficient unidirectional polarization-controlled excitation of surface plasmon polaritons. *Light Sci Appl.* (2014) 3:e197. doi:10.1038/lsa.2014.78
 36. Spektor G, David A, Gjonaj B, Bartal G, Orenstein M. Metafocusing by a metaspiral plasmonic lens. *Nano Lett.* (2015) 15:5739–43. doi:10.1021/acs.nanolett.5b01571
 37. Genevet P, Wintz D, Ambrosio A, She A, Blanchard R, Capasso F. Controlled steering of Cherenkov surface plasmon wakes with a one-dimensional metamaterial. *Nat Nanotechnol.* (2015) 10:804–9. doi:10.1038/nnano.2015.137
 38. Xiao S, Zhong F, Liu H, Zhu S, Li J. Flexible coherent control of plasmonic spin-Hall effect. *Nat Commun.* (2015) 6:8360. doi:10.1038/ncomms9360
 39. Tanemura T, Balram KC, Ly-Gagnon DS, Wahl P, White JS, Brongersma ML, Miller DA, et al. Multiple-wavelength focusing of surface plasmons with a nonperiodic nanoslit coupler. *Nano Lett.* (2011) 11:2693–8. doi:10.1021/nl200938h
 40. Wintz D, Genevet P, Ambrosio A, Woolf A, Capasso F. Holographic metalens for switchable focusing of surface plasmons. *Nano Lett.* (2015) 15:3585–9. doi:10.1021/acs.nanolett.5b01076
 41. Zhang X, Xu Q, Li Q, Xu Y, Gu J, Tian Z, et al. Asymmetric excitation of surface plasmons by dark mode coupling. *Sci. Adv.* (2016) 2:e1501142. doi:10.1126/sciadv.1501142
 42. Allen L, Beijersbergen MW, Spreeuw RJ, Woerdman JP. Orbital angular momentum of light and the transformation of Laguerre-Gaussian laser modes. *Phys. Rev. A.* (1992) 45:8185–8189. doi:10.1103/physreva.45.8185
 43. Jeon T, Grischkowsky D. THz Zenneck surface wave (THz surface plasmon) propagation on a metal sheet. *Appl. Phys. Lett.* (2006) 88:061113. doi:10.1063/1.2171488
 44. Gong M, Jeon TI, Grischkowsky D. THz surface wave collapse on coated metal surfaces. *Opt. Express.* (2009) 17:17088–101. doi:10.1364/OE.17.017088
 45. Zhang X, Xu Y, Yue W, Tian Z, Gu J, Li Y, et al. Anomalous surface wave launching by handedness phase control. *Adv. Mater. Weinheim.* (2015) 27: 7123–9. doi:10.1002/adma.201502008

Conflict of Interest: The authors declare that the research was conducted in the absence of any commercial or financial relationships that could be construed as a potential conflict of interest.

Copyright © 2021 Hu, Wang, Zhou, Hu, Xiong, Xu, Li, Xu and Wang. This is an open-access article distributed under the terms of the Creative Commons Attribution License (CC BY). The use, distribution or reproduction in other forums is permitted, provided the original author(s) and the copyright owner(s) are credited and that the original publication in this journal is cited, in accordance with accepted academic practice. No use, distribution or reproduction is permitted which does not comply with these terms.



Magnetically Tunable Graphene-Based Terahertz Metasurface

Yafeng Lu^{1,2}, Chen Wang¹, Shiqiang Zhao¹ and Yongzheng Wen^{1*}

¹State Key Laboratory of New Ceramics and Fine Processing, School of Materials Science and Engineering, Tsinghua University, Beijing, China, ²Army Aviation Institute of PLA, Beijing, China

Graphene is a promising platform for configurable terahertz (THz) devices due to its reconfigurability, but most researches focus on its electrical tunability. Here, we propose a graphene-based THz metasurface comprised of graphene cut-wire arrays for magnetic manipulation of the THz wave. With the external magnetostatic field applied, the resonant currents of the graphene cut-wire can be effectively affected by the Lorentz force, leading to an evident tuning of the response of the metasurface. The simulated results fully demonstrate that the resonance frequencies of the graphene THz metasurface can be efficiently modulated under a vertical magnetostatic field bias, resulting in the manipulation of the transmittance and phase of the THz wave. As a new method of the tunable THz metasurface, our structure shows promising applications in the THz regime, including the ultracompact THz modulators and magnetic field sensors.

OPEN ACCESS

Edited by:

Fuli Zhang,
Northwestern Polytechnical
University, China

Reviewed by:

Weiren Zhu,
Shanghai Jiao Tong University, China
Xiaojun Wu,
Beihang University, China

*Correspondence:

Yongzheng Wen
wenyongzheng@tsinghua.edu.cn

Specialty section:

This article was submitted to
Optics and Photonics,
a section of the journal
Frontiers in Physics

Received: 29 October 2020

Accepted: 22 December 2020

Published: 25 January 2021

Citation:

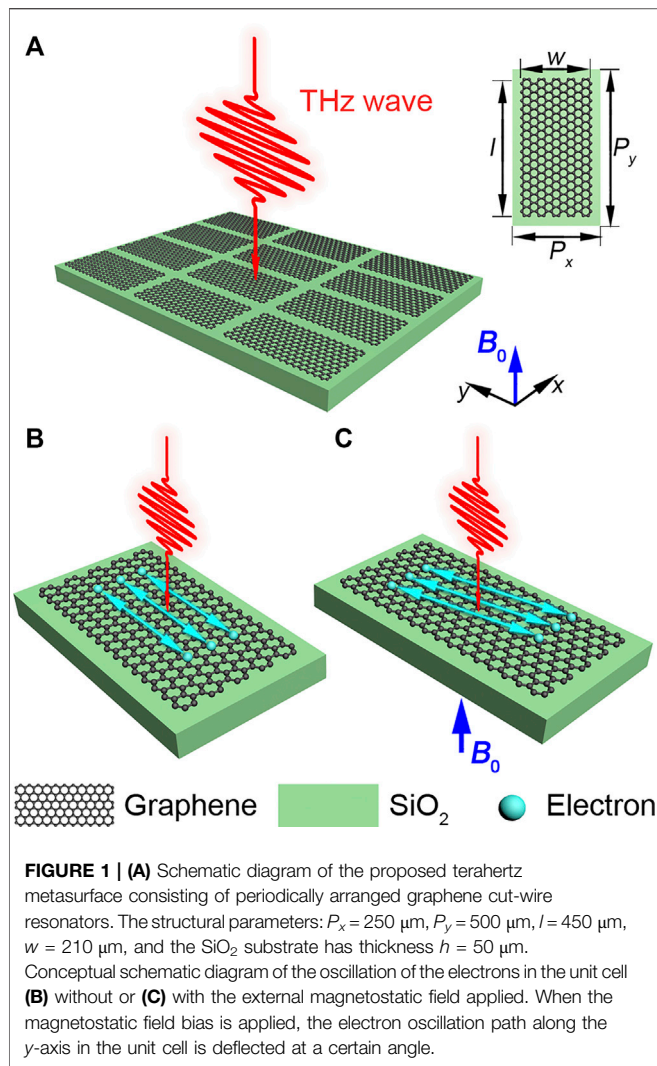
Lu Y, Wang C, Zhao S and Wen Y
(2021) Magnetically Tunable
Graphene-Based
Terahertz Metasurface.
Front. Phys. 8:622839.
doi: 10.3389/fphy.2020.622839

Keywords: graphene, magnetostatic field, dynamically tunable, terahertz metasurface, Lorentz force

INTRODUCTION

The terahertz (THz) band lies in the frequency gap between the infrared and microwaves and possesses the characteristics of both photonics and electronics [1], making the THz wave of great perspective in material characterization [2], biomedical sciences [3], and wireless communication [4–7]. In the development of THz technology, effective manipulation of THz waves is particularly important, which still remains challenging in practical application. The emergence of metamaterial provides an approach to surmount this dilemma. Metamaterials are composed of periodic or aperiodic subwavelength scale artificial unit structures, exhibiting extraordinary electromagnetic properties [8–12]. The electromagnetic response of the incident waves can be flexibly customized to satisfy the application needs [13]. As a two-dimensional metamaterial, metasurfaces have been widely applied in THz modulators, switchers, phase shifters, and sensors [14–17] due to their advantages of ultrathin and easy to implement.

Early studies on the THz metasurface mainly rely on changing the structural parameters to meet the required electromagnetic characteristics. Although excellent functions can be achieved, once the devices are prepared, their electromagnetic response characteristics are fixed and cannot be tuned, which limits the practical applications of metasurfaces. The tunable THz metasurface can simplify device design [17], and can effectively reduce cost [17], and make it multifunctional. On the other hand, graphene has the intriguing properties of high mobility, strong light-matter interaction, and excellent chemical stability [18]. Although there are still many challenges, graphene with ultra-high mobility and ultra-thin thickness may produce transistors with higher speed and shorter channel length [19], which might have the potential to replace conventional silicon-based semiconductors as the next generation of mainstream semiconductor materials. Some recent work has demonstrated



that graphene can be utilized to realize tunable THz metasurface by changing the Fermi level by electrical bias [20–24]. Besides that, the unique responses of graphene to the light, heat, and force also allow one to actively tune the metasurface with various physical fields [23, 25, 26]. Using this feature, many active tunable graphene devices with excellent performance have been designed and verified by simulation [27–29] or/and experiments [30, 31]. These results indicate that the graphene platform can play an important role in the design of actively tunable THz metasurfaces. Among them, however, the modulation characteristics of the graphene metasurface by the magnetostatic field seems less investigated. It is a well-known fact that when a magnetostatic field is applied in the vertical direction of a two-dimensional conductor, the carrier's motion in which will be deflected due to the Lorentz force [32]. We postulate that when the magnetostatic field is applied perpendicularly to a patterned graphene metasurface, the resonance properties of which under the irradiation of THz waves would be apparently modulated due to the deflection of the direction of the carrier's oscillation in graphene.

In this work, we suggest a magneto-controlled method to manipulate the transmittance properties of the incident THz wave, and proposed a graphene-based THz metasurface comprised of graphene cut-wire arrays for proof-of-principle demonstration. By applying different values of magnetic flux density, the transmittance related parameters of the proposed metasurface can be dynamically controlled. We show that the transmittance properties of graphene THz metasurface can be dynamically controlled by applying an external magnetostatic field perpendicular to the metasurface.

STRUCTURE DESIGN AND PHYSICAL MECHANISM

Figure 1A shows the schematic diagram of the proposed tunable graphene metasurface on top of a SiO_2 substrate. The graphene pattern, cut-wire resonators, are periodically arranged in the x - y plane and the structural parameters are denoted. The proposed graphene metasurface is excited by the electric field of a normally incident THz plane wave propagating in the z -axis direction.

When electromagnetic waves irradiate perpendicularly to planar graphene, plasmonic oscillation will occur on the surface of the graphene, and the direction of carrier oscillation is along the electric field, as shown in **Figure 1B**. In this case, if the magnetostatic field is applied vertically to the planar graphene, the oscillation direction of the carriers will no longer follow the direction of the electric field and would be deflected at a certain angle, as shown in **Figure 1C**. The angle is related to the value of the applied magnetic flux density. If the graphene layer is patterned, different angle corresponds to different oscillation environments, the changes of carriers' oscillation will lead to the changes of transmittance properties and result in the resonance frequency shifts and the transmittance shifts.

As a two-dimensional (2D) material, graphene can be described by surface conductivity. In our case, the photonic energy of the terahertz frequency is far below the double Fermi level of graphene, and only the intra-band conductivity of graphene is considered, which can be described as [33]:

$$\sigma_s(\omega) = \frac{i \cdot e^2 k_B T}{\pi \hbar^2 (\omega + i\tau^{-1})} \ln \left[2 \cosh \left(\frac{E_F}{2k_B T} \right) \right], \quad (1)$$

where e is the electron charge, k_B is the Boltzmann's constant, T is the environmental temperature, \hbar is the reduced Planck's constant, and ω is the angular frequency of incident THz, τ is the relaxation time, E_F is the Fermi energy away from the Dirac point. To achieve the evident resonance of the metamaterial, the Fermi level of the graphene should satisfy $E_F \gg k_B T$, the graphene surface conductivity is further simplified to

$$\sigma_s(\omega) = \frac{i \cdot e^2 E_F}{\pi \hbar^2 (\omega + i\tau^{-1})}, \quad (2)$$

As we referred previously, when the magnetostatic field is applied in the direction perpendicular to the planar graphene, the oscillation direction of the carriers will be deflected. In our proposed configuration, the carriers' motion would be

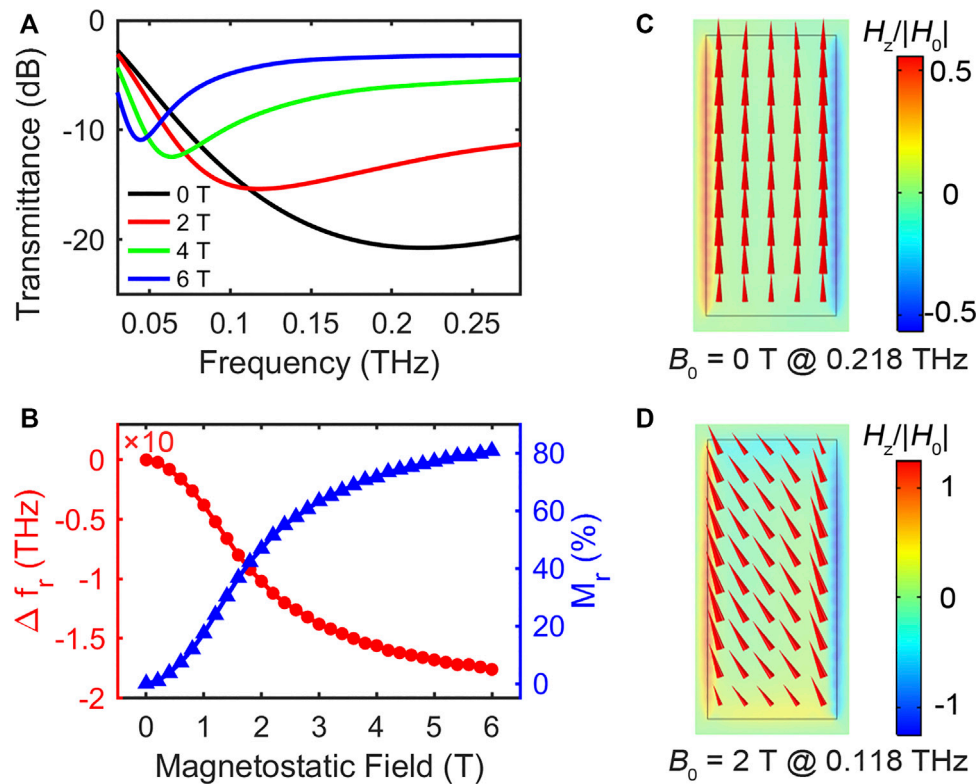


FIGURE 2 | (A) The transmittance spectra of the graphene THz metasurface under different external uniform magnetic flux densities applied. **(B)** The resonance frequency shifts and the frequency modulation index M_f as functions of the values of applied magnetic flux density. The normalized magnetic field H_z/H_0 (H_0 is the magnetic field amplitude of the incident THz wave) and surface currents distributions of the cut-wire resonator at resonant frequencies **(C)** without ($B_0 = 0$ T) or **(D)** with ($B_0 = 2$ T) the magnetostatic field applied in the direction perpendicular to the graphene THz metasurface.

deflected by the Lorentz force. Accordingly, the graphene surface conductivity should include the presence of the magnetic field. Then, in the configuration of **Figures 1A,C**, the new graphene surface conductivity can be described by an anisotropic conductivity tensor [32, 34]:

$$\vec{\sigma}_s(\omega) = \sigma_s(\omega) \begin{bmatrix} \frac{1}{1 + (\mu_e B)^2} & -\frac{\mu_e B}{1 + (\mu_e B)^2} & 0 \\ \frac{\mu_e B}{1 + (\mu_e B)^2} & \frac{1}{1 + (\mu_e B)^2} & 0 \\ 0 & 0 & 1 \end{bmatrix}, \quad (3)$$

where $\sigma = \sigma_0/(1 - i\omega\tau^{-1})$, and $\mu_e = \mu_{e0}/(1 - i\omega\tau^{-1})$, are the optical conductivity and mobility at frequency ω , respectively. σ_0 and μ_{e0} are dc conductivity and mobility, respectively.

The modeling and simulation of the designed terahertz tunable graphene metasurface were performed by COMSOL Multiphysics package, using a lossless dielectric constant $\epsilon = 3.5$ for the SiO_2 substrate and Fermi level $E_F = 0.35$ eV for the graphene. The complex surface conductivity of the graphene patterns in the model is calculated by the anisotropic conductivity tensor described in **Eq. 3**. Periodic boundary conditions are used in the x - y plane and the y -polarized terahertz wave is normally incident from the top. The

magnetostatics fields are set along the z -axis. In this scheme, although all graphene patches are separated from each other, it is still feasible to control the Fermi level of the whole graphene metasurface in practice. Possible approaches include electrostatic bias and chemical doping. For electrostatic bias, a sandwich structure of ion gel/graphene patterns/ITO configuration [35] could be designed and the electrical bias could be applied at both ends to achieve the modulation of Fermi level. For chemical doping, the graphene patterns could be exposed to nitric acid vapor or nitrogen dioxide [36]. By adjusting the doping and baking time to obtain different doping concentrations, the desired Fermi level could be obtained.

RESULTS AND DISCUSSIONS

We calculated the transmittance spectra of patterned graphene metasurface on SiO_2 substrates with different uniform magnetic flux densities. The wave vector of the planar THz wave is parallel to the z -axis and the electric field is along the y -axis. **Figure 2A** shows the transmittance spectra of the patterned graphene THz metasurface under different external uniform magnetic flux densities applied. It is found that there is an evident resonance dip existing around 0.218 THz without the external

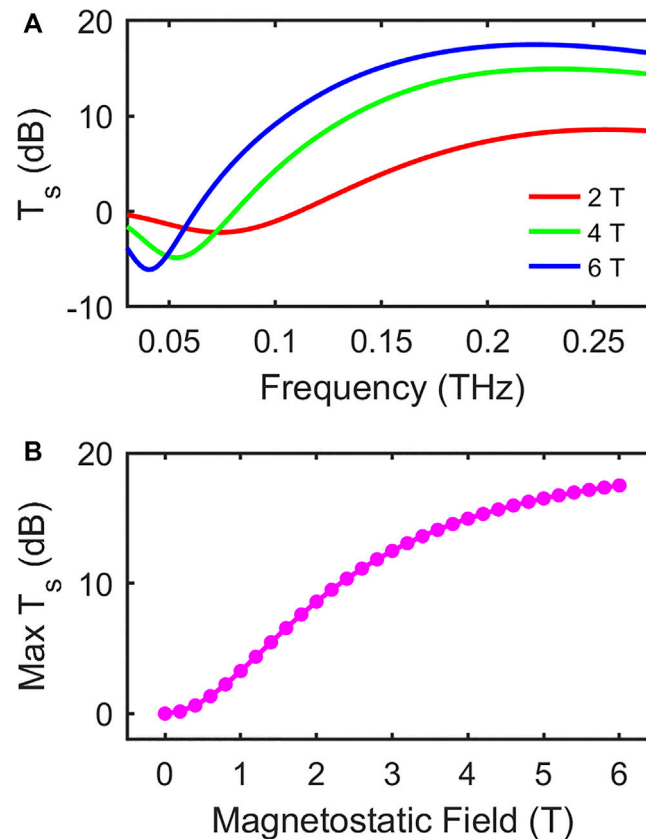


FIGURE 3 | (A) The difference between the transmittance curves of $B_0 = 2$ T/4 T/6 T and the transmittance curve of $B_0 = 0$ T. **(B)** The maximum of transmittance shift as a function of the values of the magnetic flux density applied.

magnetostatic field applied (the value of the applied magnetic flux density is 0, black curve). The resonance dip of the metasurface redshifts continuously from 0.218 to 0.044 THz with the increase of the values of magnetic flux density of the applied magnetostatic field from 0 to 6 T, as shown in **Figure 2A**. The resonance frequency shift (Δf_r), defined as the offset between the resonance frequencies with and without the external magnetostatic field is applied, as a function of the values of the applied magnetic flux density is revealed in **Figure 2B**. The effect of frequency modulation is mainly represented by the frequency modulation index [37], here we show the connection of the frequency modulation index and the applied external magnetostatic field. The frequency modulation index was defined as the ratio of the maximum frequency absolute deviation to the operating frequency

$$M_f = \frac{|\Delta f_r|}{f_0} \times 100\%, \quad (4)$$

where f_0 is the resonance frequency when the external magnetostatics field is not applied, and Δf_r is the resonance frequency shift induced by the applied external magnetostatics field. The frequency modulation index M_f is also a function of the values of the applied magnetic flux density, as shown in **Figure 2B**. To accurately understand the physical principles

behind this phenomenon, we study the magnetic field H_z and surface currents distributions of the cut-wire resonator at resonant frequencies under corresponding magnetostatic fields. **Figures 2C,D** give the field distributions at 0.218 THz under 0 T magnetic flux density and at 0.118 THz under 2 T magnetic flux density, respectively.

The resonance that occurred at 0.218 THz is obvious a fundamental electric dipolar mode [28], in which the surface currents oscillate straightly along the axial direction driven by the electric field of the incident THz wave, as shown in **Figure 2C**. The introduction of the magnetic field provides the transverse component of the currents and causes the apparent currents deflection due to the Lorentz force on the charge carriers in the graphene cut-wire resonator, **Figure 2D**. Due to the restriction from the pattern, the change of carrier oscillation direction would lead to the change of the field distribution in the cut-wire resonator, resulting in the shift of the resonance frequency. Therefore, the resonance frequency shift in **Figure 2B** and the simulated field distribution at the resonance frequency given in **Figure 3D** well supported our hypothesis.

To now, we have clarified the physics of the metasurface proposed and directly given the numerical proof of carrier deflection under the bias of the external magnetostatic field. The frequency shifts and the changes of the field distribution show that we can control the resonance frequency of the patterned metasurface

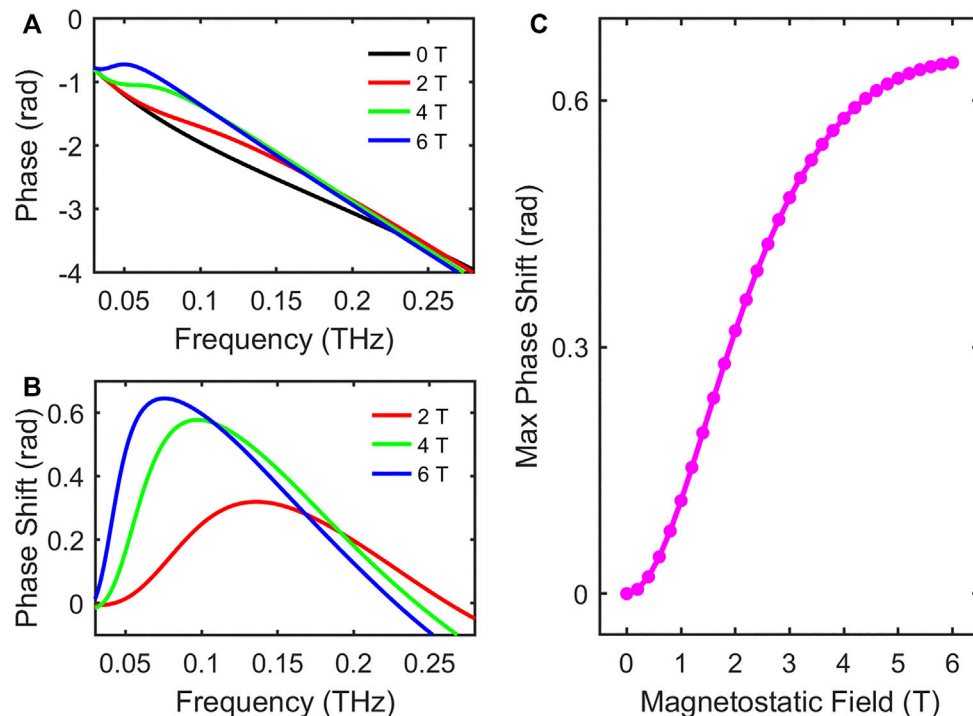


FIGURE 4 | (A) The transmitted phase spectra of the graphene THz metasurface under different external uniform magnetic flux densities applied. **(B)** The difference between the transmitted phase curves of $B_0 = 2$ T/4 T/6 T and the transmitted phase curve of $B_0 = 0$ T. **(C)** The maximum of phase shift as a function of the values of the magnetic flux density applied.

through an external magnetostatic field. By introducing different values of the magnetic flux density, dynamic control of the resonance characteristics of the metasurface is achieved.

Besides the resonance frequency shifts, we also investigated the transmittance and the transmitted phase characteristics of graphene THz metasurface. It is found that the transmittance changes significantly when different magnetostatic fields are applied, and the transmitted phase was sensitive to the external magnetostatic field. The change in the transmittance shift was defined as [38].

$$T_s \text{ (dB)} = T_{\text{on}} \text{ (dB)} - T_{\text{off}} \text{ (dB)}, \quad (5)$$

where T_{on} (dB) is the transmittance of the graphene metasurface when a magnetostatic field is applied; T_{off} (dB) is the transmittance of the graphene metasurface without magnetostatic field (or $B_0 = 0$ T) applied. Taking the transmittance curve of $B_0 = 0$ T (black curve in Figure 2A) as a reference, the difference between the transmittance curve of $B_0 = 2$ T/4 T/6 T and the transmittance curves of $B_0 = 0$ T are shown in Figure 3A. It can be seen easily in Figure 3B that the maximum values of the transmittance shifts increase with the increase of applied flux density.

Figure 4A plots the transmitted phase spectra for different values of magnetic flux density applied. It is shown that the transmitted phase response of the metasurface varies greatly under different magnetostatic fields applied. Additionally, we notice that the increase in the values of magnetic flux density applied leads to a clear increase variation of the transmitted phase. To better analyze the variation of transmitted phases, we

take the transmitted phase curve of $B_0 = 0$ T (black curve in Figure 4A) as a reference, the difference between the transmitted phase curves of $B_0 = 2$ T/4 T/6 T and the transmittance curve of $B_0 = 0$ T are shown in Figure 4B. We can perceive that the transmitted phase changes significantly when different magnetic flux density is applied to the graphene metasurface and caused different phase shifts. Similar to the transmittance shifts, the maximum value of the phase shifts increases with the applied flux density, shown in Figure 4C.

Starting with an easy-to-understand physical phenomenon, we postulate that the carrier's motion in the two-dimensional graphene surface will be deflected under the vertical magnetostatic field applied. If graphene is patterned as a THz metasurface, its resonance properties are closely related to the oscillation direction of the carriers in the pattern. When a magnetostatic field is applied, the oscillation deflection of the carriers causes a significant change in the transmittance properties of the graphene metasurface. Therefore, the external magnetostatic field can be used to control the transmittance characteristics of graphene metasurface and could be used to realize a dynamically tunable THz graphene metasurface. The postulation is confirmed by a simply designed metasurface. Parameters such as resonance frequency, transmittance, and transmitted phase of the metasurface are numerically studied. It is shown that these parameters are obviously changed when different magnetostatic fields are applied, and the shifts of these parameters are increasing with the increase of the applied magnetostatic field. Therefore, this study demonstrates that

the magnetostatic field can be used as an effective magneto-controlled method for the design of dynamically tunable metasurfaces in the THz regime.

It should be noted that the conventional electrostatic-controlled method [39] mainly regulates the Fermi level of graphene through electrical bias to control the properties of graphene metasurface, while our magneto-controlled one regulates the oscillating current of the carriers to control the transmittance properties of graphene metasurface. There are essential differences between the two. Compared with the conventional method, one advantage of the magneto-controlled method is that when the magnetic bias is used for control, it is not necessary to connect all the graphene patterns, as this will severely limit the flexibility of metasurface design. Although the magneto-controlled mechanism also depends on adjusting the Fermi level of graphene to an appropriate value, it essentially adds a new degree of tunable freedom. The combination of the magneto-controlled method and other control methods may give new opportunities for dynamically controlled graphene metasurface.

Finally, since the main purpose of this work is to demonstrate our new method of dynamically controlling the transmittance characteristics of the patterned graphene metasurface using a magnetostatic field, our focus is on the analysis and numerical verification of its working principle. Therefore, we have designed an intuitive and simple cut-wire structure to facilitate our interpretation of the principle. In recent years, several important local field enhancement mechanisms in the field of electromagnetic metasurface research, such as bound states in the continuum (BIC) [40], anapole [41, 42], and Fano [43, 44], may indicate the direction for further improvement of the efficiency of the magneto-controlled metasurface. The introduction of one or more of the above mechanisms into the magneto-controlled metasurface would increase the response sensitivity while reducing the value of excitation magnetic field intensity.

REFERENCES

- Williams GP. Filling the THz gap—high power sources and applications. *Rep Prog Phys* (2006) 69(2):301–26. doi:10.1088/0034-4885/69/2/R01
- Cunningham PD, Valdes NN, Vallejo FA, Hayden LM, Polishak B, Zhou X-H, et al. Broadband terahertz characterization of the refractive index and absorption of some important polymeric and organic electro-optic materials. *J Appl Phys* (2011) 109(4):043505. doi:10.1063/1.3549120
- Tonouchi M. Cutting-edge terahertz technology. *Nat Photon* (2007) 1(2): 97–105. doi:10.1038/nphoton.2007.3
- Nagatsuma T, Ducournau G, Renaud CC. Advances in terahertz communications accelerated by photonics. *Nat Photon* (2016) 10(6):371–9. doi:10.1038/nphoton.2016.65
- Saeedkia D. *Handbook of terahertz technology for imaging, sensing and communications*. Woodhead Publishing Limited (2013).
- Withayachumnankul W, Yamada R, Fujita M, Nagatsuma T. All-dielectric rod antenna array for terahertz communications. *APL Photonics* (2018) 3(5): 051707. doi:10.1063/1.5023787
- Tripathi SK, Kumar M, Kumar A. Graphene based tunable and wideband terahertz antenna for wireless network communication. *Wireless Network* (2019) 25(7):4371–81. doi:10.1007/s11276-019-02101-8

CONCLUSION

In conclusion, we proposed a magneto-controlled method to manipulate the transmittance properties of the incident THz wave. To confirm this idea, a graphene-based THz metasurface comprised of graphene cut-wire arrays was investigated for proof-of-principle demonstration. The introduced vertical electrostatic field deflects the carriers in graphene and changes the transmittance characteristics of the metasurface. By adjusting the value of the applied magnetic flux density, the transmittance characteristics related parameters can be dynamically controlled, and the dynamically tunable metasurface is realized. Our results provide a new dimension for the design of graphene-based dynamically tunable THz metasurfaces.

DATA AVAILABILITY STATEMENT

The raw data supporting the conclusions of this article will be made available by the authors, without undue reservation.

AUTHOR CONTRIBUTIONS

YL designed and simulated the structure. All authors analyzed and discussed the results. YL and YW wrote the manuscript. The project was conceived and supervised by YW.

FUNDING

This work was supported by the Basic Science Center Project of NSFC under Grant No. 51788104, National Natural Science Foundation of China under Grant Nos. 51532004 and 52072203, and Beijing Municipal Science & Technology Commission under Grant No. Z191100004819001.

- Zhao Q, Zhou J, Zhang F, Lippens D. Mie resonance-based dielectric metamaterials. *Mater Today* (2009) 12(12):60–9. doi:10.1016/S1369-7021(09)70318-9
- Smith DR, Padilla WJ, Vier DC, Nemat-Nasser SC, Schultz S. Composite medium with simultaneously negative permeability and permittivity. *Phys Rev Lett* (2000) 84(18):4184–7. doi:10.1103/PhysRevLett.84.4184
- Shelby RA, Smith DR, Schultz S. Experimental verification of a negative index of refraction. *Science* (2001) 292(5514):77–9. doi:10.1126/science.1058847
- Sihvola A. Metamaterials in electromagnetics. *Metamaterials* (2007) 1(1):2–11. doi:10.1016/j.metmat.2007.02.003
- Pendry JB, Schurig D, Smith DR. Controlling electromagnetic fields. *Science* (2006) 312(5781):1780–2. doi:10.1126/science.1125907
- Yu N, Capasso F. Flat optics with designer metasurfaces. *Nat Mater* (2014) 13(2):139–50. doi:10.1038/nmat3839
- Fan KB, Suen JY, Liu X, Padilla WJ. All-dielectric metasurface absorbers for uncooled terahertz imaging. *Optica* (2017) 4(6):601–4. doi:10.1364/OPTICA.4.000601
- Cole MA, Powell DA, Shadrivov IV. Strong terahertz absorption in all-dielectric Huygens' metasurfaces. *Nanotechnology* (2016) 27(42):424003. doi:10.1088/0957-4484/27/42/424003
- Wang J, Hao T, Wang Y, Li X, Liu J, Zhou Z. Liquid crystal terahertz modulator with plasmon-induced transparency metamaterial. *Optic Express* (2018) 26(5): 5769–76. doi:10.1364/OE.26.005769

17. Grebenchukov AN, Zaitsev AD, Novoselov MG, Kovalska EO, Baldycheva AV, Khodzitsky MK. Multi-layer graphene based tunable metasurface for terahertz wave control. In: Zhang C, Zhang XC, Tani M, editors. *Infrared, millimeter-wave, and terahertz technologies V* (2018).
18. Xing Q, Wang C, Huang S, Liu T, Xie Y, Song C, et al. Tunable graphene splitting resonators. *Physical Review Applied* (2020) 13(4):041006. doi:10.1103/PhysRevApplied.13.041006
19. Schwierz F. Graphene transistors. *Nat Nanotechnol* (2010) 5(7):487–96. doi:10.1038/nnano.2010.89
20. Su W, Liu YC, Chen BY. Multiple Fano resonances in asymmetric rectangular ring resonator based on graphene nanoribbon. *Results in Physics* (2020) 17: 103121. doi:10.1016/j.rinp.2020.103121
21. Liu CX, Zha S, Liu P, Yang C, Zhou Q. Electrical manipulation of electromagnetically induced transparency for slow light purpose based on metal-graphene hybrid metamaterial. *Applied Sciences-Basel* (2018) 8(12): 2672. doi:10.3390/app8122672
22. Kim TT, Oh SS, Kim H-D, Park H-S, Hess O, Min B, et al. Electrical access to critical coupling of circularly polarized waves in graphene chiral metamaterials. *Sci Adv* (2017) 3(9):e1701377. doi:10.1126/sciadv.1701377
23. Dabidian N, Kholmanov IN, Khanikaev A, Tatar K, Trendafilov S, Mousavi SH, et al. Electrical switching of infrared light using graphene integration with plasmonic Fano resonant metasurfaces. *ACS Photonics* (2015) 2(2):216–27. doi:10.1021/ph5003279
24. Rath S, Lee I, Lim D, Wang J, Ochiai Y, Aoki N, et al. Tunable electrical and optical characteristics in monolayer graphene and few-layer MoS₂ heterostructure devices. *Nano Lett* (2015) 15(8):5017–24. doi:10.1021/acs.nanolett.5b01030
25. Balandin AA, Ghosh S, Bao W, Calizo I, Teweldebrhan D, Miao F, et al. Superior thermal conductivity of single-layer graphene. *Nano Lett* (2008) 8(3): 902–7. doi:10.1021/nl0731872
26. Weber P, Güttinger J, Noury A, Vergara-Cruz J, Bachtold A. Force sensitivity of multilayer graphene optomechanical devices. *Nat Commun* (2016) 7:12496. doi:10.1038/ncomms12496
27. Fan Y, Wei Z, Zhang Z, Li H. Enhancing infrared extinction and absorption in a monolayer graphene sheet by harvesting the electric dipolar mode of split ring resonators. *Opt Lett* (2013) 38(24):5410–3. doi:10.1364/OL.38.005410
28. Fan YC, Shen N-H, Koschny T, Soukoulis CM. Tunable terahertz meta-surface with graphene cut-wires. *ACS Photonics* (2015) 2(1):151–6. doi:10.1021/ph500366z
29. Wang XF, Liu G-D, Xia S-X, Haiyu M, Shang X, He P, et al. Dynamically tunable Fano resonance based on graphene metamaterials. *IEEE Photon Technol Lett* (2018) 30(24):2147–50. doi:10.1109/LPT.2018.2879540
30. Zhang J, Wei X, Rukhlenko ID, Chen H-T, Zhu W. Electrically tunable metasurface with independent frequency and amplitude modulations. *ACS Photonics* (2020) 7(1):265–71. doi:10.1021/acsp Photonics.9b01532
31. Zhang J, Zhang H, Yang W, Chen K, Wei X, Feng Y, et al. Dynamic scattering steering with graphene-based coding metamirror. *Advanced Optical Materials*. (2020) 8:2000683. doi:10.1002/adom.202000683
32. Wen Y, Zhou J. Artificial nonlinearity generated from electromagnetic coupling metamolecule. *Phys Rev Lett* (2017) 118(16):167401. doi:10.1103/PhysRevLett.118.167401
33. Liu C, Bai Y, Zhou J, Zhao Q, Qiao L. A review of graphene plasmons and its combination with metasurface. *J Kor Chem Soc* (2017) 54(5):349–65.
34. Wen Y, Zhou J. Artificial generation of high harmonics via nonrelativistic thomson scattering in metamaterial. *Research* (2019) 2019:8959285. doi:10.34133/2019/8959285
35. Fang Z, Thongrattanasiri S, Schlather A, Liu Z, Ma L, Wang Y, et al. Gated tunability and hybridization of localized plasmons in nanostructured graphene. *ACS Nano* (2013) 7(3):2388–95. doi:10.1021/nn3055835
36. Yan HG, Low T, Zhu W, Wu YQ, Freitag M, Li XS, et al. Damping pathways of mid-infrared plasmons in graphene nanostructures. *Nat Photon* (2013) 7(5): 394–9. doi:10.1038/nphoton.2013.57
37. Pol BVD. Frequency modulation. *Proc Inst Radio Eng* (1930) 18(7):1194–205.
38. Li G, Wen-jun G, Yan-jun Z, Yan-li L, Yu-long H, Yan-hu S, et al. Polarization-controlled optical switch based on surface plasmon. *Acta Photonica Sin* (2020) 49(3):326001. doi:10.3788/gzxb20204903.0326001
39. Vakil A, Engheta N. Transformation optics using graphene. *Science* (2011) 332(6035):1291–4. doi:10.1126/science.1202691
40. Hsu CW, Zhen B, Stone AD, Joannopoulos JD, Soljačić M. Bound states in the continuum. *Nature Reviews Materials* (2016) 1(9):16048. doi:10.1038/natrevmats.2016.48
41. Miroshnichenko AE, Evlyukhin AB, Yu YF, Bakker RM, Chipouline A, Kuznetsov AI, et al. Nonradiating anapole modes in dielectric nanoparticles. *Nat Commun* (2015) 6:8069. doi:10.1038/ncomms9069
42. Zhang TY, Che Y, Chen K, Xu J, Xu Y, Wen T, et al. Anapole mediated giant photothermal nonlinearity in nanostructured silicon. *Nat Commun* (2020) 11(1):3027. doi:10.1038/s41467-020-16845-x
43. Campione S, Guclu C, Ragan R, Capolino F. Enhanced magnetic and electric fields via Fano resonances in metasurfaces of circular clusters of plasmonic nanoparticles. *ACS Photonics* (2014) 1(3):254–60. doi:10.1021/ph4001313
44. Panaro S, De Angelis F, Toma A. Dark and bright mode hybridization: from electric to magnetic Fano resonances. *Optic Laser Eng* (2016) 76:64–9. doi:10.1016/j.optlaseng.2015.03.019

Conflict of Interest: The authors declare that the research was conducted in the absence of any commercial or financial relationships that could be construed as a potential conflict of interest.

Copyright © 2021 Lu, Wang, Zhao and Wen. This is an open-access article distributed under the terms of the Creative Commons Attribution License (CC BY). The use, distribution or reproduction in other forums is permitted, provided the original author(s) and the copyright owner(s) are credited and that the original publication in this journal is cited, in accordance with accepted academic practice. No use, distribution or reproduction is permitted which does not comply with these terms.



Dynamic Control of Ultrathin Electromagnetic Absorber Using Active High Impedance Metasurfaces

Zeyong Wei^{1,2*}, Hongkun Li^{1,2}, Weijie Xu^{1,2} and Yang Cao^{3*}

¹School of Physics Science and Engineering, Tongji University, Shanghai, China, ²Key Laboratory of Advanced Micro-structure Materials (MOE), Shanghai, China, ³Shanghai Mi Xuan Electronic Technology Co., Ltd., Shanghai, China

In recent years, active metasurfaces have induced more interests, which provides great freedom of wave manipulation and gives rise to many novel phenomena. High impedance metasurfaces are a kind of artificial structures characterized by the in-phase reflection at the resonant frequency. It works as a magnetic mirror and can be applied in subwavelength cavity, low profile reflector antenna, etc. When introduce in tunable components, it possesses versatile functionalities and broader application. In this paper, we proposed an active high impedance metasurface which exhibits highly efficient absorption to the electromagnetic incidence. As an array of diodes are loaded between the gap of periodic gratings and applied with positive bias, the absorption frequency can be dynamically controlled by the level of bias voltage. At the resonant frequency, the reflection from the metasurface can be less than 1%, implying that most of the incidence is absorbed by the magnetic resonance of high impedance metasurface. When the bias voltage is tuned from 0 to +1.33 V (the forward voltage), the resonant peak rises from 8.5 to 9.1 GHz, providing a flexible control of electromagnetic wave absorption in X band.

Keywords: high-impedance, metasurface, dynamic control, equivalent circuit model, magnetic resonance, absorption

INTRODUCTION

Recently, metasurfaces [1] have attracted a great deal of attention due to their ability to freely manipulate electromagnetic waves within the sub-wavelength thickness, obtaining desirable electromagnetic properties that are not available in nature [2–5]. They have great potential for applications in microwave communication, integrated circuits, antennas, and so on [4, 6–9]. When combined with tunable mechanism, metasurfaces present variable electromagnetic properties with respect to the external condition and provide dynamic control of the incident waves [10, 11]. Metasurfaces based on tunable mechanisms such as optical [12, 13], thermal [14], electrical [15–19], and MEMS [20, 21] have been proposed to enable the dynamic control of electromagnetic waves.

High impedance surface (HIS) [22, 23] is a kind of sandwich structures comprised of periodical metallic patterns, dielectric spacer and metallic ground plane. They behave as a highly efficient magnetic conductor (PMC) to the incident wave at resonant frequency with high surface impedance, giving zero phase shift to the reflected wave [24, 25]. HIS is widely investigated and found to be an electromagnetic band gap (EBG) material which suppresses the propagation of surface waves. These properties can be utilized for low-profile antenna, and back lobe suppression, etc [26, 27]. Meanwhile, it is worth noting that the local field is enhanced by several orders around the

OPEN ACCESS

Edited by:

Qian Zhao,
Tsinghua University, China

Reviewed by:

Jiafu Wang,
Air Force Engineering University, China
Yongqiang Pang,
Xi'an Jiaotong University, China

*Correspondence:

Zeyong Wei
weizeyong@tongji.edu.cn
Yang Cao
caoyang85@163.com

Specialty section:

This article was submitted to
Optics and Photonics,
a section of the journal
Frontiers in Physics

Received: 24 November 2020

Accepted: 29 December 2020

Published: 29 January 2021

Citation:

Wei Z, Li H, Xu W and Cao Y (2021)
Dynamic Control of Ultrathin
Electromagnetic Absorber Using
Active High Impedance Metasurfaces.
Front. Phys. 8:632902.
doi: 10.3389/fphy.2020.632902

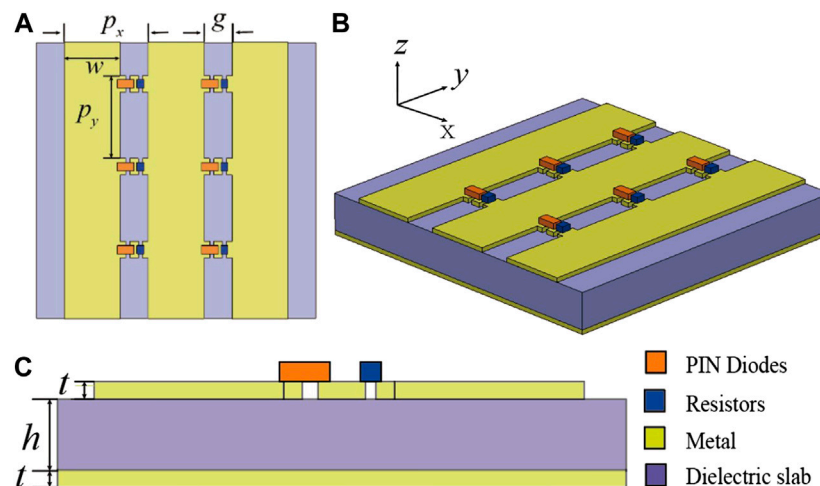


FIGURE 1 | (A) Schematic diagram of the metasurface (top view). The purple part is dielectric, the yellow part is metal, the orange part represents diodes, and the blue part represents passive resistors. **(B)** 3D view of the metasurface. **(C)** side view of the metasurface.

resonant frequency. HIS can also be used as an electromagnetic absorber when appropriate loss is introduced. It works with small loss factor and electrically thin thickness, while gives high absorption efficiency [28–30]. In 2019, Liu et al. introduced PIN diode into a HIS, making a reconfigurable metasurface with multiple applications [31].

In this paper, we have designed and measured for the first time the highly efficient absorption effect of an active high-impedance metasurface. we fabricated a HIS which consists of a metallic grating and a ground plane, with a dielectric substrate sandwiched between them. Then a diode and a passive resistor are loaded on each gap of the grating. Highly efficient electromagnetic absorption can be achieved by dedicated design of the resistance of passive resistor; and the absorption frequency can be dynamically changed with the tunable characteristics of the diode. It is observed with finite-difference time-domain (FDTD) simulations that, the absorption efficiency is 99% at 8.5 GHz without the DC bias; while applied with positive bias voltage, the series resistance of the diode decreases, resulting in a higher resonant frequency of HIS; and at the forward voltage +1.33 V of the diode, the absorption frequency increases to 9.7 GHz. Reflection from the sample is measured with microwave experiments. The tuning range is from 8.5 to 9.1 GHz with a minimum reflection of -30 dB observed during the measurements, which agrees well with the theoretical predictions. This work can make good contributions to instrument protection, electromagnetic wave shielding and other areas.

STRUCTURE AND SIMULATIONS

The proposed active HIS is a three-layered periodic structure as schematically shown in **Figure 1**. A metallic grating is on the top surface with a period of $p_x = 12.2$ mm and a gap of $g = 3$ mm, so that the width of the grating is $w = 9.2$ mm. Then a diode and a

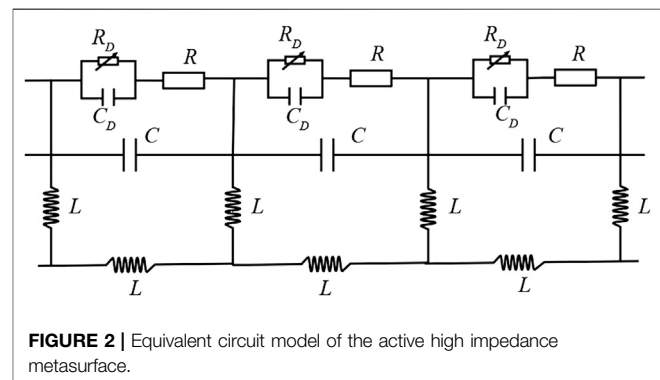


FIGURE 2 | Equivalent circuit model of the active high impedance metasurface.

passive resistor are loaded in series across each gap and periodically arrayed along y direction with an interval of $p_y = 12$ mm. We adopted Aluminum Gallium Arsenide (AlGaAs) flip-chip PIN diodes (MA4AGP907) with a small junction capacitance of 0.025 pF, and the resistance of the passive resistor is $R = 100 \Omega$. On the bottom layer is a metallic ground plane. The thickness of the dielectric layer is $h = 0.78$ mm, and that of each metallic layer is $t = 0.017$ mm, giving rise to a total thickness of 0.814 mm of the sample. The dielectric constant of the substrate is $\epsilon_r = 2.65$.

According to the equivalent circuit model theory [23], a HIS can be modeled as a parallel RLC resonant circuit. The gap of grating behaves as a capacitor and the resonant loop forming among the top and the bottom layer provides an equivalent inductance, giving rise to a constant resonant frequency determined by the structural geometry. When the gap is loaded with a diode and a passive resistor, it turns into an active HIS with equivalent circuit model as shown in **Figure 2**. The diode forms a parallel RC circuit with the junction capacitance C_D and a variable resistance R_D , in series with the passive resistor R , integrated into the HIS circuit. The variable

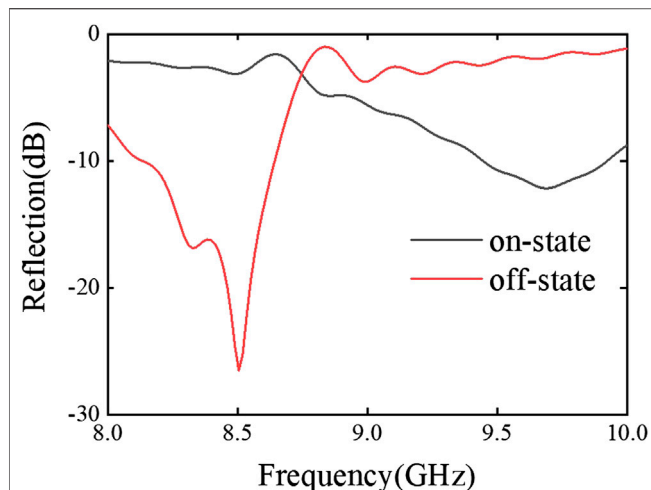


FIGURE 3 | The simulated reflection spectra of the active high impedance metasurface when the loaded PIN diodes are on-state (black line) and off-state (red line).

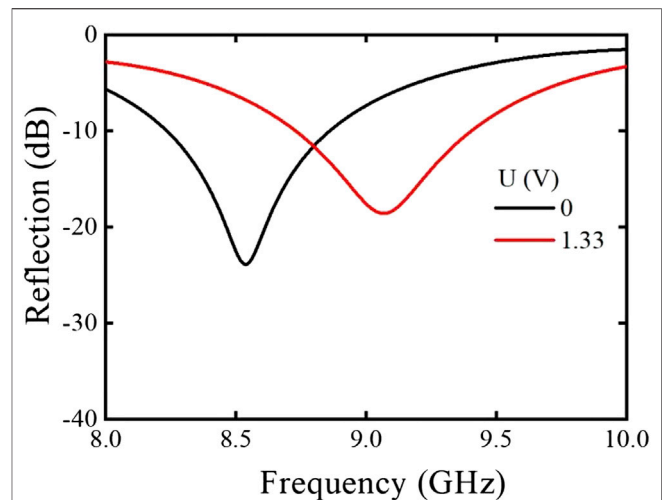


FIGURE 5 | The measured reflection spectra of the active high impedance metasurface when the PIN diodes are loaded with +1.33 V bias voltage (red line) and in open-circuit state (black line).

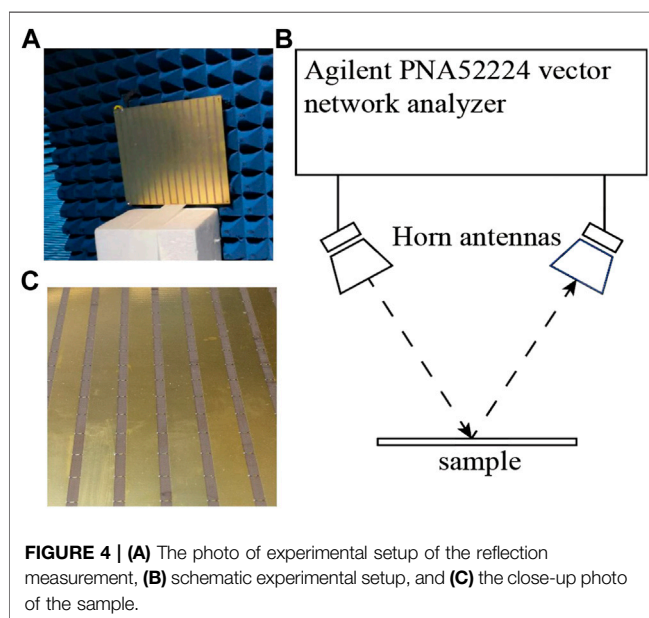


FIGURE 4 | (A) The photo of experimental setup of the reflection measurement, (B) schematic experimental setup, and (C) the close-up photo of the sample.

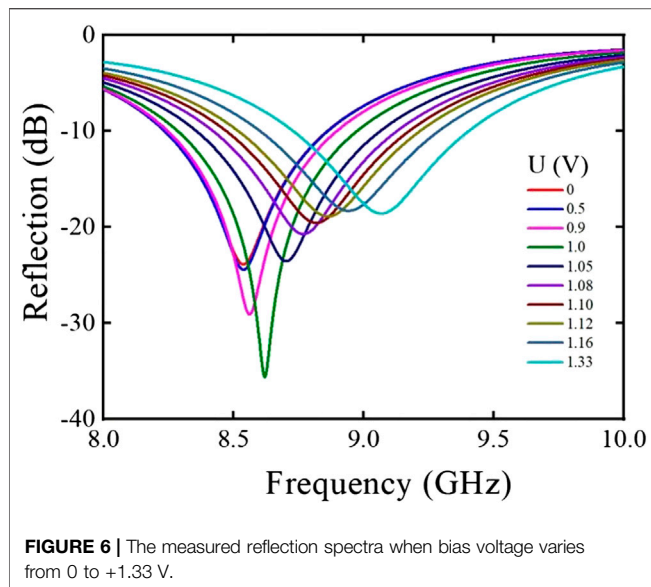
resistance of diode changes from infinite to $R_D = 4.2 \Omega$, while the bias voltage increases positively from 0 to +1.33 V, resulting in an observable shift of the resonant frequency. The value of the passive resistor R is carefully optimized for impedance matching, and highly efficient absorbing the incident power, thanks to the field enhancement on resonant state. FDTD simulations are employed to calculate the reflection for both cases, $R_D = 4.2 \Omega R_D \Omega$ (on-state) and $R_D = \infty \Omega R_D \Omega$ (off-state). In the simulation, periodical boundary conditions are imposed along x axis and y axis. The incident wave propagates along z^- direction and is ensured with no reflection at z^+ boundary by UPML boundary condition. The excitation in time domain is a Gauss pulse. The diode is simulated using passive components

with $C_D = 0.025$ pF, and $R_D = 4.2 \Omega$ (on-state) or $R_D = \infty \Omega$ (off-state). z component of Poynting vector is probed at 5 mm above the sample by setting a probe plane. Calculated reflection spectrum is shown in **Figure 3**. For on-state, highly efficient absorption happens at 8.5 GHz with a reflection coefficient of -26.5 dB, while the electromagnetic incidence is mostly reflected back with a reflection coefficient of -1.8 dB at 9.7 GHz. For off-state, the absorption peak is blue shifted to 9.7 GHz with a low reflection level of -11 dB, while the reflection rises to -3 dB at 8.5 GHz. At this point, the dynamic control of resonant absorption peak, that is the switch between absorption and reflection state at 8.5 GHz and 9.7 GHz, can be achieved by using the on-state and off-state of the diode.

EXPERIMENTS AND DISCUSSIONS

For verification, a HIS sample is fabricated with printed circuit board (Taconic TLX-8) with a lateral size of 180×180 mm, as shown in **Figure 4**. 224 chip diodes and an equal number of chip resistors are surface mounted with gold silk bonding technology on the top layer of the sample. By alternatively applying positive and negative DC voltage on adjacent gratings, the diode is biased with tuneable voltage level.

The reflection is measured in a microwave anechoic chamber, with the sample placed on a foam and two standard gain horn antennas placed in front of it. The main lobe of horn antennas is perpendicularly incident on the sample surface, as schematically shown in **Figure 4B**. The horn emitter and the horn receiver are connected to an Agilent PNA52224 vector network analyzer to measure the S parameter S_{21} . At first, a metal plate with the same size as the sample is measured to record the calibration field intensity. When the sample is under test, we get the reflected field intensity. Then the reflection coefficient is derived from the difference between these data.



We measured the reflection spectra for 0 V and +1.33 V bias voltage, corresponding to the off-state and on-state of diode respectively. **Figure 5** shows the normalized reflection coefficient for both states from measurements. It can be observed that, when the bias is not loaded (0 V), the resonant absorption peak appears at 8.5 GHz with a reflection minimum of -24 dB. While applied with +1.33 V bias voltage, the absorption peak shifts to a higher frequency of 9.1 GHz, which agrees well with the theoretical calculation.

In addition to the on-state and off-state, the resistance of the diode will continuously vary during the increase of positive bias voltage from 0 V to +1.33 V. The reflection of the sample is measured at several intermediate levels of bias voltage as shown in **Figure 6**. It is proved that the resonant absorption peak can be dynamically tuned between 8.5 and 9.1 GHz, by adjusting the bias voltage. The reflection of the sample is low than -18 dB during the whole range. When +1 V bias voltage is applied, the reflection coefficient drops below -30 dB, implying a wonderful absorption of incidence.

CONCLUSION

In conclusion, we have designed an active HIS to achieve dynamic control of the electromagnetic absorption. The impedance matching between the HIS and the incident wave is met by

REFERENCES

1. Yu N, Genevet P, Kats MA, Aieta F, Tetienne JP, Capasso F, et al. Light propagation with phase discontinuities: generalized laws of reflection and refraction. *Science* (2011) 334(6054):333–337. doi:10.1126/science.1210713
2. Yu N, Capasso F. Flat optics with designer metasurfaces. *Nat Mater* (2014) 13(2):139–150. doi:10.1038/nmat3839

introducing a passive series resistor on the top surface of the HIS. By adjusting the positive bias voltage of the diode, the resistance of the diode can be tuned in a range to achieve dynamic control of the highly efficient electromagnetic absorption. Experimental samples are fabricated and measured to verify this phenomenon for the first time. Both theoretical simulations and experimental measurements demonstrate that the active HIS can achieve electromagnetic absorption with an absorption efficiency greater than 99% at resonant frequencies. By changing the diode from off-state to on-state, a dynamic switch between the electromagnetic absorption and reflection is observed at 8.5 and 9.1 GHz in experiments. Furthermore, continuous changing of the absorption peak between 8.5 and 9.1 GHz can be achieved by gradually varying the positive bias voltage of the diode. This work has great potential in electromagnetic wave stealth, shielding, and electromagnetic compatibility.

DATA AVAILABILITY STATEMENT

The original contributions presented in the study are included in the article/Supplementary Material, further inquiries can be directed to the corresponding authors.

AUTHOR CONTRIBUTIONS

ZW conceived the idea and supervised the whole study. HL and WX conducted the numerical calculations and performed the experiments. YC derived the theory, carried out the analysis and drafted the manuscript. All authors contributed to the review of manuscript.

FUNDING

This work is supported by the National Natural Science Foundation of China (Grant NOs 11674248, 11874285, 11204218, 62020106009, 61925504); supported by the Fundamental Research Funds for the Central Universities; Major Projects of Science and Technology Commission of Shanghai (Grant No. 17JC1400801); Pudong New Area Science and Technology Development Fund Industry-University-Research Special-Antenna Calibration and Test Equipment Research of 5G base Stations (Project No. PKX2019-D15).

3. Chen HT, Taylor AJ, Yu N. A review of metasurfaces: physics and applications. *Rep Prog Phys* (2016) 79(7):076401. doi:10.1088/0034-4885/79/7/076401
4. Glybovski SB, Tretyakov SA, Belov PA, Kivshar YS, Simovski CR. Metasurfaces: from microwaves to visible. *Phy Rep* (2016) 634:1–72. doi:10.1016/j.physrep.2016.04.004
5. Zhang L, Mei ST, Huang K, Qiu CW. Advances in full control of electromagnetic waves with metasurfaces. *Adv Opt Mater* (2016) 4(6): 818–833. doi:10.1002/adom.201500690

6. Cheng KY, Wei ZY, Fan YC, Zhang XM, Wu C, Li HQ. Realizing broadband transparency via manipulating the hybrid coupling modes in metasurfaces for high-efficiency metalens. *Adv Opt Mater* (2019) 7(15):1900016. doi:10.1002/adom.201900016
7. Fan YC, Shen NH, Zhang FL, Zhao Q, Wei ZY, Zhang P, et al. Photoexcited graphene metasurfaces: significantly enhanced and tunable magnetic resonances. *ACS Photonics* (2018) 5(4):1612–1618. doi:10.1021/acsp Photonics.8b00057
8. Wei Z, Cao Y, Su X, Gong Z, Long Y, Li H. Highly efficient beam steering with a transparent metasurface. *Opt Express* (2013) 21(9):10739–10745. doi:10.1364/OE.21.010739
9. Wei ZY, Cao Y, Fan YC, Yu X, Li HQ. Broadband polarization transformation via enhanced asymmetric transmission through arrays of twisted complementary split-ring resonators. *Appl Phys Lett* (2011) 99(22):221907. doi:10.1063/1.3664774
10. Bang S, Kim J, Yoon G, Tanaka T, Rho J. Recent advances in tunable and reconfigurable metamaterials. *Micromachines* (2018) 9(11):560. doi:10.3390/mi9110560
11. Fan K, Padilla WJ. Dynamic electromagnetic metamaterials. *Mater Today* (2015) 18(1):39–50. doi:10.1016/j.mattod.2014.07.010
12. Chowdhury DR, Singh R, O'Hara JF, Chen H-T, Taylor AJ, Azad AK. Dynamically reconfigurable terahertz metamaterial through photo-doped semiconductor. *Appl Phys Lett* (2011) 99:231101. doi:10.1063/1.3667197
13. Sun L, Zhang H, Dong G, Li P, Zhu Z, Li Y, et al. Dynamically tunable terahertz anomalous refraction and reflection based on graphene metasurfaces. *Opt Commun* (2019) 446:10–15. doi:10.1016/j.optcom.2019.04.058
14. Luo H, Cheng Y. Thermally tunable terahertz metasurface absorber based on all dielectric indium antimonide resonator structure. *Opt Mater* (2020) 102 doi:10.1016/j.optmat.2020.109801
15. Shadrivov IV, Morrison SK, Kivshar YS. Tunable split-ring resonators for nonlinear negative-index metamaterials. *Opt Express* (2006) 14(20):9344–9349. doi:10.1364/oe.14.009344
16. Xu HX, Tang S, Ma S, Luo W, Cai T, Sun S, et al. Tunable microwave metasurfaces for high-performance operations: dispersion compensation and dynamical switch. *Sci Rep* (2016) 6:38255. doi:10.1038/srep38255
17. Chen HT, Padilla WJ, Zide JM, Gossard AC, Taylor AJ, Averitt RD. Active terahertz metamaterial devices. *Nature* (2006) 444(7119):597–600. doi:10.1038/nature05343
18. Li Y, Lin J, Guo H, Sun W, Xiao S, Zhou L. A tunable metasurface with switchable functionalities: from perfect transparency to perfect absorption. *Adv Opt Mater* (2020) 8(6):1901548. doi:10.1002/adom.201901548
19. Sun Y, Tong Y-W, Xue C-H, Ding Y-Q, Li Y-H, Jiang H, et al. Electromagnetic diode based on nonlinear electromagnetically induced transparency in metamaterials. *Appl Phys Lett* (2013) 103(9):091904. doi:10.1063/1.4819854
20. Liu X, Padilla WJ. Dynamic manipulation of infrared radiation with MEMS metamaterials. *Adv Opt Mater* (2013) 1(8):559–562. doi:10.1002/adom.201300163
21. Arbabi E, Arbabi A, Kamali SM, Horie Y, Faraji-Dana M, Faraon A. MEMS-tunable dielectric metasurface lens. *Nat Commun* (2018) 9(1):812. doi:10.1038/s41467-018-03155-6
22. Sievenpiper D, Zhang L, Broas RF, Alexopolous NG, Yablonovitch E. High-impedance electromagnetic surfaces with a forbidden frequency band. *IEEE Trans Microw Theor Tech* (1999) 47(11):2059–2074. doi:10.1109/22.798001
23. Sievenpiper DF. High-impedance electromagnetic surfaces. *IEEE Trans Microw Theor Tech* (1999) 47(11):2059–2074. doi:10.1109/9780470545324.ch8
24. Zhou L, Wen W, Chan CT, Sheng P. Multiband subwavelength magnetic reflectors based on fractals. *Appl Phys Lett* (2003) 83(16):3257–3259. doi:10.1063/1.1622122
25. Hendevari MS, Bemani M, Nikmehr S. A novel dual-band double-sided high-impedance surface (DB-DS-HIS) with systematic design methodology. *Int J Electron Commun* (2020) 115:153039. doi:10.1016/j.aue.2019.153039
26. Panda PK, Ghosh D. Wideband and high gain tuning fork shaped monopole antenna using high impedance surface. *Int J Electron Commun* (2019) 111:152920. doi:10.1016/j.aue.2019.152920
27. Rao M, Sowmya N. Design and analysis of High impedance surface modified 3D antennas. *CSI Transactions on ICT* (2018) 6(2):173–177. doi:10.1007/s40012-018-0194-z
28. Wang L-L, Liu S-B, Zhang H-F, Kong X-K, Liu L-L. High-impedance surface-based flexible broadband absorber. *J Electromagn Waves Appl* (2017) 31(13):1216–1231. doi:10.1080/09205071.2017.1326850
29. Costa F, Monorchio A, Manara G. Analysis and design of ultra thin electromagnetic absorbers comprising resistively loaded high impedance surfaces. *IEEE T Antenn Propag* (2010) 58(5):1551–1558. doi:10.1109/tap.2010.2044329
30. Tretyakov SA, Maslovski SI. Thin absorbing structure for all incidence angles based on the use of a high-impedance surface. *Microw Opt Technol Lett* (2003) 38(3):175–178. doi:10.1002/mop.11006
31. Liu F, Tsilipakos O, Pitilakis A, Tasolamprou AC, Mirmoosa MS, Kantartzis NV, et al. Intelligent metasurfaces with continuously tunable local surface impedance for multiple reconfigurable functions. *Phys Rev Appl* (2019) 11(4):044024. doi:10.1103/PhysRevApplied.11.044024

Conflict of Interest: Author YC was employed by the company Shanghai Mi Xuan Electronic Technology Co., Ltd.

The remaining authors declare that the research was conducted in the absence of any commercial or financial relationships that could be construed as a potential conflict of interest.

Copyright © 2021 Wei, Li, Xu and Cao. This is an open-access article distributed under the terms of the Creative Commons Attribution License (CC BY). The use, distribution or reproduction in other forums is permitted, provided the original author(s) and the copyright owner(s) are credited and that the original publication in this journal is cited, in accordance with accepted academic practice. No use, distribution or reproduction is permitted which does not comply with these terms.



Infrared and Terahertz Compatible Absorber Based on Multilayer Film

Mingyang Yang¹, Ming Zhou^{2*}, Jianwen Yu¹, Yibo Zhang¹, Benyan Xu¹, Wenjun Cheng¹ and Xuyin Li¹

¹State Key Laboratory of Tribology, School of Mechanical Engineering, Tsinghua University, Beijing, China, ²Key Laboratory for Advanced Materials Processing Technology, Ministry of Education, Beijing, China

In this paper, a similar Fabry-Perot cavity structure utilizing a multilayer film structure consisting of an ultrathin metal film is demonstrated for absorbing the infrared ray. This structure has low emissivity in the atmospheric window (3–5 and 8–14 μm) and high emissivity in the nonatmospheric window (5–8 μm). These properties improved the stealth performance which causes the high emissivity in 5–8 μm to radiate more energy to reduce its temperature. Based on this, the periodic microstructures were added to the surface of the materials that enhanced the absorption of terahertz wave (0.1–2.7 THz). The absorber based on multilayer film has a simple structure and low manufacturing cost. This work may provide a new strategy for infrared and terahertz compatible stealth technology.

Keywords: wavelength-selective, compatible absorber, infrared, terahertz, multilayer, microstructure

OPEN ACCESS

Edited by:

Fuli Zhang,
Northwestern Polytechnical
University, China

Reviewed by:

Yongqiang Pang,
Xi'an Jiaotong University, China
Jiafu Wang,
Air Force Engineering University, China

*Correspondence:

Ming Zhou
zhouming@tsinghua.edu.cn

Specialty section:

This article was submitted to
Optics and Photonics,
a section of the journal
Frontiers in Physics

Received: 26 November 2020

Accepted: 04 January 2021

Published: 17 February 2021

Citation:

Yang M, Zhou M, Yu J, Zhang Y, Xu B,
Cheng W and Li X (2021) Infrared and
Terahertz Compatible Absorber Based
on Multilayer Film.
Front. Phys. 9:633971.
doi: 10.3389/fphy.2021.633971

INTRODUCTION

Materials with wavelength-selective absorption capacity have application potential in selective thermal radiation [1–6], thermal photovoltaic systems [7–12], infrared stealth [13–18], etc., which attracted the attention of many scholars. Radiation cooling is to achieve cooling effect by radiating its own heat to outer space in the form of electromagnetic waves. According to Kirchhoff's law, the emissivity of an object is equal to its absorptivity in thermal equilibrium. To improve efficiency, the materials should have a high emissivity in 8–14 μm and have a low emissivity in nonatmospheric window to reduce the absorption of radiation from other objects in the environment. In the field of thermal photovoltaics, the spectral selective absorption coating is the core component, which directly determines the light-to-heat conversion efficiency of the entire system. The wavelength-selective absorber needs to have high emissivity in the visible-near infrared band (0.3–2.5 μm) and the lowest possible emissivity in the mid-and-far infrared band (2.5–25 μm), where the thermal radiation at its own working temperature is located. This property plays the role of restraining energy loss caused by radiation heat dissipation while absorbing the energy of sunlight.

In the field of infrared stealth, the performance requirements for wavelength-selective absorption materials are opposite to that of radiation cooling. The materials need to have low emissivity in the two atmospheric windows (3–5 and 8–14 μm) to reduce the possibility of being detected by the detection equipment. According to Stephen-Boltzmann's law, the radiation energy of an object, defined as the radiant exitance W , $W = \varepsilon\sigma T^4$, where σ is Stephen-Boltzmann's constant and ε and T are the emissivity and absolute temperature of the object, respectively. Therefore, reducing object radiation can be achieved by cooling or reducing emissivity. The main means to achieve stealth is to reduce the emissivity which causes the cost of cooling to be high [19]. There is a serious problem that the low emissivity of the whole band will affect the heat exchange process, making it difficult for heat to diffuse out in time. This may cause heat accumulation and increase the temperature of the target, thus increasing the radiation energy of the object and weakening the stealth performance. Materials

with wavelength-selective absorption capabilities also have great application potential in infrared stealth technology. Specifically, the material needs to have a low emissivity in 3–5 and 8–14 μm to reduce detectability, while having a high emissivity in 5–8 μm outside the atmospheric window, which can diffuse the heat in time and lower its temperature to realize better infrared stealth. Most of the existing materials do not have such characteristics, so it is difficult to achieve the selective absorption performance to meet the stealth requirement by using traditional material systems.

Metamaterials or photonic crystals can be used to modulate the spectral absorption characteristics [20–22], so they have application prospects in the field of wavelength-selective absorption. The existence of the photonic bandgap in the photonic crystal makes it attract attention, and its absorption spectrum can be controlled through structural design. Similarly, the plasmonic structure has attracted attention due to its excellent electromagnetic response performance [23–25] and usually consists of a top patterned metal layer, a middle dielectric spacer, and a reflective metal substrate. Adjusting the absorptivity of these structures is mainly through electromagnetic resonance, which can tune the resonant frequency according to the reasonable structure design and even expand or move the resonance region. Due to the high manufacturing cost and the difficulty in realizing the excitation of ultrawideband resonance mode, the practical application of these materials is still limited.

In recent years, the researches of metamaterial functional devices in the terahertz band have made great progress, such as terahertz perfect absorbers [26], filters [27], stealth devices [28–30], and EIT devices [31]. As the improvement of related research about terahertz radar, the development of stealth devices has received a lot of attention. The metamaterials currently used for stealth in the terahertz band are mainly designed through microstructures, utilizing subwavelength structure arrays to control conductivity and magnetic permeability, thereby generating strong absorption at specific frequencies. Because of the contradiction between terahertz and infrared stealth requirements for material (low reflection and high absorption in terahertz; high reflection and low absorption in infrared), there are many problems in stealth materials compatible with the two wavebands.

In this work, the radiation characteristics of ultrathin Pt layer and impedance matching were utilized to design a wavelength-selective absorber based on planarized platinum/silicon (Pt/Si) multilayer film for infrared stealth. This absorber can effectively suppress thermal radiation in two atmospheric windows and enhance thermal radiation in the nonatmospheric window. Meanwhile, the absorber has the advantages of simple structure and easy to mass manufacturing. The overall resonance frequency of the structure was tuned by changing the thickness of the film. Also, microstructures were added to the surface to meet the requirements to enhance the absorption of terahertz waves. This research may provide a new strategy for stealth materials compatible with infrared and terahertz.

RESULT AND DISCUSSION

The Wavelength-Selective Absorber in Infrared Band

The wavelength-selective absorber used for infrared stealth in 3–14 μm consists of four layers, including one ultrathin Pt layer, one bottom reflective Pt layer, and two Si dielectric spacers, shown in **Figure 1A**. For the unique radiation characteristics of metals, the ultrathin Pt layer plays an important role as the main radiation layer. The silicon used in this research is crystalline silicon. The two Si layers tuned the characteristics of wavelength-selective absorption through impedance matching. The thickness of each layer was calculated by COMSOL; finally, the whole structure met the requirements of infrared stealth, shown in **Figure 1B**. The absorber has low absorptivity in the two atmospheric windows (3–5 and 8–14 μm), and high absorptivity in the nonatmospheric window (5–8 μm). Meanwhile, the manufacturing method of the designed structure is relatively simple; large-scale manufacturing could be realized through electron beam evaporation and magnetron sputtering.

The enhancement of thermal radiation in 5–8 μm is quite distinct from the traditional metal-based absorber (plasmonic resonance in metamaterials); this work utilized the radiation characteristics of the ultrathin Pt layer. The Pt has a large extinction coefficient and a high density of free electrons in the infrared band. Because the ultrathin Pt layer cannot shield the fluctuating current from radiating to free space due to the tunneling effect, this layer has a higher absorptivity in the infrared band [32]. But the bulk metal can screen the fluctuating current, so the bottom Pt layer played a role in reflecting the infrared wave. Therefore, the ultrathin Pt layer is essential for increasing the absorptivity.

However, a single ultrathin Pt layer cannot achieve the requirements of wavelength-selective absorption in the infrared band. The overall absorption characteristics are adjusted through the dielectric Si to meet the design requirements. In this work, the root-mean-square deviation (RMSD) is used for quantification of the wavelength-selective absorptivity between the calculated and ideal absorber as **Eq. 1**.

$$RMSD = \sqrt{\frac{\sum_{3\mu\text{m}}^{14\mu\text{m}} (\epsilon_{cal,\lambda} - \epsilon_{ideal,\lambda})^2}{N}}, \quad (1)$$

where $\epsilon_{cal,\lambda}$ and $\epsilon_{ideal,\lambda}$ are the absorptivity of calculated and ideal absorber within 3–14 μm and N is the number of wavelengths.

The thickness of the top and middle Si layers was obtained when the value of RMSD between calculated and ideal absorber reached the minimum as shown in **Figure 2**.

The wavelength-selective absorptivity requirements of infrared stealth could be met when the top Si layer is 333 nm and the middle Si layer is 623 nm. Because the bottom Pt layer is used for reflecting the infrared wave, the thickness should not be less than 50 nm. In this research, the thickness of the bottom Pt layer is 100 nm. Meanwhile, the ultrathin Pt layer is 15 nm, considering the film-forming property and the radiation performance. The absorptivity of the material was shown in

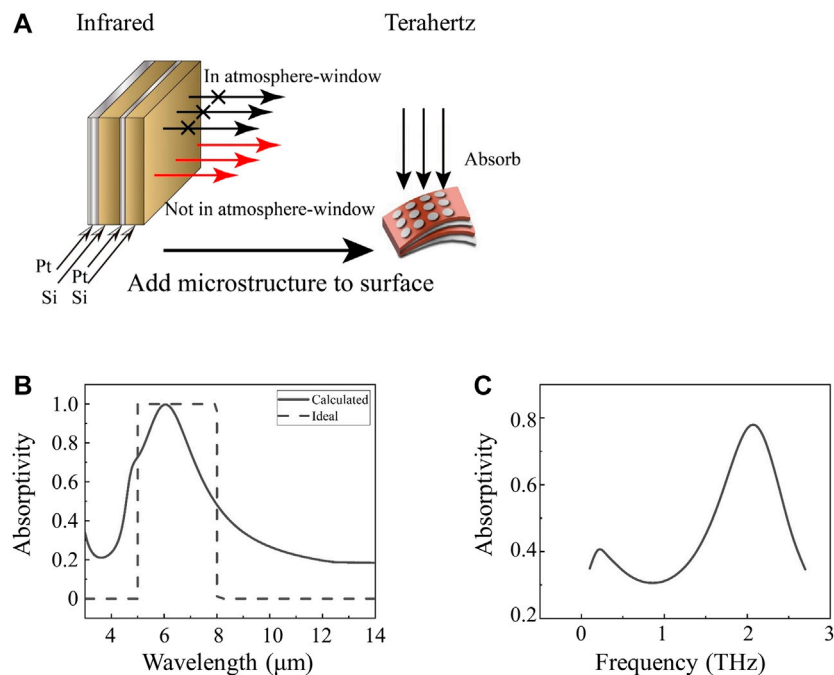


FIGURE 1 | (A) Schematic of wavelength-selective absorber in infrared and added microstructure in terahertz; **(B)** calculated and ideal absorptivity of the absorber in infrared; **(C)** absorptivity in terahertz (added microstructure).

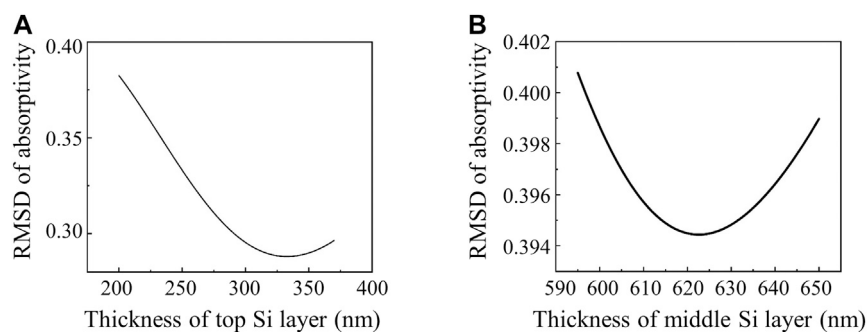


FIGURE 2 | Root-mean-square deviation (RMSD) of the absorptivity relative to the ideal absorber with thickness changes. **(A)** in the top Si spacer; **(B)** in the middle Si space.

Figure 1B. Based on the impedance matching principle, the addition of Si dielectric spacer adjusted the wavelength-selective absorptivity. Within a certain spectral range, the impedance of a structure matches the impedance of air (the real part of impedance close to 1 and imaginary part close to 0); the incident electromagnetic waves can enter the structure instead of being reflected on the surface. The impedance can be calculated by Eq. 2.

$$Z = \sqrt{\frac{(1 + S_{11})^2 - S_{21}^2}{(1 - S_{11})^2 - S_{21}^2}}, \quad (2)$$

where S_{11} and S_{21} are the S-parameters of the wavelength-selective absorber. The results showed that the similarity of the

impedance of absorber to the impedance of air (quantified by RMSD) in the high absorptivity region (5–8 μm) is $1.6 + 0.9i$, while the value of the similarity in atmospheric windows is $3.01 + 3.06i$ (3–5 μm) and $1.38 + 2.26i$ (8–14 μm). The calculation results are shown in Figure 3.

According to the result of impedance calculation, in the high absorptivity band, the impedance of the absorber is closer to the impedance of air than in the low absorptivity band. Therefore, the incident electromagnetic wave can reach the ultrathin Pt layer in 5–8 μm band, causing a higher absorptivity, while most of the electromagnetic waves are reflected by the surface in atmospheric windows, resulting in a low absorptivity. Consequently, based on the impedance matching principle, the absorption characteristics of the absorber can be tuned by changing the thickness of Si

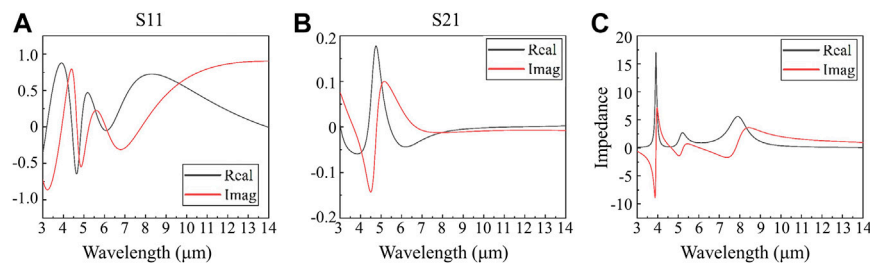


FIGURE 3 | Calculated parameters of the Pt/Si multilayer based wavelength-selective absorber in 3–14 μm . **(A)** S11; **(B)** S21; **(C)** impedance.

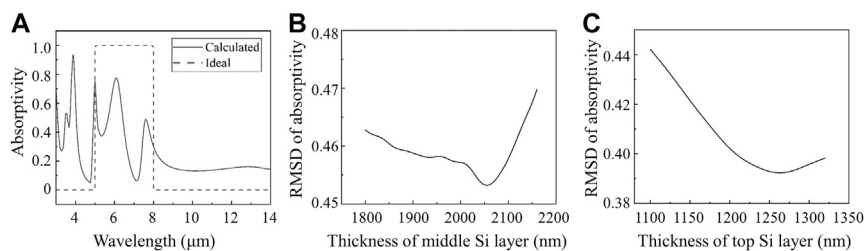


FIGURE 4 | **(A)** Absorptivity of wavelength-selective absorber. Root-mean-square deviation (RMSD) of the absorptivity relative to the ideal absorber with thickness changes. **(B)** in the middle Si spacer; **(C)** in the top Si spacer.

layers. The four-layer structure can be prepared on substrates like stainless steel, polylactic acid (PLA), and other materials. Platinum can be deposited by magnetron sputtering or electron beam evaporation to control the thickness accurately, and silicon will be fabricated through electron beam evaporation for large-scale manufacturing.

The Wavelength-Selective Absorber in Terahertz Band (Compatible With Infrared)

Because the wavelength of electromagnetic waves in 0.1–2.7 THz is different from the infrared band, the designed wavelength-selective absorber above is not applicable. It is necessary to make some adjustments to the structure to maintain the selective absorption characteristics in the infrared band while improving the absorption performance of terahertz waves by constructing a certain microstructure on the surface.

Since the material has a structure similar to the Fabry-Perot cavity, the absorption performance requirements can be met by adjusting the thickness of the two Si dielectric spacers, while keeping the thickness of the ultrathin metal Pt layer and the bottom reflective Pt layer unchanged. For the reason of the wavelength of the terahertz band, the middle Si layer should be about 2000 nm thick to meet the absorption requirements. The RMSD between the calculated and ideal absorber is shown in **Figure 4**, as the thickness of the top and middle Si layer changed.

According to **Figure 4**, the thickness of the middle Si layer is 2055 nm and the thickness of the top Si layer is 1,263 nm which can relatively well achieve the wavelength-selective absorption that meets the requirements of infrared stealth. The thickness of

the bottom Pt layer and the middle ultrathin Pt layer is 100 nm and 15 nm, respectively. At the same time, this structure can provide a foundation for the compatible absorption of terahertz waves.

Considering the convenience of processing and good absorption for both TE and TM waves, the surface microstructure should be designed as simple as possible with high symmetry. It was finally decided to select the surface microstructure as a periodic array of cylinders. Based on the Pt/Si four-multilayer structure, add a periodic array of Pt cylinders to the surface of the top Si layer to improve the absorption of the terahertz wave. Fix the height of cylinders to 0.2 μm , and calculate the absorptivity of the material at 0.1–2.7 THz while changing the radius of the cylinders; the curve of absorptivity is shown in **Figure 5A**.

It can be seen that the position of the absorption peak in the terahertz band changes with the change of the radius of cylinders. In order to make the material absorb more electromagnetic waves in the target band, the area of absorptivity curves enclosed with the X-axis should be as large as possible. According to **Figure 5B**, when the radius of cylinders is 9.3 μm , the material has the best absorptive capacity. In 1–2.4 THz, the absorptivity of the material is all over 0.4.

Then adjust the height of cylinders and calculate the absorptivity curves of the material in 0.1–2.7 THz, shown in **Figure 5C**. At the same time, it is necessary to consider that the addition of microstructures should not have much influence on the absorptivity in the infrared band. Finally, the height of cylinders is determined to be 0.8 μm . It can be seen that the absorptivity curve has an absorption peak in 1.9–2.2 THz and the

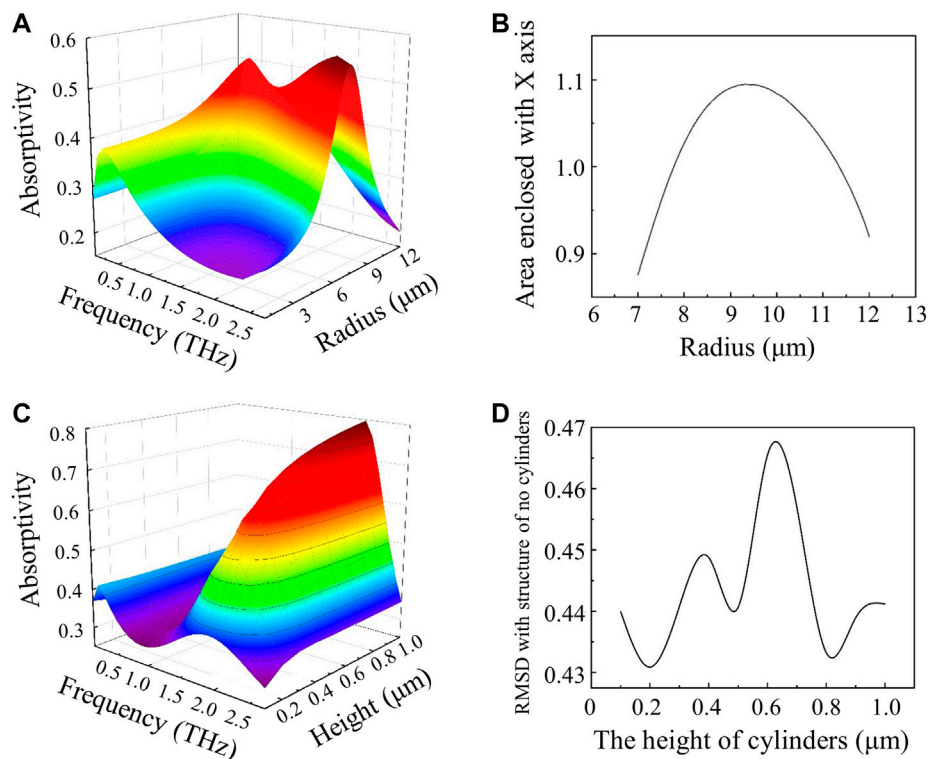


FIGURE 5 | The absorptivity of material with parameters of cylinders changing in 0.1–2.7 THz. **(A)** radius; **(C)** height; **(B)** the area of absorptivity curves enclosed with X axis when radius of cylinders changing; **(D)** the root-mean-square deviation of absorptivity between structure with and without cylinders in infrared band when there are changes in the height of cylinders.

numerical value of the absorption peak is over 0.7. The absorptivity of the material in terahertz is shown in **Figure 1C**.

For the processing of the microstructure on the surface, it can use laser to process the array of cylinders, because platinum is not very hard to process. In order to improve the absorptivity of terahertz further, cylinders with different radius in a period could be used. As the radius of cylinder determines the position of the absorption peak, the superposition of several absorption peaks can broaden the absorption bandwidth that improves the absorption performance. This work proved that, by utilizing multilayer films and metamaterials, we can achieve compatible stealth in infrared and terahertz bands.

CONCLUSION

In conclusion, this research proposed a material with a simple structure and could be mass manufacturing based on multilayer film. The material has the ability of wavelength-selective absorption that meets the requirements of infrared stealth. By structural design, the calculated wavelength-selective absorber has low absorptivity in the two atmospheric windows (3–5 and

8–14 μm) and high absorptivity in the nonatmospheric window (5–8 μm), which has excellent stealth performance in the infrared band. Moreover, with the addition of a periodic array of Pt cylinders on the surface, the absorption capacity of the material in terahertz is significantly enhanced. Meanwhile, the material can still meet the performance requirements of stealth in an infrared band. This work may provide a new strategy for the compatible stealth in infrared and terahertz bands.

DATA AVAILABILITY STATEMENT

The raw data supporting the conclusions of this article will be made available by the authors, without undue reservation.

AUTHOR CONTRIBUTIONS

MZ and MY conceived and designed the research work. MY carried out the simulations. MY, JY, and YZ analyzed the data. MY wrote the paper. BX, WC, and XL contributed to helpful discussions to research and modification to the article.

REFERENCES

- Liu X, Tyler T, Starr T, Starr AF, Jokerst NM, Padilla WJ. Taming the blackbody with infrared metamaterials as selective thermal emitters. *Phys Rev Lett* (2011) 107(4):045901. doi:10.1103/PhysRevLett.107.045901
- Yang ZY, Ishii S, Yokoyama T, Dao TD, Sun M-G, Pankin PS, et al. Narrowband wavelength selective thermal emitters by confined tamm plasmon polaritons. *ACS Photonics* (2017) 4(9):2212–219. doi:10.1021/acsp Photonics.7b00408
- Shahsafi A, Joe G, Brandt S, Shneidman AV, Stanisic N, Xiao Y, et al. Wide-angle spectrally selective absorbers and thermal emitters based on inverse opals. *ACS Photonics* (2019) 6(11):2607–611. doi:10.1021/acsp Photonics.9b00922
- Du KK, Li Q, Lyu YB, Ding JC, Lu Y, Cheng ZY, et al. Control over emissivity of zero-static-power thermal emitters based on phase-changing material GST. *Light Sci Appl* (2017) 6(1):e16194. doi:10.1038/lsa.2016.194
- Kecebas MA, Menguc MP, Kosar A, Sendur K. Passive radiative cooling design with broadband optical thin-film filters. *J Quant Spectrosc Radiat Transf* (2017) 198:179–86. doi:10.1016/j.jqsrt.2017.03.046
- Doiron CF, Naik GV. Non-hermitian selective thermal emitters using metal-semiconductor hybrid resonators. *Adv Mater* (2019) 31(44):e1904154. doi:10.1002/adma.201904154
- Mu X, Yu X, Xu D, Shen X, Xia Z, He H, Zhu H, et al. High efficiency organic/silicon hybrid solar cells with doping-free selective emitter structure induced by a WO₃ thin interlayer. *Nano Energy* (2015) 16:54–61. doi:10.1016/j.nanoen.2015.06.015
- Ding D, Lu G, Li Z, Zhang Y, Shen W. High-efficiency n-type silicon PERT bifacial solar cells with selective emitters and poly-Si based passivating contacts. *Solar Energy* (2019) 193:494–501. doi:10.1016/j.solener.2019.09.085
- Kim J, Yun JH, Kim H, Cho Y, Park HH, Kumar MM, et al. Transparent conductor-embedding nanocones for selective emitters: optical and electrical improvements of Si solar cells. *Sci Rep* (2015) 5(1):9256–8. doi:10.1038/srep09256
- Bhatt R, Kravchenko I, Gupta M. High-efficiency solar thermophotovoltaic system using a nanostructure-based selective emitter. *Solar Energy* (2020) 197:538–45. doi:10.1016/j.solener.2020.01.029
- Chen Y B, Parashar P, Yang YH, Rawat T S, Chen SW, Shen CH, et al. Transparent planar indium tin oxide for a thermo-photovoltaic selective emitter. *Opt Mater Express* (2020) 10(9):2330–44. doi:10.1364/OME.397246
- Hassan S, Doiron CF, Naik GV. Optimum selective emitters for efficient thermophotovoltaic conversion. *Appl Phys Lett* (2020) 116(2):023903. doi:10.1063/1.5131367
- Park C, Kim J, Hahn JW. Selective emitter with engineered anisotropic radiation to minimize dual-band thermal signature for infrared stealth technology. *ACS Appl Mater Interfaces* (2020) 12(38):43090–97. doi:10.1021/acsaami.0c12283
- Zhao L, Liu H, He Z, Dong S. All-metal frequency-selective absorber/emitter for laser stealth and infrared stealth. *Appl Opt* (2018) 57(8):1757–64. doi:10.1364/AO.57.001757
- Kim J, Han K, Hahn JW. Selective dual-band metamaterial perfect absorber for infrared stealth technology. *Sci Rep* (2017) 7(1):6740–9. doi:10.1038/s41598-017-06749-0
- Chen X, Tian C, Che Z, Chen T. Selective metamaterial perfect absorber for infrared and 1.54 μm laser compatible stealth technology. *Optik* (2018) 172:840–46. doi:10.1016/j.ijleo.2018.07.091
- Zhong S, Wu L, Liu T, Huang J, Jiang W, Ma Y. Transparent transmission-selective radar-infrared bi-stealth structure. *Opt Express* (2018) 26(13):16466–76. doi:10.1364/OE.26.016466
- Peng L, Liu D, Cheng H, Zhou S, Zu M. A multilayer film based selective thermal emitter for infrared stealth technology. *Adv Opt Mat* (2018) 6:1801006. doi:10.1002/adom.201801006
- Moghim M J, Lin G, Jiang H. Broadband and ultrathin infrared stealth sheets. *Adv Eng Mater*. (2018) 20(11):1800038. doi:10.1002/adem.201800038
- Cen C, Zhang Y, Liang C, Chen X, Yi Z, Duan T, et al. Numerical investigation of a tunable metamaterial perfect absorber consisting of two-intersecting graphene nanoring arrays. *Phys Lett A* (2019) 383(24):3030–35. doi:10.1016/j.physleta.2019.06.028
- Kawamoto Y, Tanaka Y, Ishizaki K, De Zoysa M, Asano T, Noda S. Structural optimization of photonic crystals for enhancing optical absorption of thin film silicon solar cell structures. *IEEE Photonics J* (2014) 6(1):1–10. doi:10.1109/jphot.2014.2302800
- Hajian H, Ghobadi A, Butun B, Ozbay E. Nearly perfect resonant absorption and coherent thermal emission by hBN-based photonic crystals. *Opt Express* (2017) 25(25):31970–87. doi:10.1364/OE.25.031970
- Gomez-Diaz JS, Tymchenko M, Lee J, Belkin MA, Alù A. Nonlinear processes in multi-quantum-well plasmonic metasurfaces: electromagnetic response, saturation effects, limits, and potentials. *Phys Rev B* (2015) 92(12):125429. doi:10.1103/PhysRevB.92.125429
- Shvonski AJ, Kong J, Kempa K. Nonlocal extensions of the electromagnetic response of plasmonic and metamaterial structures. *Phys Rev B* (2017) 95(4):045149. doi:10.1103/PhysRevB.95.045149
- Dai J, Xu R, Lin YS, Chen CH. Tunable electromagnetic characteristics of suspended nanodisk metasurface. *Opt Laser Technol* (2020) 128:106214. doi:10.1016/j.optlastec.2020.106214
- Zhao X, Zhang J, Fan K, Duan G, Metcalfe GD, Wraback M, et al. Nonlinear terahertz metamaterial perfect absorbers using GaAs [Invited]. *Photon Res* (2016) 4(3):A16–21. doi:10.1364/PRJ.4.000A16
- Yang J, Gong C, Sun L, Chen P, Lin L, Liu W. Tunable reflecting terahertz filter based on chirped metamaterial structure. *Sci Rep* (2016) 6:38732. doi:10.1038/srep38732
- Manjappa M, Pitchappa P, Wang N, Lee C, Singh R. Active control of resonant cloaking in a terahertz MEMS metamaterial. *Adv Opt Mat* (2018) 6(16):1800141. doi:10.1002/adom.201800141
- Dao R, Kong X, Zhang H, Su X. A tunable broadband terahertz metamaterial absorber based on the vanadium dioxide. *Optik* (2019) 180:619–25. doi:10.1016/j.ijleo.2018.12.004
- Zhu J, Ma Z, Sun W, Ding F, He Q, Zhou L, et al. Ultra-broadband terahertz metamaterial absorber. *Appl Phys Lett* (2014) 105(2):021102. doi:10.1063/1.4890521
- Jung H, Jo H, Lee W, Kim B, Choi H, Kang MS, et al. Electrical control of electromagnetically induced transparency by terahertz metamaterial funneling. *Adv Opt Mat* (2019) 7(2):1801205. doi:10.1002/adom.201801205
- Wang Z, Luk TS, Tan Y, Ji D, Zhou M, Gan Q, et al. Tunneling-enabled spectrally selective thermal emitter based on flat metallic films. *Appl Phys Lett*. (2015) 106(10):101104. doi:10.1063/1.4914886

Conflict of Interest: The authors declare that the research was conducted in the absence of any commercial or financial relationships that could be construed as a potential conflict of interest.

Copyright © 2021 Yang, Zhou, Yu, Zhang, Xu, Cheng and Li. This is an open-access article distributed under the terms of the Creative Commons Attribution License (CC BY). The use, distribution or reproduction in other forums is permitted, provided the original author(s) and the copyright owner(s) are credited and that the original publication in this journal is cited, in accordance with accepted academic practice. No use, distribution or reproduction is permitted which does not comply with these terms.



A Review of Tunable Electromagnetic Metamaterials With Anisotropic Liquid Crystals

Jing Xu, Ruisheng Yang, Yuancheng Fan*, Quanhong Fu and Fuli Zhang*

Key Laboratory of Light-Field Manipulation and Information Acquisition, Ministry of Industry and Information Technology and School of Physical Science and Technology, Northwestern Polytechnical University, Xi'an, China

OPEN ACCESS

Edited by:

Petra Granitzer,
University of Graz, Austria

Reviewed by:

Iam Choon Khoo,
Pennsylvania State University,
United States
Andrey Miroshnichenko,
University of New South Wales,
Australia

*Correspondence:

Yuancheng Fan
phyfan@nwpu.edu.cn
Fuli Zhang
fuli.zhang@nwpu.edu.cn

Specialty section:

This article was submitted to
Optics and Photonics,
a section of the journal
Frontiers in Physics

Received: 24 November 2020

Accepted: 25 January 2021

Published: 24 February 2021

Citation:

Xu J, Yang R, Fan Y, Fu Q and Zhang F
(2021) A Review of Tunable
Electromagnetic Metamaterials With
Anisotropic Liquid Crystals.
Front. Phys. 9:633104.
doi: 10.3389/fphy.2021.633104

The performance of metamaterial is limited to a designed narrow band due to its resonant nature, it is highly desirable to incorporate active inclusions in metamaterials to extend the operation bandwidth. This review summarizes the development in realizing the tunability of electromagnetic response in metamaterials incorporated with nematic liquid crystal (LC). From rigorous comparison, it is found that the anisotropic property of nematic LC is essential in predicting the influence of LC molecular director orientation on the resonant frequency of metamaterials. By carefully designing the metamaterials and properly infiltrating LC, the operation frequency of single/double negative parameters of metamaterials can be dynamically modulated with remarkable red/blue-shift, depending on the LC molecular orientation angle. Moreover, the recent liquid crystal-based developments and novel applications are investigated and highlighted.

Keywords: tunable metamaterials, negative index metamaterial, liquid crystals, Liquid crystals reorientations, reconfigurable metamaterials

1 INTRODUCTION

In most cases, the electromagnetic parameters of natural materials are positive and larger than unity, while the materials whose optical parameters are less than unity or even negative are only investigated in specific hypotheses. Recently, metamaterials with customizable performance have attracted a great deal of attention in the fields of optics, electronics, physics, and materials, since their optical properties can be arbitrarily tailored by rationally designing their micro/nanostructures. Theoretically, the electromagnetic parameters of metamaterials (including the permittivity, permeability, and refractive index) can be designed with any desired values (even to negative), which provides an ideal platform for the free manipulation of electromagnetic waves.

In 1968, Veselago theoretically proposed a medium with both negative permittivity and permeability for the first time [1]. According to a rigorous analytical investigation, such a medium can exhibit various intriguing properties such as negative index, reversed Doppler effects, and perfect lens, etc. [2–5]. In natural materials, ferrite can exhibit negative permeability around its resonant frequencies, while metal can exhibit negative permittivity below its electron plasmon frequency [6]. However, research related to negative electromagnetic parameters has seldom been reported for a long time since natural materials rarely exhibit such special properties. To broaden the design strategies of material parameters, in 1996, Pendry proposed a kind of artificial structure with periodic split ring resonators (SRR), to significantly enhance the magnetic resonance and realize negative effective permeability [7]. Moreover, Pendry also designed a thin wire array to lower the plasma frequency and obtain a limited negative permittivity in a microwave frequency band [8]. Inspired by Pendry's works, D. R. Smith combined periodic metallic SRR and a wire array

together to promote simultaneous negative permittivity and permeability in a certain frequency band, and thus realized a negative refractive index for the first time in experiment [9]. They found that periodic SRR exhibited an effective negative permeability, and the wire array alone exhibited a negative permittivity below its effective plasma frequency, while with the SRR and wire array together, a passband would appear when both permittivity and permeability were negative. The experimental demonstration of negative index along with a serial confirmation of extraordinary behaviors has attracted increased interest for studies on metamaterials [10–12]. During the last few decades, metamaterials with various different structural designs including Omega [13], S type [14], and fishnet [15, 16], have been proposed. The rapid development of metamaterials has also stimulated many promising applications such as diffraction-unlimited imaging [17–19], invisible cloaks [20, 21], subwavelength high-Q cavities [22–25], polarization manipulation [26], and electromagnetic absorbers [27–30]. It is significant that the freely designable electromagnetic parameters of metamaterials are important for the implementation of such devices.

Metamaterials have shown exterior capability to manipulate electromagnetic waves, but there are still some problems hindering their development toward practical applications. As for traditional metamaterials, once the structural units are determined, they can only work well at a certain frequency range, which greatly limits their applications in practical engineering. The ever-increasing demand on designing versatile photonic devices inspires the rapid development of tunable metamaterials [31–35]. Several methods have been proposed to broaden their operation bandwidth with the incorporation of active inclusions, such as varactor diodes [36–38], semiconductors [39–41], ferroelectric [42], phase change materials [43], graphene [44–46], and anisotropic materials [47–50].

Liquid crystal (LC) has emerged as a promising candidate for the manipulation of light waves since its director axis and optical properties are strongly dependent on the surface effect and ambient temperature, and its optical properties are very sensitive to the variation of external fields (such as the electric field, magnetic field, light field, sound field, etc.) [51, 52]. The anisotropy of LC covers a wide frequency range from ultraviolet to microwave. Moreover, LC-based devices have many advantages such as small size, light weight, low cost, simple process, and continuous tunability. Therefore, as an excellent tunable functional material, LC is widely used in the optoelectronic fields. Recently, tunable metamaterials incorporated with liquid crystals have been widely reported in microwave, terahertz (THz), and even infrared bands. LC-based tunable metamaterials taking advantage of a large birefringence that can be dynamically controlled by applying external fields, have shown great potential to actively modulate the electromagnetic waves over a broad spectrum [15, 16, 47, 49, 50, 53–60].

Tunable LC metamaterials were first demonstrated in a microwave regime by applying external voltage [53, 59]. The reorientation of the nematic crystals takes a response time of 300 ms to obtain a frequency shift of 360 MHz with the voltage changing from 0 V to 100 V [59]. Khoo et al. theoretically

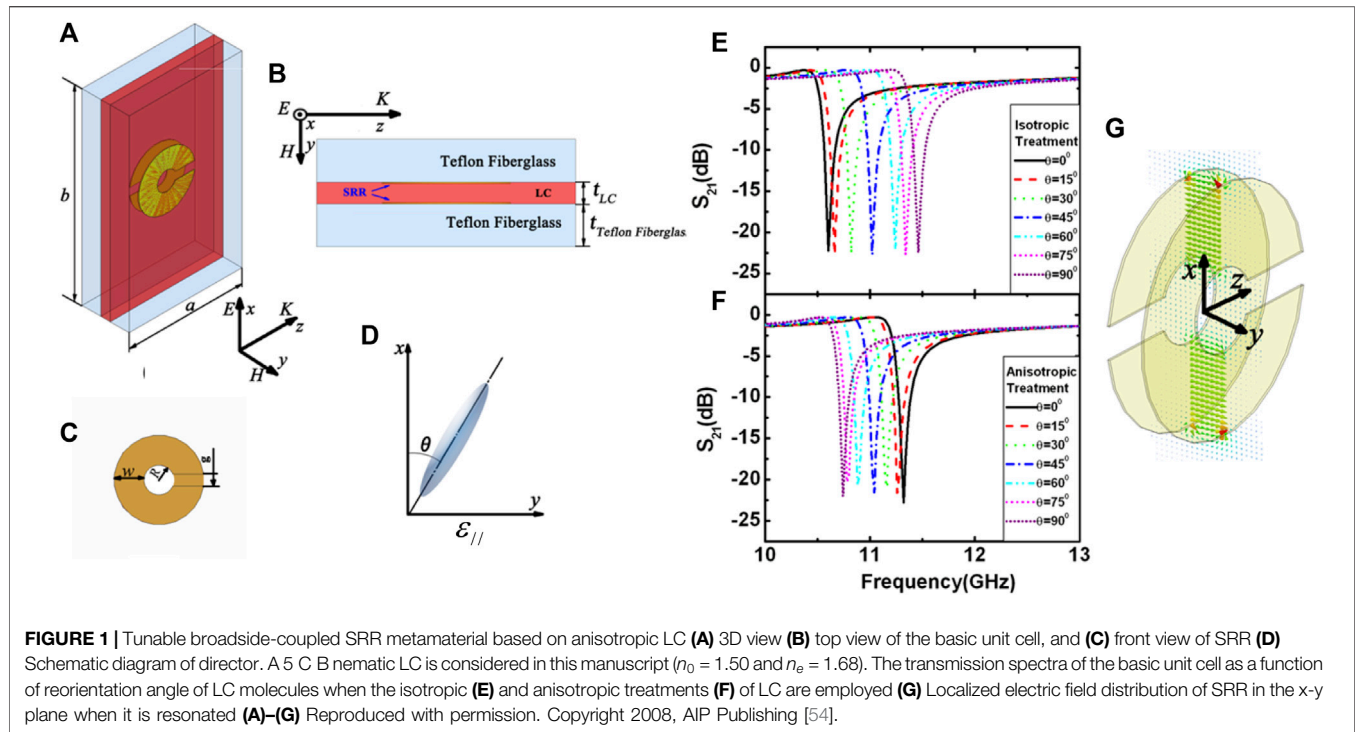
reported an analysis on tunable metamaterials based on core-shell nanospheres randomly dispersed in LC [47]. Werner et al. presented a reconfigurable metamaterial by sandwiching a nematic LC as a substrate into the conventional negative index metamaterial [50]. Wang et al. numerically investigated the tunability of metamaterials using a rigorous treatment for the LC director reorientation [49]. Compared to the control of microwaves, the manipulation of THz waves can be realized under a lower applied voltage with faster response speed due to the smaller required thickness of LCs. LC metamaterials with real-time control functions, such as polarization controllers [61], absorbers [62], and spatial light modulators [63] are employed in THz communications, imaging, sensing, detection, and other fields [64–69]. In 2013, Padilla et al. designed and implemented an LC-based tunable metamaterial absorber in the THz regime for the first time [70]. Subsequently, they also designed a THz spatial light modulation which could be independently controlled by a single pixel, and the overall modulation depth of the device reached 75% [71]. In 2017, Yang et al. used liquid crystals to achieve tunable THz metamaterial-like electromagnetically induced transparency and electromagnetically induced absorption, with modulation depths of 18.3 dB and 10.5 dB, respectively [72]. Vasić et al. realized an electrically adjustable liquid crystal THz metamaterial polarization converter based on a metal dielectric metal cavity structure [61]. Shen and others designed and implemented a multi-functional THz metamaterial device integrated with liquid crystal, which further expanded the application of liquid crystal metamaterial devices in the THz regime [73].

In this context, we will give a brief review for the development of tunable metamaterials incorporating liquid crystals. In **Section 2**, we will discuss the analytical approach for liquid crystals inside metamaterials in detail. **Section 3** presents tunable electromagnetic parameter metamaterials based on liquid crystals. A survey of the recent novel liquid crystal-based developments and application is conducted in **Section 4**. Finally, we will discuss some of the major limitations of LCs and envision a promising future of tunable metamaterials incorporating liquid crystals. Hopefully this review can promote the research on tunable and reconfigurable metamaterials with various active inclusions for the improvement of the operation bandwidth and smart electromagnetic responses.

2 ANALYTICAL APPROACH FOR LIQUID CRYSTALS INSIDE METAMATERIALS

During previous analysis for LCs incorporated into an artificial microstructure, an isotropic treatment was found to be effective provided that the EM fields exhibited isotropic field distributions as is the case for most of the 2D photonic crystals. This means that only consideration of the effective permittivity change of anisotropic LC along the incident electric field axis is required. For metamaterial, such an assumption is more doubtful and clearly the anisotropic distribution has to be taken into account.

In this section, we present a comparison of anisotropic and isotropic treatments for a C-type metamaterial. As shown in **Figure 1**, the SRR design used in the present work is composed of



double C-shaped strips with a back-to-back direction (Figure 1A) to avoid a magneto-electric response. The metal patterns are printed onto the surface of fiberglass slabs made by Teflon with voids, and then permeated with nematic LC [54]. It is assumed that the electric field of the incident beam is polarized along the x direction and the magnetic field of the incident beam is polarized along the y direction to illuminate the structure along z .

The LC layer is treated as a homogenous isotropic material during the first analysis. For aligned nematic liquid crystal, the electric field of the incident beam is polarized along the x direction (Figure 1), and its dielectric constant is approximately given as [56]:

$$\varepsilon = \frac{\varepsilon_{//}\varepsilon_{\perp}}{\varepsilon_{//}\sin^2\theta + \varepsilon_{\perp}\cos^2\theta} \quad (1)$$

Where ε_{\perp} and $\varepsilon_{//}$ represent the respective permittivities for the polarized beam perpendicular and parallel to the director axis n , θ denotes the rotation angle of the molecular director with respect to the x axis.

On the other hand, a rigorous tensor description for LC is introduced for the anisotropic permittivity of LC. For the LC plate with the initial vector of the molecules in the x direction, the director axis n can take all values $\{\cos\theta, \sin\theta, 0\}$ by applying a magneto/electric field based on the Fréedericksz effect. LC permittivity is described as follows [49, 55]:

$$\varepsilon = \begin{pmatrix} \varepsilon_{\perp} + \Delta\varepsilon\cos^2\theta & 0 & \Delta\varepsilon\cos\theta\sin\theta \\ 0 & \varepsilon_{\perp} + \Delta\varepsilon\sin^2\theta & 0 \\ \Delta\varepsilon\cos\theta\sin\theta & 0 & \varepsilon_{\perp} \end{pmatrix} \quad (2)$$

Where $\Delta\varepsilon = \varepsilon_{//} - \varepsilon_{\perp}$

Figure 1 shows the frequency dependence of the metamaterial transport response on the liquid crystal reorientation angle. For the isotropic treatment (Figure 1E), when the LC orients from 0° to 90° , the resonance frequency of SRR increases gradually from 10.9 to 11.4 GHz whose change is 0.8 GHz. On the contrary, for an anisotropic treatment as shown in Figure 1F, the resonance frequency of SRR shifts toward a lower frequency with the increase of the liquid crystal orientation angle. Figure 1G shows the electric field distribution in the x-y plane when the SRR is resonated. It is observed that the localized electric field around SRR is mostly concentrated on the space between two C strips and parallel to the y -direction, instead of being polarized along the x -direction where the incident beam is polarized. Therefore, isotropic treatment is no longer so valid for the tunability analysis for the metamaterial [55]. As a matter of fact, the capacitance of the SRR depends on the permittivity component of ε_x , ε_y , and ε_z , of which ε_y dominates as shown in Figure 1C. When an external field orientates the liquid crystal director from paralleling x to paralleling y , ε_y will grow from ε_0 to ε_e , resulting in an increase in the capacitance and a decrease in the resonance frequency.

3 TUNABLE ELECTROMAGNETIC PARAMETER METAMATERIALS BASED ON LIQUID CRYSTALS

3.1 Tunable Negative Permeability Metamaterial

In this section, we will introduce two types of negative permeability metamaterial with frequency tunability via LC

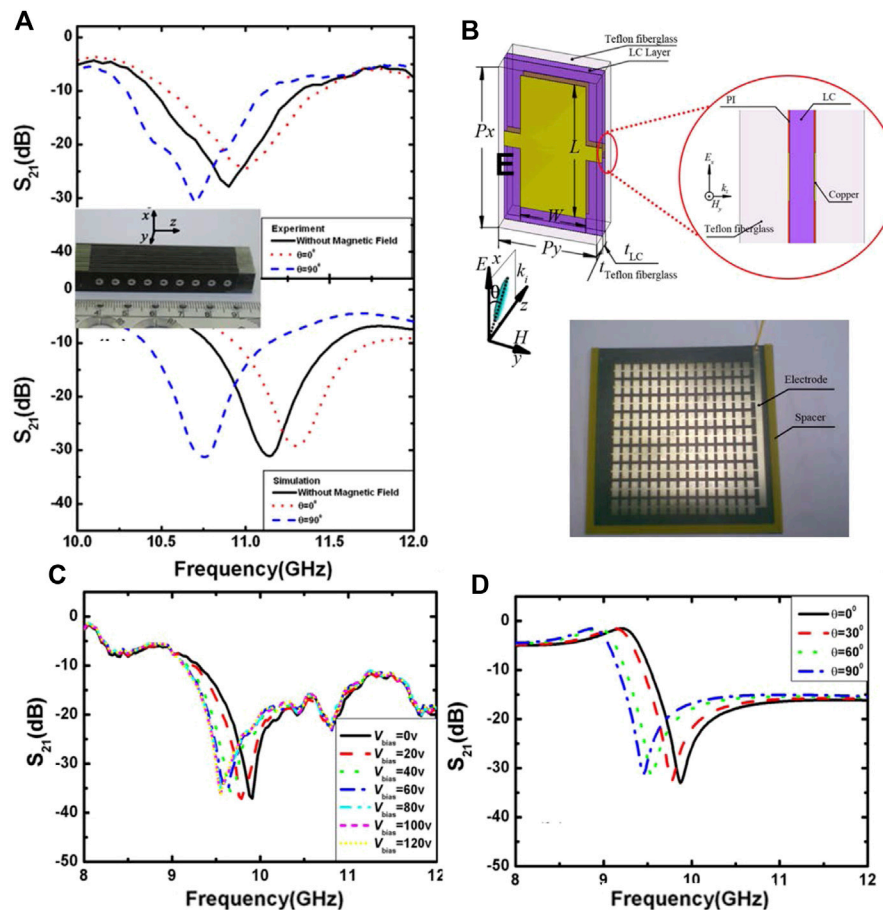


FIGURE 2 | (A) Demonstration of magnetically tunable SRR metamaterial. Inset is the view for the SRR prototype prepared for the infiltration of LC **(B)** Tunable short-wire pair-type of negative permeability metamaterial based on anisotropic LC **(C)** Experimental transmission magnitude for short-wire pair metamaterial as a function of external DC bias voltage **(D)** Numerical prediction of transmission spectra versus LC reorientation angle **(A)** Reproduced with permission. Copyright 2012, AIP Publishing [54] **(B)-(D)** Reproduced with permission. Copyright 2008, AIP Publishing [59].

reorientation. In **Figure 1**, a typical broadside coupling SRR incorporates an LC layer between two reversed C-type metallic patterns. The prototype sample was prepared using printed circuit board technology, as shown in the inset of **Figure 2A** [54]. The transfer rate of the tunable SRR archetype is measured in the following three conditions; i) the SRR without magnets (in this case the average permittivity is $\epsilon_0 = (2\epsilon_{\perp} + \epsilon_{\parallel})/3$), ii) applying the magnetic field along x ($\theta = 90^\circ$), and iii) along y ($\theta = 90^\circ$). The calculated results and experimental shown in **Figure 2A** indicate that a noticeable decrease occurs at 10.9 GHz for the instance without the external magnetic field. The resonance frequency increases to 11.0 and 10.7 GHz when the magnetic field is then applied parallel to the x and y axes, respectively. It can be seen that the dependency of the resonance frequency to the liquid crystal director reorientation corresponds to the calculating results that involve the description of the permittivity tensor of the nematic substance.

Unlike an SRR operating under grazing incidence with magnetic field perpendicular to its surface, **Figure 2B** shows an electrically tunable short-wire pair-type of negative

permeability metamaterial which can work under normal excitation of electromagnetic waves [59]. The unit cell of tunable metamaterial is made up of a couple of short wires put on the surface of fiberglass slabs made from Teflon with voids in between which were infiltrated with a nematic compound. And by adding an extra couple of narrower in-plane bars to connect neighbor unit cells. It can be assessed that such interconnecting bars do not change the magnetic resonance behavior of a short-wire pair. To give a preliminary orientation of LC, on the surface of the Teflon substrate and copper element is covered with a thin layer of polyimide (PI) to compel the nematic liquid crystal parallel to the short-wire surface in an alignment state [57, 59].

The transmission spectra for the short-wire metamaterial as a bias voltage function are given in **Figure 2C**. For zero-bias voltage, an obvious decrease takes place at 9.91 GHz, around that the effective permeability is anticipated to be negative. And the resonant frequency falls to 9.55 GHz as bias voltage gradually grows from 0 to 100 V. Then the saturation was adjusted and even the bias voltage was increased further. Therefore, the total

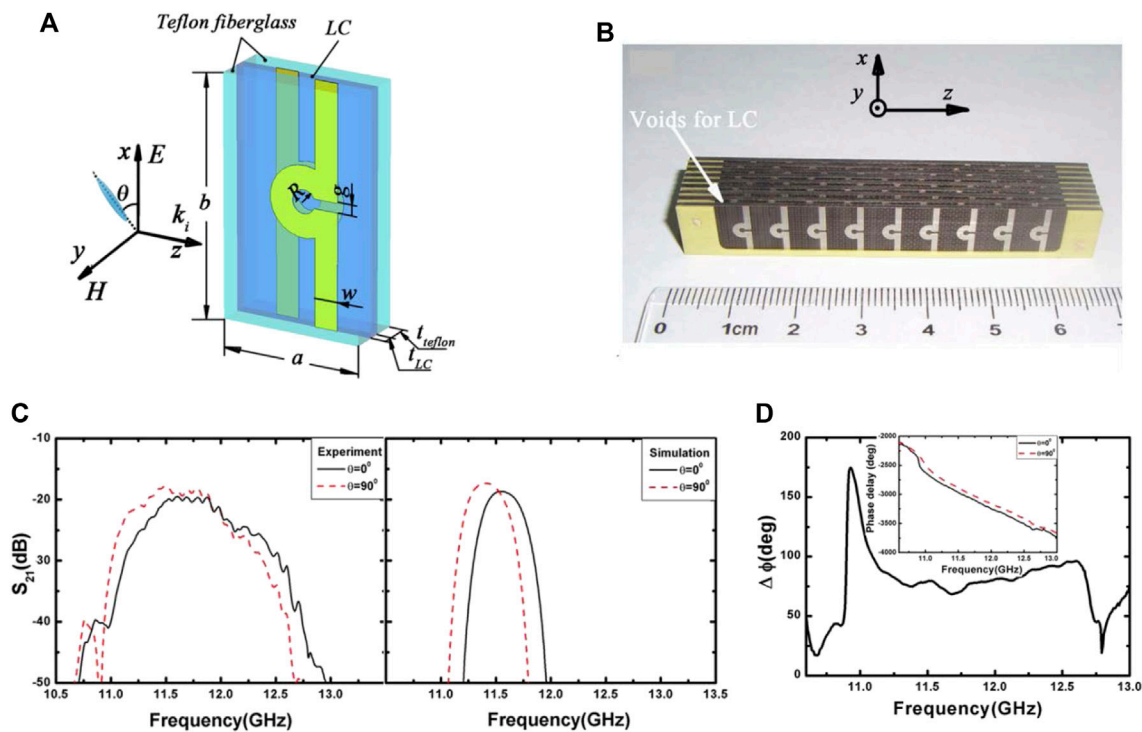


FIGURE 3 | (A) Schematic of the basic unit cell of the tunable negative index metamaterial as well as the reorientation of the LC molecule in the x - y plane **(B)** Close-up view of the mid-plane of the sample with the other part removed to clarify the configuration of the voids **(C)** The experimental and simulation transmission responses of the metamaterial with infiltration by LC under different molecules orientations: $\theta = 0^\circ$ (solid black line) and 90° (dashed red line), respectively **(D)** The measured phase shift for the tunable metamaterial when the LC molecules are reorientated from $\theta = 0^\circ$ – 90° . The inset shows the phase delays for the metamaterial under different reorientations of LC **(A)–(D)** Reproduced with permission. Copyright 2008, OSA Publishing [58].

frequency shift of 360 MHz can be achieved experimentally. From the full wave numerical calculation for the transmission spectra as a function of the LC molecular reorientation angle, as shown in **Figure 2D**, it is obvious that when the director of LC is redirected from 0° to 90° , magnetic resonance frequency of the short-wire pair gradually reduces to 9.45 GHz, which results in a 0.42 GHz variation. A slightly narrow frequency variation is most probably due to the existence of a pre-tilted angle of liquid crystal via the PI surface. This means actual LC reorientation will be less than 90° , resulting in less permittivity alteration as well as the changes of resonance frequency.

3.2 Negative Index Metamaterial

On the basis of the successful demonstration of a frequency tunable metamaterial with a single negative parameter, we will present a double negative metamaterial with a dynamically varied left-handed passband. The idea is to add negative permittivity via a wire array to the original negative components. In view of tunability requirements, it is necessary to employ unit cells with a combination of negative permittivity and negative permeability parts. **Figure 3** shows a tunable omega metamaterial sample with a broadside coupling SRR connected with infinite wire [58]. By utilizing external magnets, it is able to orientate the LC molecular director angle with respect to the x axis from 0° to 90° .

Figure 3C shows the experimental transmission spectra of the metamaterial. When applying the magnetic field along the x axis ($\theta = 0$), the omega array shows a clear transfer passband, and it has a negative index of refraction as expected, of which the peak is located at 11.72 GHz, whereas a redshift of the passband can be observed with the peak shifts at 11.50 GHz under an orthogonal magnetic field excitation ($\theta = 90$). Although this passband deviation of 210 MHz is not wide, it is clearly perceptible with the comparatively broad bandwidth. The frequency shift is in accordance with numerical results calculated using the full tensor description for LC permittivity, as shown in **Figure 3C**. Experimental broader bandwidth is mainly due to a slight variation of the voids interspacing since the Teflon fiberglass is not so rigid, resulting in different magnetic resonances between layers, causing multi conjoined passbands and consequently a wider transmission window. **Figure 3D** plots the phase shift for the omega sample with different LC direction angles. From the variation of phase shift, it can be seen that phase difference increases around 10.6 GHz and reaches a peak of 174.5° at 10.93 GHz, corresponding to an approximate index variation of 0.25 for a 5.4-cm-long sample along the propagation path.

Figure 4 shows the schematic view of the fishnet type of negative index metamaterial [60]. Due to the intrinsic structural characteristic, one layer of unit cells was connected to the other, therefore designing extra connecting bars for bias voltage is not

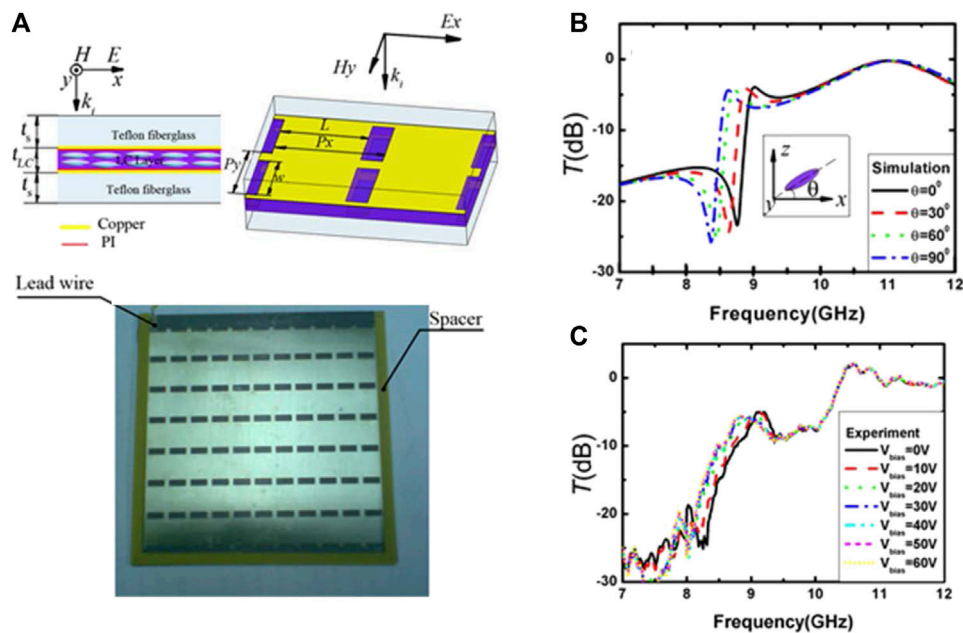


FIGURE 4 | (A) Tunable fishnet type of NIM based on nematic LC. Side view, 3D view of four elementary cells and photograph of metamaterial sample **(B)** Simulated transmission of tunable fishnet metamaterial when the LC director was reorientated. The inset is the schematic view of LC molecular reorientation in the x-z plane **(C)** Experimental transmission magnitude of the fishnet metamaterial as a function of external DC bias voltage **(A)–(C)** Reproduced with permission. Copyright 2008, OSA Publishing [60].

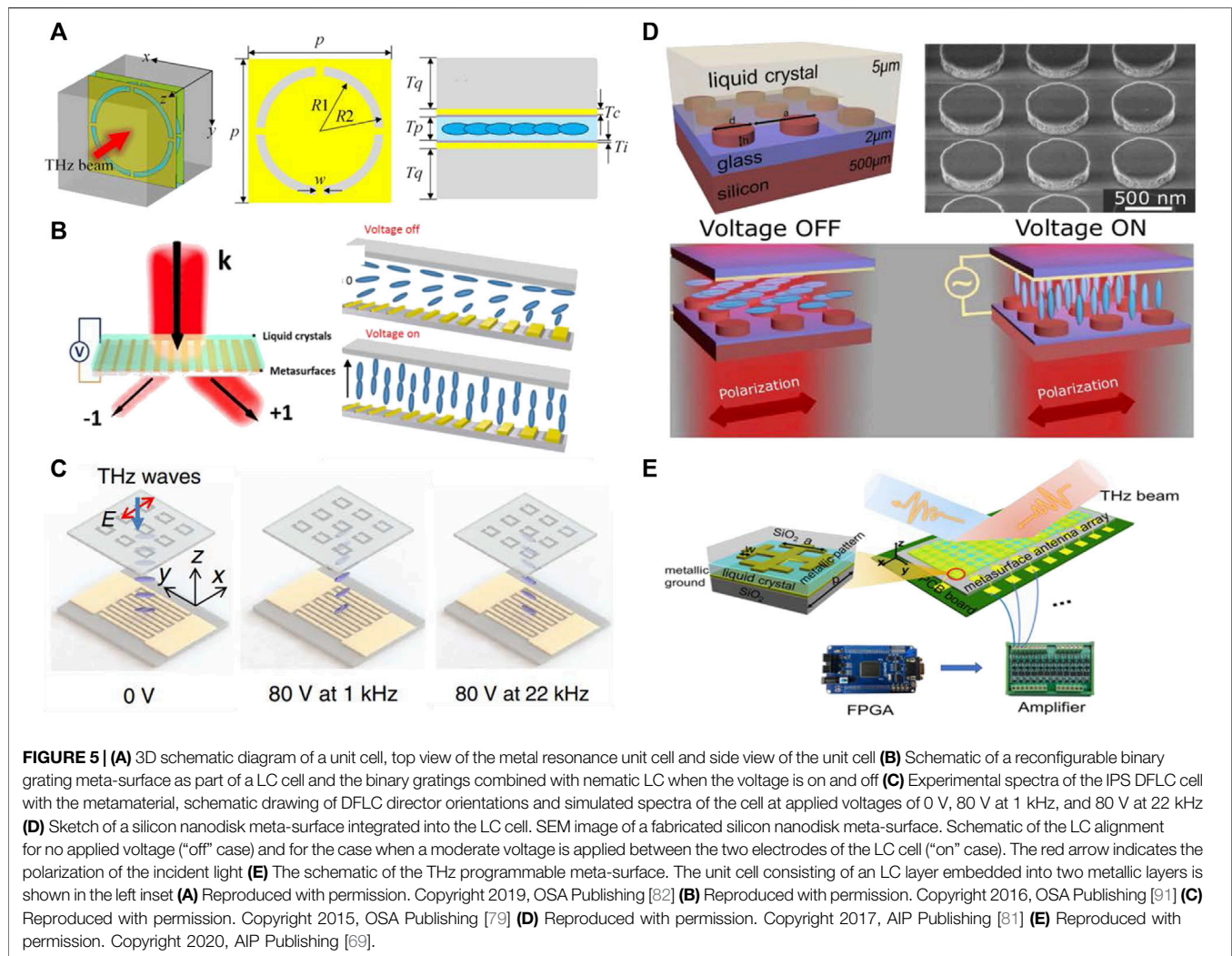
required. **Figure 4** gives the transmission spectra variation of the fishnet sample. As shown in **Figure 4B**, toward the initial target of liquid crystal director parallel to the fishnet surface, there is a well-resolved and high strength transfer summit around 9.01 GHz. The liquid crystal director redirecting from 0° to 90° shows that the ground transfer summit moves downward to 8.60 GHz. **Figure 4C** demonstrates the fishnet array's measured transmission spectra under different bias voltages. For zero-bias voltage, the fishnet structure displays a transfer passband starting at 9.14 GHz and another higher passband starting at 10.60 GHz with a smaller decrease in the gap. Quantitatively, as the bias voltage grows up to 60 V, the first transfer summit moves from 9.14 GHz downward to 8.80 GHz, accounting for a frequency shift of 340 MHz. The frequency shift for the passband is saturated beyond 60 V, indicating that the LC director is nearly perpendicular to the surface of the fishnet pattern.

4 RECENT DEVELOPMENT AND APPLICATIONS

4.1 Tunable Metamaterials With Liquid Crystals

Liquid crystals have the dual properties of crystals and fluids. As mentioned in **Section 3**, LC reorientations would result in a dramatic change in the refractive index of LC, which in turn, would further change the response to electromagnetic waves. In nematic LCs, the crystal is in a rod-shape and the external

stimulations such as thermal heating, pressure, and the magnetic and electric field, can control its directional order, resulting in good refractive index tunability [42, 59, 74–91]. Therefore, LCs are extensive used as the liquid background of solid metamaterials [51, 52, 92]. The manipulations on the LC background metamaterial are first protested against in the microwave regime. The resonant frequency of the metamaterial is shifted under a DC voltage [93–97]. Compared to the operation under microwave conditions, the control of the THz wave can be obtained with a much faster response at a lower electrical voltage since the needed thickness of LC is much smaller [69, 98, 99]. For liquid crystals in a particular phase such as NLC, it is necessary to discuss their collective crystal responses. The timescale of collective crystal response is usually in the order of milliseconds–microseconds. The thickness of the liquid crystal will influence its response speed. To achieve certain modulations requires a very thick LC layer, leading to several disadvantages such as high operating voltage, slow response, and poor pre-alignment. A large birefringent liquid crystal material can reduce the thickness of the liquid crystal device, ensure the good orientation of the liquid crystal, and improve the response speed of the device. For a liquid crystal layer of the same thickness, it can increase the modulation range of the liquid crystal device. Compared with the thermal and UV irradiation-induced tunability of optical metamaterials, which have been experimentally tested, showing a slow temporal response, electrical tuning has a faster time response, which is the most attractive due to its easy integration and high reliability.



Recently, a nematic liquid crystal-based tunable terahertz metamaterial which has large modulation depth and low insertion loss was designed [82]. The structure of the proposed compositive metamaterial is shown in **Figure 5A**, which consists of a two-layer sub-wavelength circular air loop array fabricated on a quartz glass substrate and embedded into the liquid crystal. The obtained results show that the amplitude modulation depth and insertion loss for normally incident electromagnetic waves are about 96% and 1.19 dB at 0.4212 THz, respectively, with the bias voltage varying from 0 to 16 V. Meanwhile, the transmission peak frequency gradually decreases from 0.42 to 0.38 THz. Differing from the resonant frequency shifted under a DC voltage, another literature paper about the continuously tunable and fast-response terahertz metamaterial was studied using in-plane switching (IPS) dual-frequency liquid crystal (DFLC) cells, in which dielectric anisotropy could be changed with the variation of applied voltage frequency [79]. When the frequency of an external voltage is switched, the resonance peak of the metamaterial can move to the high frequency or the low frequency, and the response times of the redshift and blueshift are 1.044 and 1.376 ms, respectively. **Figure 5C** shows the dual-

frequency liquid crystal director orientations at the three applied voltages (voltages of 0, 80 V at 1 kHz, and 80 V at 22 kHz). More recently, a THz programmable meta-surface integrated with LC was proposed to manipulate the THz beam dynamically [69]. **Figure 5E** shows the 3D view of the THz programmable meta-surface. In **Figure 5E**, a 24-element linear array consists in the meta-surface, and a multichannel amplifier is in connection with each element. The control signal is outputted by the FPGA, and the amplified signals are utilized to control the phase of every element individually.

By further shrinking LC background metamaterials, the real-time control of IR and visible light are realized. Andrei Komar et al. presented an electrically tunable all-dielectric optical meta-surface consisting of silicon nanodisks embedded into liquid crystals, as shown at **Figure 5D** [81]. The reorientation of nematic liquid crystals under an external electric field can change the anisotropic permittivity tensor of the meta-surface, which in turn, alters the response to electromagnetic waves. By controlling voltage "on" and "off" to achieve reorientation of the nematic liquid crystals and obtain 75% modulation depth and a phase change of up to approximately π . Similarly, a new

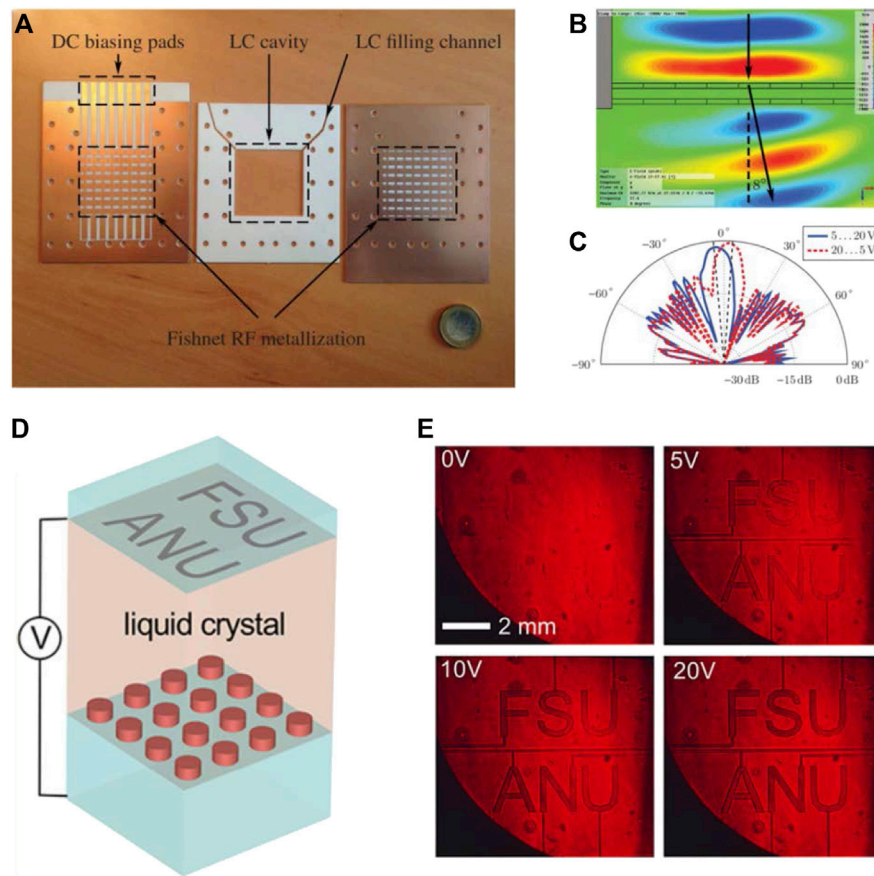


FIGURE 6 | (A) Photograph of a single opened fishnet unit-cell layer (B) Simulated electric near-field distribution of the two-layer fishnet array with a gradient of the LC permittivity at 27.4 GHz (C) Measured normalized far-field patterns at 27.5 GHz for two tuning states (D) Electrical tuning of the LC meta-surface (E) Real color images of the meta-surface at 0, 5, 10, and 20 V recorded in transmission (A)–(C) Reproduced with permission. Copyright 2014, IEEE [78] (D)–(E) Reproduced with permission. Copyright 2019, American Chemical Society [83].

combination of nematic liquid crystals and a binary-grating meta-surface was presented to control the diffraction efficiency by altering the applied voltage in the visible region, as shown in **Figure 5B** [91].

In addition, the effective tuning of the LC background metamaterial for wavefront manipulation has a wide prospect such as in tunable gradient indexed lenses [78, 94]. By introducing a voltage gradient over the fishnet metamaterial based on liquid crystals, the phase distribution over the aperture can be tuned, and thus the radiation direction can be manipulated. Thus, we can develop novel applications for wavefront manipulation based on liquid crystal metamaterials. In a recent study based on fishnet metamaterials, the unit cells of the fishnet were embedded with nematic liquid crystal which provided a continuous tuning of each column of the array [78]. The photograph of a single opened fishnet unit-cell layer is shown in **Figure 6A**. **Figure 6B** shows the simulated electric field distribution at 27.4 GHz. By using liquid crystal as a tunable dielectric layer, the authors could achieve a voltage-tunable phase gradient over the aperture array, and obtain a measured continuous maximum beam-scanning angle of 5° at 27.5 GHz, as shown in **Figure 6C**. The meta-

surface based on liquid crystals can also be used to achieve tunable transparent displays for visible light [83]. As shown at **Figure 6D**, an all-dielectric meta-surface composed of silicon nanocylinders integrated into a nematic liquid crystal cell is presented. A switchable dielectric meta-surface display is achieved by varying the applied voltage from 0 V to 20 V in steps of 5 V. **Figure 6E** shows the real-color images of the proposed meta-surface at 0, 5, 10, and 20 V recorded in transmission. It is worth noting that the demonstrated meta-surface display uses a different operation theory than normal liquid crystal displays.

In addition to the applied voltage, temperature can be also used as an external control parameter [57, 76, 85, 100–105]. Heating of the sample over the liquid crystal transition temperature leads to the phase transition of the liquid crystal between nematic and isotropic, which can be used to realize the tunability of response to electromagnetic waves. In 2009, a thermally tunable optical metamaterial was demonstrated based on aligned nematic liquid crystals in the visible range [57]. Structure of the coupled sample is shown in **Figure 7A**. By changing the ambient temperature (from 20° to 50°C , which is beyond the phase transition temperature T_c , 35°C), the phase

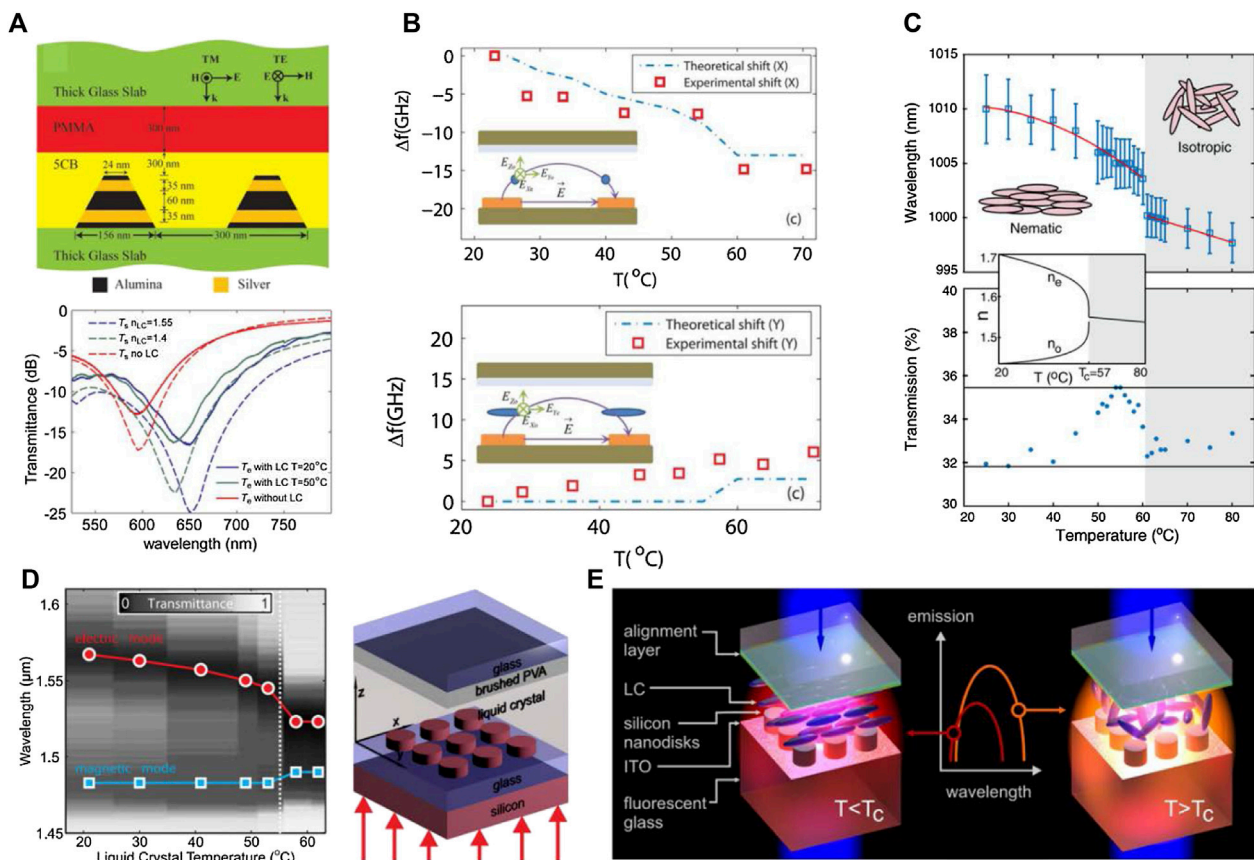


FIGURE 7 | (A) Structure of the coupled nanostrip sample and demonstration of a thermally tunable magnetic response in a metamaterial. **(B)** Experimentally measured results with the LC aligned in the *x*- and *y*-direction. **(C)** The shift of the resonance with temperature and the minimum transmission of the resonance as a function of temperature. The inset shows the temperature dependence of the refractive index. **(D)** Schematic of the silicon nanodisk meta-surface integrated into an LC cell and the temperature-dependent transmittance spectra of electric/magnetic modes. **(E)** Sketch of a silicon nanocylinder meta-surface integrated into a liquid crystal cell. When the liquid crystal is heated, it changes its state from nematic to isotropic, resulting in a spectral shift of the meta-surface resonances and the tuning of the emission enhancement. **(A)** Reproduced with permission. Copyright 2009, AIP Publishing [57]. **(B)** Reproduced with permission. Copyright 2013, IEEE [76]. **(C)** Reproduced with permission. Copyright 2017, AIP Publishing [102]. **(D)** Reproduced with permission. Copyright 2015, American Chemical Society [100]. **(E)** Reproduced with permission. Copyright 2018, American Chemical Society [103].

transition of nematic LCs from the ordered phase to the isotropic phase can be realized, which in turn means the magnetic response wavelength can be effectively changed, as shown in **Figure 7A**. Temperature control of metamaterials with liquid crystals can also work in the terahertz region. The tunability of resonant response is realized due to the orientations of liquid crystals by changing temperature [76]. The two arrangements of liquid crystals lead to different modulations to the terahertz wave. It is illustrated that the resonant frequency decreases when the liquid crystal is aligned in the *x*-direction, whereas it increases when the liquid crystal is aligned in the *y*-direction in **Figure 7B**. In essence, the temperature control of metamaterials with liquid crystal is due to the changes in the refractive index of the liquid crystal. In **Figure 7C**, the results showed that the shift of the resonance fits the form of the temperature dependence of the liquid crystals' refractive index [102]. Furthermore, dynamic manipulation of electric and magnetic resonances can be both realized based on the temperature-dependent refractive-index tunability of the liquid crystal [100]. As shown in **Figure 7D**,

the very different degrees of tunability of the two resonances allows for dynamically adjusting the spectral mode separation. In this experiment, the effect of temperature change on the refractive index of liquid crystal and the influence of phase transition on the resonant mode are both investigated. Besides the realization of dynamic tuning of the electromagnetic response of such metamaterials based on liquid crystals and the dynamic control of the light-emission properties of active liquid crystal meta-surfaces by an external control parameter were also demonstrated by Justus Bohn and coworkers [103]. **Figure 7E** shows the schematic of a meta-surface integrated into a liquid crystal cell. When heating the liquid crystal, its state changes from nematic to isotropic, resulting in a spectral shift of the meta-surface resonances and the enhancement of tuning of the emission.

4.2 Liquid Crystals-Based Applications

Liquid crystals have dielectric and optical anisotropy. The directors of liquid crystal molecules can be adjusted through

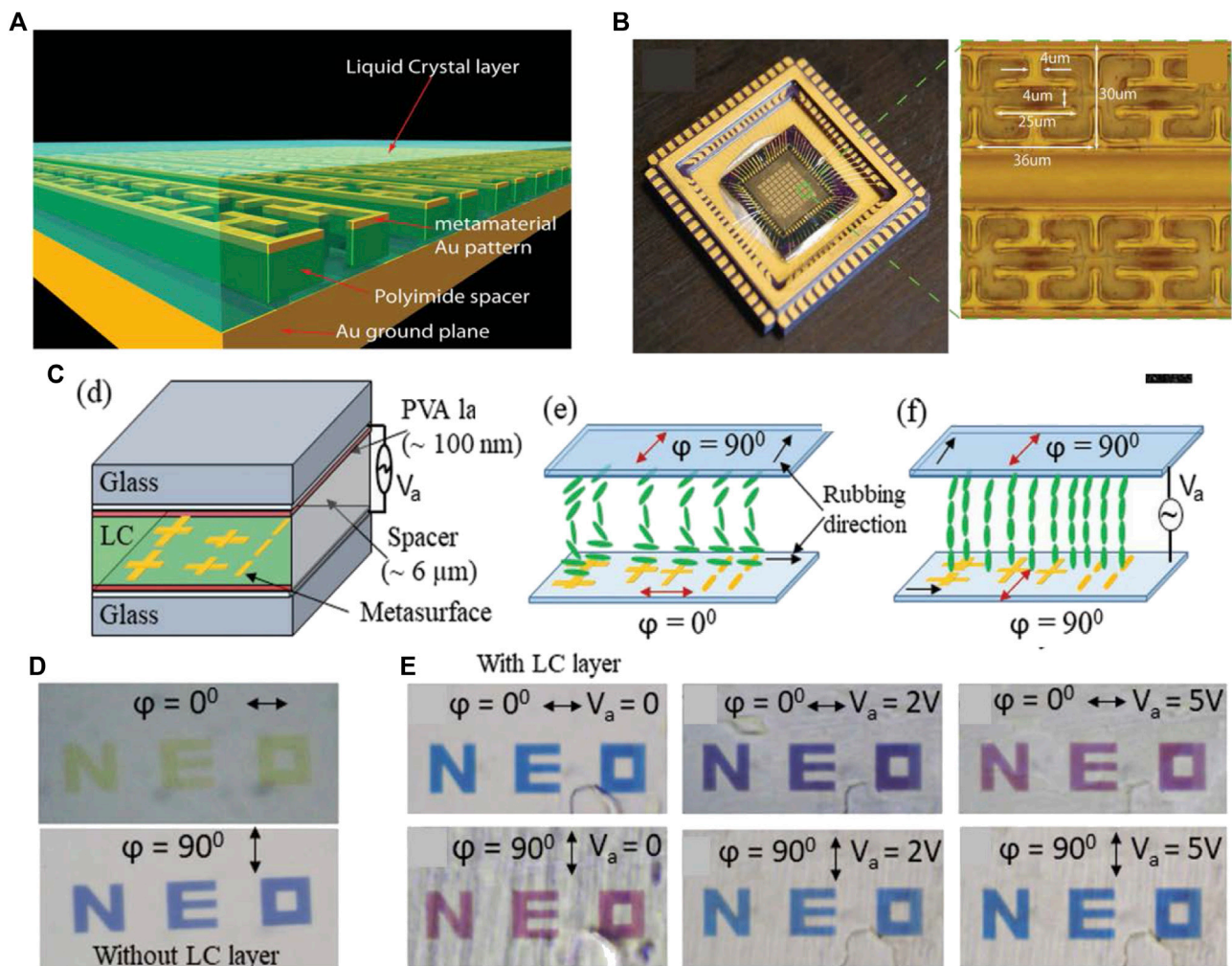


FIGURE 8 | (A) Schematic of the liquid crystal metamaterial absorber spatial light modulator. (B) Camera image of the MMA spatial light modulator device coated with LC. Close-up of MMA unit cells and corresponding dimensions. (C) Schematic view of the integrated liquid crystal meta-surface device and the working principle to rotate the polarization of incident y-polarized light. (D) Transmission images of the NEO tag, without an LC layer for x-polarized incident light ($\phi = 0^\circ$) and for y-polarized incident light ($\phi = 90^\circ$). (E) Transmission image of the NEO tag, with an LC layer for $\phi = 0^\circ$ and $\phi = 90^\circ$ at 0, 2, and 5 V. (A) Reproduced with permission. Copyright 2014, Wiley-VCH [110]. (A), (B) Reproduced with permission. Copyright 2017, American Chemical Society [108]. (C)–(E) Reproduced with permission. Copyright 2020, Wiley-VCH [113].

external fields, thereby effectively controlling the intensity, phase, and polarization of light waves and electromagnetic waves in various frequency bands, giving the liquid crystal materials a huge application potential. Using the controllability of liquid crystals and the special properties of metamaterials, meta-devices with real-time control functions can be realized, such as polarization controllers, absorbers, beam scanning, and spatial light modulators for information communication, imaging, and transmission. It can effectively solve the problems of the slow response speed of traditional liquid crystal devices, and has the advantages of small size, light weight, and easy integration.

The free control of liquid crystal orientation can promote the development of manipulability of metamaterial-based devices. Based on the tunability of the refractive index of liquid crystal, more latent applications of liquid crystal background

metamaterials have been discussed such as the perfect absorber [62, 70, 106, 107], polarization converter [108, 109], and modulators [110–113]. Salvatore Savo et al. have illustrated the ability of functional liquid crystals in a metamaterial absorber array working as a spatial light modulator during THz wavelengths by experiments. The 3D artistic impression of the metamaterial array is shown in **Figures 8A** and **8B** [110]. The narrow band frequency response of the metamaterials can be electronically controlled by the orientation of the liquid crystal molecules. Polarization converters using liquid crystal metamaterials are also demonstrated. The physical underlying principle of efficient polarization converters consists in their operation in the regime in which the radiative losses are larger than the non-radiative ones [108]. The polarization of the incident electric field is linear. Depending on the applied

voltage, the linearly polarized incident light is converted to RCP, linear, and LCP light. Moreover, in a recent literature paper, an electrically switchable color tag on account of an active liquid-crystal meta-surface platform was realized [113]. The realization of the proposed active color tags utilized the ability of the tunability of nematic liquid crystal reorientations controlled by an external electric field which would rotate the polarization of incident light. **Figure 8C** shows the schematic view of the integrated liquid crystal meta-surface device and the working principle to rotate the polarization of incident y-polarized light. **Figure 8D** shows the transmission pictures of a NEO tag, without an LC layer for x-polarized incident light ($\phi = 0^\circ$) and for y-polarized incident light ($\phi = 90^\circ$). Correspondingly, **Figure 8E** shows the transmission image of the NEO tag, with an LC layer for $\phi = 0^\circ$ and $\phi = 90^\circ$ at 0, 2, and 5 V.

5 PROSPECTIVE AND CONCLUSION

Incorporating active inclusions into metamaterial structures is of fundamental importance for increasing the operation bandwidth and dynamically manipulating electromagnetic waves. Artificially micro/nano-structured metamaterials with nematic LC provide a novel way to actively modulate the electromagnetic response. Nematic liquid crystals (NLC) dominate strong optical nonlinearities for photonics applications covering the femtoseconds to milliseconds time scales, and across a wide spectral range. The combination of the optical nonlinear behavior of liquid crystals and the peculiar physical properties of metamaterials is also one of the important advances in the field of liquid crystals. Many promising results on the tunability of metamaterials incorporated with nematic liquid crystal are reviewed, and these experimental studies have also reflected the inherent drawbacks of nematic liquid crystals as the active component. The foremost is the immobile layer in the immediate vicinity of the plasmonic structures [51]. This together with local inhomogeneous director axis alignment on the nanostructures all act to diminish the effective birefringence of the NLC for modulation/tuning effects. The theoretical tuning range due to complete realignment of the director axis with orthogonally polarized illuminating light is usually larger than the experimentally measured tuning range. This defect can be taken into account in the design of the metamaterial, and the optimization of the microstructure of the metamaterial may promote the agreement between the experimental value and the theoretical value. It is also very urgent and important to further design and fabricate liquid crystal materials with broadband, greater birefringence, smaller loss, faster response speed, and taking into account the wide liquid crystal phase temperature and other excellent characteristics. Furthermore, recent studies of another phase of chiral nematic liquid crystals, namely, blue-phase liquid crystals (BPLC) have presented promising alternatives. The second question that should be discussed is molecular anchoring. The realization of the LC tunability of metamaterials in the near infrared and optical regime is a

much harder task, since the effects of molecular anchoring to the nanostructured surfaces becomes important when the dimensions of the individual meta-atoms become comparable to the size of the LC molecules, which has a significant impact on the tunability of optical metamaterials [114, 115]. For example, under hard-anchoring conditions, the LC director axis in the immediate vicinity of the alignment layer remains unchanged while the bulk undergoes reorientation by the applied field. Liquid-crystal tuning of plasmonic resonances crucially rely on the ability to reorient the LC molecules within the near-fields of the plasmonic structure. One promising way of influencing the anchoring energy of the LC and to enhance tunability is the chemical functionalization of the metamaterial surface. In a recent study, it was found that after reducing the contribution of the supporting substrate to the metamaterial surface area it became possible to minimize the anchoring forces in the resulting hybrid and engage in-plane switching of the LC director at a nanoscale dimension [89].

In this paper, we present a brief review for tunable single/double negative metamaterials based on nematic LC. And we discuss the development of the tunable behavior of metamaterials induced by liquid crystals. By utilizing an LC director controlled by applied voltage and temperature, it is possible to reversely modulate the metamaterials' operation frequency along with the unique value of effective electromagnetic parameters. LC reorientations will result in a change of the LC refractive index, which in turn, changes the response to electromagnetic waves. The ease of incorporation and large birefringence of LC enable it to become an ideal candidate for metamaterial substrates with varied permittivity. It is worth noting that the birefringence of LC increases with frequency. It is demonstrated that LC-based metamaterials are promising for the remarkable improvement of the bandwidth and may facilitate related applications at terahertz or even optical regimes. Hopefully this review can promote research on tunable and reconfigurable metamaterials with various active inclusions for the improvement of the operation bandwidth and smart electromagnetic responses.

AUTHOR CONTRIBUTIONS

FZ and YF conceived the idea. FZ, XJ, and YF prepared the draft. All authors contributed to the discussion and revision of the manuscript.

FUNDING

The authors would like to acknowledge financial support from National Natural Science Foundation of China (NSFC) (Grants Nos. 61771402, 11674266, 12074314), NPU AoXiang New Star program, Science, Technology and Innovation Commission of Shenzhen Municipality (JCYJ20170817162221169), Shaanxi Province Postdoctoral Science Foundation (No. 2018BSHEDZZ64), and Natural Science Basic Research Plan in Shaanxi Province of China (Nos. 2018JM6024, 2020JM-145).

REFERENCES

- Veselago VG, The electrodynamics of substances with simultaneously negative values of ϵ and μ . *Sov Phys Usp* (1968) 10:509–14. doi:10.1070/PU1968v010n04ABEH003699
- Ran L, Huangfu J, Chen H, Li Y, Zhang X, Chen K, et al. Microwave solid-state left-handed material with a broad bandwidth and an ultralow loss. *Phys Rev B* (2004) 70:073102. doi:10.1103/PhysRevB.70.073102
- Ran L, Huangfu J, Chen H, Zhang X, Cheng K, Grzegorzczak TM, et al. Experimental study on several left-handed metamaterials. *Electromag Waves* (2005) 51:249–79. doi:10.2528/pier04040502
- Dolling G, Enkrich C, Wegener M, Soukoulis CM, Linden S, Simultaneous negative phase and group velocity of light in a metamaterial. *Science* (2006) 312: 892–4. doi:10.1126/science.1126021
- Zhao H, Kang L, Zhou J, Zhao Q, Li L, Peng L, et al. Experimental demonstration of tunable negative phase velocity and negative refraction in a ferromagnetic/ferroelectric composite metamaterial. *Appl Phys Lett* (2008) 93: 201106. doi:10.1063/1.3033397
- Kang L, Zhao Q, Zhao H, Zhou J, Ferrite-based magnetically tunable left-handed metamaterial composed of SRRs and wires. *Opt Express* (2008) 16: 17269–75. doi:10.1364/oe.16.017269
- Pendry JB, Holden AJ, Stewart WJ, Youngs I, Extremely low frequency plasmons in metallic mesostructures. *Phys Rev Lett* (1996) 76:4773–6. doi:10.1103/PhysRevLett.76.4773
- Pendry JB, Holden AJ, Robbins DJ, Stewart WJ, Magnetism from conductors and enhanced nonlinear phenomena. *IEEE Trans Microw Theory Tech* (1999) 47:2075–84. doi:10.1109/22.798002
- Smith DR, Kroll N, Negative refractive index in left-handed materials. *Phys Rev Lett* (2000) 85:2933–6. doi:10.1103/PhysRevLett.85.2933
- Shelby RA, Smith DR, Schultz S, Experimental verification of a negative index of refraction. *Science* (2001) 292:77–9. doi:10.1126/science.1058847
- Greger R, Parazzoli C, Li K, Koltenbah B, Tanielian M, Experimental determination and numerical simulation of the properties of negative index of refraction materials. *Opt Express* (2003) 11:688–95. doi:10.1364/oe.11.000688
- Parazzoli CG, Greger RB, Li K, Koltenbah BE, Tanielian M, Experimental verification and simulation of negative index of refraction using Snell's law. *Phys Rev Lett* (2003) 90:107401. doi:10.1103/PhysRevLett.90.107401
- Huangfu JT, Ran LX, Chen HS, Zhang XM, Chen KS, Grzegorzczak TM, et al. Experimental confirmation of negative refractive index of a metamaterial composed of Omega-like metallic patterns. *Appl Phys Lett* (2004) 84:1537–9. doi:10.1063/1.1655673
- Chen H, Ran L, Huangfu J, Zhang X, Chen K, Grzegorzczak TM, et al. Left-handed materials composed of only S-shaped resonators. *Phys Rev E Stat Nonlin Soft Matter Phys* (2004) 70:057605. doi:10.1103/PhysRevE.70.057605
- Minovich A, Neshev DN, Powell DA, Shadrivov IV, Kivshar YS, Tunable fishnet metamaterials infiltrated by liquid crystals. *Appl Phys Lett* (2010) 96: 193103. doi:10.1063/1.3427429
- Minovich A, Farnell J, Neshev DN, McKerracher I, Karouta F, Tian J, et al. Liquid crystal based nonlinear fishnet metamaterials. *Appl Phys Lett* (2012) 100:121113. doi:10.1063/1.3695165
- Pendry JB, Negative refraction makes a perfect lens. *Phys Rev Lett* (2000) 85: 3966–9. doi:10.1103/PhysRevLett.85.3966
- Fang N, Lee H, Sun C, Zhang X, Sub-diffraction-limited optical imaging with a silver superlens. *Science* (2005) 308:534. doi:10.1126/science.1108759
- Liu Z, Durant S, Lee H, Pikus Y, Fang N, Xiong Y, et al. Far-field optical superlens. *Nano Lett* (2007) 7:403–8. doi:10.1126/science.113736810.1021/nl062635n
- Schurig D, Mock JJ, Justice BJ, Cummer SA, Pendry JB, Starr AF, et al. Metamaterial electromagnetic cloak at microwave frequencies. *Science* (2006) 314:977–80. doi:10.1126/science.1133628
- Zhang FL, Li C, Fan YC, Yang RS, Shen NH, Fu QH, et al. Phase-modulated scattering manipulation for exterior cloaking in metal-dielectric hybrid metamaterials. *Adv Mater* (2019) 31:1903206. doi:10.1002/adma.201903206
- Zhou L, Li H, Qin Y, Wei Z, Chan CT, Directive emissions from subwavelength metamaterial-based cavities. *Appl Phys Lett* (2005) 86:101101. doi:10.1063/1.1881797
- Li H, Hao J, Zhou L, Wei Z, Gong L, Chen H, et al. All-dimensional subwavelength cavities made with metamaterials. *Appl Phys Lett* (2006) 89: 104101. doi:10.1063/1.2338795
- Ourir A, de Lustrac A, Lourtioz J-M, All-metamaterial-based subwavelength cavities ($\lambda/60$) for ultrathin directive antennas. *Appl Phys Lett* (2006) 88: 084103. doi:10.1063/1.2172740
- Fan Y, Zhang F, Shen N-H, Fu Q, Wei Z, Li H, et al. Achieving a high-Q response in metamaterials by manipulating the toroidal excitations. *Phys Rev A* (2018) 97:033816. doi:10.1103/PhysRevA.97.033816
- Zhu W, Yang R, Fan Y, Fu Q, Wu H, Zhang P, et al. Controlling optical polarization conversion with Ge₂Sb₂Te₅-based phase-change dielectric metamaterials. *Nanoscale* (2018) 10:12054–61. doi:10.1039/C8NR02587H
- Fan Y, Tu L, Zhang F, Fu Q, Zhang Z, Wei Z, et al. Broadband terahertz absorption in graphene-embedded photonic crystals. *Plasmonics* (2017) 13: 1153–8. doi:10.1007/s11468-017-0615-0
- Luo M, Zhou Y, Wu S, Chen L, Wide-angle broadband absorber based on one-dimensional metasurface in the visible region. *Appl Phys Express* (2017) 10: 092601. doi:10.7567/apex.10.092601
- Qian Q, Sun T, Yan Y, Wang C, Large-area wide-incident-angle metasurface perfect absorber in total visible band based on coupled mie resonances. *Adv Opt Mater* (2017) 5:1700064. doi:10.1002/adom.201700064
- Yang F, Fan Y, Yang R, Xu J, Fu Q, Zhang F, et al. Controllable coherent perfect absorber made of liquid metal-based metasurface. *Opt Express* (2019) 27: 25974–82. doi:10.1364/Oe.27.025974
- Soukoulis CM, Wegener M, Past achievements and future challenges in the development of three-dimensional photonic metamaterials. *Nat Photonics* (2011) 5:523–30. doi:10.1038/nphoton.2011.154
- Sun X, Fu Q, Fan Y, Wu H, Qiu K, Yang R, et al. Thermally controllable Mie resonances in a water-based metamaterial. *Sci Rep* (2019) 9:5417. doi:10.1038/s41598-019-41681-5
- Xu J, Fan Y, Yang R, Fu Q, Zhang F, Realization of switchable EIT metamaterial by exploiting fluidity of liquid metal. *Opt Express* (2019) 27: 2837–43. doi:10.1364/OE.27.002837
- Yang RS, Fu QH, Fan YC, Cai WQ, Qiu KP, Zhang WH, et al. Active control of EIT-like response in a symmetry-broken metasurface with orthogonal electric dipolar resonators. *Photon Res* (2019) 7:955–60. doi:10.1364/Prj.7.000955
- Lou J, Liang J, Yu Y, Ma H, Yang R, Fan Y, et al. Silicon-based terahertz meta-devices for electrical modulation of fano resonance and transmission amplitude. *Adv Opt Mater* (2020) 8:2000449. doi:10.1002/adom.202000449
- Gil I, Garcia-Garcia J, Bonache J, Martin F, Sorolla M, Marques R, Varistor-loaded split ring resonators for tunable notch filters at microwave frequencies. *Electron Lett* (2004) 40:1347–8. doi:10.1049/el:20046389
- Chen H, Wu B-I, Ran L, Grzegorzczak TM, Kong JA, Controllable left-handed metamaterial and its application to a steerable antenna. *Appl Phys Lett* (2006) 89:053509. doi:10.1063/1.2335382
- Shadrivov IV, Morrison SK, Kivshar YS, Tunable split-ring resonators for nonlinear negative-index metamaterials. *Opt Express* (2006) 14:9344–9. doi:10.1364/oe.14.009344
- Degiron A, Mock JJ, Smith DR, Modulating and tuning the response of metamaterials at the unit cell level. *Opt Express* (2007) 15:1115–27. doi:10.1364/oe.15.001115
- Carbonell J, Boria VE, Lippens D, Nonlinear effects in split ring resonators loaded with heterostructure barrier varistors. *Microw Opt Technol Lett* (2008) 50:474–9. doi:10.1002/mop.23122
- Chen H-T, O'Hara JF, Azad AK, Taylor AJ, Averitt RD, Shrekenhamer DB, et al. Experimental demonstration of frequency-agile terahertz metamaterials. *Nat Photon* (2008) 2:295–8. doi:10.1038/nphoton.2008.52
- Gorkunov MV, Osipov MA, Tunability of wire-grid metamaterial immersed into nematic liquid crystal. *J Appl Phys* (2008) 103:036101. doi:10.1063/1.2837099
- Zhu W, Fan Y, Li C, Yang R, Yan S, Fu Q, et al. Realization of a near-infrared active Fano-resonant asymmetric metasurface by precisely controlling the phase transition of Ge₂Sb₂Te₅. *Nanoscale* (2020) 12:8758–67. doi:10.1039/C9NR09889E
- Fan Y, Shen N-H, Zhang F, Wei Z, Li H, Zhao Q, et al. Electrically tunable goos-hänchen effect with graphene in the terahertz regime. *Adv Opt Mater* (2016) 4:1824–8. doi:10.1002/adom.201600303

45. Fan Y, Shen N-H, Zhang F, Zhao Q, Wei Z, Zhang P, et al. Photoexcited graphene metasurfaces: significantly enhanced and tunable magnetic resonances. *ACS Photon* (2018) 5:1612–8. doi:10.1021/acsphotonics.8b00057
46. Fan YC, Shen NH, Zhang FL, Zhao Q, Wu HJ, Fu QH, et al. Graphene plasmonics: a platform for 2D optics. *Adv Opt Mater* (2019) 7:1800537. doi:10.1002/adom.201800537
47. Khoo IC, Werner DH, Liang X, Diaz A, Weiner B, Nanosphere dispersed liquid crystals for tunable negative-zero-positive index of refraction in the optical and terahertz regimes. *Opt Lett* (2006) 31:2592–4. doi:10.1364/OL.31.002592
48. Wangberg R, Elser J, Narimanov EE, Podolskiy VA, Nonmagnetic nanocomposites for optical and infrared negative-refractive-index media. *J Opt Soc Am B* (2006) 23:498–505. doi:10.1364/josab.23.000498
49. Wang X, Kwon DH, Werner DH, Khoo IC, Kildishev AV, Shalae VM, Tunable optical negative-index metamaterials employing anisotropic liquid crystals. *Appl Phys Lett* (2007) 91:143122. doi:10.1063/1.2795345
50. Werner DH, Kwon DH, Khoo IC, Kildishev AV, Shalae VM, Liquid crystal clad near-infrared metamaterials with tunable negative-zero-positive refractive indices. *Opt Express* (2007) 15:3342–7. doi:10.1364/oe.15.003342
51. Khoo IC, Nonlinear optics, active plasmonics and metamaterials with liquid crystals. *Prog Quantum Electron* (2014) 38:77–117. doi:10.1016/j.pquantelec.2014.03.001
52. Zhang W, Song QH, Zhu WM, Shen ZX, Chong P, Tsai DP, et al. Metafluidic metamaterial: a review. *Adv Phys X* (2018) 3:20. doi:10.1080/23746149.2017.1417055
53. Zhao Q, Kang L, Du B, Li B, Zhou J, Tang H, et al. Electrically tunable negative permeability metamaterials based on nematic liquid crystals. *Appl Phys Lett* (2007) 90:011112. doi:10.1063/1.2430485
54. Zhang F, Zhao Q, Kang L, Gaillot DP, Zhao X, Zhou J, et al. Magnetic control of negative permeability metamaterials based on liquid crystals. *Appl Phys Lett* (2008) 92:193104. doi:10.1063/1.2926678
55. Zhang FL, Zhao Q, Gaillot DP, Zhao XP, Lippens D, Numerical investigation of metamaterials infiltrated by liquid crystal. *J Opt Soc Am B* (2008) 25:1920–5. doi:10.1364/josab.25.001920
56. Khoo IC, Nonlinear optics of liquid crystalline materials. *Phys Rep* (2009) 471:221–67. doi:10.1016/j.physrep.2009.01.001
57. Xiao S, Chettiar UK, Kildishev AV, Drachev V, Khoo IC, Shalae VM, Tunable magnetic response of metamaterials. *Appl Phys Lett* (2009) 95:033115. doi:10.1063/1.3182857
58. Zhang F, Kang L, Zhao Q, Zhou J, Zhao X, Lippens D, Magnetically tunable left handed metamaterials by liquid crystal orientation. *Opt Express* (2009) 17:4360–6. doi:10.1364/oe.17.004360
59. Zhang F, Zhao Q, Zhang W, Sun J, Zhou J, Lippens D, Voltage tunable short wire-pair type of metamaterial infiltrated by nematic liquid crystal. *Appl Phys Lett* (2010) 97:134103. doi:10.1063/1.3496034
60. Zhang F, Zhang W, Zhao Q, Sun J, Qiu K, Zhou J, et al. Electrically controllable fishnet metamaterial based on nematic liquid crystal. *Opt Express* (2011) 19:1563–8. doi:10.1364/oe.19.001563
61. Vasić B, Zografopoulos DC, Isić G, Beccherelli R, Gajić R, Electrically tunable terahertz polarization converter based on overcoupled metal-isolator-metal metamaterials infiltrated with liquid crystals. *Nanotechnology* (2017) 28:124002. doi:10.1088/1361-6528/aa5bbd
62. Isić G, Vasić B, Zografopoulos DC, Beccherelli R, Gajić R, Electrically tunable critically coupled terahertz metamaterial absorber based on nematic liquid crystals. *Phys Rev Appl* (2015) 3:064007. doi:10.1103/PhysRevApplied.3.064007
63. Wang J, Tian H, Wang Y, Li X, Cao Y, Li L, et al. Liquid crystal terahertz modulator with plasmon-induced transparency metamaterial. *Opt Express* (2018) 26:5769–76. doi:10.1364/oe.26.005769
64. Lu H, Jing S, Xia T, Yang J, Yin Z, Deng G, Measurement of LC dielectric constant at lower terahertz region based on metamaterial absorber. *IEICE Electron Express* (2017) 14:20170469. doi:10.1587/ele.14.20170469
65. Wang PY, Jin T, Meng FY, Lyu YL, Erni D, Wu Q, et al. Numerical investigation of nematic liquid crystals in the THz band based on EIT sensor. *Opt Express* (2018) 26:12318–29. doi:10.1364/oe.26.012318
66. Yin Z, Lu Y, Xia T, Lai W, Yang J, Lu H, et al. Electrically tunable terahertz dual-band metamaterial absorber based on a liquid crystal. *RSC Adv* (2018) 8:4197–203. doi:10.1039/C7RA13047C
67. Shen ZX, Zhou SH, Ge SJ, Hu W, Lu YQ, Liquid crystal enabled dynamic cloaking of terahertz Fano resonators. *Appl Phys Lett* (2019) 114:5. doi:10.1063/1.5082224
68. Ji Y, Fan F, Zhang X, Cheng J, Chang S, Active terahertz anisotropy and dispersion engineering based on dual-frequency liquid crystal and dielectric metasurface. *J Light Technol* (2020) 38:4030–6. doi:10.1109/jlt.2020.2985667
69. Wu JB, Shen Z, Ge SJ, Chen BW, Shen ZX, Wang TF, et al. Liquid crystal programmable metasurface for terahertz beam steering. *Appl Phys Lett* (2020) 116:5. doi:10.1063/1.5144858
70. Shrekenhamer D, Chen WC, Padilla WJ, Liquid crystal tunable metamaterial absorber. *Phys Rev Lett* (2013) 110:177403. doi:10.1103/PhysRevLett.110.177403
71. Savo S, Shrekenhamer D, Padilla WJ, Liquid crystal metamaterial absorber spatial light modulator for THz applications. *Adv Opt Mater* (2014a) 2:275–9. doi:10.1002/adom.201300384
72. Yang L, Fan F, Chen M, Zhang X, Chang S-J, Active terahertz metamaterials based on liquid-crystal induced transparency and absorption. *Opt Commun* (2017) 382:42–8. doi:10.1016/j.optcom.2016.07.055
73. Shen Z, Zhou S, Ge S, Duan W, Chen P, Wang L, et al. Liquid-crystal-integrated metadvice: towards active multifunctional terahertz wave manipulations. *Opt Express* (2018) 43:4695–8. doi:10.1364/ol.43.004695
74. Ha NY, Jeong SM, Nishimura S, Takezoe H, Color-temperature tunable white reflector using bichiral liquid crystal films. *Opt Express* (2010) 18:26339–44. doi:10.1364/oe.18.026339
75. Khoo IC, Diaz A, Liou J, Stinger MV, Huang J, Ma Y, Liquid crystals tunable optical metamaterials. *IEEE J Sel Top Quantum Electron* (2010) 16:410–7. doi:10.1109/jstqe.2009.2032246
76. Liu L, Shadrivov IV, Powell DA, Raihan MR, Hattori HT, Decker M, et al. Temperature control of terahertz metamaterials with liquid crystals. *IEEE Trans Terahertz Sci Technol* (2013) 3:827–31. doi:10.1109/tthz.2013.2285570
77. Kowrdziej R, Olifierczuk M, Parka J, Wrobel J, Terahertz characterization of tunable metamaterial based on electrically controlled nematic liquid crystal. *Appl Phys Lett* (2014) 105:022908. doi:10.1063/1.4890850
78. Maasch M, Roig M, Damm C, Jakoby R, Voltage-tunable artificial gradient-index lens based on a liquid crystal loaded fishnet metamaterial. *IEEE Antennas Wirel Propag Lett* (2014) 13:1581–4. doi:10.1109/lawp.2014.2345841
79. Chen CC, Chiang WF, Tsai MC, Jiang SA, Chang TH, Wang SH, et al. Continuously tunable and fast-response terahertz metamaterials using in-plane-switching dual-frequency liquid crystal cells. *Opt Lett* (2015) 40:2021–4. doi:10.1364/ol.40.002021
80. Zografopoulos DC, Beccherelli R, Tunable terahertz fishnet metamaterials based on thin nematic liquid crystal layers for fast switching. *Sci Rep* (2015) 5:13137. doi:10.1038/srep13137
81. Komar A, Fang Z, Bohn J, Sautter J, Decker M, Miroshnichenko A, et al. Electrically tunable all-dielectric optical metasurfaces based on liquid crystals. *Appl Phys Lett* (2017) 110:4. doi:10.1063/1.4976504
82. Yang J, Wang P, Shi T, Gao S, Lu H, Yin Z, et al. Electrically tunable liquid crystal terahertz device based on double-layer plasmonic metamaterial. *Opt Express* (2019) 27:27039–45. doi:10.1364/OE.27.027039
83. Zou CJ, Komar A, Fasold S, Bohn J, Muravsky AA, Murauski AA, et al. Electrically tunable transparent displays for visible light based on dielectric metasurfaces. *ACS Photonics* (2019) 6:1533–40. doi:10.1021/acsphotonics.9b00301
84. Bhardwaj A, Sridurai V, Puthoor NM, Nair AB, Ahuja T, Nair GG, Evidence of tunable fano resonance in a liquid crystal-based colloidal metamaterial. *Adv Opt Mater* (2020) 8:1901842. doi:10.1002/adom.201901842
85. Liu Y, Song J, Zhao W, Ren X, Cheng Q, Luo X, et al. Dynamic thermal camouflage via a liquid-crystal-based radiative metasurface. *Nanophotonics* (2020) 9:855–63. doi:10.1515/nanoph-2019-0485
86. Sandford O'Neill JJ, Salter PS, Booth MJ, Elston SJ, Morris SM, Electrically-tunable positioning of topological defects in liquid crystals. *Nat Commun* (2020) 11:2203. doi:10.1038/s41467-020-16059-1
87. Kossyrev PA, Yin A, Cloutier SG, Cardimona DA, Huang D, Alsing PM, et al. Electric field tuning of plasmonic response of nanodot array in liquid crystal matrix. *Nano Lett* (2005) 5:1978–81. doi:10.1021/nl0513535
88. Yaghmaee P, Karabey OH, Bates B, Fumeaux C, Jakoby R, Electrically tuned microwave devices using liquid crystal technology. *Int J Antennas Propag* (2013) 2013:9. doi:10.1155/2013/824214

89. Buchnev O, Podoliak N, Kaczmarek M, Zheludev NI, Fedotov VA, Electrically controlled nanostructured metasurface loaded with liquid crystal: toward multifunctional photonic switch. *Adv Opt Mater* (2015) 3:674–9. doi:10.1002/adom.201400494
90. Lee YU, Kim J, Wu JW, Electro-optic switching in metamaterial by liquid crystal. *Nano Conver* (2015) 2:23. doi:10.1186/s40580-015-0054-6
91. Chen KP, Ye SC, Yang CY, Yang ZH, Lee W, Sun MG, Electrically tunable transmission of gold binary-grating metasurfaces integrated with liquid crystals. *Opt Express* (2016) 24:16815–21. doi:10.1364/OE.24.016815
92. Lagerwall JPF, Scalia G, A new era for liquid crystal research: applications of liquid crystals in soft matter nano-, bio- and microtechnology. *Curr Appl Phys* (2012) 12:1387–412. doi:10.1016/j.cap.2012.03.019
93. Khoo IC, DC-field-assisted grating formation and nonlinear diffractions in methyl-red dye-doped blue phase liquid crystals. *Opt Lett* (2015) 40:60–3. doi:10.1364/OL.40.000060
94. Giden IH, Eti N, Rezaei B, Kurt H, Adaptive graded index photonic crystal lens design via nematic liquid crystals. *IEEE J Quantum Electron* (2016) 52:7. doi:10.1109/jqe.2016.2605398
95. Ho TJ, Chen CW, Khoo IC, Polarization-free and high-resolution holographic grating recording and optical phase conjugation with azo-dye doped blue-phase liquid crystals. *Liq Cryst* (2018) 45:1944–52. doi:10.1080/02678292.2018.1491068
96. Vaskin A, Bohn J, Chong KE, Bucher T, Zilk M, Choi D-Y, et al. Directional and spectral shaping of light emission with mie-resonant silicon nanoantenna arrays. *ACS Photonics* (2018) 5:1359–64. doi:10.1021/acsp Photonics.7b01375
97. Guo DY, Chen CW, Li CC, Jau HC, Lin KH, Feng TM, et al. Reconfiguration of three-dimensional liquid-crystalline photonic crystals by electrostriction. *Nat Mater* (2020) 19:94–101. doi:10.1038/s41563-019-0512-3
98. Buchnev O, Wallauer J, Walther M, Kaczmarek M, Zheludev NI, Fedotov VA, Controlling intensity and phase of terahertz radiation with an optically thin liquid crystal-loaded metamaterial. *Appl Phys Lett* (2013) 103:4. doi:10.1063/1.4823822
99. Chikhi N, Lisitskiy M, Papari G, Tkachenko V, Andreone A, A hybrid tunable THz metadvice using a high birefringence liquid crystal. *Sci Rep* (2016) 6:34536. doi:10.1038/srep34536
100. Sautter J, Staude I, Decker M, Rusak E, Neshev DN, Brener I, et al. Active tuning of all-dielectric metasurfaces. *ACS Nano* (2015) 9:4308–15. doi:10.1021/acsnano.5b00723
101. Liang X, Chen M, Guo S, Zhang L, Li F, Yang H, Dual-band modulation of visible and near-infrared light transmittance in an all-solution-processed hybrid micro-nano composite film. *ACS Appl Mater Interf* (2017) 9:40810–9. doi:10.1021/acsnano.7b11582
102. Parry M, Komar A, Hopkins B, Campione S, Liu S, Miroshnichenko AE, et al. Active tuning of high-Q dielectric metasurfaces. *Appl Phys Lett* (2017) 111:053102. doi:10.1063/1.4997301
103. Bohn J, Bucher T, Chong KE, Komar A, Choi DY, Neshev DN, et al. Active tuning of spontaneous emission by mie-resonant dielectric metasurfaces. *Nano Lett* (2018) 18:3461–5. doi:10.1021/acsnanolett.8b00475
104. Ke YJ, Zhou CZ, Zhou Y, Wang SC, Chan SH, Long Y, Emerging thermal-responsive materials and integrated techniques targeting the energy-efficient smart window application. *Adv Funct Mater* (2018) 28:18. doi:10.1002/adfm.201800113
105. Sentker K, Yildirim A, Lippmann M, Zantop AW, Bertram F, Hofmann T, et al. Self-assembly of liquid crystals in nanoporous solids for adaptive photonic metamaterials. *Nanoscale* (2019) 11:23304–17. doi:10.1039/c9nr07143a
106. Hokmabadi MP, Tareki A, Rivera E, Kung P, Lindquist RG, Kim SM, Investigation of tunable terahertz metamaterial perfect absorber with anisotropic dielectric liquid crystal. *AIP Adv* (2017) 7: 015102. doi:10.1063/1.4973638
107. Yin ST, Xiao D, Liu JX, Li K, He H, Jiang SZ, et al. Reconfigurable chiral metasurface absorbers based on liquid crystals. *IEEE Phot J* (2018) 10:9. doi:10.1109/jphot.2018.2878775
108. Vasic B, Zografopoulos DC, Isic G, Beccherelli R, Gajic R, Electrically tunable terahertz polarization converter based on overcoupled metal-isolator-metal metamaterials infiltrated with liquid crystals. *Nanotechnology* (2017) 28:11. doi:10.1088/1361-6528/aa5bbd
109. Sasaki T, Nishie Y, Kambayashi M, Sakamoto M, Noda K, Okamoto H, et al. Active terahertz polarization converter using a liquid crystal-embedded metal mesh. *IEEE Phot J* (2019) 11:1–7. doi:10.1109/jphot.2019.2950021
110. Savo S, Shrekenhamer D, Padilla WJ, Liquid crystal metamaterial absorber spatial light modulator for THz applications. *Adv Opt Mater* (2014b) 2:275–9. doi:10.1002/adom.201300384
111. Zeng BB, Huang ZQ, Singh A, Yao Y, Azad AK, Mohite AD, et al. Hybrid graphene metasurfaces for high-speed mid-infrared light modulation and single-pixel imaging. *Light Sci Appl* (2018) 7:51. doi:10.1038/s41377-018-0055-4
112. Ting TL, Technology of liquid crystal based antenna [Invited]. *Opt Express* (2019) 27:17138–53. doi:10.1364/oe.27.017138
113. Sharma M, Hendler N, Ellenbogen T, Electrically switchable color tags based on active liquid-crystal plasmonic metasurface platform. *Adv Opt Mater* (2020) 8:1901182. doi:10.1002/adom.201901182
114. Buchnev O, Ou JY, Kaczmarek M, Zheludev NI, Fedotov VA, Electro-optical control in a plasmonic metamaterial hybridised with a liquid-crystal cell. *Opt Express* (2013) 21:1633–8. doi:10.1364/oe.21.001633
115. Decker M, Kremers C, Minovich A, Staude I, Miroshnichenko AE, Chigrin D, et al. Electro-optical switching by liquid-crystal controlled metasurfaces. *Opt Express* (2013) 21:8879–85. doi:10.1364/oe.21.008879

Conflict of Interest: The authors declare that the research was conducted in the absence of any commercial or financial relationships that could be construed as a potential conflict of interest.

Copyright © 2021 Xu, Yang, Fan, Fu and Zhang. This is an open-access article distributed under the terms of the Creative Commons Attribution License (CC BY). The use, distribution or reproduction in other forums is permitted, provided the original author(s) and the copyright owner(s) are credited and that the original publication in this journal is cited, in accordance with accepted academic practice. No use, distribution or reproduction is permitted which does not comply with these terms.



Multifunctional Metasurface Lens With Tunable Focus Based on Phase Transition Material

Yongkang Song¹, Weici Liu², Xiaolei Wang³, Faqiang Wang^{1*}, Zhongchao Wei¹, Hongyun Meng¹, Ning Lin¹ and Hongqiang Zhang¹

¹ Guangzhou Key Laboratory for Special Fiber Photonic Devices, Laboratory of Nanophotonic Functional Materials and Devices, School of Information and Optoelectronic Science and Engineering, South China Normal University, Guangzhou, China, ² Department of Electronic Information Engineering, Guangzhou College of Technology and Business, Foshan, China, ³ Institute of Modern Optics, Nankai University, Tianjin, China

OPEN ACCESS

Edited by:

Fuli Zhang,
Northwestern Polytechnical
University, China

Reviewed by:

Qian Sun,
Nankai University, China
Jifeng Liu,
Dartmouth College, United States
Peng Zhang,
Seagate Technology, United States

*Correspondence:

Faqiang Wang
fqwang@scnu.edu.cn

Specialty section:

This article was submitted to
Optics and Photonics,
a section of the journal
Frontiers in Physics

Received: 11 January 2021

Accepted: 01 April 2021

Published: 29 April 2021

Citation:

Song Y, Liu W, Wang X, Wang F,
Wei Z, Meng H, Lin N and Zhang H
(2021) Multifunctional Metasurface
Lens With Tunable Focus Based on
Phase Transition Material.
Front. Phys. 9:651898.
doi: 10.3389/fphy.2021.651898

Metasurfaces have powerful light field manipulation capabilities, which have been extensively studied in the past few years and have developed rapidly in various fields. At present, the focus of metasurface research has shifted to the tunable functionality. In this paper, a temperature-controllable multifunctional metasurface lens based on phase transition material is designed. First of all, by controlling the temperature of the desired working area and the polarization of the incident light, switching among multiple focus, single focus, and no focus at any position can be achieved, and the intensity and helicity of the output light can be adjusted. In addition, a polarization-sensitive intensity-tunable metalens based on the P-B phase principle is designed, when the incident light is linearly polarized light, left-handed circularly polarized light, or right-handed circularly polarized light, it has the same focal point but with different light field intensities. Therefore, the focused intensity can be tunable by the polarization state of the incident light.

Keywords: multifunctional metasurface, tunable meta-lens, phase transition material, multiple focus, polarization-sensitive

INTRODUCTION

Metasurfaces, the corresponding two-dimensional metamaterials, can flexibly control the amplitude, phase, and polarization of light through sub-wavelength units, compared with the traditional lens that relies on the modulated light beam to accumulate the phase delay during the transmission, it is smaller in size, lighter in weight, and suitable for device miniaturization and system integration. Thanks to the special properties of metasurfaces, various new applications can be realized, such as hologram [1–4], polarization measurement [5–7], vortex beam generator [8, 9], non-linear dynamics [10–12], beam shaping, etc. [13, 14].

The bifocal and multifocal lenses that can focus on different positions can be used in imaging systems [15, 16], optical communication [17, 18], and medical applications [19], etc. Previous studies have also used Pancharatnam-Berry (P-B) phase metasurface to achieve multi-focus focusing function [15, 20]. However, their work has some limitations: firstly, once the lens structure is produced, its function cannot be changed; secondly, based on the principle of P-B phase modulation, it demands higher requirements of the helicity of the incident light. Usually, the requirement is circular-polarized incident light, and polarization-independent focusing cannot be achieved.

Phase transition materials are a good choice to provide a wide range of tunable metamaterials, whose electronic properties can be tuned in real time during structural phase transitions. By using phase transition materials, the optical response of metamaterials can be significantly adjusted by external excitations [21]. Currently, the common phase transition materials used in metasurfaces are $\text{Ge}_2\text{Se}_2\text{Te}_5$ [22, 23], vanadium dioxide (VO_2) [24], or graphene [25], etc. In terms of thermal control materials, vanadium dioxide has the capability of insulating-metal phase transition, and its structure can change reversibly with temperature. Its phase transition temperature is $T_C = 68^\circ$. When temperature is below the phase transition temperature T_C , it exhibits a monoclinic phase structure, in a semiconductor insulation state (I- VO_2), the infrared transmittance is higher at this state; When temperature is higher than the phase transition temperature T_C , it presents a rutile tetragonal phase structure, in a metallic state (M- VO_2), and has a lower infrared transmittance [26–28]. In recent years, there have been many studies on metasurfaces based on vanadium dioxide, including controlling temperature or heat flux [29, 30], asymmetric transmission [31], switchable focus lens [32–34], switchable wave-plates [35], beam control [36], and the like. However, most of these designs can only achieve fixed function, or only work under a specific condition [37].

In this article, we propose a temperature-controllable metalens based on VO_2 material working in the mid-infrared band. By controlling the temperature, the conversions among bifocal, single focus, and no focus can be realized, and the helicity of the focal light is changable, as shown in **Figure 1**. In addition, based on the principle of P-B phase, the co-focal lens which works for linear polarized light, left-handed circularly polarized light, and right-handed circularly polarized light is designed, and the intensity of the focal spot is different for different incident polarized light. Thus, a polarization sensitive lens with tunable intensity is realized.

More importantly, we showed a multifunctional lens made of thermally controlled phase transition materials, and provided a new design method for adjustable multifocal lenses. As an extension, other phase transition materials and different control methods, such as electric control, can also be used to complete focus switchable, polarization independent metasurface lenses.

MATERIAL AND DESIGN THEORY

Based on the vanadium dioxide material, the conductor model parameter is used below the phase transition temperature T_C (when in I- VO_2), corresponding permittivity $\varepsilon = 9$ [38]. When temperature is higher than the phase transition temperature T_C (at M- VO_2), the Drude model is used to determine the parameters.

The complex permittivity of vanadium dioxide can be given by the following dispersion relation [39–41]:

$$\varepsilon(\omega) = \varepsilon_\infty - \frac{\sigma}{\sigma_0} \frac{\omega_n^2(\sigma_0)}{\omega(\omega + i\gamma)} \quad (1)$$

Among them, the first item represents ultimate high frequency permittivity, $\varepsilon_\infty = 12$; $\gamma = \frac{e}{km^*}$ represents the collision frequency, here m^* is the optical effective mass of electrons. $\omega_n(\sigma)$ represents electrical conductivity, which is related to plasma frequency. Because σ are directly proportional to the free carrier density; According to the reference, it can be known as $\sigma_0 = 3 \times 10^5 \text{ S/m}$, $\omega_n(\sigma_0) = 1.4 \times 10^{15} \text{ rad/s}$, $\gamma = 5.75 \times 10^{13} \text{ rad/s}$.

Figure 2 shows the transmittance properties of VO_2 film [40]. The two curves in **Figure 2A** represent the change of transmittance in the frequency range of 0.25–5eV when the temperature is 300 K and 355 K, respectively. We can get that when the temperature of the VO_2 film is 300 K and 355 K, the transmittance of 0.31 eV ($4\mu\text{m}$) incident light shows a huge contrast. The red and blue curves in **Figure 2B** show the transmittance of VO_2 film (at $4\mu\text{m}$) between heating and cooling, respectively. It can be seen from the figure that there is a short temperature change interval within which the transmittance changes rapidly with temperature, and the change is reversible. Outside the corresponding temperature in the phase transition zone, the transmittance is relatively stable.

In summary, the transmittance of the VO_2 film at $4\mu\text{m}$ changes drastically in the phase transition interval, and the heating and cooling process is reversible. Therefore, it can exhibit stable performance outside the phase change region.

Theory

According to the P-B phase modulation principle, The electric field generated by an incident plane wave of arbitrary polarization passing through the lens can be expressed as [42]:

$$|E_{out}\rangle = \sqrt{\eta_E} |E_{in}\rangle + \sqrt{\eta_R} e^{i2\theta(x,y)} |R\rangle + \sqrt{\eta_L} e^{-i2\theta(x,y)} |L\rangle \quad (2)$$

In the formula, η_E, η_R, η_L represents the polarization level coupling efficiency, which can be expressed as:

$$\eta_E = \left| \frac{1}{2} (t_x + t_y e^{i\phi}) \right|^2 \quad (3)$$

$$\eta_R = \left| \frac{1}{2} (t_x - t_y e^{i\phi}) \langle E_{in} | L \rangle \right|^2 \quad (4)$$

$$\eta_L = \left| \frac{1}{2} (t_x - t_y e^{i\phi}) \langle E_{in} | R \rangle \right|^2 \quad (5)$$

Among them, t_x, t_y , respectively, represent the real amplitude transmission coefficients perpendicular and parallel to the optical axis, and ϕ represent the phase delay between the two polarizations. Symbols $\langle E_{in} | L \rangle$ ($\langle E_{in} | R \rangle$) denote the dot product of the incident polarized plane wave $|E_{in}\rangle$ and left-handed circularly polarized plane wave $|L\rangle$ (right-handed circularly polarized plane wave $|R\rangle$).

From the above formula, we can get that the outgoing electric field contains three components. The first component maintains the original polarization and phase of the incident beam; the second term is right-handed circular polarization with $2\theta(x, y)$ phase modulation; The last term is opposite to the previous term which is left-hand circular polarization light with a modulation phase of $-2\theta(x, y)$.

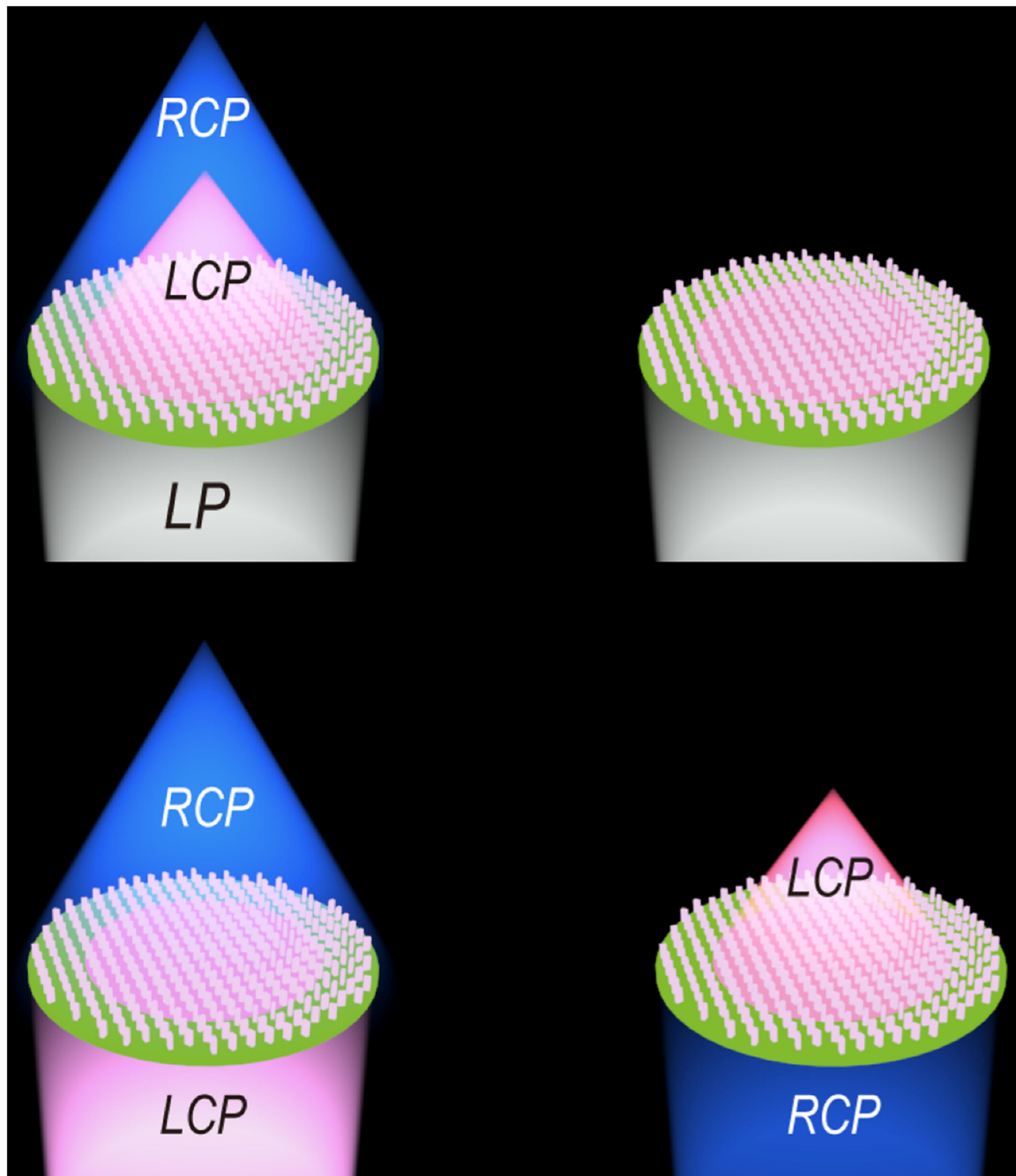


FIGURE 1 | Working principle diagram. The two pictures on the top show the wavefront reshaping pictures at different temperatures when LP light is incident, and the two pictures on the bottom are the wavefront reshaping pictures under LCP and RCP light incidents.

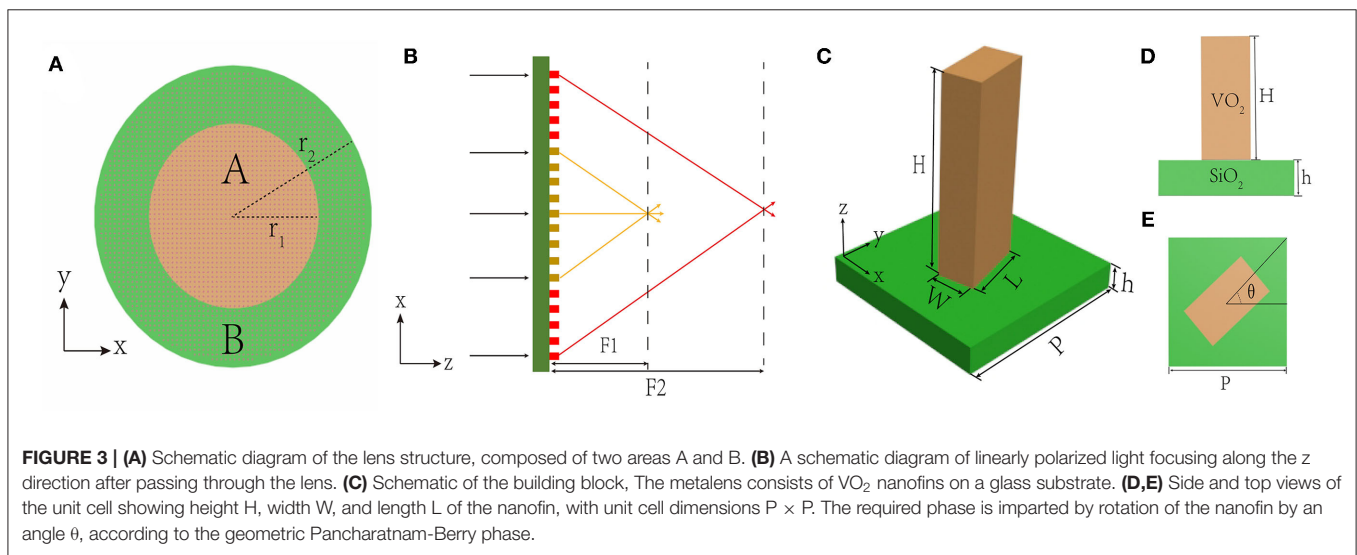
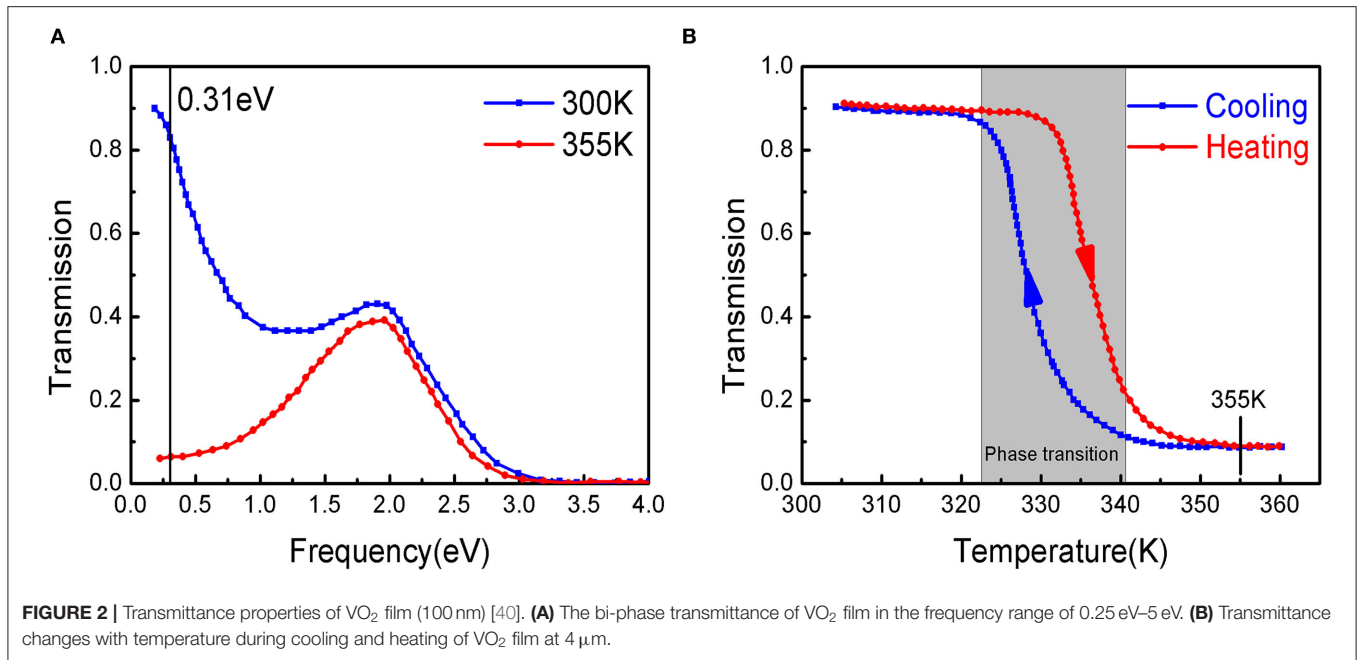
For a special case: $t_x = t_y, \phi = \pi$, when the left-handed circularly polarized light is incident, the outgoing beam will undergo full polarization conversion:

$$|E_{out}\rangle = \frac{t_x + t_y}{2} e^{i2\theta(x,y)} |R\rangle \quad (6)$$

It can be seen from the above formula that the phase modulation depends on the local orientation of the sub-wavelength grating.

Design Method

In the design of this article, glass is used as the substrate, and vanadium dioxide (VO_2) is used for the structural unit. We control the changing of temperature so that it undergoes a mutual



conversion from I-VO₂ state to M-VO₂ state. In order to achieve the purpose of lens focusing, the unit cell at different positions (x, y) need to meet the phase condition [43]:

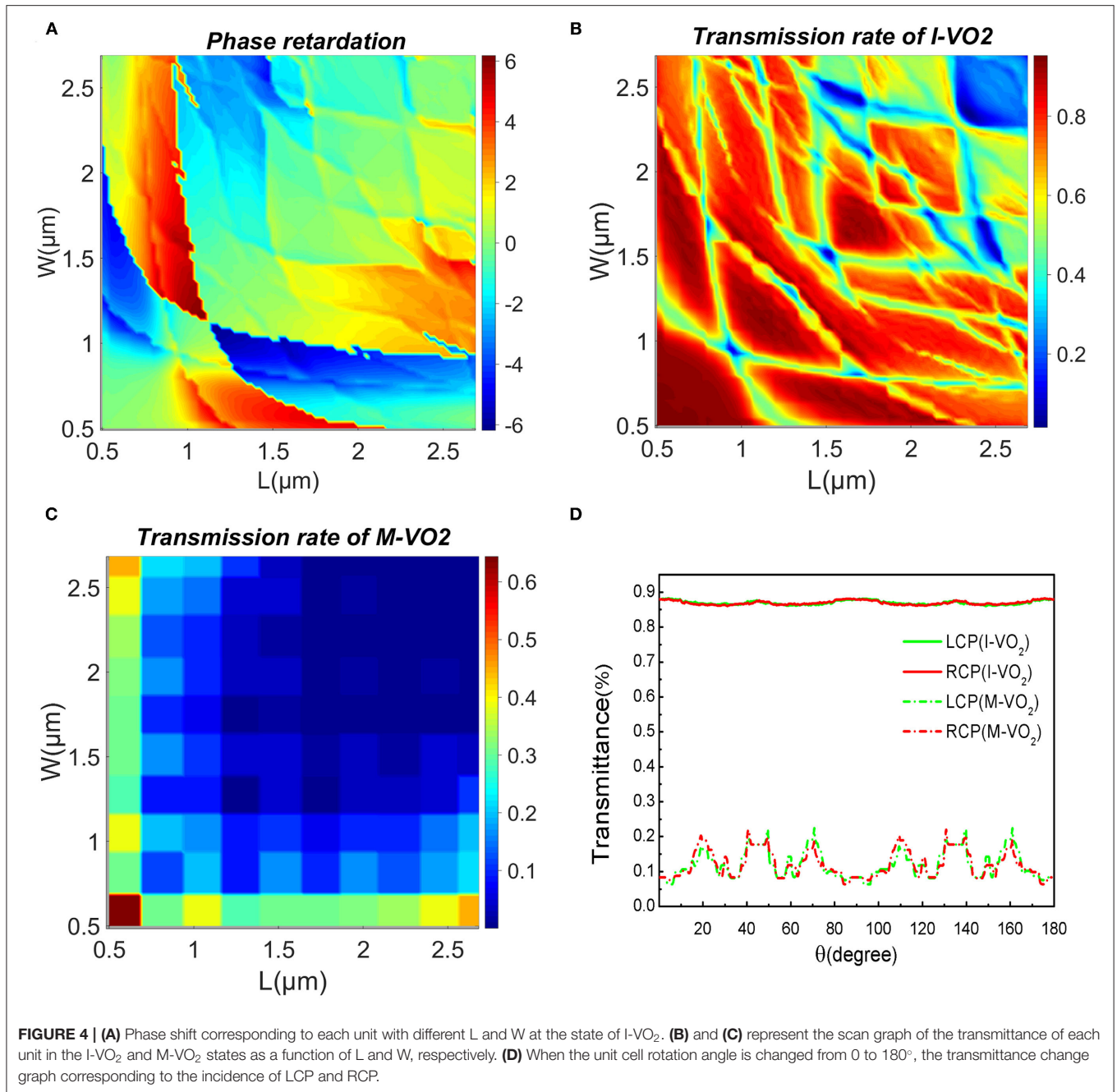
$$\varphi(x, y) = \frac{2\pi}{\lambda_{in}} \left(\sqrt{(x - x_0)^2 + (y - y_0)^2 + f^2} - f \right) \quad (7)$$

Here, λ_{in} is the desired wavelength, f is the focal length, and (x_0, y_0) is the initial position of the focus. Based on the Equation (6), the unit cell at different positions (x, y) need to meet $\theta = \pm\varphi/2$ to ensure that the left-handed circularly polarized light or the right-handed circularly polarized light can pass through the structure and is converted into the opposite direction of rotation

[44]. The rotation angle is:

$$\theta(x, y) = \pm \frac{\pi}{\lambda_{in}} \left(\sqrt{(x - x_0)^2 + (y - y_0)^2 + f^2} - f \right) \quad (8)$$

Figure 3A is a schematic diagram of the structure. The lens is composed of two areas, A and B, which are a circle in the area $(0, r_1)$ and a ring in the area (r_1, r_2) . **Figure 3B** is a schematic diagram of lens focusing when linearly polarized light is incident, and two focal points are formed. **Figures 3C–E** are perspective view, front view, and top view, respectively. We used a commercial three-dimensional (3D) finite-difference time-domain (FDTD) solver (FDTD solutions, Lumerical Inc.) to simulate the unit in the frequency domain with periodic



boundary conditions in the x and y directions, and a perfectly matched layer in the z direction. By optimizing the structure, we determine that the incident wavelength $\lambda_{in} = 4 \mu\text{m}$, the period of each unit cell is $P = 2.8 \mu\text{m}$, and the height of the structural unit $H = 3.2 \mu\text{m}$. Scanning the phase change and transmittance of different circular polarizations light in I-VO₂ and M-VO₂ to determine the best choice of length and width. **Figure 4A** is a scan diagram of the phase delay varying with the length and width, **Figures 4B,C** are the schematic diagrams of the transmittance varying with the length and width in the two states of I-VO₂ and M-VO₂, respectively.

We choose the appropriate length and width to make the I-VO₂ nanorods in the state of a half-wave plate, that is, the phase retardation $\phi = \pi$, $t_x = t_y$, and the transmittance is as high as possible in the I-VO₂ state, on the contrary, the transmittance is as low as possible in the M-VO₂ state. Through scanning optimization and data analysis, we choose the length $L = 1.25 \mu\text{m}$ and the width $W = 0.75 \mu\text{m}$ of the VO₂ structural unit.

In order to verify the feasibility of the lens, we observe the changes in the transmittance of the corresponding I-VO₂ and M-VO₂ under different polarized light incidence when the rotation angle of the unit cell changes from 0 to π . It can be seen from

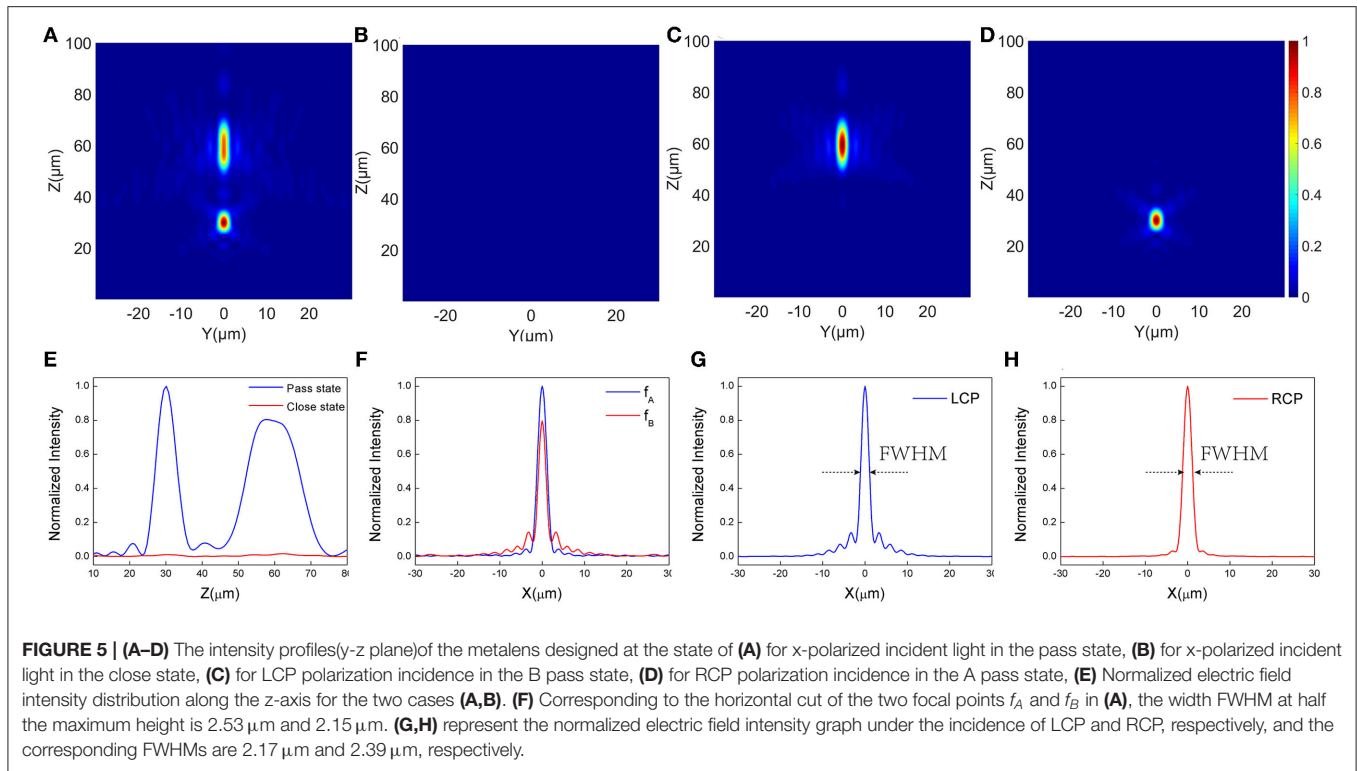


Figure 4D that the transmittance of I-VO₂ always remains at about 0.88, whether the incident light is left-handed circularly polarized light or right-handed circularly polarized light, while the transmittance of M-VO₂ varies between 0 and 0.2. It is in line with the situation that the transmittance of I-VO₂ is much greater than that of M-VO₂.

RESULTS AND DISCUSSION

Focus Switchable Lens Controlled by Combination of Polarization and Temperature

Here, we design a kind of adjustable lens that realizes multi-focus, single-focus, and non-focus conversion by incident different polarized light (LP, LCP, RCP) and temperature control. The lens consists of two areas, (0, r_1) area A, and (r_1 , r_2) area B, respectively, focusing on the incident light of RCP and LCP, as shown in **Figures 2A,B**. Here, the radius of the lens are set as $r_1 = 50.4\ \mu\text{m}$, $r_2 = 92.4\ \mu\text{m}$. The conditions for the rotation angles of the structural unit in the two regions are as follows:

$$\theta_A = -\frac{\pi}{\lambda_{in}} \left(\sqrt{\rho^2 + f_A^2} - f_A \right) \quad \rho \in [0, r_1] \quad (9)$$

$$\theta_B = \frac{\pi}{\lambda_{in}} \left(\sqrt{\rho^2 + f_B^2} - f_B \right) \quad \rho \in [r_1, r_2] \quad (10)$$

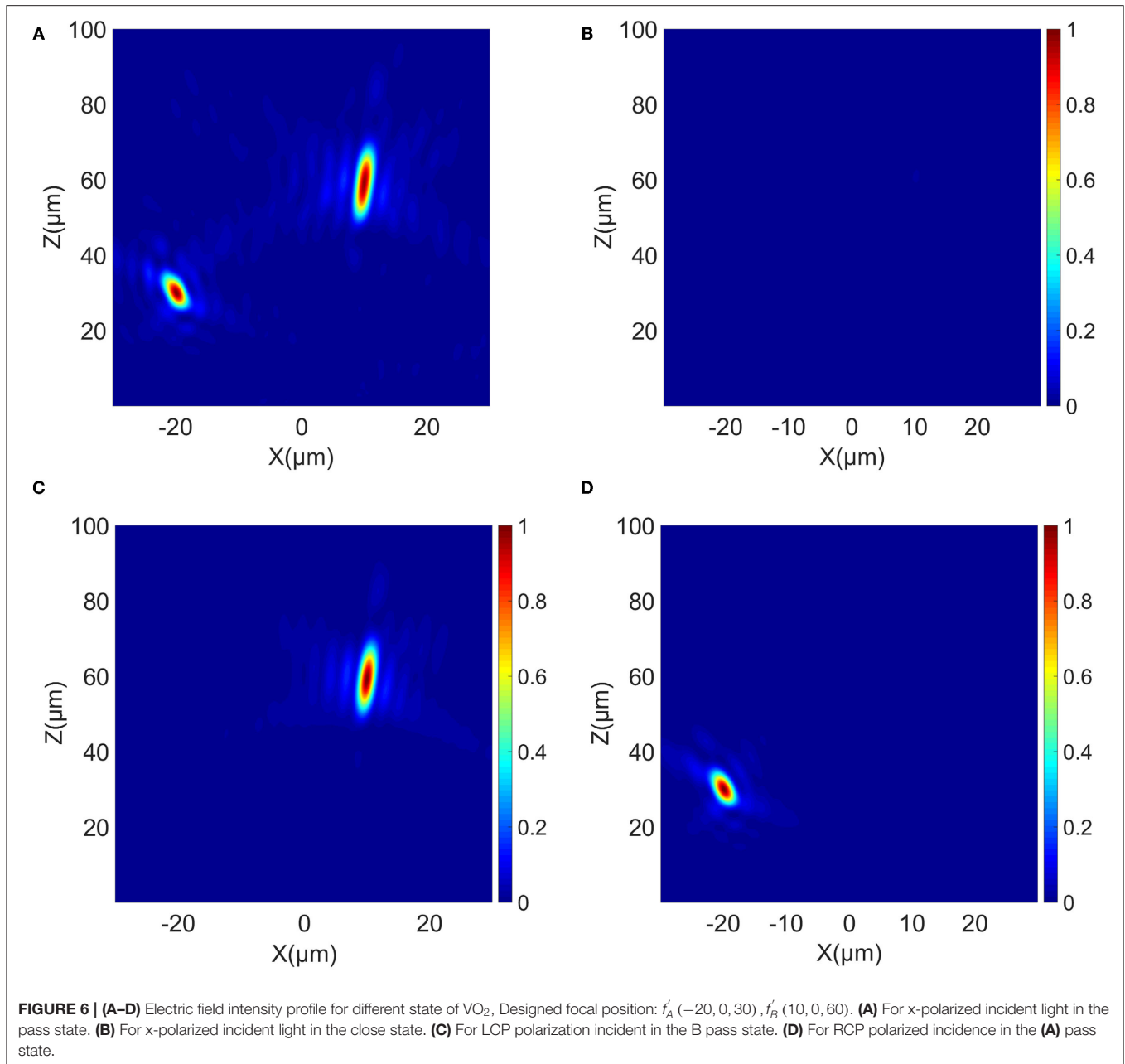
Here, f_A, f_B are the focal lengths of the two areas A and B, respectively.

Without loss of generality, we set $f_A = 30\ \mu\text{m}$, $f_B = 60\ \mu\text{m}$ as an example. When the temperature is lower than T_C , the two

areas A and B are both in I-VO₂ state (pass state), which can maintain high transmittance. As we all know, LP can be regarded as a combination of LCP and RCP of equal amplitude. Linearly polarized light will form two focal points with focal lengths f_A and f_B after passing through the metalens, as shown in **Figure 5A**. The helicity of f_A and f_B is RCP and LCP, respectively, so as to realize dual focus focusing. When the temperature is higher than T_C , the two regions A and B are in the M-VO₂ state (close state), as shown in **Figure 5B**, no focus is formed at this time.

Figure 5E is a schematic diagram of the normalized electric field intensity along the z-axis in the above two cases. It can be seen from the figure that the intensity of the light field at the focal point in the passing state is much greater than the intensity in the closed state. In contrast, the intensity at high temperatures can be approximately ignored. The focal depth at $f_2 = 60\ \mu\text{m}$ is longer. This is because the NA at the two focal points are different, and the focal plane size is different, which results in different intensity distributions. Large depth of focus, has great advantages in many fields such as microscopes, endoscopes, inspection cameras, etc. [45].

In addition, we control the two regions A and B to result in different states. As for the isolation of the states of the VO₂ materials in area A and area B, a thin insulating material can be added between the area A and the area B to avoid heat conduction. Both active heating and passive heating can achieve. Our cell structure is on the micron scale, and the temperature of each nanofins can be controlled by the semiconductor Partier effect. In order to maintain the optical transparency, one can select transparent semiconductor for desired wavelength to construct temperature controller. Let area A in the M-VO₂ state



while area B in the I-VO₂ state (B pass state). At this time, when the LCP beam is incident, a focal point with a helicity of RCP will be formed, and its focal length is f_B , as shown in **Figure 5C**. In the same way, the area A is in the I-VO₂ state, and the area B is in the M-VO₂ state (A pass state). At this time, the RCP beam is irradiated to form a focal point with a helicity of LCP, and its focal length is f_A , as shown in **Figure 5D**.

Figure 5F demonstrates the normalized intensity map of the electric field corresponding to the f_A and f_B focal points in the **Figure 5A**. The FWHM is 2.53 μm and 2.15 μm , respectively. **Figures 5G,H** correspond to the normalized intensities figures of the focal spot shown in **Figures 5C,D**, respectively, and the FWHM is 2.17 μm and 2.39 μm , respectively. The focusing

efficiency in the case of pass state, A pass state and B pass state are 31.53%, 32.45%, and 41.76%, respectively (focusing efficiency is defined as the ratio of the energy of the focal spot to the energy of the incident light).

We can also extend the focus to any position in space. As shown in Equation (7), the initial value (x_0 , y_0) can be set to change the position of the horizontal plane of the focus. We assume $f'_A = (-20\mu\text{m}, 0\mu\text{m}, 30\mu\text{m})$, $f'_B = (10\mu\text{m}, 0\mu\text{m}, 60\mu\text{m})$. Through the simulation of FDTD SOLUTIONS, we obtain the simulation figures of the focal spot in four states.

It can be seen from **Figures 6A–D** that the switching of dual focus, single focus, and no focus can be achieved at any position

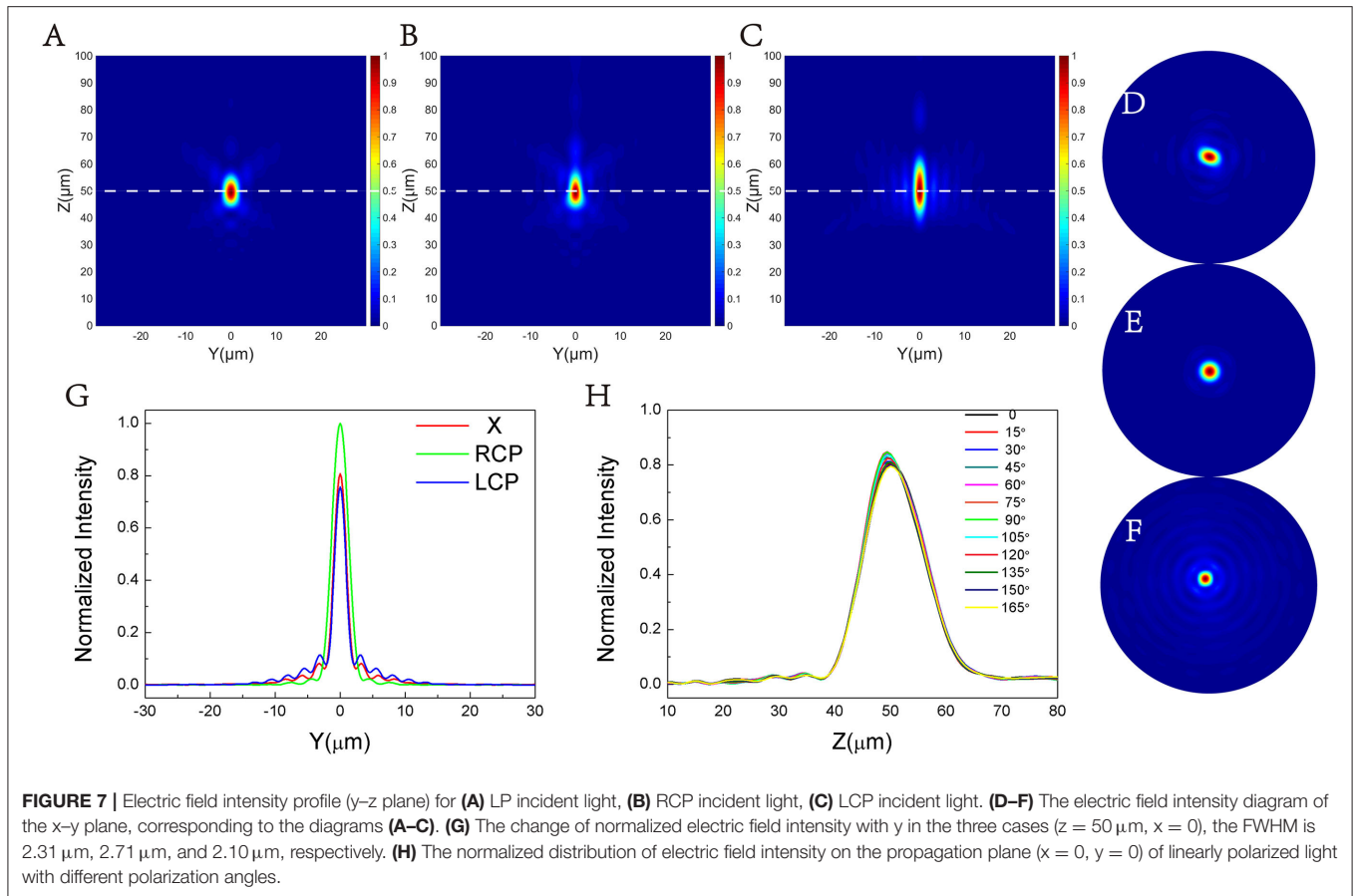


FIGURE 7 | Electric field intensity profile (y-z plane) for (A) LP incident light, (B) RCP incident light, (C) LCP incident light. (D-F) The electric field intensity diagram of the x-y plane, corresponding to the diagrams (A-C). (G) The change of normalized electric field intensity with y in the three cases (z = 50 μm, x = 0), the FWHM is 2.31 μm, 2.71 μm, and 2.10 μm, respectively. (H) The normalized distribution of electric field intensity on the propagation plane (x = 0, y = 0) of linearly polarized light with different polarization angles.

in a certain space, and the focusing effect is good. In the pass state, the FWHM corresponding to the two focal points are 2.55 μm and 2.21 μm, respectively. In A pass state and B pass state, the FWHMs of the two focal points are 2.55 μm and 2.19 μm, respectively. The focusing efficiency under pass state, A pass state, and B pass state are 32.74%, 29.78%, 41.92%, respectively.

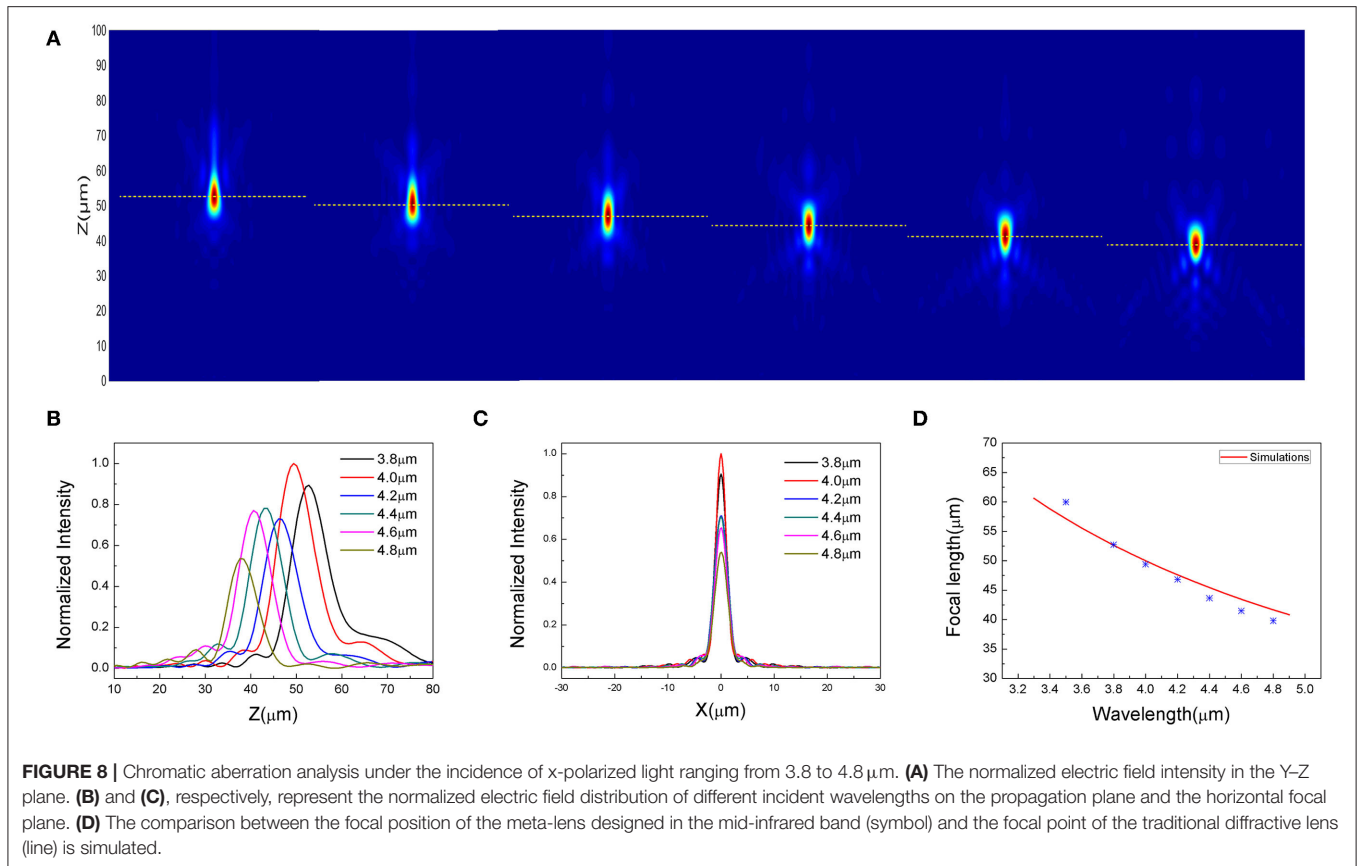
Intensity-Controllable Lens by Polarization

Assigning the same focal point $f_A = f_B = 50 \mu\text{m}$ to the two regions A and B, so that under different incident polarized light, combining with temperature control, the intensity-adjustable polarization sensitive lens with same focal point can be obtained. When LP, RCP, LCP light is incident, adjusting the regional temperature so that the meta-lens is in the passing state, A passing state and B passing state. After the radius parameter is determined (here, $r_1 = 47.6 \mu\text{m}$, $r_2 = 84 \mu\text{m}$), the intensity of the focal point is different under the incidence of different polarized light, thus realizing a polarization-dependent lens, and its intensity can be controlled by the polarization state of the incident light.

The metalens has a numerical aperture $\text{NA} = 0.859$, which has a larger resolution. In the above three cases, different polarized light has the same focal point but different intensities, which realizes the intensity-adjustable polarization-dependent metasurface lens based on the P-B phase principle.

Figures 7A-C represent the focal spots on the y-z plane formed by X, LCP and RCP incident light after passing through the lens, and the focal spots on the x-y plane correspond to Figures 7D-F respectively. From the comparison in the figure, it can be seen that the focal lengths show good consistency in these three cases, and polarization-insensitive focusing under the conditions of X, RCP, and LCP is realized. Corresponding to X, RCP, LCP polarized light incident, the focusing efficiency is 38.33%, 42.94%, 35.38%, respectively. Figure 7G gives the normalized transmitted intensity under different polarized light incidence. The three intensities have certain differences, and the maximum intensity of x-polarized light is between the LCP and RCP intensities, realizing the focus of different incident light. This function can be applied in biomedical technology, through the polarization of incident light to control the intensity of the focal electric field after passing through the lens, which can adjust the resultant of all the external forces of cells, thereby achieving the function of capturing cells. In addition, we can also adjust the area size of the unit cell in the A and B areas to control the intensity ratio of the focus.

We change the angle between the linearly polarized light and the x-axis to explore the effect of linearly polarized light with different deflection angles on the focus. Figure 7H shows the normalized distribution of electric field intensity on the propagation plane (x = 0, y = 0) of linearly polarized light with different polarization angles after passing through the metalens.



It can be found that the position of the focal spot under different polarization angles is about 50 μm , and the intensity is basically the same. Therefore, we can conclude that the focus of linearly polarized light with different angles to the x-axis is basically the same after passing through the metalens.

The metalens designed in two regions: A and B, and there will be some optical losses in the two regions when different light sources incident, which is also the main cause of optical losses. There is a scheme in which the two types of structural elements can be interlaced. This arrangement can reduce optical loss to a certain extent. Our future work will also focus on this aspect.

Characterization of Aberration

In order to characterize the performance of the above designed metasurface lens, we simulated the change of the focal length when it deviated from the design wavelength, as shown in **Figure 8A**, where the focal change simulated here is consistent with the focal shift of the diffractive lens. The focal shift of the diffractive lens can be given by [46]:

$$f(\lambda) = \frac{f(\lambda_0) \lambda_0}{\lambda} \quad (11)$$

Here, λ represents the wavelength of the incident light, λ_0 represents the design wavelength, and f_0 represents the design focal length. **Figures 8B,C**, respectively, show the normalized electric field distribution on the propagation plane and the

horizontal focal plane when the incident wavelength is changed from 3.8 μm to 4.5 μm . We can intuitively see that as the incident wavelength increases within a certain range, the focal length gradually decreases, and when the incident wavelength is far from the design wavelength, the focal spot intensity gradually decreases. It can be seen from **Figure 8D** that the designed metasurface lens (symbol) is very consistent with the focal position of the diffractive lens (line) with the same geometric parameters.

CONCLUSIONS

In conclusion, we design a multifunctional metalens based on vanadium dioxide material. By changing the state of the two areas of the temperature control lens, it is possible to switch among dual focus, single focus and no focus at any position, and the lens with the opposite helicity conversion and adjustable focus can be realized. The focusing efficiency in pass state, A pass state and B pass state are 31.53%, 32.45%, and 41.76%, respectively. At the same time, we verify that the focal point of the lens can be extended to any position within a certain area and has a good focusing effect. In addition, a polarization dependent lens is designed based on the same principle, and a polarization sensitive lens with adjustable intensity under LP, LCP, and RCP is realized by controlling the incident light of different polarization combining with temperature adjustment of the region. Finally,

we investigate the aberration of the lens, which showed good consistency with the diffractive lens.

DATA AVAILABILITY STATEMENT

The raw data supporting the conclusions of this article will be made available by the authors, without undue reservation.

AUTHOR CONTRIBUTIONS

YS: conceptualization, software, data curation, writing—original draft preparation, and visualization. YS and WL: methodology.

YS, XW, and FW: validation. FW, ZW, HM, and WL: formal analysis. YS and FW: investigation. FW, ZW, WL, XW, HM, HZ, and NL: writing—review and editing. FW: supervision and project administration. All authors contributed to the article and approved the submitted version.

FUNDING

This work is supported by National Natural Science Foundation of China (Grant No. 61774062 and No. 11674109), The Science and Technology Planning Project of Guangdong Province, China (Grant No. 2017A020219007), and Project of Department of Education of Guangdong Province, China (No.2019KTSCX257).

REFERENCES

- Wen D, Yue F, Li G, Zheng G, Chan K, Chen S, et al. Helicity multiplexed broadband metasurface holograms. *Nat Commun.* (2015) 6:8241. doi: 10.1038/ncomms9241
- Zheng G, Muhlenbernd H, Kenney M, Li G, Zentgraf T, Zhang S. Metasurface holograms reaching 80% efficiency. *Nat Nanotechnol.* (2015) 10:308–12. doi: 10.1038/nnano.2015.2
- Chen WT, Yang KY, Wang CM, Huang YW, Sun G, Chiang ID, et al. High-efficiency broadband meta-hologram with polarization-controlled dual images. *Nano Lett.* (2014) 14:225–30. doi: 10.1021/nl403811d
- Jin L, Dong Z, Mei S, Yu YF, Wei Z, Pan Z, et al. Noninterleaved metasurface for (2(6)-1) spin- and wavelength-encoded holograms. *Nano Lett.* (2018) 18:8016–24. doi: 10.1021/acs.nanolett.8b04246
- Grady N, Heyes J, Roy Chowdhury D, Zeng Y, Reiten M, Azad A, et al. Terahertz metamaterials for linear polarization conversion and anomalous refraction. *Science (New York, NY).* (2013) 340:1304–7. doi: 10.1126/science.1235399
- Cong L, Xu N, Gu J, Singh R, Han J, Zhang W. Highly flexible broadband terahertz metamaterial quarter-wave plate. *Laser Photon Rev.* (2014) 8:626–32. doi: 10.1002/lpor.201300205
- Zhang X, Yang S, Yue W, Xu Q, Tian C, Zhang X, et al. Direct polarization measurement using a multiplexed Pancharatnam–Berry metahologram. *Optica.* (2019) 6:1190–6. doi: 10.1364/OPTICA.6.001190
- Yue F, Wen D, Zhang C, Gerardot BD, Wang W, Zhang S, et al. Multichannel polarization-controllable superpositions of orbital angular momentum states. *Adv Mater.* (2017) 29:1603838. doi: 10.1002/adma.201603838
- Devlin RC, Ambrosio A, Rubin NA, Mueller JPB, Capasso F. Arbitrary spin-to-orbital angular momentum conversion of light. *Science.* (2017) 358:896–901. doi: 10.1126/science.aao5392
- Almeida E, Shalem G, Prior Y. Subwavelength nonlinear phase control and anomalous phase matching in plasmonic metasurfaces. *Nat Commun.* (2016) 7:10367. doi: 10.1038/ncomms10367
- Ye W, Zeuner F, Li X, Reineke B, He S, Qiu C-W, et al. Spin and wavelength multiplexed nonlinear metasurface holography. *Nat Commun.* (2016) 7:11930. doi: 10.1038/ncomms11930
- Walter F, Li G, Meier C, Zhang S, Zentgraf T. Ultrathin nonlinear metasurface for optical image encoding. *Nano Lett.* (2017) 17:3171–5. doi: 10.1021/acs.nanolett.7b00676
- Walther B, Helgert C, Rockstuhl C, Setzpfandt F, Eilenberger F, Kley EB, et al. Photonics: spatial and spectral light shaping with metamaterials (Adv. Mater. 47/2012). *Adv Mater.* (2012) 24:6251. doi: 10.1002/adma.201290300
- Yin X, Ye Z, Rho J, Wang Y, Zhang X. Photonic spin hall effect at metasurfaces. *Science.* (2013) 339:1405. doi: 10.1126/science.1231758
- Chen X, Chen M, Mehmood MQ, Wen D, Yue F, Qiu CW, et al. Longitudinal multifoci metalens for circularly polarized light. *Adv Opt Mater.* (2015) 3:1201–6. doi: 10.1002/adom.201500110
- YS, XW, and FW: validation. FW, ZW, HM, and WL: formal analysis. YS and FW: investigation. FW, ZW, WL, XW, HM, HZ, and NL: writing—review and editing. FW: supervision and project administration. All authors contributed to the article and approved the submitted version.
- Khorasaninejad M, Chen W, Zhu A, Oh J, Devlin R, Rousso D, et al. Multispectral chiral imaging with a meta-lens. *Nano Lett.* (2016) 16:4595–600. doi: 10.1364/CLEO_AT.2016.JTh4A.5
- Zhang F, Pu M, Luo J, Yu H, Luo X. Symmetry breaking of photonic spin-orbit interactions in metasurfaces. *Opto Electron Eng.* (2017) 44:319–25. doi: 10.3969/j.issn.1003-501X.2017.03.006
- Ji R, Chen K, Ni Y, Hua Y, Long K, Zhuang S. Dual-foci metalens for copolarized and cross-polarized transmission waves. *Adv Condens Matter Phys.* (2018) 2018:1–7. doi: 10.1155/2018/2312694
- de Gracia P, Dorronsoro C, Marcos S. Multiple zone multifocal phase designs. *Opt Lett.* (2013) 38:3526–9. doi: 10.1364/OL.38.003526
- Lin R, Li X. Multifocal metalens based on multilayer Pancharatnam–Berry phase elements architecture. *Opt Lett.* (2019) 44:2819. doi: 10.1364/OL.44.002819
- Liu H, Lu J, Wang XR. Metamaterials based on the phase transition of VO₂. *Nanotechnology.* (2017) 29:024002. doi: 10.1088/1361-6528/aa9cb1
- Chu CH, Tseng ML, Chen J, Wu PC, Chen YH, Wang HC, et al. Active dielectric metasurface based on phase-change medium. *Laser Photon Rev.* (2016) 10:986–94. doi: 10.1002/lpor.201600106
- Bai W, Yang P, Wang S, Huang J, Chen D, Zhang Z, et al. Tunable duplex metalens based on phase-change materials in communication range. *Nanomaterials.* (2019) 9:993. doi: 10.3390/nano9070993
- Xu N, Liang Y, Hao Y, Mao M, Guo J, Liu H, et al. A thermal tuning Meta-Duplex-Lens (MDL): design and characterization. *Nanomaterials (Basel).* (2020) 10:1135. doi: 10.3390/nano10061135
- Kim TT, Kim H, Kenney M, Park HS, Kim HD, Min B, et al. Amplitude modulation of anomalously refracted terahertz waves with gated-graphene metasurfaces. *Adv Opt Mater.* (2018) 6:1700507. doi: 10.1002/adom.201700507
- Wen QY, Zhang HW, Yang QH, Xie YS, Chen K, Liu YL. Terahertz metamaterials with VO₂ cut-wires for thermal tunability. *Appl Phys Lett.* (2010) 97:021111. doi: 10.1063/1.3463466
- Barker AS, Verleur HW, Guggenheim HJ. Infrared optical properties of vanadium dioxide above and below the transition temperature. *Phys Rev Lett.* (1966) 17:1286–9. doi: 10.1103/PhysRevLett.17.1286
- Long L, Taylor S, Wang L. Enhanced infrared emission by thermally switching the excitation of magnetic polariton with scalable microstructured VO₂ metasurfaces. *ACS Photon.* (2020) 8: 2219–27. doi: 10.1021/acsp Photonics.0c00760
- Kort-Kamp WJM, Kramadhati S, Azad AK, Reiten MT, Dalvit DAR. Passive radiative “thermostat” enabled by phase-change photonic nanostructures. *ACS Photon.* (2018) 5:4554–60. doi: 10.1021/acsp Photonics.8b01026
- Ito K, Nishikawa K, Iizuka H, Toshiyoshi H. Experimental investigation of radiative thermal rectifier using vanadium dioxide. *Appl Phys Lett.* (2014) 105:253503. doi: 10.1063/1.4905132
- Liu M, Xu Q, Chen X, Plum E, Li H, Zhang X, et al. Temperature-controlled asymmetric transmission of electromagnetic waves. *Sci Rep.* (2019) 9:4097. doi: 10.1038/s41598-019-40791-4

32. He J, Xie Z, Sun W, Wang X, Ji Y, Wang S, et al. Terahertz tunable metasurface lens based on vanadium dioxide phase transition. *Plasmonics*. (2016) 11:1285–90. doi: 10.1007/s11468-015-0173-2
33. Solyankin PM, Esaulkov MN, Chernykh IA, Kulikov IV, Zhanavskiy ML, Kaul AR, et al. Terahertz switching focuser based on thin film vanadium dioxide zone plate. *J Infrared Millimeter Terahertz Waves*. (2018) 39:1203–10. doi: 10.1007/s10762-018-0540-0
34. Chen W, Chen R, Zhou Y, Ma Y. A switchable metasurface between meta-lens and absorber. *IEEE Photon Technol Lett*. (2019) 31:1187–90. doi: 10.1109/LPT.2019.2917439
35. Ding F, Zhong S, Bozhevolnyi SI. Vanadium dioxide integrated metasurfaces with switchable functionalities at terahertz frequencies. *Adv Opt Mater*. (2018) 6:1701204. doi: 10.1002/adom.201701204
36. Hashemi MRM, Yang SH, Wang T, Sepúlveda N, Jarrahi M. Electronically-controlled beam-steering through vanadium dioxide metasurfaces. *Sci Rep*. (2016) 6:35439. doi: 10.1038/srep35439
37. Chen W, Chen R, Zhou Y, Chen R, Ma Y. Spin-dependent switchable metasurfaces using phase change materials. *Opt Express*. (2019) 27:25678–87. doi: 10.1364/OE.27.025678
38. Butakov NA, Valmianski I, Lewi T, Urban C, Ren Z, Mikhailovsky AA, et al. Switchable plasmonic–dielectric resonators with metal–insulator transitions. *ACS Photon*. (2017) 5:371–7. doi: 10.1021/acsphotonics.7b00334
39. Mao M, Liang Y, Liang R, Zhao L, Xu N, Guo J, et al. Dynamically temperature-voltage controlled multifunctional device based on VO₂ and graphene hybrid metamaterials: perfect absorber and highly efficient polarization converter. *Nanomaterials*. (2019) 9:1101. doi: 10.3390/nano9081101
40. Verleur HW, Barker AS, Berglund CN. Optical properties of VO₂ between 0.25 and 5 eV. *Phys Rev*. (1968) 172:788–98. doi: 10.1103/PhysRev.172.788
41. Choi HS, Ahn JS, Jung J, Kim DH. Mid-infrared properties of a VO₂ film near the metal-insulator transition. *Phys Rev B Condens Matter*. (1996) 54:4621–8. doi: 10.1103/PhysRevB.54.4621
42. Hasman E, Kleiner V, Biener G, Niv A. Polarization dependent focusing lens by use of quantized Pancharatnam–Berry phase diffractive optics. *Appl Phys Lett*. (2003) 82:328–30. doi: 10.1063/1.1539300
43. Aieta F, Genevet P, Kats MA, Yu N, Blanchard R, Gaburro Z, et al. Aberration-free ultrathin flat lenses and axicons at telecom wavelengths based on plasmonic metasurfaces. *Nano Lett*. (2012) 12:4932–6. doi: 10.1021/nl302516v
44. Berry MV. The adiabatic phase and pancharatnam's phase for polarized light. *J Modern Opt*. (1987) 34:1401–7. doi: 10.1080/09500348714551321
45. Bai W, Yang P, Wang S, Huang J, Chen D, Zhang Z, et al. Actively tunable metalens array based on patterned phase change materials. *Appl Sci*. (2019) 9:4927. doi: 10.3390/app9224927
46. Dobson SL, Sun PC, Fainman Y. Diffractive lenses for chromatic confocal imaging. *Appl Opt*. (1997) 36:4744–8. doi: 10.1364/AO.36.004744

Conflict of Interest: The authors declare that the research was conducted in the absence of any commercial or financial relationships that could be construed as a potential conflict of interest.

The reviewer QS declared a shared affiliation with one of the authors, XW, to the handling editor at time of review.

Copyright © 2021 Song, Liu, Wang, Wang, Wei, Meng, Lin and Zhang. This is an open-access article distributed under the terms of the Creative Commons Attribution License (CC BY). The use, distribution or reproduction in other forums is permitted, provided the original author(s) and the copyright owner(s) are credited and that the original publication in this journal is cited, in accordance with accepted academic practice. No use, distribution or reproduction is permitted which does not comply with these terms.

Advantages of publishing in Frontiers



OPEN ACCESS

Articles are free to read
for greatest visibility
and readership



FAST PUBLICATION

Around 90 days
from submission
to decision



HIGH QUALITY PEER-REVIEW

Rigorous, collaborative,
and constructive
peer-review



TRANSPARENT PEER-REVIEW

Editors and reviewers
acknowledged by name
on published articles

Frontiers

Avenue du Tribunal-Fédéral 34
1005 Lausanne | Switzerland

Visit us: www.frontiersin.org

Contact us: frontiersin.org/about/contact



REPRODUCIBILITY OF RESEARCH

Support open data
and methods to enhance
research reproducibility



DIGITAL PUBLISHING

Articles designed
for optimal readership
across devices



FOLLOW US

@frontiersin



IMPACT METRICS

Advanced article metrics
track visibility across
digital media



EXTENSIVE PROMOTION

Marketing
and promotion
of impactful research



LOOP RESEARCH NETWORK

Our network
increases your
article's readership